

Plasma breakdown and current formation in single core and doublet configurations on TCV

THÈSE N° 7825 (2017)

PRÉSENTÉE LE 15 SEPTEMBRE 2017
À LA FACULTÉ DES SCIENCES DE BASE
SPC - PHYSIQUE DU TOKAMAK TCV
PROGRAMME DOCTORAL EN PHYSIQUE

ÉCOLE POLYTECHNIQUE FÉDÉRALE DE LAUSANNE

POUR L'OBTENTION DU GRADE DE DOCTEUR ÈS SCIENCES

PAR

Joyeeta SINHA

acceptée sur proposition du jury:

Prof. H. M. Rønnow, président du jury
Dr B. Duval, Dr H. Reimerdes, directeurs de thèse
Dr G. Jackson, rapporteur
Dr F. Felici, rapporteur
Dr I. Furno, rapporteur



ÉCOLE POLYTECHNIQUE
FÉDÉRALE DE LAUSANNE

Suisse
2017

Abstract

This thesis presents an experimental investigation of the plasma formation in the TCV tokamak. The primary goal of this work was to program a reliable and smooth plasma formation at several positions within the TCV vessel and then use the gained understanding to revisit the creation of doublet plasma formation.

The first part of this thesis is dedicated to understanding and improving the single-axis plasma formation scenario in TCV. A database for the single-axis TCV plasma formation scenario was created for discharges spanning several years of operation to understand the physics of the plasma formation dynamics. The database shows that most of the failed plasma formation in TCV were during the burn-through and ramp-up phase with only 0.5% of the discharges failing at breakdown. The failed plasma breakdowns are mainly attributed to technical issues, such as no injection of neutral gas into the vacuum vessel, absence of the toroidal field or the Ohmic coil current, and issues with the plasma control system. The improvement of the single-axis plasma formation was separated into two parts: improvement of the breakdown scenario and improvement of the plasma burn-through and ramp-up scenario.

During the breakdown phase, a large mismatch was exposed between the intended and experimentally obtained vertical breakdown position, for both the $Z = 0.05$ m and the $Z = +0.23$ m standard vertical breakdown positions and for both I_p and B_ϕ directions. This mismatch was caused by an additional poloidal field mainly due to errors in the back-off of the stray field generated by vessel currents. The use of a vessel resistivity assuming axisymmetry in the TCV discharge preparation procedure to model the vessel currents was identified as the main reason for the mismatch in the breakdown positions. Correction of the breakdown position was important to obtain a better agreement between the entire programmed and experimental magnetic field configuration, and thereby, provide a better control of the breakdown time and plasma current ramp rate. The correction of the mismatch was necessary to obtain a simultaneous double breakdown that requires that the two magnetic null points have similar effective connection lengths.

The analysis of the plasma formation database revealed that most of the failed plasma formation during the burn-through and ramp-up phase occurred due to insufficient, albeit often temporary, Ohmic heating to sustain the plasma. The insufficient Ohmic heating was either due an insufficient initial I_p ramp rate, or a combined effect of strong I_p and/or radial position oscillations caused by the feedback control system due to too high initial I_p ramp rate. A *bump-less transfer* control technique was implemented to improve the reliability of plasma formation by avoiding the strong oscillations in I_p and radial position that resulted in reliable

and sufficient Ohmic heating. Experiments showed that the use of bump-less transfer control technique resulted in successful plasma formation, despite, very high initial plasma current ramp rate.

Understanding gained through the analysis of the breakdown phase and of the burn-through and ramp-up phase was combined to propose an improved plasma formation scenario. The breakdown position mismatch was reduced using a new breakdown scenario preparation employing the experimental vessel resistivity to model the vessel currents. Experiments proved that for all three standard breakdown positions within the TCV vessel the mismatch between the intended and experimental obtained vertical position was reduced, and a wider operational range of breakdown parameters for breakdown time and ramp rate control obtained. Furthermore, a plasma current ramp-up phase with reduced plasma current and radial position oscillations was obtained. The improvements were also applied to create two new scenarios at the top ($Z = +0.4$ m) and bottom part ($Z = -0.4$ m) of the vessel in preparation of the creation of a doublet shaped plasma.

The second part of this thesis focuses on developing a doublet shaped plasma configuration. The doublet configuration is a highly unconventional plasma configuration, that was researched in the 1970's but, that research was abandoned due to the difficulties to control the configuration. TCV's modern and unique shaping capabilities warrant an effort to revisit the configuration. Successful simultaneous breakdown at two locations in TCV was achieved by using the improved inductive breakdown scenario. The similar magnetic properties of the two magnetic null points ensured that the plasma current ramp rate in the two droplets were close and the plasma current in both droplets was ramped up to 50 kA each with Ohmic heating alone. A feedback control of plasma current and plasma position was then implemented by using the poloidal field coils and the ECH as the actuators, respectively. A highly reproducible doublet formation scenario was finally achieved and was verified by several diagnostics. A highest plasma current of $I_p = 130$ kA was achieved in each droplet, with a core electron temperature at 1.3 keV, core electron density at $1.3 \times 10^{19} \text{ m}^{-3}$, and 30 ms duration with ECRH heating. Experiments show that the ECRH heating leads to strong pressure temperature gradients in the vicinity of the separatrix. These experiments also reveal a surprising result that heating one droplet leads to an almost equal temperature increase in the other droplet. This suggest that the transport barrier is located outside the separatrix. As a consequence ECRH is not an effective tool to control the current sharing between the droplets. Although a stationary doublet regime was not yet obtained, the basis for further experimental investigations for the physics of doublets was established.

Key words: plasma, tokamak, fusion, breakdown, plasma formation, doublet, plasma control, plasma current ramp-up, plasma burn-through.

Résumé

Cette thèse de doctorat présente une étude expérimentale de la formation de plasma dans le Tokamak à Configuration Variable (TCV). L'objectif premier de ce travail a été de programmer une formation de plasma fiable, et ayant lieu en douceur, à plusieurs positions au sein de l'enceinte à vide de TCV. Le savoir acquis durant cette première phase a ensuite été mis à profit pour revisiter la création d'un doublet de plasma.

La première partie de cette thèse est dédiée à la compréhension et à l'amélioration du scénario de formation d'un plasma mono-axial dans TCV. Une base de données pour le scénario de formation du plasma mono-axial de TCV a été créée pour des décharges s'étalant sur plusieurs années d'opération afin de comprendre la physique sous-jacente de la formation dynamique du plasma. La base de données montre que la plupart des formations de plasma avortées l'ont été durant la phase de burn-through ou de ramp-up avec seulement 0.5% des décharges échouant lors du claquage. Les plasmas avortés durant le claquage le sont principalement à cause de problèmes techniques, comme par exemple l'absence d'injection de gaz neutre dans l'enceinte à vide, l'absence de champ toroidal ou de courant dans les bobines Ohmiques, ainsi que des dysfonctionnements du système de contrôle du plasma. L'amélioration de la formation du plasma mono-axial a été réalisée en deux étapes : l'amélioration du scénario de claquage et l'amélioration des scénarii de burn-through et ramp-up.

Durant la phase de claquage, un grand décalage a été observé entre la position de claquage programmée et celle obtenue expérimentalement, et ce pour les deux positions standards de claquage $Z = +0.05m$ et $Z = +0.23m$ ainsi que pour les deux directions de I_p et B_ϕ . Le décalage a été causé par un champ poloidal additionnel dû aux erreurs d'estimation des champs parasites générés par les courants circulant dans l'enceinte à vide. L'utilisation d'une résistivité de l'enceinte obtenue en supposant une asymétrie dans la procédure de préparation de la décharge de TCV a été identifiée comme étant la principale cause du décalage des positions de claquage. La correction de la position de claquage a été une étape importante pour l'obtention d'un meilleur accord entre l'intégralité de la configuration magnétique programmée et celle obtenue expérimentalement, et pour obtenir ainsi un meilleur contrôle de temps de claquage et du taux de rampe du courant plasma. La correction du décalage a été nécessaire pour l'obtention d'un double claquage simultané qui nécessite que les deux points de champ magnétique nul aient des longueurs de connexions similaires.

L'analyse de la base de données de la formation du plasma a révélé que la plupart des formations de plasma avortées durant les phases de burn-through ou de ramp-up l'ont été à cause d'un chauffage Ohmique insuffisant pour maintenir le plasma. L'insuffisance du chauffage

Ohmique était due soit à un taux de rampe I_p initial trop faible soit à un effet combiné d'un grand I_p et/ou d'oscillations de la position radiale causées par le système de contrôle de la rétroaction et trouvant ses origines dans un taux de rampe initial I_p trop élevé. Une technique de contrôle dite de *bump-less transfer* a été implémentée en vue d'une amélioration de la fiabilité de la formation du plasma par la suppression des fortes oscillations de I_p et de la position radiale. Cette dernière a permis un chauffage Ohmique fiable et suffisant. Experimentalement, il a été montré que l'utilisation de la technique de *bump-less transfer control* entraîne une formation de plasma réussie et ce malgré un taux de rampe initial de courant plasma très élevé. Les savoirs acquis à travers l'analyse de la phase de claquage et celui acquis à travers l'analyse des phases de burn-through et de ramp-up ont été combinés afin de proposer un scénario de formation de plasma amélioré. Le décalage constaté dans la position de claquage a été réduit en utilisant une nouvelle préparation du scénario de claquage utilisant la résistivité de l'enceinte à vide expérimentale afin de modéliser les courants de l'enceinte. Les expériences ont prouvé que pour l'ensemble des trois positions standards de claquage au sein de l'enceinte de TCV, le décalage entre les positions verticales programmées et obtenues a été réduit, et une large gamme de paramètres utiles au contrôle du temps de claquage et du taux de rampe a été obtenue. De plus, une phase de montée du courant plasma caractérisée par réduction du courant plasma et des oscillations de la position radiale a été obtenue. Les améliorations ont aussi été appliquées à la création de deux nouveaux scénarii dans la partie supérieure ($Z = +0.4m$) et la partie inférieure ($Z = -0.4m$) de l'enceinte à vide dans la préparation de la création d'un plasma de type doublet.

La seconde partie de cette thèse se focalise sur le développement d'une configuration de plasma de type doublet. Cette configuration est une configuration de plasma inconventionnelle. Des recherches ont été entreprises dans les années 70 mais l'idée d'obtenir cette configuration a été abandonnée à cause des difficultés de contrôle qu'elle représente. Les capacités modernes et uniques de TCV en terme de profilage ont permis d'explorer à nouveau cette configuration. Un claquage simultané et réussi à deux positions de TCV a été obtenu en utilisant un scénario amélioré de claquage inductif. Les propriétés magnétiques similaires des deux points de champ magnétique nul ont garanties des taux de rampe proche des courants plasma dans les deux goutelettes. Les courants plasma dans les deux goutelettes ont été élevés jusqu'à $50kA$ chacun en utilisant uniquement un chauffage Ohmique. Un contrôle rétroactif du courant plasma et de la position du plasma a ensuite été implémenté en utilisant respectivement les bobines de champ poloïdal et le chauffage électron cyclotron (ECH) en tant qu'actuateurs. Un scénario de formation de doublet fortement reproductible a finalement été réalisé et vérifié grâce à plusieurs diagnostics. Un courant plasma plus grand, de $I_p = 130kA$, a été obtenu dans chaque goutelette, avec une température électron au coeur de $1.3keV$, une densité électronique au coeur de $1.3 \times 10^{19} m^{-3}$, et une durée de chauffage ECH de $30ms$. Les expériences ont montré que le chauffage ECH conduit à de forts gradients de température proche de la séparatrice. Ces expériences ont également révélé un résultat surprenant : le chauffage d'une seule des goutelettes produit une augmentation de température presque égale dans l'autre goutelette. Ceci suggère que la barrière de transport est située à l'extérieure de la séparatrice. Par conséquent, le chauffage ECH n'est pas un outil efficace pour le contrôle de la

répartition de courant entre les goutelettes. Malgré le fait qu'un régime stationnaire de plasma de type doublet n'ait pas été obtenu, une base d'étude pour une exploration expérimentale plus approfondie de la physique des doublets a été établie.

Mots clés : plasma, tokamak, fusion, claquage, formation du plasma, doublet, contrôle du plasma, ramp-up du courant plasma, burn-through du plasma.

Contents

Abstract (English/Français/Deutsch)	i
List of figures	xi
List of tables	xix
1 Introduction	1
1.1 Need for sustainable energy	1
1.2 Thermonuclear fusion and magnetic confinement	1
1.3 Tokamak	5
1.4 Motivation of the thesis	6
1.4.1 Improve the single-axis plasma formation scenario in TCV	7
1.4.2 Develop a doublet shaped plasma configuration in TCV	8
1.5 Synopsis of results	9
1.6 Outline of thesis	10
2 TCV Tokamak	11
2.1 Tokamak components	11
2.1.1 Coil system	12
2.1.2 Vacuum vessel	14
2.1.3 First wall	15
2.2 Electron Cyclotron Resonance Heating system	16
2.3 Diagnostics	18
2.3.1 Magnetic Diagnostics	18
2.3.2 Baratron pressure gauges	20
2.3.3 Far infrared interferometer	21
2.3.4 Thomson scattering	22
2.3.5 Photodiodes	24
2.3.6 Fast Visible Camera	26
2.3.7 Soft X-ray diagnostic	27
2.4 Free Boundary Tokamak Equilibrium	29
2.5 Matrix Generation Algorithm and Measurement Simulation	29
2.6 TCV plasma control system	30
2.6.1 Hybrid control system	30

Contents

2.6.2	Digital control system	31
3	Physics of the plasma formation in tokamaks	33
3.1	Physics of the breakdown phase	35
3.2	Physics of the burn-through phase	37
3.3	Physics of plasma current ramp-up phase	39
3.4	Conclusion	40
4	Breakdown scenario	41
4.1	Breakdown strategy in TCV and comparison to other tokamaks	41
4.1.1	Breakdown strategy in TCV	41
4.1.2	Breakdown strategy in other tokamaks	43
4.1.3	Comparison of the breakdown strategy in TCV with other tokamaks . . .	44
4.2	Programming of the breakdown magnetic configuration in TCV using MGAMS	45
4.3	Estimation of the breakdown parameters	48
4.3.1	Estimation of the neutral gas pressure	48
4.3.2	Estimation of the toroidal electric field	50
4.3.3	Estimation of the magnetic configuration up to the time of breakdown .	51
4.3.4	Estimation of the breakdown time	54
4.4	Analysis of the present TCV breakdown scenario database	55
4.5	Experiments to empirically reduce the discrepancy in breakdown position . .	58
4.6	Experiments to study the effect of breakdown parameters on breakdown time .	59
4.6.1	Effect of the gradient of the poloidal field	59
4.6.2	Effect of neutral gas pressure	60
4.6.3	Effect of toroidal electric field	62
4.7	Conclusion	63
5	Plasma burn-through and ramp-up scenario	65
5.1	Programming of plasma current ramp-up scenario in TCV	65
5.2	Estimation of plasma parameters during the plasma current ramp-up phase . .	68
5.2.1	Single filament approach	69
5.2.2	Multiple filament approach	70
5.2.3	LIUQE reconstruction	71
5.2.4	Interferometer measurements	73
5.3	Analysis of the plasma current ramp-up scenario in TCV	74
5.4	Experiments to improve the TCV plasma current ramp-up scenario	79
5.4.1	Experiments to reduce the I_p ramp rate	79
5.4.1.1	Reduction of the loop voltage	79
5.4.1.2	Modification of the gradient of the quadrupole field	80
5.4.2	Experiments to control the I_p oscillations	81
5.4.2.1	Early activation of the plasma current feedback control	81
5.4.2.2	Bump-less transfer control technique for plasma current and radial position feedback control in TCV	83

5.4.2.3	Modification of the reference plasma current ramp rate	86
5.5	Conclusion	87
6	New plasma formation scenario in TCV	89
6.1	Modifications to improve the plasma formation in TCV	89
6.2	Experimental results for the improved plasma formation scenario	92
6.3	Development of new plasma formation scenarios (at $Z = \pm 0.4$ m)	95
6.4	Conclusion	96
7	Development of a doublet configuration in TCV	99
7.1	Programming of simultaneous double breakdown	101
7.2	Feedback phase of doublet shaped plasma configuration	102
7.2.1	Plasma current control for the two droplet shaped plasmas	102
7.2.2	Plasma model for the doublet shaped plasma	104
7.2.3	Strategies to control the position of the two droplet shaped plasmas . . .	107
7.2.3.1	Position control system actuators	109
7.2.4	Stability analysis of the vertical position control for doublet shaped plasma	110
7.3	Experimental results to create doublet shaped plasma scenario	111
7.3.1	Experimental results in simultaneous double breakdown	111
7.3.2	Experimental results in the ramp-up phase with Ohmic heating	112
7.3.3	Experimental results in the ramp-up phase with ECH feedback control .	117
7.4	Conclusion	120
8	Conclusion	123
A	Appendix	127
	Bibliography	138
	Acknowledgements	139
	Curriculum Vitae	141

List of Figures

1.1	Binding energy curve for different atomic elements. Image: www.nuceng.ca/igna/binding_energy.htm	2
1.2	Cross-section of a few possible fusion reactions as a function of the particle energy. Image: www-fusion-magnetique.cea.fr/gb/fusion/principes/principes01.htm	3
1.3	Drift motion of the charged particles in a toroidal magnetic field. Image: [70].	4
1.4	Illustration of the tokamak configuration. Image: www.euro-fusion.org/2011/09/tokamak-principle-2/	5
1.5	Flux contours of (a) a limited plasma configuration and (b) a diverted plasma configuration. Image: [65].	7
2.1	Cutout view of TCV showing poloidal and toroidal field coils, ohmic coils, vacuum vessel and the plasma flux surfaces with the magnetic field lines. Image: [20].	12
2.2	Poloidal cross section of TCV with the main sources of the poloidal magnetic field, which include the Ohmic coils (A-D), PF coils (E-F), the fast internal coils (G) and the coils approximating the toroidal field bus bar (T).	13
2.3	Fisheye view of the TCV first wall covered with approximately 1692 graphite tiles.	14
2.4	Poloidal cross section of the TCV tokamak showing the X2 and X3 launchers of the ECRH system and indicating the range of poloidal mirror steering.	16
2.5	Schematic of the X2 launcher showing the 3 fixed mirrors and 1 real-time steerable mirror. Also the steering angle conventions used for the launchers is shown. Image: [20].	17
2.6	Schematic of a single turn magnetic probe. Image: [32].	18
2.7	TCV poloidal cross section with the poloidal flux loops (red crosses), the magnetic field probes (red rectangles).	20
2.8	Schematic of the far infrared interferometer on TCV.	21
2.9	TCV poloidal cross-section showing the line of sight for the far infrared interferometer system. The red line represent the central chord of FIR used for density control.	23
2.10	TCV poloidal cross-section showing the Thomson scattering measurement points.	24
2.11	Schematic showing the different D_α photodiode chords and their positions in TCV.	25
2.12	Photron Ultima APX-RS fast framing visible camera used in TCV. (a) Front view of the camera and (b) back view of the camera.	27
2.13	TCV poloidal cross section showing the lines of sight of the XTOMO diagnostic.	28

List of Figures

2.14 Schematic of the TCV hybrid control system showing its connections to the diagnostics and the actuators. Image: [48]	30
2.15 Top view of the SCD. Image: [3].	32
3.1 Schematic figure of the time evolution of (a) plasma current, (b) D_α emission, (c) radiation and ionization power loss, and (d) the electron temperature in a typical deuteron plasma formation. The breakdown (blue), burn-through (green), plasma current ramp-up (red) phases and the overlap between the burn-through and plasma current ramp-up phase (brown) are color labeled, respectively. The vertical dashed line represents the radiation barrier.	34
3.2 Condition for the Townsend criterion ($v_{ion} = v_{loss}$) for different connection lengths for deuterium gas with $A = 3.9 \text{ Pa}^{-1}\text{m}^{-1}$ and $B = 96.6 \text{ VPa}^{-1}\text{m}^{-1}$	37
4.1 Breakdown strategy in TCV. Evolution of (a) the Ohmic coil current (I_{OH}), (b) the resulting loop voltage (V_{loop}), (c) the toroidal field (B_{tor}), and (d) the measured gas flux.	42
4.2 Townsend diagram showing the comparison of the breakdown strategies in TCV, JET and KSTAR.	44
4.3 Schematic showing the programming of a typical breakdown scenario in TCV at the $Z = +0.23 \text{ m}$ breakdown location. A subset of PF coils is selected as <i>quadrupole coils</i> (blue) and another subset as the <i>back-off coils</i> (red). The 'o' denotes the two quadrupole control points on the HFS and LFS of the magnetic axis of the first FBTE equilibrium marked with an 'x'.	45
4.4 Evolution of (a) the imposed quadrupole vertical field (B_Z^\pm), (b) the equilibrium field obtained from FBTE, (c) the vertical field to prevent a early breakdown, (d) the total field at the two quadrupole control points in MGAMS during a standard breakdown scenario, (e) the resulting radial position of the null point and, (f) the gradient of the poloidal field at the intended null point.	46
4.5 (a) Evolution of the neutral pressure measured with baratrons in the outboard mid-plane ('mid') and under the floor ('div') in failed He discharge attempts. (b) Decay time of the neutral gas (τ_{pump}) obtained from exponential fits of the baratron measurements for failed helium and deuterium discharge attempts in TCV.	49
4.6 Comparison of (a) the two baratron measurements with the fitted neutral gas pressure values obtained from three parameter fit for a helium discharge in TCV, (b) the amplitude modification factor ($c^{\text{mid,div}}$) for the two baratrons for helium and deuterium gas, and (c) the time response ($\tau_b^{\text{mid,div}}$) for the two baratrons for helium and deuterium discharges.	50

4.7	Reconstruction of the magnetic field configuration at the time of breakdown obtained using the breakdown code. The green 'x' denotes the programmed breakdown location in MGAMS, and the black 'x' denote the position of the experimental null points. The dotted blue lines denote B_p contours with the numbers indicating its magnitude in mT. The solid black lines are the poloidal flux contours.	53
4.8	Comparison of (a) the reconstructed magnetic field configuration and (b) the inverted fast framing camera image obtained using the GTI package. The 'x' denotes the experimental null point locations obtained from the <i>breakdown</i> code.	54
4.9	The estimation of the breakdown time using the plasma current and the D_α signal. (a) I_p evolution from the magnetic measurements, and (b) D_α signal from the vertical PD. The vertical black dashed line represents the respective breakdown time estimates.	55
4.10	Probability density function of experimentally obtained vertical breakdown position Z_b for (a) $B_\phi > 0$, $I_p > 0$ and (b) $B_\phi < 0$, $I_p < 0$ scenarios. Programmed breakdown at $Z = 0.23$ m (blue), $Z = 0.05$ m (green) and $Z = -0.23$ m (red).	56
4.11	Experimentally obtained breakdown time t_b as a function of (left) loop voltage V_{loop} and (right) effective connection length L_{eff} , for (top) $B_\phi > 0$, $I_p > 0$ and (bottom) $B_\phi < 0$, $I_p < 0$ scenarios. Magnetic axis of the first FBTE equilibrium at $Z = 0.23$ m (blue), $Z = 0.05$ m (green) and $Z = -0.23$ m (red).	57
4.12	Comparison of the reconstructed magnetic field configuration at the time of breakdown for (a) $B_R^\pm = 0$ mT and (b) $B_R^\pm = -1$ mT.	59
4.13	Time evolution of (a) poloidal field gradient, (b) effective connection length at the experimentally obtained null point. Effect of programmed value of poloidal field gradient in MGAMS for $t = 0$ on experimentally obtained (c) breakdown time, (d) L_{eff} at null point, (e) initial plasma current ramp rate.	60
4.14	(a) Required effective connection length L_{eff} to breakdown as a function of neutral gas pressure p_n at constant loop voltage $V_{loop} \approx 10$ V, theoretical (red) and experimental (blue). Experimentally obtained (b) breakdown time, (c) initial plasma current ramp rate.	61
4.15	(a) Required effective connection length L_{eff} to breakdown as a function of toroidal electric field E_ϕ at constant pressure $p_n = 0.04$ Pa, theoretical (red) and experimental (blue). Experimentally obtained (b) breakdown time, (c) initial plasma current ramp rate.	62
5.1	Evolution of the programmed (a) plasma current, (b) plasma cross section, (c) radial position of the magnetic axis, (d) safety factor q_{95} and, (e) plasma internal inductance.	66
5.2	Schematic to describe the radial position observer in TCV. Black cross denotes the magnetic axis, a and b are the two fixed control points located on the HFS and LFS respectively where the flux is being extrapolated. The black contour represents the plasma boundary for a single-axis limited plasma configuration	67

List of Figures

5.3	(a) Poloidal flux and field distributions at the time of breakdown. Programmed (green cross) and experimental (black cross) null points and evolution of the single filament plasma position (blue line). Evolution of (b) plasma current, (c) plasma radial position, and (d) plasma vertical position obtained using the single filament method. The green line denotes the programmed plasma radial position and the magenta lines correspond to the inner and outer wall of TCV. .	69
5.4	(a) Plasma current distribution in the different filaments and plasma position (R_{ax}^{mf}, Z_{ax}^{mf}) obtained by the multiple filament method the multiple filament plasma position (blue line). Evolution of (b) the plasma current, (c) plasma radial position, and (d) plasma vertical position obtained using the multiple filament method. The green line denotes the programmed radial position reference.	72
5.5	Estimation of the (a) plasma current, (b) plasma radial and, (c) plasma vertical positions obtained from the LIUQE code by using only one base function to characterize the plasma current distribution.	73
5.6	(a) Comparison of the FIR measurements with the Gaussian fit yielding the estimates of the radial position of the magnetic axis and the plasma width, (b) evolution of the estimated radial position of the plasma and (c) of the plasma width.	74
5.7	Typical TCV plasma current ramp up scenario with current ramp rate close to reference. (a) Evolution of the radial position of the plasma along with the line-integrated plasma density obtained using interferometer (FIR), (b) evolution of I_p , (c) D_α signal from the vertical photo diode, (d) evolution of V_{loop} , and (e) raw magnetic fluctuation signal from the magnetic probe during the plasma formation in TCV.	75
5.8	Typical TCV plasma current ramp up scenario with a high initial plasma current ramp rate. (a) Evolution of the radial position of the plasma along with the line-integrated plasma density obtained using interferometer (FIR), (b) evolution of I_p , (c) D_α signal from the vertical photo diode, (d) evolution of V_{loop} , and (e) raw magnetic fluctuation signal from the magnetic probe during the plasma formation in TCV.	76
5.9	Magnetic fluctuation amplitude as a function of (a) maximum experimental plasma current ramp rate and (b) minimum experimental current ramp rate during the successful (blue) and failed (red) TCV ramp-up phases.	77
5.10	Probability density function of maximum experimental plasma current ramp rate for the TCV plasma current ramp-up scenario. The threshold for with or without MHD activity is shown in Fig. 5.9.	78
5.11	Effect of the loop voltage on the burn-through and ramp-up phase. (a) Comparison of different applied V_{loop} . Evolution of (b) I_p , (c) D_α emission along a vertical chord, and (d) the plasma radial position (R_{ax}) obtained from FIR measurements. The black vertical line denotes the activation of the I_p and plasma position feedback control system.	80

5.12	Effect of the modification of the gradient of the quadrupole field on the burn-through and ramp-up phase. (a) Comparison of I_P for different gradients of the quadrupole field, (b) evolution of V_{loop} , (c) evolution of D_α emission observed using vertical photodiode, and (d) evolution of the plasma radial position (R_{ax}) obtained from FIR measurements. The black vertical line denotes the activation of the I_P and plasma position feedback control system.	81
5.13	Effect of implementation of IP feedback control from $t = 0$ s on the evolution of plasma. (a) Comparison of the I_P evolution for different proportional gains for the I_P feedback control at $t = 0$ s onwards, (b) evolution of V_{loop} , (c) evolution of D_α emission observed using vertical photodiode, and (d) evolution of the plasma radial position obtained from FIR measurements.	82
5.14	SIMULINK simulations to show the effect of the bump-less transfer control technique on the I_P feedback control using the RZIP model. (a) Evolution of I_P for different values of τ_{bl} , the blue dotted horizontal line represents the I_P^{ref} and the black dotted vertical line denotes the time corresponding to the bump-less control technique activation, and (b) evolution of the I_P error (ϵ_{IP}) for different values of τ_{bl} for I_P feedback control.	84
5.15	Effect of the implementation of bump-less transfer control technique for I_P and radial position feedback control with different τ_{bl} for $z = 0.05$ m breakdown scenario in TCv. (a) Evolution of I_P , black dotted line denotes the I_P reference, (b) evolution of the I_P error, (c) evolution of V_{loop} , (d) D_α signal from the vertical photo diode, and (e) evolution of the plasma radial position (R_{ax}) obtained from FIR measurements. The black vertical line denotes the activation of the bump-less I_P and plasma position feedback control system and the black horizontal line shows the I_P threshold value.	85
5.16	Effect of different I_P^{ref} on the ramp-up phase. $I_P^{ref} = 2 \text{ MAs}^{-1}$ (blue), 4 MAs^{-1} (red) and 8 MAs^{-1} (black). (a) Evolution of I_P , the dotted lines represent the different I_P references and the solid lines represent the different experimental I_P , (b) evolution of the I_P error, (c) evolution of V_{loop} , (d) D_α signal from the vertical photo diode, and (e) evolution of the plasma radial position (R_{ax}) obtained from FIR measurements. The vertical lines (blue and red) denote the activation of the bump-less I_P and plasma position feedback control system for the different reference I_P ramp rates respectively. The black horizontal line shows the I_P threshold value.	86
6.1	(a) The nominal and experimentally obtained vessel filament resistivity and (b) the percentage of difference in resistivity.	90

6.2	Comparison of the evolution of the programmed gradient of the quadrupole magnetic field in MGAMS for the legacy and improved breakdown scenarios in TCV. Evolution of (a) the imposed vertical quadrupole field (B_Z^\pm), (b) the equilibrium vertical field obtained from FBTE (B_Z^{FBTE}), (c) the external vertical field to prevent a early breakdown, (d) the total vertical field at the two quadrupole control points in MGAMS during a standard breakdown scenario, (e) the radial position of the null point (R_{npt}) with the minimum ∇B_p , and (f) ∇B_p at the null point with time.	91
6.3	Comparison of the reconstructed (a) residual poloidal field and flux after back-off, (b) quadrupole field and flux and (c) final poloidal field at the breakdown time for standard scenario, and (d,e,f) for the improved scenario, respectively, in TCV. The intended null point position (green cross) and the experimental null point position (black cross).	93
6.4	Time evolution of (a) poloidal field gradient, (b) effective connection length at the experimentally obtained null point with different imposed gradient of the quadrupole field in the improved scenario. Comparison of the effect of programmed value of poloidal field gradient in MGAMS for $t = 0$ on experimentally obtained (c) breakdown time (t_b), (d) L_{eff} at null point, (e) initial plasma current ramp rate ($(dI_P/dt)_{\text{max}}$) for the improved (cross) and legacy (circle) scenarios.	94
6.5	Comparison of the effect of the neutral gas pressure for the improved and legacy breakdown scenario on (a) effective connection length (L_{eff}), (b) experimental breakdown time (t_b) and, (c) the maximum of the experimental plasma current ramp rate ($(dI_P/dt)_{\text{max}}$). The standard scenario (blue) and improved scenario (red). In addition, the 'x' denote failed burn-through discharges and the squares denote the successful discharges.	95
6.6	(a) Reconstructed poloidal field at the breakdown time. Evolution of (b) plasma current, (c) I_P error, (d) D_α signal and, (e) radial position of the magnetic axis of the plasma.	96
6.7	(a) Reconstructed poloidal field at the breakdown time. Evolution of (b) plasma current, (c) I_P error, (d) D_α signal and, (e) radial position of the magnetic axis of the plasma.	97
7.1	Schematic showing the doublet shaped plasma configuration. The red circles denote the two plasma magnetic axes and the red cross denotes the X-point. Image source: [68]	100
7.2	Poloidal field magnetic reconstruction obtained using MGAMS code for doublet scenario, with coil currents in [kA] and the quadrupole PF coils (red).	101
7.3	Comparison of the programmed plasma current and vertical position with the estimation from the droplet observer. Red crosses denote the vertical position of the two droplet plasmas obtained using vertical position observer, and blue pluses denote the programmed vertical position in FBTE.	107

7.4	Schematic block diagram for the vertical position control system of the two droplet shaped plasma configuration in TCV.	110
7.5	Stability of the vertical position control system of the two droplet shaped plasma configuration as a function of the proportional gain (G_P) and derivative gain (G_D). The open loop growth rate of S mode ($\gamma_S = 900 \text{ s}^{-1}$) and that of Q mode ($\gamma_Q = 25 \text{ s}^{-1}$). Vertically unstable (red 'x') and stable (blue 'x').	111
7.6	(a) Poloidal field magnetic reconstruction obtained using the <i>breakdown</i> code, with coil currents in [kA], the quadrupole PF coils (red), and the schematic view of two lateral D_α line-of-sights. (b) FastCam measurements for the double breakdown. (c) D_α measurements obtained from top (blue) and bottom (green) PDs, normalized w.r.t. the ionization peak.	113
7.7	(a) Plasma current, (b) vertical position and (c) radial position of the top (red) and bottom (blue) droplet, obtained from a double filament model (dashed) and LIUQE equilibrium reconstruction (solid) in a doublet shaped plasma with Ohmic heating alone. The two droplets converge into one single-axis plasma after $t = 0.02 \text{ s}$ (black line).	114
7.8	(a) Plasma current evolution with time for TCV discharge #54346 (blue), #54573 (green) and #54574 (red) with Thomson measurement at $t = 0.006, 0.008$ and 0.017 s , respectively, and the available LIUQE reconstruction time $t = 0.009 \text{ s}$. (b) Vertical distribution of electron density and (c) temperature measured by Thomson scattering in the three discharges, with the vertical position of separatrix (black dashed) and two magnetic axis (green solid) at LIUQE time. A double peak Gaussian fitting was made for the temperature measurement for each time. (d) LIUQE reconstruction at $t = 0.009 \text{ s}$ with separatrix (black) and LCFS (blue), as well as Thomson measurement position (red).	116
7.9	(a) plasma current, (b) vertical position and (c) radial position of the top (red) and bottom (blue) droplet, obtained from a double filament model (dashed) and LIUQE equilibrium reconstruction (solid) in a doublet shaped plasma with 900 kW heating the top and 750 kW heating the bottom.	117
7.10	Thomson measurements for the doublet shaped plasma configuration with ECRH heating for both plasma. (a) LIUQE equilibrium reconstruction of the doublet shaped plasma showing the Thomson measurement points, (b) temperature profile, and (c) density profile.	119
7.11	Tomographic inversion of XTOMO measurements for a doublet shaped plasma discharge in TCV.	120
7.12	LIUQE reconstructed equilibrium of doublet discharge (a) #55645 with ECH heating top plasma core, (b) #55648 with ECH heating bottom plasma core, (c) #55658 with ECH heating center mantle, (a) #55582 with ECH heating top mantle. The first three discharge are heated from two ECH launchers from the mid-plane, the fourth one uses one launcher from mid-plane and the other from $Z = 0.4 \text{ m}$. Vertical profile of (d) electron temperature and (e) density measured by Thomson scattering system in these discharges.	121

List of Tables

2.1	Main machine and plasma parameters of the TCV tokamak	11
2.2	Rectifier characteristics of the different TCV coil power supplies.	14
4.1	Relationship between the orientation of the null point α_{npt} and positional (radial and vertical) stability of the plasma for both directions of the plasma current. .	47
4.2	Numbers of 6 standard breakdown scenarios analyzed in the database.	56

1 Introduction

Research has been on going for more than 40 years to develop a controlled thermonuclear fusion reactor and provide a sustainable and environment friendly energy source as a solution to the world's energy problem. This chapter briefly discusses the reasons why it is necessary to develop alternative energy sources which are renewable and clean (section 1.1) and how controlled thermonuclear fusion can be used for energy production (section 1.2 and 1.3). The main scientific objectives that are addressed in this thesis is discussed in section 1.4, and the outline of the thesis are presented in section 1.6.

1.1 Need for sustainable energy

One of the main concerns in today's world is the growing population, which in turn increases the energy demand. Presently, fossil fuels are the world's dominant energy source, making up 82% of the global energy supply [1]. However, fossil fuels are not renewable and according to the International Energy Agency the fossil fuel reserves will decline by 40-60% in the next twenty years. Also fossil fuels are the biggest source of carbon dioxide which contributes to climate change, and causes environmental and human health harms. These concerns are triggering the world to look at alternative sources of energy that are both renewable and less harmful to the environment. One of the possible renewable energy sources that can be used to generate electricity is nuclear fusion. The fusion of lighter nuclei is an exothermic process that can be used to produce electricity. Research in this field mainly focuses on developing solutions to overcome the scientific and technological challenges to build an experimental nuclear fusion reactor which can be used to demonstrate the feasibility of using nuclear fusion reactions to produce electricity.

1.2 Thermonuclear fusion and magnetic confinement

Nuclear fusion is a nuclear reaction in which two or more lighter atomic nuclei fuse together to form one or more heavier atomic nuclei and subatomic particles (neutrons or protons). The

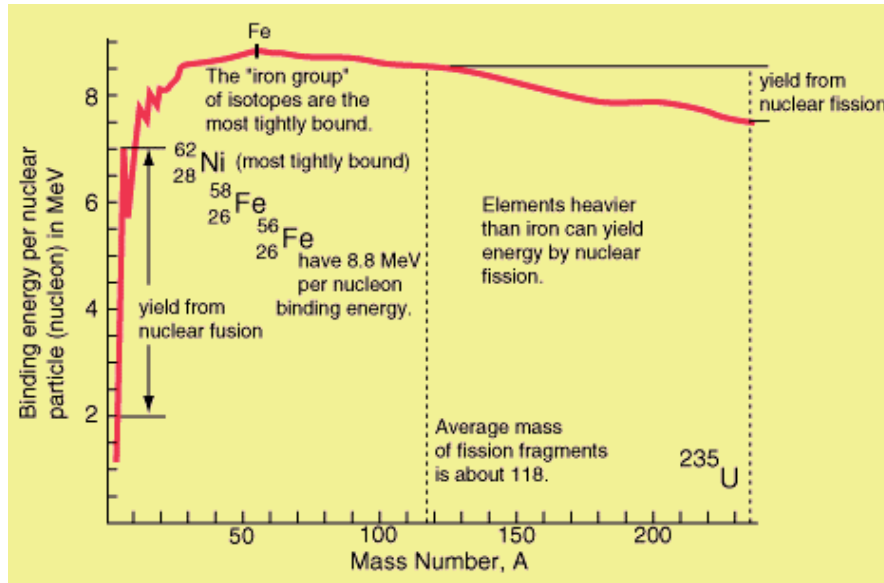


Figure 1.1: Binding energy curve for different atomic elements. Image: www.nuceng.ca/igna/binding_energy.htm

fusion of two nuclei with atomic masses lower than iron, generally releases energy while the fusion of nuclei heavier than iron requires additional energy (Fig. 1.1).

In order to induce the fusion of two light nuclei, it is necessary that the nuclei have sufficiently high kinetic energy to overcome the electrostatic repulsion between the two positively charged nuclei (Coulomb barrier). Analysis of the cross section of fusion reactions as a function of the energy of the particles shows that the Deuterium-Tritium (D-T) reaction is the one with the highest cross-section for the lowest particle energies (Fig. 1.2). Each D-T fusion reaction produces an alpha particle and a neutron and releases 17.6 MeV as particle kinetic energy,



The cross section of the D-T fusion reaction reaches its maximum value at 100 keV. At these particle energies matter is usually in the plasma state and the probability of Coulomb scattering is much higher than the probability of a nuclear fusion reaction. The most promising way to achieve nuclear fusion is by heating a mixture of deuterium and tritium until the thermal velocity of the particles is sufficiently high to produce the required fusion reactions. This way of achieving nuclear fusion is referred to as thermonuclear fusion [76]. The actual temperature needed for the D-T thermonuclear fusion reaction is lower than the temperature corresponding to the maximum cross-section for the D-T reaction as high energy particles in the tail of the Maxwellian velocity distribution can cause the fusion reactions.

In order to become an economically viable energy source, thermonuclear fusion reactors need to achieve ignition (or operate close to ignition). The ignition condition for thermonuclear fusion reactors is met, when the plasma temperature can be sustained by α -particle heating alone. A simple condition for the ignition can be derived based on the power balance and

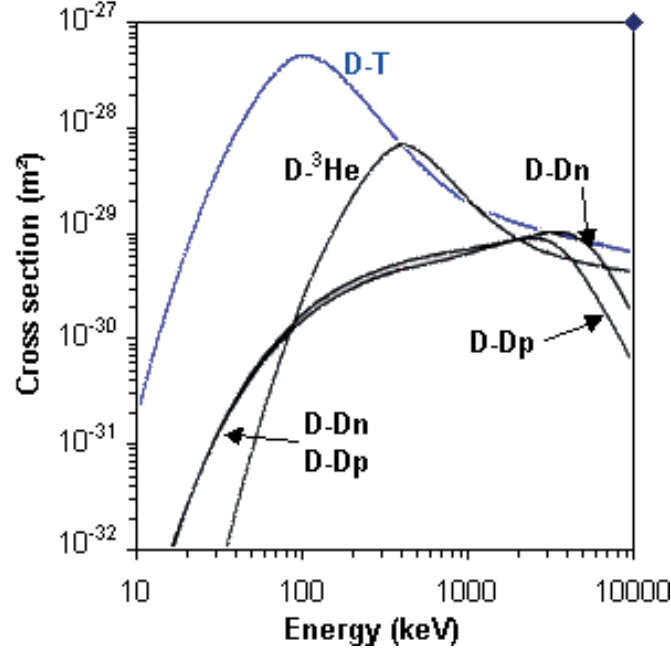


Figure 1.2: Cross-section of a few possible fusion reactions as a function of the particle energy. Image: www-fusion-magnetique.cea.fr/gb/fusion/principes/principes01.htm

assuming a constant plasma density and temperature,

$$n\tau_E \geq \frac{12k_B T}{\langle \sigma v \rangle \epsilon_\alpha}. \quad (1.2)$$

In eq.(1.2), n is the plasma density, τ_E the energy confinement time, T the plasma temperature, $\langle \sigma v \rangle$ the reaction rate for the D-T fusion reaction and ϵ_α the kinetic energy of the α particles produced during the fusion reactions. The R.H.S of eq.(1.2) depends only on the temperature and $n\tau_E$ has a broad minimum at approximately 30 keV. However, since τ_E is also a function of temperature, the temperature at which the minimum in $n\tau_E$ occurs overestimates the optimum operating point of a reactor. In the temperature range, 10-20 keV, the fusion reaction rate can be expressed by, $\langle \sigma v \rangle = 1.1 \times 10^{-24} T^2 \text{ m}^3 \text{ s}^{-1}$, where T is in keV. With $\epsilon_\alpha = 3.5 \text{ MeV}$, the ignition condition becomes,

$$nT\tau_E > 3 \times 10^{21} \text{ m}^{-3} \text{ keV s}. \quad (1.3)$$

This condition is referred to as the *triple product*, and shows the requirements on the plasma density, temperature, and energy confinement time to achieve ignition. For example, the ignition condition in a thermonuclear fusion reactor would be reached for $n = 10^{20} \text{ m}^{-3}$, $T = 10 \text{ keV}$ and $\tau_E = 3 \text{ s}$. Therefore, the hot plasma needs to be confined for a sufficiently long time to achieve the ignition condition for thermonuclear fusion reactors.

The contact between the high temperature plasma and the material walls should be minimized in order to avoid the melting of the wall as well as deleterious effects of the plasma-wall

interaction on the plasma. One possibility to minimize the contact with the wall is to confine the hot plasma in a magnetic field. In the presence of a magnetic field, the charged particles are subjected to the Lorentz force, and particles follow helical trajectories around the magnetic field line. The Larmor radius, which represents the radial extent of this trajectory for a particle of mass m and charge q is given by,

$$r_L = \frac{mv_{\perp}}{qB}, \quad (1.4)$$

where v_{\perp} is the velocity of the charged particles perpendicular to the magnetic field B . In the case of a Maxwellian velocity distribution, v_{\perp} can be expressed by, T as $v_{\perp} = \sqrt{2k_B T/m}$, where T is the plasma temperature. Therefore, the motion of charged particles in a magnetic field results in a good confinement perpendicular to the direction of the magnetic field and no confinement parallel to the magnetic field. However, collisions among particles, introduce a diffusive perpendicular cross field transport of particles and also gives rise to a resistivity in the parallel direction.

In a linear magnetic field configuration the plasma is lost at both ends, which can be avoided by closing the magnetic field lines. A torus, is the simplest configuration with closed magnetic field lines, however, a purely toroidal field varies as $1/R$. The gradient of the field amplitude and the curvature of the field lines lead to drift motions of ions and electrons in opposite vertical directions, which results in a separation of charge, which in turn creates an electric field. The electric field is perpendicular to the magnetic field and causes an outward $\vec{E} \times \vec{B}$ drift motion of the entire plasma (Fig. 1.3). The outward drift motion can be avoided by twisting the magnetic field lines, so that each field line passes both the upper and lower parts of the torus, such that averaging along the path of particles leads to a cancellation of the vertical drift motions and avoids the build up of an electric field. Therefore, a combination of toroidal and poloidal magnetic fields can suitably confine the plasma. Most of the magnetic confinement devices that are developed are toroidal devices, such as tokamaks, stellarators and reversed field pinches. Out of all these magnetic confinement devices, the tokamak configuration is presently considered the most promising candidate to achieve controlled thermonuclear fusion, and details about the tokamak configuration are discussed in the next section.

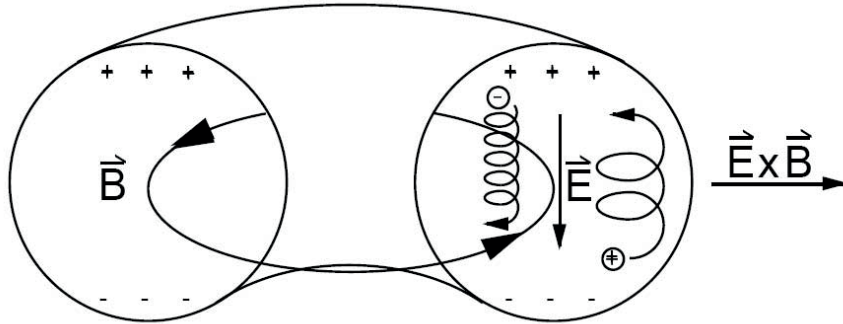


Figure 1.3: Drift motion of the charged particles in a toroidal magnetic field. Image: [70].

1.3 Tokamak

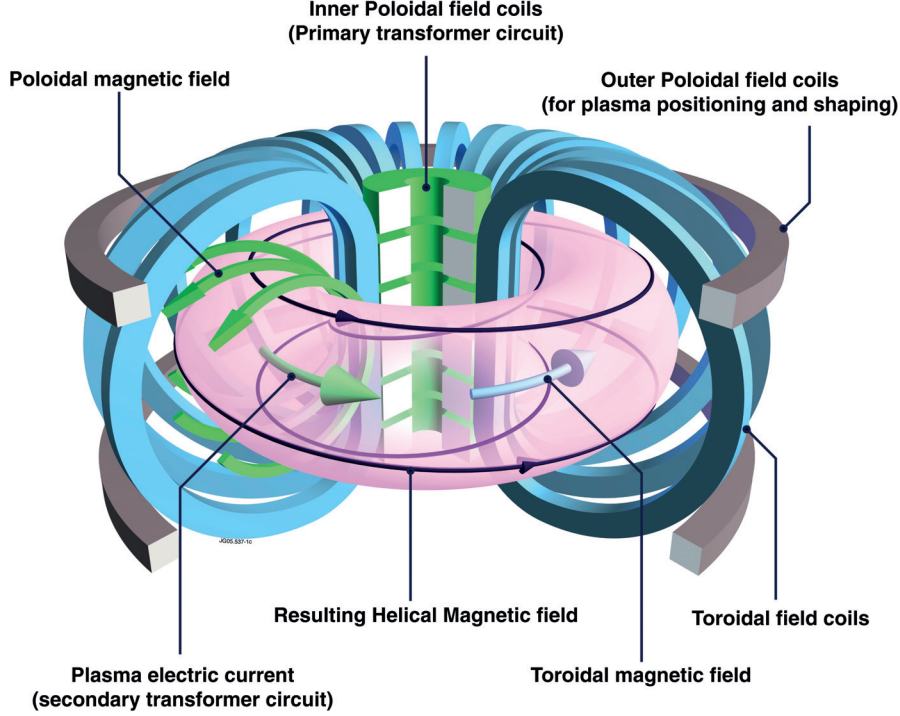


Figure 1.4: Illustration of the tokamak configuration. Image: www.euro-fusion.org/2011/09/tokamak-principle-2/

The tokamak is a toroidal magnetic confinement device in which the toroidal magnetic field (B_ϕ), is generated by a set of external toroidal field (TF) coils (Fig. 1.4), and a poloidal magnetic field (B_θ), produced by the current flowing in the plasma in the toroidal direction. The toroidal geometry along with the plasma pressure results in a force trying to expand the plasma ring radially. This force is balanced by applying a vertical magnetic field (B_v), which interacts with the toroidal plasma current to give an inward radial force. Tokamaks are also equipped with poloidal field (PF) coils, which produce the field required to control the plasma position as well as the plasma shape.

The plasma current (I_p) in a tokamak is usually induced by a variation in the magnetic flux of the central solenoid (details discussed in chapter 3), which allows tokamak operation only in a pulsed mode. However, it is possible to develop advanced scenarios that allow steady state operation by using the bootstrap current and/or other non-inductive current drive techniques. In tokamaks, the combination of the toroidal and poloidal magnetic field results in helical field lines, which form the closed magnetic flux surfaces. The plasma is confined to these magnetic surfaces. The *safety factor* (q) is used to characterize the helicity of the magnetic field lines associated with each magnetic flux surface. The safety factor of this magnetic surface is then defined by [76],

$$q = \frac{\Delta\phi}{2\pi}, \quad (1.5)$$

where $\Delta\phi$ is the toroidal angle it takes a field line to return to the same poloidal location. If $q = m/n$, with m and n being integers, the magnetic field line joins up on itself after m toroidal and n poloidal rotations around the torus. Rational values of q play an important role in determining the magnetohydrodynamic (MHD) stability of the plasma as well as for the transport properties of the plasma. Plasma instabilities result in the reduction of the confinement of particles and energy, and can lead to the loss of the plasma and the disruption of the plasma current.

There are two main plasma configurations, which are employed to separate the plasma from the vacuum vessel wall of the tokamak. In the *limited* plasma configuration the *last closed flux surface* is defined by a material limiter (Fig. 1.5 a). In the *divertor* plasma configuration the magnetic field structure is modified to form a null of the poloidal field in the poloidal plane, also called X-point, which isolates the confined plasma from the vessel wall (Fig. 1.5 b). The flux surface that contains the X-point and separates open and closed flux surfaces is called *separatrix*. The diverted configuration facilitates access to a high-confinement mode where a transport barrier forms just inside the separatrix.

Due to the plasma resistivity (η), it is possible to use the plasma current to heat up the plasma through Ohmic heating, $P_{OH} \propto \eta j_P^2$, where j_P is the plasma current density. As $\eta \propto T_e^{-1.5}$, the plasma resistivity decreases with increasing plasma temperature. Since the plasma current density is limited by the MHD stability, Ohmic heating can only heat typical fusion plasmas up to temperatures in the range of 1-3 keV. Therefore, additional heating is required to raise the plasma temperature to 10 keV to achieve thermonuclear fusion. The main external heating systems used for heating the plasma in tokamaks are, electron cyclotron resonance heating (ECRH), ion cyclotron resonance heating (ICRH), lower hybrid (LH) heating and neutral beam heating (NBH).

The present day tokamaks have been able to achieve the temperatures and densities required for the ignition condition (eq.(1.3)), but the energy confinement time needs to be increased further for ignition. Since the energy confinement time increases with the size of the tokamak and total plasma current, the world's largest tokamak, the International Thermonuclear Experimental Reactor (ITER) is being built in Southern France, through a collaboration of 35 countries. ITER is designed to produce ten times more fusion power compared to the external heating power required to maintain the plasma temperature, and thus, demonstrate the feasibility of net-energy production.

1.4 Motivation of the thesis

The TCV tokamak has been designed to study the effect of plasma shaping on tokamak operation and has the unique ability to create a wide variety of plasma shapes [30]. Since the plasma control system in TCV is presently only set up for a limited vertical shift of the plasma, it is necessary to vary the location of the plasma formation. Also TCV is not constrained to unique directions of the plasma current and the toroidal magnetic field increasing the range of possible magnetic configurations. In addition, the particularly low vessel resistivity ($50 \mu\Omega$)

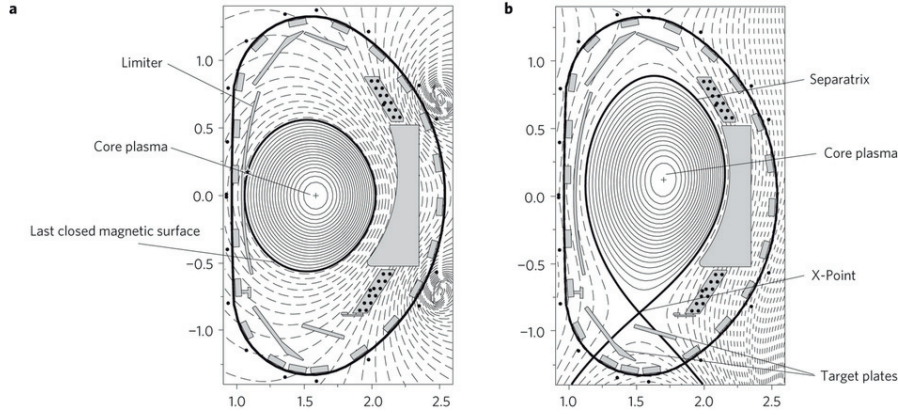


Figure 1.5: Flux contours of (a) a limited plasma configuration and (b) a diverted plasma configuration. Image: [65].

results in vessel eddy currents that significantly alter the magnetic configuration during the initial plasma formation.

The aim of this thesis is to improve the robustness and reliability of the single-axis plasma formation scenario in the TCV tokamak by understanding the dynamics of the plasma formation. This will be able to broaden the range of the prefll neutral gas pressure to obtain a successful plasma formation for the different TCV discharge positions, plasma current and toroidal magnetic field directions (section 1.4.1). Another goal is to apply the improved understanding of the plasma formation gained during this thesis to develop simultaneous breakdown at two locations (double breakdown scenario) and, thereby, create the basis for a doublet research program on TCV (section 1.4.2).

1.4.1 Improve the single-axis plasma formation scenario in TCV

A database for the TCV plasma formation scenario obtained from shot number #35000 to #54000 reveals that approximately 15% of the discharge attempts fail during the plasma formation phase. The dynamics of the plasma formation are greatly affected by the regularly occurring difference between the programmed and experimentally obtained I_p ramp rate which leads to oscillation in I_p when the I_p feedback control system is activated. This mismatch in I_p also propagates into the radial position control. Failed plasma formation occurs when insufficient Ohmic heating is available to sustain the plasma during the burn-through phase. This is either due to slow rise in I_p or a combined effect of the I_p feedback oscillations and a regularly occurring MHD instability. The physics of the plasma formation dynamics in TCV is, therefore, revisited with the goal to improve the present single-axis plasma formation scenario. This requires a better understanding of the physics associated with the plasma formation dynamics and estimates of the various parameters, such as, neutral gas pressure, magnetic field configuration, toroidal electric field and the power balance which strongly influence the different phases of the plasma formation (see chapter 3). In this thesis, different strategies are implemented to separately improve the breakdown and the plasma current

ramp-up scenario in TCV and thus, achieve a robust plasma formation scenario with a wider prefill neutral gas pressure range for the different TCV discharge positions and also limit the initial damage caused by the combined effect of the oscillation in I_p and MHD instability (chapters 4, 5 and 6).

1.4.2 Develop a doublet shaped plasma configuration in TCV

The concept of the doublet shaped plasma configuration was proposed by T. Ohkawa in 1968, and studied in a series of dedicated devices at the General Atomics, San Diego, California [64, 63]. While theory and experiments indicated advantageous stability and confinement properties of the doublet configurations, research was abandoned in the early eighties in favor of tokamaks as the control of the doublet configuration proved to be challenging.

The doublet shaped plasma configuration is characterized by two current carrying plasma channels with the current flowing in the same toroidal direction. This results in the formation of a poloidal magnetic X-point with an internal separatrix between the two plasma magnetic axes. This configuration is suspected to have an internal transport barrier which may be similar to the H-mode edge transport barrier, and therefore, could provide valuable knowledge concerning the transport barriers and H-mode physics. In the doublet shaped plasma configuration, a region of cold plasma, referred to as the mantle, separates the internal separatrix from the last closed flux surface (LCFS), which may lead to advantageous power exhaust properties. Another advantage of doublet shaped plasma configuration is the smaller vertical instability growth rate compared to the single axis plasmas with the same overall elongation (κ). Higher values of κ allows for a higher plasma current, which increases the beta limit. Lastly, the doublet shaped plasma configuration experiments may help in understanding the magnetic reconnection physics that takes place in the vicinity of the X-point when the two current channels merge.

TCV has unique capabilities, such as 16 independently powered shaping coils, a highly elongated vacuum vessel, a flexible control system and the ability to independently heat the droplets, which makes it suitable to create the doublet shaped plasma configuration. The merging of the two droplet shaped plasmas is considered to be the most promising strategy to create the doublet shaped plasma configuration in TCV [26]. The creation of two droplet shaped plasmas requires simultaneous breakdown at two locations with the two magnetic null points having similar magnetic properties so that the plasma current in both droplets is approximately equal. An earlier attempt, resulted in a transient Ohmic doublet configuration with a total plasma current of 100 kA [26], but could not be repeated [68]. With the improved understanding of the plasma formation dynamics and recent advances in the plasma control system, a fresh attempt is made to create and control the doublet shaped plasma configuration in TCV (chapter 7).

1.5 Synopsis of results

The legacy (1990 to present day) single-axis plasma formation scenario used on TCV was revisited and a performance database was developed that revealed several recurrent problems. Discrepancies between the planned and experimental vertical positions were observed, which were found to be primarily caused by an inaccurate vessel current estimation in the back-off process. Plasma formation failures mostly occurred during the burn-through and plasma current ramp-up phases where a temporarily insufficient plasma heating would cause, or trigger, a discharge termination. In simple cases, the current ramp rate was insufficient to drive the Ohmic heating, which led to failed plasma formation. However, an over rapid ramp, combined with a poorly pre-estimated plasma model, would cause the control system to over reduce the current ramp rate, which could also lead to formation failures. Similarly, poor radial position control, again due to a poorly pre-estimated plasma current evolution often led to a poor plasma position control response that terminated the discharge.

A new single-axis plasma formation scenario was designed and implemented to improve the legacy scenario. The new breakdown preparation process included using experimentally obtained vessel resistivity, the use of a non-linear digital control system to reduce the coil current error and modification of the evolution of the quadrupole and first equilibrium field to ensure a workable null point position during the breakdown phase. The vertical discrepancy was reduced by a factor of 10 from 0.33 m to 0.03 m for the $Z = 0.23$ m scenario, and similar results were obtained for the $Z = 0.05$ m scenario. Several methods were proposed and implemented to reduce the plasma current and position mismatches during the burn-through and plasma current ramp-up phases. The strong oscillation in plasma current and radial position induced by the plasma control reaction was reduced using a bump-less transfer control technique. Two new scenarios at $Z = \pm 0.4$ m were also developed with improvements implemented for both the breakdown and burn-through phases to expand the new scenarios operation range. This approach was also in preparation of the creation of a doublet plasma configuration where a simultaneous breakdown at two vertical positions inside the TCV vessel was envisaged.

A doublet shaped plasma configuration was then developed with a simultaneous double breakdown. A doublet with 50 kA plasma current and 200 eV core electron temperature in each droplet was obtained with Ohmic heating only. The upper droplet was observed to vertically drift downwards in time towards the lower one. This vertical shift, although not completely understood, was partially stabilized using ECH heating. A highest plasma current of $I_p = 130$ kA was achieved in both droplets, with a core electron temperature at 1.3 keV when ECH was applied. It was observed experimentally that heating of either droplet with ECH would heat both droplets impeding the initial plasma control approach where a real-time independent heating of each droplet was to be used to keep the doublet balanced. This power sharing between the droplets and sharp temperature and density gradients in the mantle surrounding the doublet suggests some kind of transport barrier located outside the separatrix encompassing both of the doublet's droplets.

1.6 Outline of thesis

In this chapter, a brief introduction to nuclear fusion and the tokamak device as a possible concept for exploiting thermonuclear fusion as an energy source was presented. The scientific and technological challenges that are encountered in developing controlled nuclear fusion, that will be addressed in this thesis, were discussed.

Chapter 2 provides a description of the TCV tokamak on which the experiments described in this thesis were performed. After a description of the magnetic coil and auxiliary heating systems, which were the main plasma actuators used in this work, the diagnostics which are used to determine the important plasma parameters in this thesis are described.

Chapter 3 presents the physics associated with the different phases of the plasma formation in a tokamak and the models that can be used to describe them. Also the different parameters which play a significant role in determining a successful plasma formation in tokamaks are introduced in this chapter.

Chapter 4 presents the breakdown strategy used in the TCV tokamak and its comparison with the breakdown strategy in other tokamaks. The estimation of the different parameters used to model the breakdown phase and their influence on the breakdown scenario in TCV is investigated and experimental results are discussed. This chapter mainly focuses on the problems associated with the present breakdown scenario in TCV and the strategies proposed to improve the present breakdown scenario.

Chapter 5 describes the plasma burn-through and current ramp-up strategy used in the TCV tokamak. The main focus of this chapter is to highlight the problems associated with the present plasma burn-through and plasma current ramp-up scenario and the different strategies which can be implemented to improve them.

Chapter 6 describes the effect of the modifications made in the present breakdown and plasma current ramp-up scenario. Also a comparison between the new and the old plasma formation scenario in TCV is made to show the effect of the new improved plasma formation scenario.

Chapter 7 describes the strategies developed to create the doublet shaped plasma configuration in TCV. This part is divided into a feed forward phase and a feedback phase. The feed forward phase requires a successful simultaneous breakdown at two locations and a ramp-up of the plasma currents in the two droplet shaped plasmas up to 20 kA so that magnetic feedback control becomes possible. The experimental results for the feed forward phase using Ohmic heating alone are presented. The feedback phase proposes strategies to independently control the plasma current, radial and vertical position of the two droplet shaped plasmas. A rigid model (RZIP2) is developed to determine the stability of the droplet shaped plasma configuration and results of the simulation are presented. The experimental results of the different feedback control schemes are presented here.

Chapter 8 summarizes the main results and conclusions of this work.

2 TCV Tokamak

The Tokamak á Configuration Variable (TCV) is a medium sized, highly elongated tokamak [30] located at the Swiss Plasma Center (SPC) in Lausanne, Switzerland. The main machine and plasma parameters of the TCV tokamak are listed in table 2.1.

All the experiments presented in this thesis were performed on TCV. This chapter describes the main tokamak components (section 2.1), the electron cyclotron heating system (section 2.2), the main plasma diagnostics used in this thesis (section 2.3), the code used for the plasma discharge design in TCV (section 2.4 and 2.5) and the TCV control system (section 2.6).

Parameter	Symbol	Value
Vacuum vessel height	b	1.50m
Major radius	R_0	0.88 m
Minor radius	a	0.25 m
Toroidal magnetic field on axis	B_0	$\leq 1.54 T$
Plasma current	I_P	$\leq 1 \text{ MA}$
Elongation	κ	$0.9 \leq \kappa \leq 2.8$
Triangularity	δ	$-0.8 \leq \delta \leq 1$
Core plasma density	n_e	$0.5 \times 10^{19} \leq n_e \leq 2 \times 10^{20} \text{ m}^{-3}$
Electron temperature	T_e	$\leq 15 \text{ keV (with ECH)}$
Ion temperature	T_i	$\leq 1 \text{ keV (2.5 keV with NBH)}$
ECH power	P_{ECH}	4.5 MW ($6 \times 0.5 \text{ MW X2} + 3 \times 0.5 \text{ MW X3}$)
NBH power	P_{NBH}	1 MW
Energy confinement time	τ_E	$\leq 50 \text{ ms}$

Table 2.1: Main machine and plasma parameters of the TCV tokamak

2.1 Tokamak components

This section describes the main components of the TCV tokamak, namely the TCV coil system (section 2.1.1), the vacuum vessel (VV) of TCV (section 2.1.2) and the TCV first wall (sec-

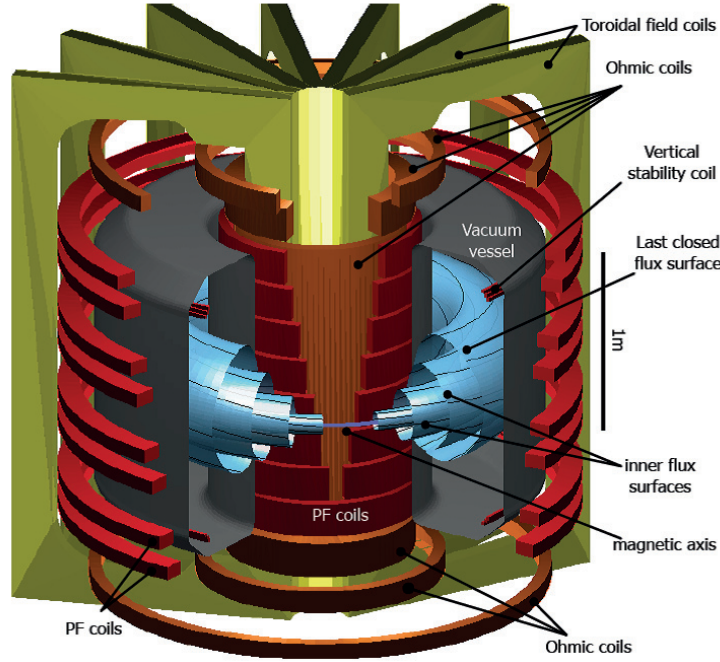


Figure 2.1: Cutout view of TCV showing poloidal and toroidal field coils, ohmic coils, vacuum vessel and the plasma flux surfaces with the magnetic field lines. Image: [20].

tion 2.1.3). The role of the TCV coil system and the TCV VV during the different phases of the plasma formation is explained in detail in chapters 4 and 5.

2.1.1 Coil system

TCV routinely initiates the plasma start up with an air-core Ohmic transformer to produce a toroidal electric field and ionize the pre-injected neutral gas. The Ohmic transformer is composed of the main coil A1, which is powered by the OH1 power supply and the coils B1, B2, C1, C2, D1 and D2, which are connected in series and powered by the OH2 power supply (Fig. 2.2). These seven coils of the Ohmic transformer are designed to minimize the poloidal magnetic field generated by the OH1 and OH2 currents inside the TCV vacuum vessel. The toroidal magnetic field in TCV is produced by 16 toroidal field coils connected in series. Adjacent TF coils are connected with bus bars. To model the stray poloidal field, the bus bars are approximated by two poloidal field coils, T1 and T2, and a return loop represented by T3 (Fig. 2.2). Sixteen independently powered poloidal field coils, provide the shaping capability of TCV (Fig. 2.2). The radial field from the shaping coils does not penetrate the vessel walls fast enough to control the most vertically unstable plasmas (growth rate $\geq 1000 \text{ s}^{-1}$) in TCV. Thus, low impedance coils, G coils, are installed inside the TCV vacuum vessel to increase the controllable vertical plasma stability range [19].

The power supplies of the Ohmic, toroidal and poloidal coils are thyristor based. The thyristors

are assembled in a compact six-pulse bridge, which is used as the basic module for the assembled rectifiers [18]. In table 2.2, the characteristics of the rectifiers used for the different coil power supplies in TCV are listed. Three regulation modes allow to control these rectifiers. The TF coils are usually operated in the *current feedback* mode where the current is controlled and limited by an internal controller. The PF coils are mostly driven in the *open loop voltage drive* mode, where the plasma control system provides voltage reference signals for each power supply that incorporate current limits to the coils. The power supplies can also be operated in *hybrid* mode, which is a combination of the current feedback and open loop voltage drive modes. This mode adds a pre-programmed current reference signal together with the ability to override this pre-programmed current with an externally driven voltage.

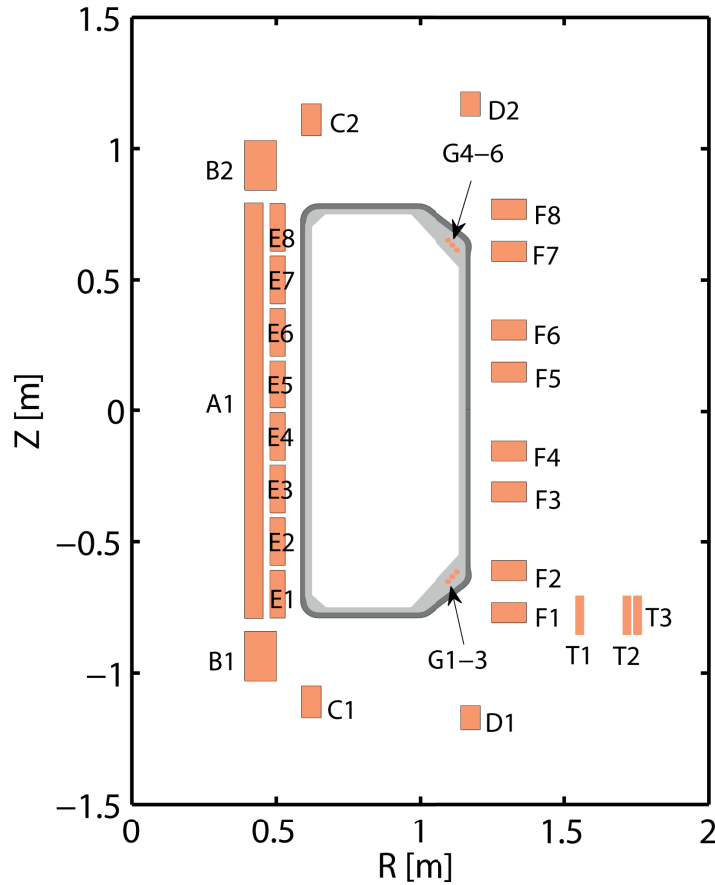


Figure 2.2: Poloidal cross section of TCV with the main sources of the poloidal magnetic field, which include the Ohmic coils (A-D), PF coils (E-F), the fast internal coils (G) and the coils approximating the toroidal field bus bar (T).

A motor generator with a nominal power of 200 MVA, nominal voltage of 10 kV and frequency in the range of 96-120 Hz, is used to power TCV's major power supplies.

Coil power supplies	U [V]	I_{max} [kA]	number of 6-pulse bridges
1 \times TOR	626	78	2 \times 10
2 \times OH	1400	31	2 \times 8
8 \times E	651	7.7	2 \times 2
8 \times F	1250	7.7	2 \times 2

Table 2.2: Rectifier characteristics of the different TCV coil power supplies.

2.1.2 Vacuum vessel

The TCV vacuum vessel (VV) was designed with a particularly low toroidal resistance ($50 \mu\Omega$) to reduce the growth rate of the vertical instability (passive stabilization). This in turn induces large eddy currents of up to 200 kA in the VV when the Ohmic transformer is used to apply the high loop voltage for inductive breakdown (section 4.4). It is, therefore, necessary to know the electromagnetic properties of the VV to estimate the poloidal magnetic field contribution from the VV during plasma start-up. The electromagnetic model of the VV is described in detail in chapter 4.

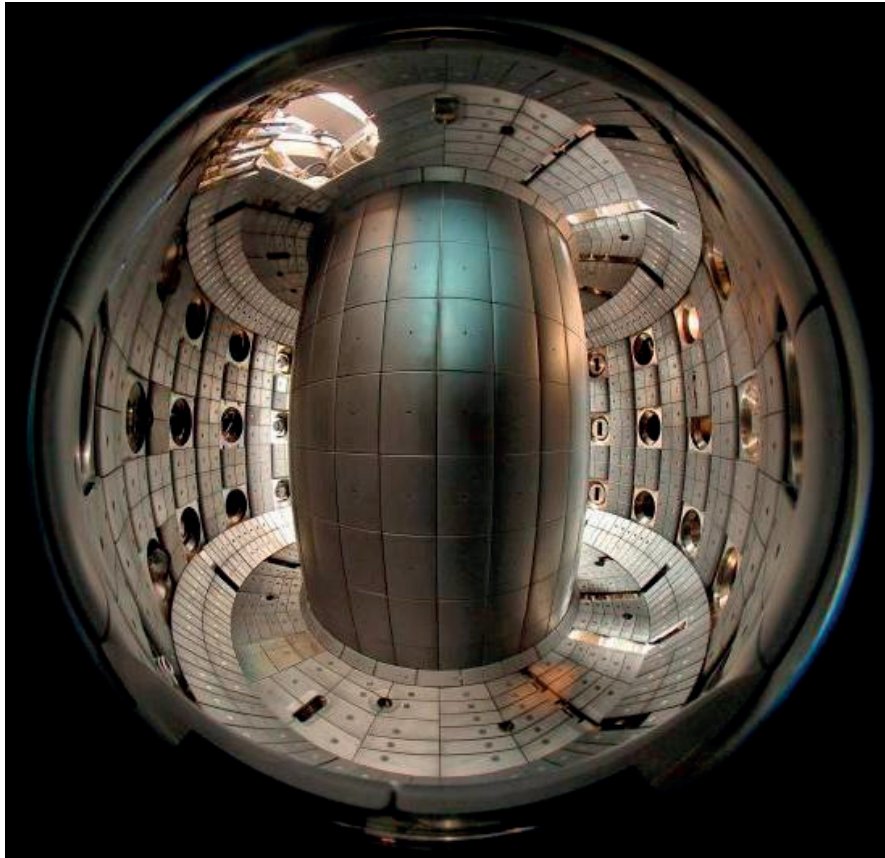


Figure 2.3: Fisheye view of the TCV first wall covered with approximately 1692 graphite tiles.

2.1.3 First wall

The first wall protects the vacuum vessel from the plasma during normal operation as well as during instabilities and disruptions. The material used for the first wall must in particular be able to withstand the thermal shocks that occur during disruptions. It must also have high thermal conductivity for heat transfer. A material with a low atomic number can reduce the radiation losses from the plasma due to impurities, but it should also have a low sputtering yield to produce only a low impurity flux during the interaction with the plasma [76]. Carbon is one of the materials, which satisfies these criteria and is commonly used in the first wall of tokamaks. The TCV first wall is almost fully covered with high purity, isotropic, polycrystalline graphite tiles to reduce the plasma contamination and increase the flexibility in plasma shaping [69] (Fig. 2.3).

During the plasma start-up phase, the presence of impurities results in radiation power losses due to the line radiation from the partly ionized impurity ions, which prevents the plasma being heated. The impurities mainly originate from the interaction of the plasma with the material surfaces that are exposed to the plasma. Most easily released impurities are those adsorbed on the surface with low binding energies, such as water, and carbon monoxide molecules, which can lead to line radiation losses from carbon and oxygen. Impurities can also be released by incident ions, neutrals, electrons and photons interacting with the first wall. The desorption processes for electrons and photons are predominantly electronic in nature, and those for the ions and neutrals are by momentum transfer. Desorption can lead to impurity accumulation in the plasma, or, in the case of desorption of the plasma species (hydrogen isotopes), to poor density control. In order to minimize the desorption processes during plasma discharges various procedures have been adopted to reduce adsorption on the wall, referred to as wall conditioning techniques. They include, baking the vacuum vessel, typically to 200 – 350 °C, using a variety of plasma discharges to remove the adsorbed gas from the wall, gettering, in which the wall is covered with a clean metal film by evaporation, and covering the wall with low Z film such as carbon or boron, known as carbonization and boronization. Successful wall conditioning removes impurities and generally results in access to a much wider range of operating conditions.

The TCV vessel is regularly baked after each exposure to air and then coated with boron through plasma chemical vapor deposition. The boronization is performed through a glow discharge in which a mixture of He (90%) and deuterated diborane (10%) is used to cover the first wall with an approximately 100 nm thin layer. Boron acts as a getter and thin boron films transiently pump both oxygen and hydrogen. Since the carbon based materials used to protect the TCV VV have a high retention of hydrogen isotopes, wall conditioning with helium glow discharges with a typical duration of 300 s is carried out between plasma discharges. Helium glow discharge cleaning also desorbs implanted hydrogen isotopes in the wall, thus reducing recycling.

2.2 Electron Cyclotron Resonance Heating system

This section describes some of the technical aspects of the electron cyclotron resonance heating (ECRH), which is one of the two auxiliary heating systems available in TCV [23]. The ECRH system has six 82.7 GHz gyrotrons (nominal power of 500 kW each), injected from the low field side for heating at the second harmonic (X2), and three 118 GHz gyrotrons (500 kW each), injected from the top of the vessel for heating at the third harmonic (X3). The radial location of the resonance layer for the EC wave can be shifted towards the high field side by lowering the applied toroidal field. In experiments performed during this thesis, only three (L1, L4 and L6) of the six ECRH-X2 gyrotrons were available. The ECRH-X2 system was used as an actuator to independently control the temperature, and thereby, the induced plasma current, in the two droplets of the doublet shaped plasma scenario in TCV (see chapter 7).

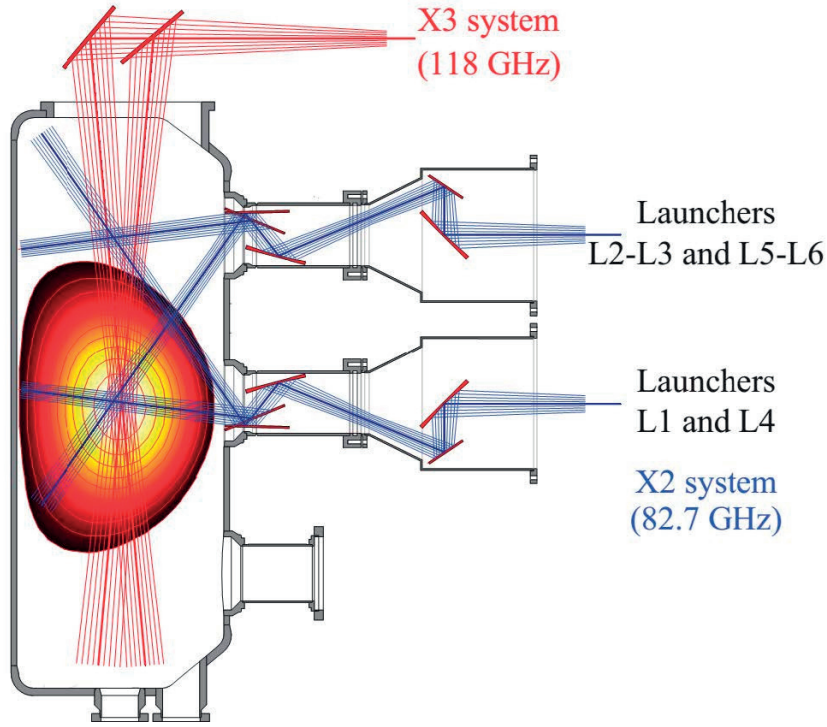


Figure 2.4: Poloidal cross section of the TCV tokamak showing the X2 and X3 launchers of the ECRH system and indicating the range of poloidal mirror steering.

Transmission line

A *Matching Optics Unit* (MOU) is attached to each gyrotron that modifies the EC wave diameter to match it to the waveguide diameter. Two remotely positionable mirror polarizers, set the polarization of the EC wave (X or O mode or a combination of both). After the MOU the EC wave propagates through a corrugated waveguide before reaching the EC launchers installed in TCV ports.

Launchers

There are two launchers (# 1,4) installed in equatorial ports ($Z = 0$ m) and four launchers (# 2,3,5,6) installed in upper ports ($Z = 0.46$ m) (Fig. 2.4). Each launcher has four mirrors. The mirror located closest to the plasma can be steered in real-time to vary the injection angle of the EC wave, and thereby, the absorption position, in the plasma. Figure 2.5 describes the injection geometry for the launchers where the launcher poloidal angle θ_L , is the angle of the EC ray leaving the final mirror with respect to the launcher axis, and the launcher toroidal angle ϕ_L , is the angle of the plane containing the optical axis of the launcher mirrors [20]. The launcher toroidal angle, ϕ_L can be varied in between shots from -180° to 180° , whereas θ_L is constrained to values between 8° and 45° .

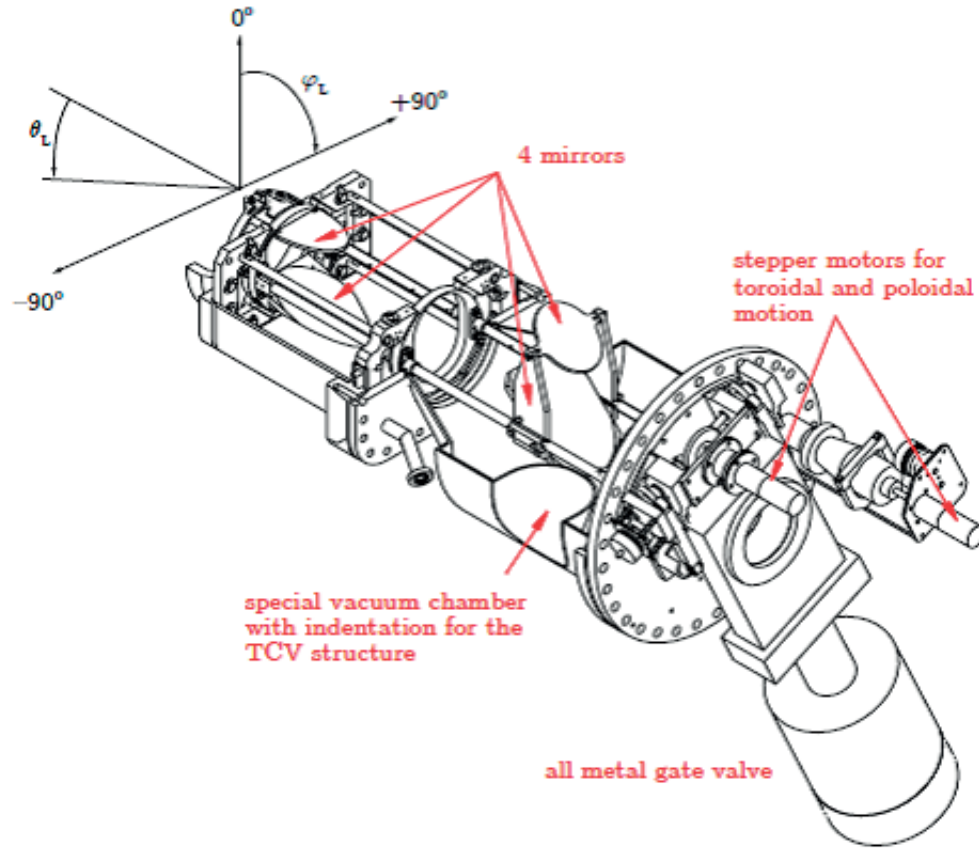


Figure 2.5: Schematic of the X2 launcher showing the 3 fixed mirrors and 1 real-time steerable mirror. Also the steering angle conventions used for the launchers is shown. Image: [20].

Power supplies

The six X2 gyrotrons are grouped into two clusters with three gyrotrons (one equatorial and two upper launchers) each. Cluster A consists of gyrotrons # 1-3 and cluster B of gyrotrons # 4-6. The minimum power output of a single gyrotron is approximately 180 kW. Technical

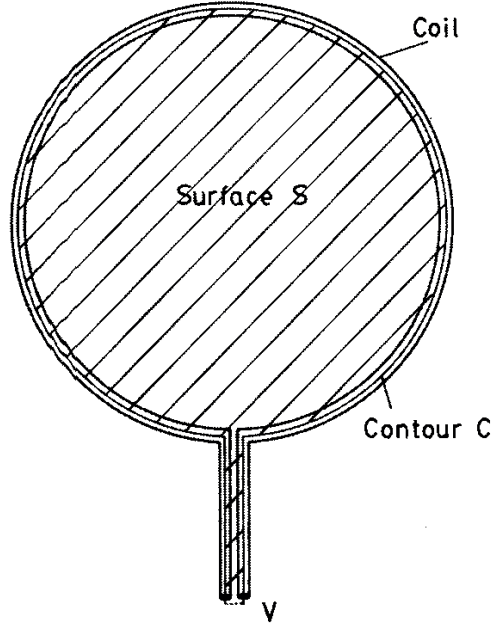


Figure 2.6: Schematic of a single turn magnetic probe. Image: [32].

constraints limit how rapidly the power can be varied when starting from zero power. The power ramp from 0 to 180 kW must take at least $700 \mu\text{s}$ to avoid current and voltage overshoots in the power supplies of the gyrotrons, which may lead to arcing of the gyrotrons. Above 180 kW the power ramp rate is only limited by the transfer function of the power supply which, damps oscillations above 25 kHz.

2.3 Diagnostics

This section briefly describes the working principles of the diagnostics that are used to determine the plasma parameters used in this thesis work.

2.3.1 Magnetic Diagnostics

Magnetic probes are used to measure the magnetic field in tokamaks. The induced voltage in the magnetic probe placed in a time varying magnetic field can be calculated by applying the integral form of Faraday's law to a chosen closed contour C , which corresponds to a wire loop and is expressed as,

$$\oint_C \vec{E} \cdot d\vec{l} = - \int_S \vec{B} \cdot d\vec{s}. \quad (2.1)$$

In eq. (2.1), \vec{E} is the electric field, \vec{B} is the magnetic field, C is a rigid contour, which can neither move nor deform enclosing the probe surface S (Fig. 2.6). By using the assumption of a small

rigid probe [32] eq. (2.1) yields the induced voltage in the probe,

$$U_{\text{probe}} = -N_C A_C \frac{d\vec{B}_\perp}{dt}, \quad (2.2)$$

where N_C denotes the number of turns, A_C denotes the area of the loop and \vec{B}_\perp is the magnetic field component normal to the probe surface. Thus, it is possible to determine the time variation of the magnetic field component normal to the probe surface from the induced probe voltage. The $d\vec{B}_\perp/dt$ signals are used for the detection of the fast-growing instabilities, such as vertical instabilities. The magnetic field component normal to the probe surface is obtained through integration of the probe voltage,

$$\vec{B}_\perp(t) = -\frac{1}{N_C A_C} \int_0^t U_{\text{probe}}(t') dt'. \quad (2.3)$$

The \vec{B}_\perp measurements are used for equilibrium reconstruction, plasma position and shape control and detection of non-rotating instabilities, such as locked modes.

In TCV, magnetic probes are mounted inside the vacuum vessel at 38, approximately poloidally evenly spaced positions, where they measure the component of the poloidal magnetic field tangential to the vacuum vessel. Four poloidal cross-sections toroidally separated by 90° are equipped with such 38 probe arrays (Fig. 2.7). The signals from two toroidally opposed sections are averaged to cancel any toroidal asymmetries with the longest wavelengths and fed to the plasma shape and position control system. In addition, two toroidal arrays, located in the equatorial mid-plane on the low field side (LFS) and high field side (HFS) and two more arrays on each side located 0.35 m above and below the mid-plane are installed for MHD mode analysis [55].

The time variation of the poloidal flux is measured by the poloidal flux loops,

$$U_{\text{fl}} = -\frac{d\psi_p}{dt}. \quad (2.4)$$

The induced voltage, (U_{fl}) is either directly used as a measurement of the loop voltage or integrated to yield a measurement of the poloidal flux, $\psi_p \equiv 2\pi \int_0^R R' B_z dR'$.

In TCV, the poloidal flux loops, which are located outside the vacuum vessel, are paired with the magnetic probes (Fig. 2.7), to facilitate the extrapolation of the poloidal flux towards the plasma. In addition, all shaping coils and Ohmic transformer coils (B,C and D coils), except the central solenoid (A1 coil), which by construction remains rather inaccessible, are equipped with a poloidal flux loop. The flux loops associated with the coils and a selected set of ten flux loops mounted on the vessel are used to estimate the full poloidal flux [55]. The signals of all loops are dominated by the ohmic transformer flux. To increase the dynamic range of the measurements, the signal from reference loop number 1 is subtracted from those of the vessel loops 2 to 38 before their amplification and acquisition.

In this thesis, the magnetic measurements are used to estimate the vessel current and reconstruct the poloidal magnetic field at the time of breakdown (discussed in detail in chapter 4).

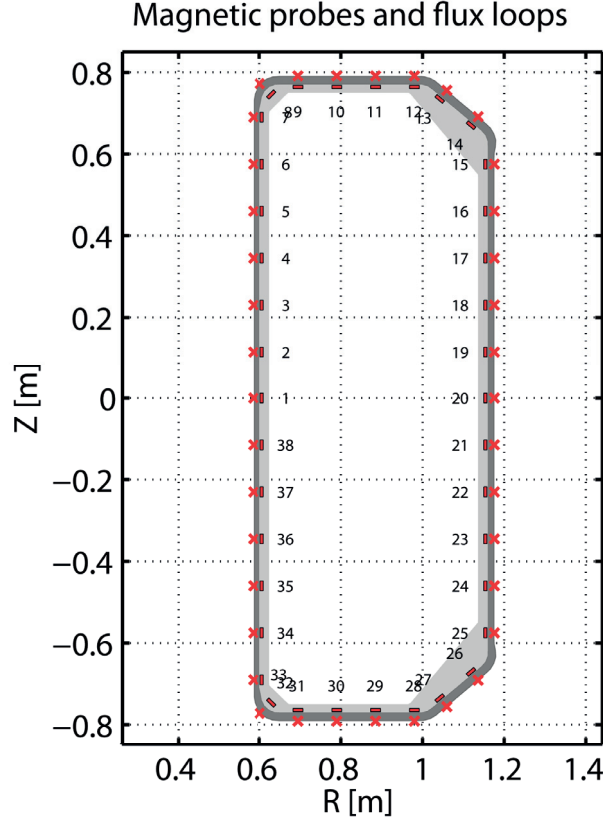


Figure 2.7: TCV poloidal cross section with the poloidal flux loops (red crosses), the magnetic field probes (red rectangles).

Also the plasma current and plasma position estimates during the initial phase of the plasma formation are obtained from magnetic measurements (chapter 5).

2.3.2 Baratron pressure gauges

The neutral pressure in the vessel is measured with baratron pressure gauges. The pressure sensor consists of a pressure inlet tube connected to a small chamber in the transducer body. One wall of this chamber is an elastic metal diaphragm, whose front side is exposed to the gas, and whose back side faces a rigidly mounted ceramic disc containing two electrodes. The diaphragm deflects with changing absolute pressure, which causes an imbalance of the sensor electrode capacitance. The pressure is thereby converted into a DC voltage in the bridge excited by a precision constant frequency oscillator. The resultant signal is linearized, zeroed and amplified through a signal conditioner to produce the output signal. Therefore, the baratron pressure measurement is an absolute measurement of the pressure.

In TCV, two baratron pressure gauges are installed and connected to the vessel by extension tubes through two different ports, one horizontally at the mid-plane and the other vertically at the bottom floor. These baratron pressure gauges are magnetically shielded and vibra-

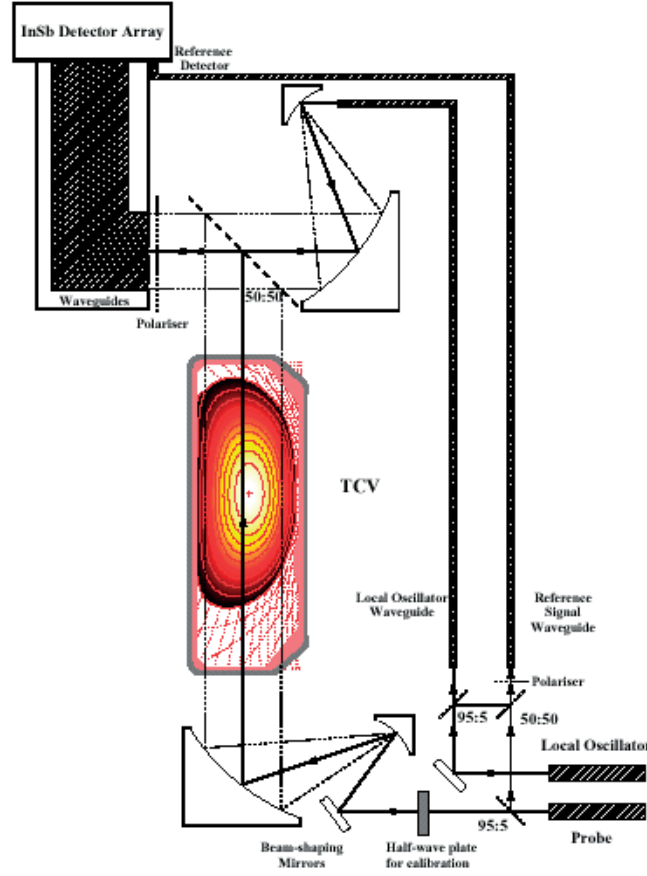


Figure 2.8: Schematic of the far infrared interferometer on TCV.

tionally isolated. The estimated time response of the entire system, which is dominated by the conductance of the tubes, is approximately 70 – 100 ms (section 4.3.1).

2.3.3 Far infrared interferometer

A commonly used method to measure the time evolution of the electron density is based on the principle of interferometry. By superimposing two or more electromagnetic waves, the refractive index of the medium through which they propagate can be estimated. The electromagnetic waves propagating through the plasma interact with the free electrons of the plasma, which can be used to determine the refractive index of the plasma. Under the assumption that the frequency of the infrared laser (ω) is much higher than the plasma frequency (ω_p) as well as the cyclotron frequency (ω_c), the refractive index of the plasma (n_p) can be expressed as,

$$n_p = \frac{kc}{\omega} \approx 1 - \frac{\omega_p^2}{2\omega^2}, \quad (2.5)$$

where k is the wave number of the electromagnetic wave and c the speed of light.

The phase shift in the electromagnetic wave introduced by the plasma can be obtained by using the WKB approximation [17],

$$\Delta\phi = k \int n_P(x) dx = r_e \lambda \int n_e dx, \quad (2.6)$$

where $r_e = 1/4\pi\epsilon_0 e^2 / m_e c^2$ is the classical electron radius, k and λ are the wave number and wavelength of the electromagnetic wave, n_e is the electron density, m_e is the mass of the electron, x is the spatial coordinate along the path of the electromagnetic wave. Thus, The phase shift is a direct measurement of the line integral of the free electron density.

A 14-channel Mach-Zehnder type interferometer (FIR) [8] is used to measure the line-integrated free electron density along parallel chords in the vertical direction in TCV (Fig. 2.9). The system consists of a far infrared laser, pumped by a CO_2 laser, and emitting a continuous wave at $184.3 \mu\text{m}$, and a multi-element detector unit (InSb hot-electron bolometer) (Fig. 2.8). The laser beam is divided into a reference beam, which is frequency shifted by a rotating grating, and 14 vertical probe beams passing the plasma at different radial positions. When the probe beams pass through the plasma, a phase delay with respect to the reference beam is introduced due to the presence of free electrons. The phase delay can be measured by comparing the detector signals at the difference frequency. Since the refractive index of the plasma is directly related to the free electron density, the FIR provides continuous measurements of the free electron line-integrated density along the 14 chords.

In this thesis the FIR measurements are used to determine the radial position and extent of the plasma during the initial plasma formation (discussed in detail in section 5.2).

2.3.4 Thomson scattering

The Thomson scattering measurements are based on the spectral analysis of the elastically scattered electromagnetic waves by free charged particles. When a laser beam (incident wave vector \vec{k}_i and frequency ω_i) is incident on an electron, the oscillating electric field of the laser light accelerates the electron, which in turn re-emits the absorbed electromagnetic wave (scattered wave vector \vec{k}_s and frequency ω_s). Under the assumption that the wavelength of the laser is much smaller than the Debye length (λ_D), there is no correlation between the emissions from different electrons and the total scattered power can be calculated by summing up of the scattered power from the individual electrons. Thus, the scattered power spectrum for the non-relativistic regime ($T_e \leq 1 \text{ keV}$) can be obtained by assuming a Maxwellian electron distribution [32],

$$\frac{d^2 P_s}{d\omega_s d\Omega} = \frac{r_e^2 n_e P_i L \sin^2 \theta}{\sqrt{\pi} k v_{th,e}} \exp \left[- \left(\frac{\omega_s - \omega_i}{k v_{th,e}} \right)^2 \right], \quad (2.7)$$

where P_s is the power of the scattered radiations, P_i is the power of the incident wave, L is the length of the scattering volume in the direction of the incident wave, θ is the angle between the scattered wave vector \vec{k}_s and the electric field of the incident wave, $d\Omega$ is the solid angle,

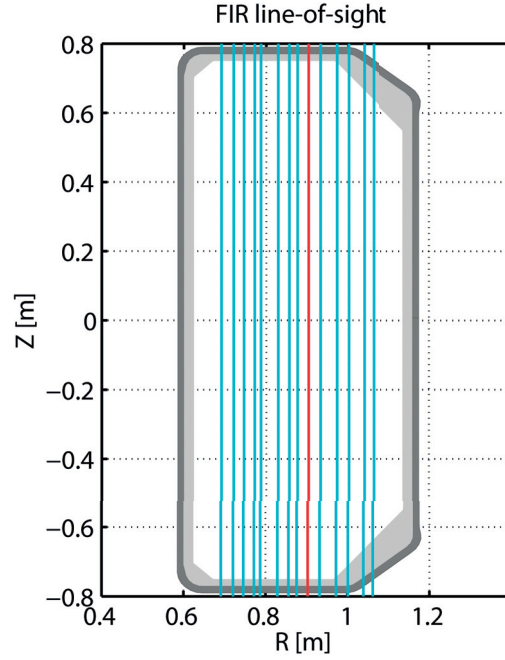


Figure 2.9: TCV poloidal cross-section showing the line of sight for the far infrared interferometer system. The red line represent the central chord of FIR used for density control.

$k = |\vec{k}_i| = |\vec{k}_s|$ due to elastic scattering and $v_{th,e} = \sqrt{2k_B T_e / m_e}$ is the electron thermal velocity. Equation (2.7) shows that the electron temperature can be determined from the width of the scattered power spectrum due to the Doppler effect while the electron density can be obtained by integrating over the scattered power spectrum.

The Thomson scattering system on TCV [9] is designed for the measurement of the spatial distribution of the electron temperature and density in the vertical direction along a laser beam, which intersects the plasma at a radial position $R = 0.9$ m close to the center of the TCV VV. The scattered light from the observation volumes in the plasma is collected using three wide-angle camera lenses. There are 47 observation positions covering the region from $Z = -31$ cm to $Z = +66$ cm with a spatial integration length that depends on the channel location (Fig. 2.10). The scattered light is analyzed using filter polychromators equipped with four or five spectral channels, which are optimized to measure different electron temperature ranges. The sampling rate of the measurements is determined by the 20 Hz repetition rate of the high-power $Nd : YAG$ lasers. The system consists of three lasers combined in a cluster to build a beam, which appears as a single laser beam when viewed by the detection optics. The relative timing between the lasers can be varied by triggering the three lasers at different times. The signal to noise ratio for low electron density measurements can be improved by triggering of the three lasers at the same time. The electron density measurements are absolutely calibrated through Raman scattering from molecular nitrogen gas filled into the TCV vessel.

In this thesis, the temperature and density profiles for the doublet shaped plasma in TCV is

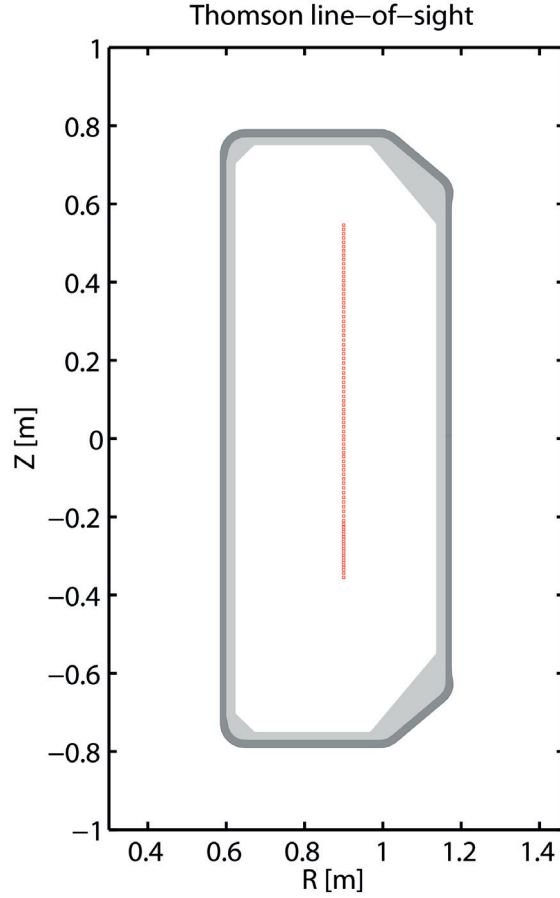


Figure 2.10: TCV poloidal cross-section showing the Thomson scattering measurement points.

obtained from Thomson measurements by using the simultaneous triggering of the three lasers to obtain sufficient signal-to-noise ratio (chapter 7).

2.3.5 Photodiodes

A photodiode is a p-n junction diode made up of light sensitive semiconductor material which generates a current proportional to the incident light energy. Provided that the photon energy is greater than the band gap energy, the incident light excites the valence band electrons to the conduction band, which generates a electron-hole pair, where they can be measured as a current that is proportional to the light intensity. Silicon (*Si*) is one of the most commonly used semiconductor material for photodiodes. At room temperature, the band gap energy is 1.12 eV, which allows to measure wavelengths up to 1100 nm. However, in the near-infrared region (900 – 1100 nm), the *Si* photodiodes have an extremely low light absorption coefficient. This allows most of the light to pass through and, thus, lowers the sensitivity of the *Si* photodiodes for infra-red radiations. In the presence of air, a silicon dioxide *SiO₂* layer is formed on the surface of *Si* photodiodes due to oxidation, which acts as an insulator for the charge

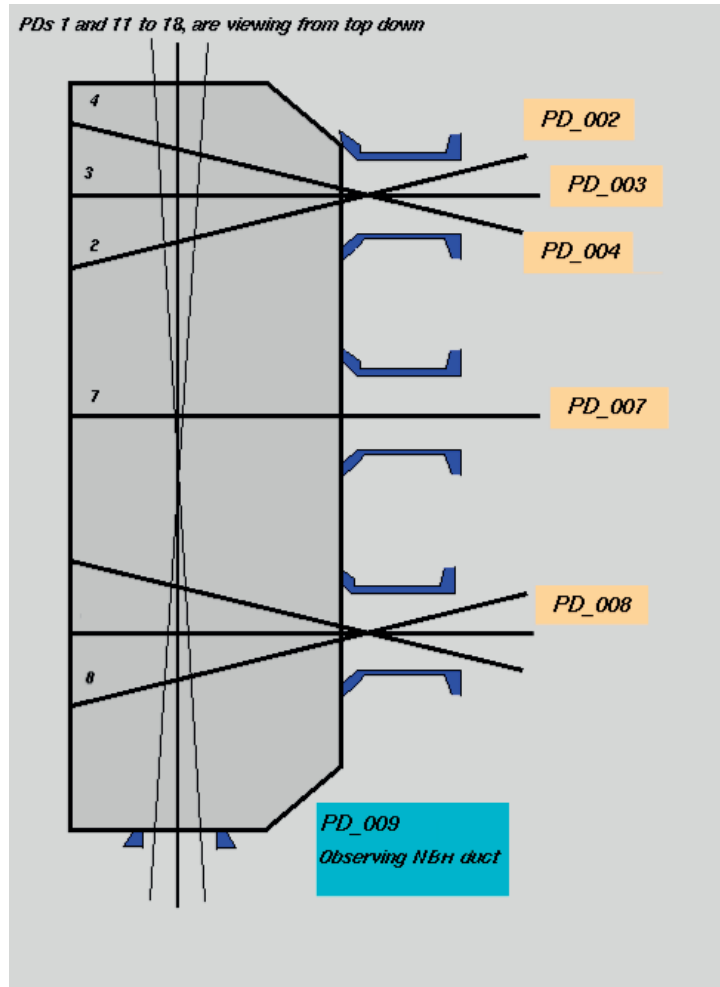


Figure 2.11: Schematic showing the different D_α photodiode chords and their positions in TCV.

generated by the photons and prevents the electrons from reaching the conduction band and does not contribute to generation of current. Since at short wavelengths (UV region), the degree of light absorption within the SiO_2 layer is very high, thus, the sensitivity of the normal Si photodiodes to UV radiations is very low. For normal Si photodiodes, the lower cut-off wavelength is 320 nm, whereas it is 190 nm for UV-enhanced Si photodiodes. The silicon photodiodes are best suited for observing the emission in the visible range of the electromagnetic spectrum. This coincides with the majority of the line radiation emitted from typical tokamak plasmas, which originates from hydrogen isotopes and charged states of low-Z impurities (like carbon).

A set of 15 photodiodes (PD) is installed in TCV. Filters are installed in front of the diodes to select the required spectral emission. Some PDs (#1-4 and #7-8) have a D_α filter (656.3 nm) with an aperture to reduce the light collection angle and are installed on the vertical and lateral ports (Fig. 2.11). The remaining photodiodes (#11-18) observe the plasma vertically

and feature a range of filters to obtain the line-emission from different impurities and charge states present in the plasma.

The photodiodes are acquired at a sampling rate of 50 kHz and are used as an essential diagnostic to determine the time of breakdown during the plasma initiation in TCV. For hydrogen, at temperatures above 15 eV, i.e. $T_e > 13.6$ eV, the ratio of the excitation rate to the ionization rate becomes constant and thus, based on the assumption of a coronal emission regime, the line intensity produced by the excitation of $D^{n=3}$ to $D^{n=2}$ becomes proportional to the ionization rate (eq.(2.8)) [39],

$$\frac{\#ionizations}{time * volume} = n_D n_e \langle \sigma_{ion} v_e \rangle \propto \frac{\#D^{3 \rightarrow 2}}{time}. \quad (2.8)$$

In eq. (2.8), n_D is the density of neutral gas (deuterium) and $\langle \sigma_{ion} v_e \rangle$ the ionization rate.

In this thesis, the D-alpha signal is used to determine the time of breakdown (chapter 4). Also comparison of the different lateral PDs provides information on the vertical position of the breakdown in the TCV VV and is particularly useful for the characterization of the doublet shaped plasma scenario (chapter 7).

2.3.6 Fast Visible Camera

A fast imaging camera is a digital high speed camera which is used to acquire images of fast moving objects with a high spatial and temporal resolution. To obtain the desired image quality it is necessary to optimize the settings of the camera. The aperture and focal length of the lens of the camera determines the range of the distances from the lens which will be in focus. A shorter focal length or a smaller aperture results in larger area being in focus whereas a longer focal length or wider aperture results in a smaller area being in focus. The shutter speed is used to control the amount of light striking the image plane and the amount of light can be decreased by using a fast shutter speed. The Complimentary Metal-Oxide Semiconductor (CMOS) and Charge-Coupled Device (CCD) imaging detectors are widely used as the image sensor for the fast imaging cameras. A pixel forms the primary building block of an image formed by a CMOS or CCD image sensors. A pixel is essentially a photodiode which converts the incident photon energy to charge carriers and stores them to improve the sensitivity of the sensors. In a CCD device, the accumulated charge is transported across the chip and read at one corner of the array where an analog-to-digital converter turns the voltage of each pixel into a digital value. In CMOS chips there are several transistors for each pixel and the corresponding charge is amplified and transferred to sensing node using wires. The pixel resolution is measured in pixels per mm^2 and a high pixel resolution is required to obtain a high spatial resolution for the images.

A Photron Ultima APX-RS fast visible camera (FastCam) can be installed on an equatorial port to for a tangential view of the TCV plasma (Fig. 2.12). The FastCam has a 1024×1024 array of $17 \mu\text{m} \times 17 \mu\text{m}$ CMOS sensors. Since the CMOS sensors are essentially *Si* photodiodes, the spectral response is similar to the spectral response of the photodiodes. The FastCam is used to measure the plasma radiation emitted in the visible range (380-700 nm) of the



Figure 2.12: Photron Ultima APX-RS fast framing visible camera used in TCV. (a) Front view of the camera and (b) back view of the camera.

electromagnetic spectrum with the main contribution coming from line radiations emitted from hydrogen isotopes and partially ionized low atomic number impurities, like carbon. It is possible to record images at the full 1024×1024 pixel resolution at a frame rate of 3000 frames per second (fps) while very high frame rates of up to 250000 fps can be attained with a reduced 128×16 pixel resolution. The camera control and acquisition system are controlled using a graphical user interface, which is fully integrated into the TCV shot cycle.

In this thesis, a tomographic inversion of the FastCam measurements using the general tomographic inversion (GTI) code [5] is used to determine the time and position of the breakdown and, thereby, used as a tool to validate the poloidal magnetic reconstruction at the time of breakdown (discussed in detail in chapter 4).

2.3.7 Soft X-ray diagnostic

When the plasma temperature reaches a few hundred eV to a few keV, the plasma primarily emits radiation in the soft X-ray range. The main processes which contribute to the radiation emission in a plasma are the line radiation and Bremsstrahlung (free-free) radiation and recombination (free-bound) radiation. The total continuum radiation emission can be obtained

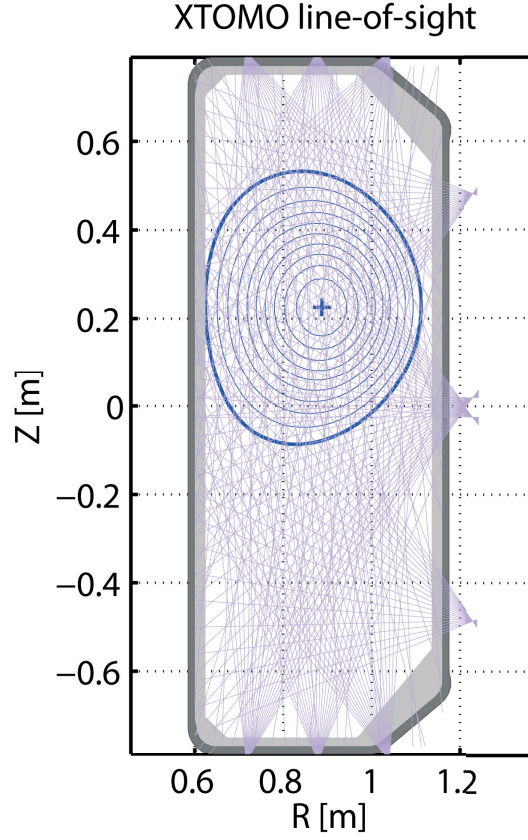


Figure 2.13: TCV poloidal cross section showing the lines of sight of the XTOMO diagnostic.

by summing over the contributions from the Bremsstrahlung and recombination radiation over all the different ion species and can be expressed as [32],

$$I(\omega) = 1.5 \times 10^{-38} n_e^2 \frac{1}{T_e} e^{-\frac{\hbar\omega}{T_e}} \zeta(T_e) \text{ Wm}^{-3} \text{ eV}^{-1}, \quad (2.9)$$

where $\zeta(T_e)$ is the enhancement factor and represents the enhancement of the radiation emission due to the presence of multiple ion species in the plasma in comparison to a pure hydrogen plasma with similar plasma parameters. When the recombination contribution becomes negligible in comparison to the Bremsstrahlung radiation, then provided $g_{ff,j}$ is equal for all the species, the total continuum emission can be expressed as [22],

$$I(\omega) = 1.5 \times 10^{-38} n_e^2 Z_{eff} \frac{1}{\sqrt{T_e}} e^{\frac{\hbar\omega}{T_e}}, \quad (2.10)$$

where $Z_{eff} = \frac{\sum_i n_i Z_i^2}{\sum_i n_i Z_i}$ is the effective ion charge and i is the index for the different ion species present in the plasma. Equation (2.10) shows that the soft X-ray emission depends strongly on n_e^2 , Z_{eff} and T_e .

The soft x-ray tomographic system (XTOMO) consists of ten pinhole cameras at a single

toroidal location. Each camera is equipped with a linear array of 20 p-n junction silicon photodiodes resulting in 200 lines of sight covering the whole plasma cross section (Fig. 2.13). Each camera has $47\mu\text{m}$ Be filter for the detection of photons with energies between 1 keV and 20 keV [4].

The XTOMO measurements are inverted using the GTI inversion code [5] to obtain the emissivity profile for doublet shaped plasma scenario (discussed in chapter 7).

2.4 Free Boundary Tokamak Equilibrium

The Free Boundary Tokamak Equilibrium code [25] allows to calculate arbitrarily shaped tokamak equilibria, with external or internal separatrices and multiple magnetic axes. The FBTE code calculates the PF coil currents required for a set of imposed boundary points, which can be either exact or approximate, with a prescribed plasma current, subject to a number of constraints and optimization criteria. The optimization problem is solved by minimizing a cost function made of the Ohmic dissipation in the PF coils, dipole moments created by the PF coils and flux error on the approximate boundary points with adjustable weights. The X-point where the poloidal field must be zero (e.g. to create a diverted plasma configuration) can be specified as one of the constraints. The FBTE calculation ignores the currents in the OH circuit as well as vessel currents. In case of doublets, it assumes a symmetric doublet equilibrium, including two symmetric droplet boundaries, droplet currents as well as pressure and current density distributions.

2.5 Matrix Generation Algorithm and Measurement Simulation

The Matrix Generation Algorithm and Measurement Simulation (MGAMS) code, is a shot preparation tool specifically developed for TCV plasma operation [29, 27]. MGAMS arranges the plasma equilibrium at various time points in the discharge invoking the FBTE code, calculates the stray field compensation with an electromagnetic modeling of TCV coil and vessel currents, and sets up breakdown magnetic configuration with the quadrupole coils. The various contributions to the PF coil currents are summed to calculate the references. It also builds observers based on estimated magnetic measurements for equilibrium control including plasma current, radial and vertical position, as well as elongation. Finally, different coil combinations are assigned by MGAMS as actuators for equilibrium and PF coil current control. MGAMS includes a Matlab GUI that allows the operator to change the various aspects of the breakdown scenario in TCV. While many relevant parameters, including the intended breakdown position, values of the imposed quadrupole magnetic field at the two quadrupole points, plasma current, Ohmic coil current ramp rate are variables that can be set in the GUI, other parameters including the *back-off coefficients* for the Ohmic and vessel field compensation, are hard coded in the preparation code (see chapter 4 for details). The original code was written in FORTRAN, but has recently been translated into Matlab [57]. The Matlab code facilitates changes of the hard-coded variables and is therefore used throughout the work performed

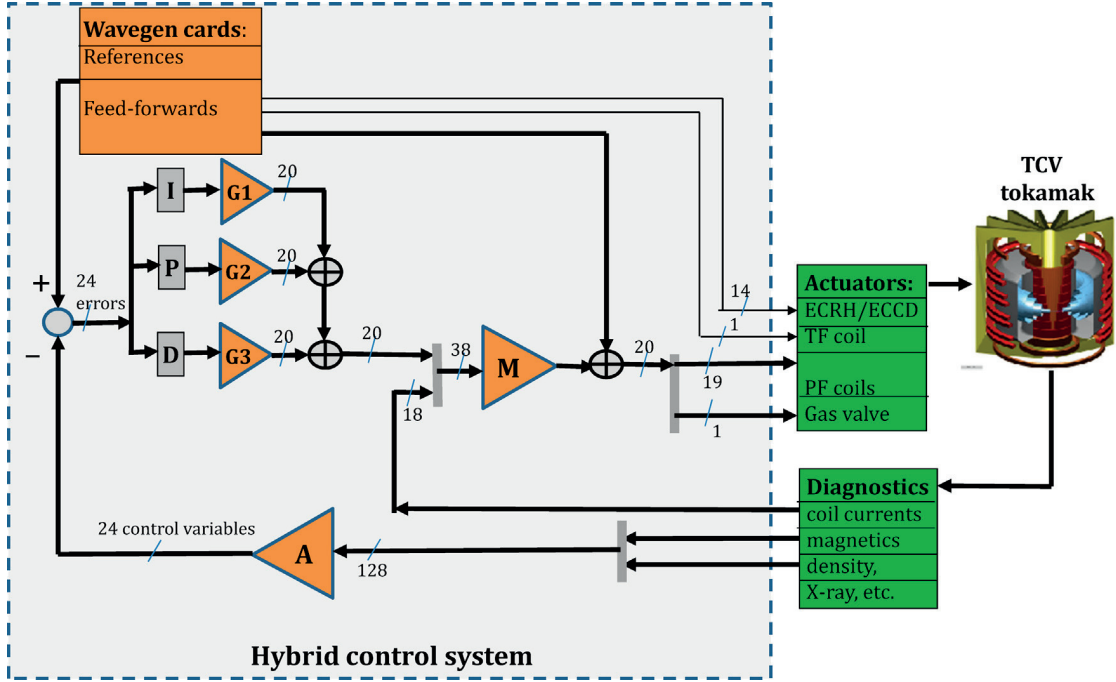


Figure 2.14: Schematic of the TCV hybrid control system showing its connections to the diagnostics and the actuators. Image: [48]

during the thesis.

2.6 TCV plasma control system

TCV has two major control systems: a legacy analogue plasma control system and more recent digital plasma control system. The analogue plasma control system [50] was originally installed in TCV and is referred to as the Hybrid control system. The digital control system [66] is mostly used for advanced control experiments and is referred to as the SCD (Système de Contrôle Distribu  ). The SCD is planned to replace the analogue system in the future. The SCD can emulate the hybrid control system and has been extensively used to implement the different control algorithms developed to improve the plasma formation in TCV (chapter 5) as well as in the development of the doublet shaped plasma scenario in TCV (chapter 7).

2.6.1 Hybrid control system

The hybrid system is a combination of analogue and digital processes. The system uses a set of analog matrix multipliers which are programmable. The multiplier coefficients can be switched at pre-defined times during a TCV plasma discharge. The inputs for the hybrid system are magnetic measurements and the line-integrated electron density measurement from the FIR interferometer. The *A matrix* of the hybrid control system uses 120 of these

diagnostic signals as inputs, and through linear combinations of the input signals constructs 24 observers. These observers are the plasma current (I_p), 16 PF coil currents (I_a), the difference between the two OH circuit currents (ΔI_{OH}), the vertical position of the plasma (parametrized as ZI_p), the radial position of the plasma (ΔR), plasma elongation (κ), the line-integrated density, signal to be differentiated for fast vertical feedback and pre-differentiated signal for fast vertical feedback (Fig. 2.14). The 24 observers are then subtracted from the reference signals, which are pre-calculated using the MGAMS code (section 2.5) and stored in waveform generators, to yield 24 error signals. Each error signal passes through a Proportional Integral Derivative (PID) amplifier with fixed gain [16]. These signals are then combined by the 22×24 *G matrix*, whose coefficients correspond to the PID gains and the combination of actuators (OH, PF, G coils and the gas valve) to be used for controlling each error signal is defined. The 22 outputs of the *G matrix* are the voltage corrections corresponding to the error signals, which have to be applied to the actuators to minimize the error signals. The 24 voltage correction signals obtained from the *G matrix* are passed through to the *M matrix*, which accounts for the effects of the mutual inductances and the coil resistive voltages. Finally, the feed-forward signals from a wave-generator, calculated in the plasma discharge design using the MGAMS code, are added to the output signals of the *M matrix* provide the real-time control of the TCV operational parameters [16]. The TCV hybrid control system has been used for more than 20 years. However, one of the disadvantages of this system is that it cannot perform non linear operations and has a limited number of output channels. These limitations are overcome in the digital control system, section 2.6.2

2.6.2 Digital control system

The SCD (Système de Contrôle Distribué) [66] has a set of independent computer nodes, which can each handle a large number of diagnostic inputs and actuator outputs. The nodes communicate across a shared reflective memory. Depending on the acquisition and computational complexity of the control algorithms, the cycle time for each node can vary between $50 \mu s$ and 1 ms. In the SCD the real-time (RT) control algorithms are first programmed in the Matlab-Simulink environment. A C code is generated from the Simulink block diagram for real-time execution which is compiled by the Simulink Embedded Coder into a Linux shared library and then distributed to target nodes in the discharge preparation phase. During the TCV discharge, an application is executed on each node that dynamically loads the shared library containing the compiled control algorithm at runtime. The data is stored in the real-time nodes by the control algorithm and then copied to the host computer and saved to the TCV database after the completion of the discharge. Figure 2.15 shows a schematic of the SCD control system layout with the connectivity to the diagnostics and actuators.

Node 1 is interfaced to different diagnostics, Duplex Multiwire Proportional soft X-ray counter (DMPX), a four filter soft-X spectrometer (XTe), and the 14 vertical chords of the FIR. The measurements obtained from these diagnostics can be used to construct observers to control various plasma parameters. Node 2 acquires all magnetic measurements from the tokamak and the central FIR channel. These measurements are used to construct observers which

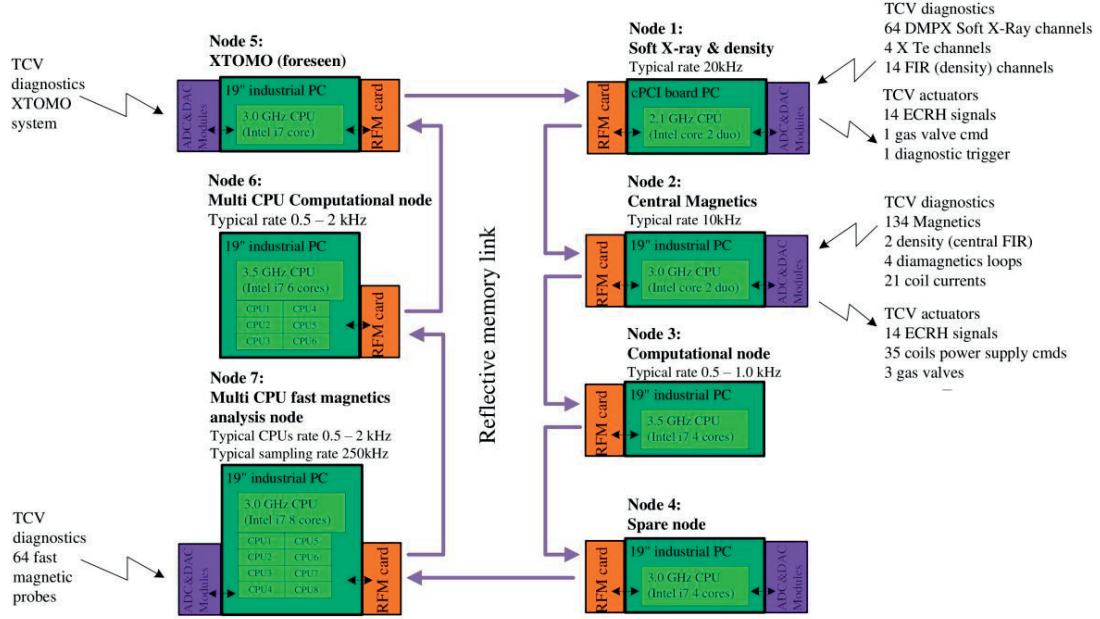


Figure 2.15: Top view of the SCD. Image: [3].

are then subtracted from the reference signals to yield error signals. These error signals can then be controlled by using the different actuators (two OH coils, 16 PF coils, ECRH launchers and the gas valves). This node is, therefore, used as the main plasma position and density controller. Node 3 is a computational node that computes the plasma magnetic equilibrium in real-time. Node 4 is a replacement node for node 2, while node 5 is an acquisition and processing node, presently under commissioning, connected to the 200 channel soft x-ray tomographic system. Node 6 is a recently installed multicore computational node that has been used to run multicore complex control codes (a faster real time equilibrium reconstruction replica and real-time modeling based advanced plasma performances controllers). Finally, node 7 is dedicated to real-time analysis of fast magnetic perturbations in the plasma [3].

The RT nodes are linked via the reflective memory which features a 128 MB memory area that is shared across all the nodes and the reflective memory network cards in each node are linked by a fiber optic ring. Data written by one node to a memory address within this shared memory area will almost instantaneously appear at the same memory address in the other nodes. Each node is assigned a separate section within the data area in which to write data, preventing the nodes from overwriting data areas outside their assigned write area [48].

3 Physics of the plasma formation in tokamaks

In an inductive plasma start-up in a tokamak, free electrons are accelerated by an applied toroidal electric field and via electron-neutral collisions they ionize the neutral atoms and molecules in the vacuum vessel [74]. This in turn, produces more electrons, which are again accelerated and induce further ionization, leading to an exponential increase of the number of electrons [67]. This process can be described as a classical Townsend *breakdown/avalanche*. The partially ionized plasma is conductive and a toroidal plasma current I_p is developed with the toroidal electric field. The poloidal magnetic field generated by the plasma current starts to increase and dominate over the stray poloidal field. Closed magnetic flux surfaces are then formed, which reduce the electron loss, and lead to an increase in the plasma current ramp rate. The ionization of the neutral gas and line-radiations from the impurities present in the plasma, result in the loss of a significant part of the heating power [52, 59]. This power loss P_{rad} is proportional to the product of electron and neutral density, and has a maximum at a certain degree of ionization, called radiation barrier. The plasma needs to *burn-through* this radiation barrier before the heating power can raise the plasma temperature. A high ionization state of impurities is normally reached after the burn-through of the main gas. A successful inductive plasma burn-through can only be obtained, if the Ohmic heating power exceeds the power loss by ionization and radiation. After the burn-through is accomplished, the plasma current is typically ramped-up further until the flattop is reached. During the *ramp-up* phase it is essential to avoid disruptions caused by MHD instabilities.

A schematic figure of a typical deuterium plasma formation is shown in Fig. 3.1, with the characteristic time evolution of plasma current, D_α emission, radiation and ionization power loss, and the electron temperature. The breakdown, burn-through and ramp-up phases are not necessarily consecutive phases but processes that may occur simultaneously. The definition of the exact start and end time of these phases also differs in the literature. This chapter describes the physics of the inductive plasma formation in tokamaks, and the dynamics of the plasma formation in TCV tokamak will be discussed in chapters 4 and 5. In this thesis, the breakdown phase is defined to start with the first ionization and lasts until Coulomb collisions start to dominate over electron-neutral collisions. The physics of the three different phases of the plasma formation discussed here are for a hydrogen and/or deuterium plasma. The physics of

the breakdown phase using a Townsend-like model is described in section 3.1. The ramp-up phase starts after the burn-through of the main gas but independent of the charge state of the impurities, and thus may overlap with the burn-through phase. For this reason, these two phases are treated together in the analysis and experiments in Chapter 5. While in this chapter, the physics in these two phases are described independently. Section 3.2 describes the physics of the burn-through phase with a power balance model, and the physics of the plasma current ramp-up phase is described in section 3.3.

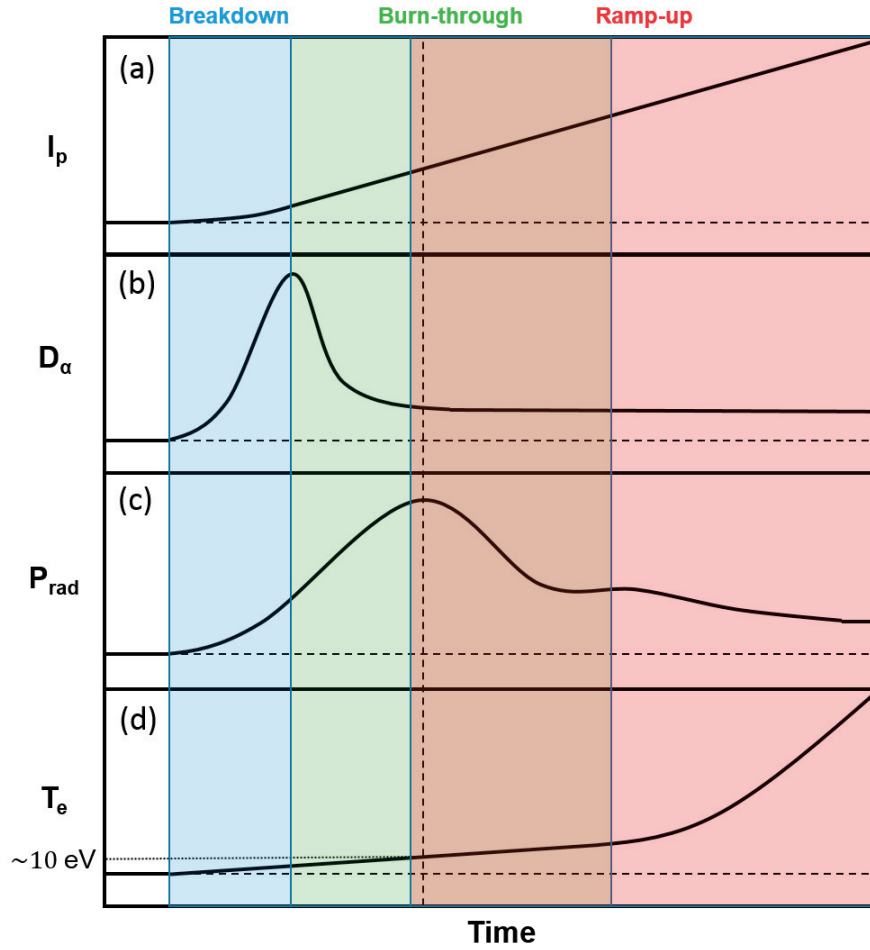


Figure 3.1: Schematic figure of the time evolution of (a) plasma current, (b) D_α emission, (c) radiation and ionization power loss, and (d) the electron temperature in a typical deuteron plasma formation. The breakdown (blue), burn-through (green), plasma current ramp-up (red) phases and the overlap between the burn-through and plasma current ramp-up phase (brown) are color labeled, respectively. The vertical dashed line represents the radiation barrier.

3.1 Physics of the breakdown phase

The breakdown phase in a tokamak is dominated by the collisions between free electrons and neutral particles and can be modeled by a Townsend-like model [53]. In this model it is assumed that the ions are stationary due to their higher mass. Following the Townsend model, the increase in the electron density is proportional to the difference between the ionization rate (ν_{ion}) and the loss rate (ν_{loss}) of the electrons,

$$\frac{dn_e}{dt} = n_e(\nu_{\text{ion}} - \nu_{\text{loss}}). \quad (3.1)$$

Therefore, the electron density during this phase can be expressed as,

$$n_e = n_{e0} \exp[(\nu_{\text{ion}} - \nu_{\text{loss}})t], \quad (3.2)$$

where n_{e0} is the initial electron density at $t = 0$ s. Breakdown occurs when the ionization rate exceeds the loss rate of the electrons. eq.(3.2) is valid as long as the degree of ionization remains small so the electron-neutral collisions dominate over the Coulomb collisions.

The electrons accelerate to a characteristic velocity due to collisions with the neutral atoms. In the tokamak a toroidal magnetic field is present. However the electric field is also toroidal and thus the acceleration is parallel to the magnetic field. The parallel speed is the same as the electron drift velocity,

$$u_{\parallel} = \text{const} \frac{E_{\varphi}}{p_n}, \quad (3.3)$$

where E_{φ} is the toroidal electric field and p_n the neutral gas pressure.

The ionization rate can be written in terms of the First Townsend coefficient (α),

$$\nu_{\text{ion}} = u_{\parallel} \alpha, \quad (3.4)$$

where

$$\alpha = A p_n \exp\left(-\frac{B p_n}{E_{\varphi}}\right). \quad (3.5)$$

In eq.(3.5), A and B are determined experimentally and found to be approximately constant over a restricted range of E_{φ}/p_n for any given gas.

During the initial breakdown, electrons are lost along the magnetic field because a stray poloidal magnetic field generated by currents in the Ohmic coils and eddy currents generated in the VV and other surrounding conducting structures leads to magnetic field lines that intersect the vessel wall. The loss rate of electrons due to their motion along the magnetic field lines can be expressed by,

$$\nu_{\text{loss}} = \frac{u_{\parallel}}{L_{\parallel}}, \quad (3.6)$$

where $L_{||}$ is the connection length, which is the distance the electrons have to travel along the magnetic field lines before they impinge on the VV wall and are lost for the avalanche. The connection length can vary greatly across the VV and is particularly large, where the poloidal field is small. This is the region where the breakdown is expected to be initiated. The start-up phase of tokamaks is therefore designed to produce a localized null in the poloidal field at the desired breakdown location at the time of breakdown. The effective loss rate of electrons in the 0-D model, eq.(3.6), can then be described using an average or effective connection length,

$$L_{\text{eff}} = \frac{r B_{\varphi}}{\langle |B_p| \rangle}. \quad (3.7)$$

In eq.(3.7), $\langle |B_p| \rangle$ is the volume averaged poloidal field in the vicinity of the null point, defined as a cylinder (large aspect ratio limit) of radius r . The expression for $\langle |B_p| \rangle$ is,

$$\langle |B_p| \rangle \approx \frac{2}{3} \frac{r}{|\nabla B_p|}.$$

Hence eq.(3.7) can be written as,

$$L_{\text{eff}} \approx \frac{3}{2} \frac{B_{\varphi}}{|\nabla B_p|} \quad (3.8)$$

It can be seen from eq.(3.8) that L_{eff} does not depend on the radial extent r of the region for volume averaging.

Setting the R.H.S. of eq.(3.1) to zero then yields the condition for the onset of the avalanche:

$$A p_n \exp\left(-\frac{B p_n}{E_{\varphi}}\right) = \frac{2}{3} \frac{|\nabla B_p|}{B_{\varphi}} \quad (3.9)$$

Equation(3.9) shows that a successful breakdown in a tokamak depends on the choice of the neutral gas pressure (p_n), the toroidal electric field (E_{φ}) and the poloidal field gradient ($|\nabla B_p|$) (Fig. 3.2). A neutral gas pressure window exists for a given toroidal electric field and effective connection length. When the pressure is too low, the ionization rate is too low for an electron to ionize an atom before it is lost. When the pressure is too high, the mean free path of electrons is too short for the electrons to be accelerated to the energy threshold for ionization before the next collision.

Once the plasma current generated poloidal field dominates over the stray field (or an intentionally applied quadrupole field), the magnetic configuration changes from open field lines to closed magnetic flux surfaces, results in a great confinement improvement.

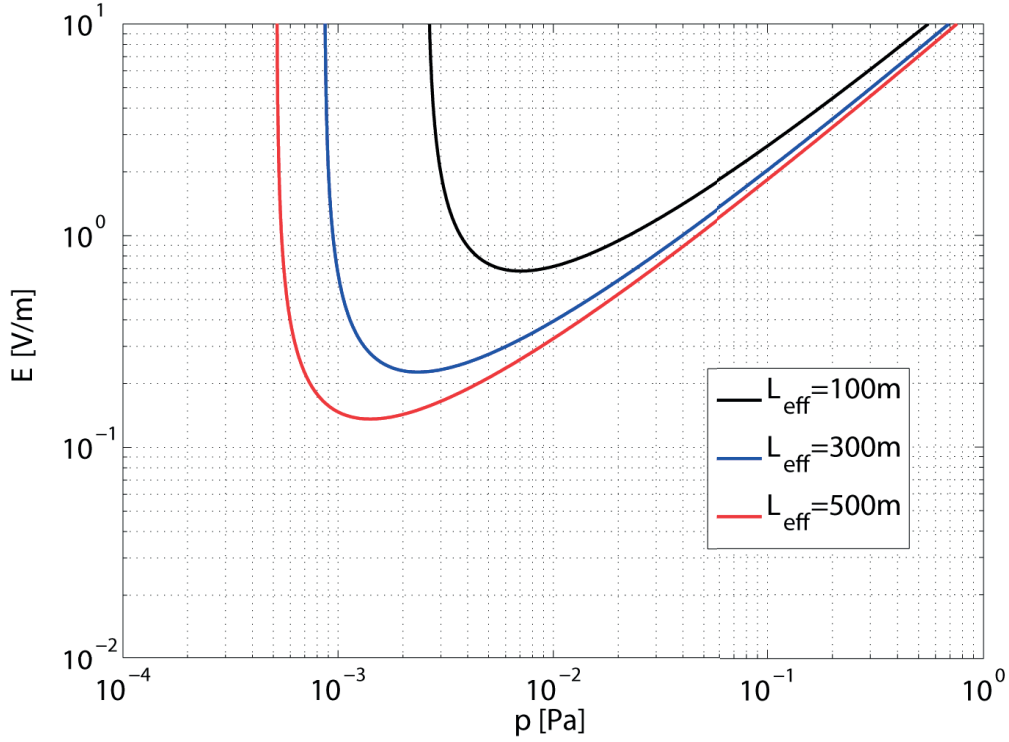


Figure 3.2: Condition for the Townsend criterion ($v_{\text{ion}} = v_{\text{loss}}$) for different connection lengths for deuterium gas with $A = 3.9 \text{ Pa}^{-1}\text{m}^{-1}$ and $B = 96.6 \text{ VPa}^{-1}\text{m}^{-1}$.

3.2 Physics of the burn-through phase

In the plasma burn-through phase, the Ohmic heating power must exceed the power loss due to radiation and ionization of the neutral gas and the main impurities originating from the interaction of the plasma with the first wall of the tokamak to sustain the plasma after a successful breakdown.

A 0-D plasma burn-through model can be used to model the plasma burn-through phase, by solving for the energy and particle balance for both the electrons and ions and the evolution of the plasma current [52]. In the model the effect of the presence of impurities during the burn-through phase as well as any auxiliary heating are neglected. The model assumes a constant plasma minor radius (a) and, hence, results in a constant plasma volume (V_p). The energy confinement time (τ_E) and particle confinement time (τ_p) are assumed to be constant and equal to each other. Although, the 0-D model described here is highly simplified, it is still able to provide a qualitative estimation of the various plasma parameters during the burn-through phase. It should be noted that the presence of the impurities, mainly carbon, plays a significant role during the burn-through phase in tokamaks with graphite first walls, such as TCV tokamak. More details about the effect of the presence of impurities on the dynamics of the plasma burn-through phase can be found in [52, 10, 42, 44, 41, 43].

The evolution of the electron energy in a deuterium plasma is given by,

$$\frac{3}{2} \frac{d}{dt} (n_e k_B T_e) = p_{OH} - (p_{ion}^D + p_{rad}^D) - p_{equi} - p_{brem} - \frac{3}{2} \frac{n_e k_B T_e}{\tau_E}. \quad (3.10)$$

The Ohmic power density (p_{OH}) in eq.(3.10) can be expressed as,

$$p_{OH} = \frac{I_p^2 R_p}{V_p}. \quad (3.11)$$

As the ionization of the neutral gas proceeds, the Coulomb (electron-ion) collisions start to dominate over the electron-neutral collisions, and the reaction of the plasma to an electric field is then well described by the Spitzer resistivity $R_p = 2R/a^2\eta$, where the Spitzer resistivity $\eta[\Omega m] = 5.1 \times 10^{-5} Z \ln \Lambda / T_e^{3/2}$, i.e. the Ohmic heating power decreases with increasing electron temperature.

The ionization and radiation losses for the neutral gas ($p_{ion}^D + p_{rad}^D$) is given by,

$$p_{ion}^D + p_{rad}^D \approx n_n n_e S_i (W_{ion} + W_{rad}). \quad (3.12)$$

In eq.(3.12), n_n is the neutral density, $W_{ion} + W_{rad} = 30$ eV is the total energy lost per ionization taking into account the energy lost during the multiple excitations before the ionization event occurs and $S_i[m^3 s^{-1}] = \frac{2 \times 10^{-13}}{6 + T_e[eV]/13.6} \sqrt{\frac{T_e[eV]}{13.6}} \exp\left(\frac{-13.6}{T_e[eV]}\right)$ is the electron ionization rate. p_{equi} is the power transferred by the electrons to the ions through elastic collisions and can be expressed by,

$$P_{equi}[Wm^{-3}] = 7.75 \times 10^{-34} (T_e[eV] - T_i[eV]) \frac{n_e[m^{-3}]^2 \ln \Lambda}{T_e[eV]^{3/2}}. \quad (3.13)$$

In eq.(3.13), T_i is the ion temperature.

$P_{brem}[Wm^{-3}] \approx 1.53 \times 10^{-38} n_e[m^{-3}]^2 T_e^{1/2}[eV] Z_{eff}$ is the power loss due to Bremsstrahlung radiations and Z_{eff} is the effective charge.

The last term in the R.H.S of eq.(3.10) denotes a generalized transport-like loss term.

In this model it is assumed that the ions are only heated by the transfer of energy from the electrons through elastic collisions and lose energy via charge exchange reactions and loss of energy due to transport. Therefore, the ion power balance is given by

$$\frac{3}{2} \frac{d}{dt} (n_e k_B T_i) = p_{equi} - p_{CX} - \frac{3}{2} \frac{n_e k_B T_i}{\tau_E}. \quad (3.14)$$

In eq.(3.14), $p_{CX}[Wm^{-3}] = \frac{3}{2} e n_e n_n (T_i[eV] - T_0[eV]) S_{CX}$ is the power loss due to charge exchange with $S_{CX}[m^3 s^{-1}] = 1.066 \times 10^{-14} T_i^{0.327}[eV]$ is the rate coefficient for the charge exchange reaction and T_0 is the neutral gas temperature.

The model assumes that the electrons are generated by the ionization of the neutral gas and are lost due to the loss of electrons from the confined plasma volume. Therefore, the electron

density evolution is given by

$$\frac{dn_e}{dt} = n_n n_e S_i - \frac{n_e}{\tau_p} \quad (3.15)$$

In eq.(3.15), τ_p is the particle confinement time and in this model is assumed to be equal to the energy confinement time (τ_E).

In this model the loss of the neutral gas due to pumping of the gas is neglected since the time constant for the chamber pumping is usually much larger than the duration of the burn-through phase. Thus, the loss of the neutrals is mainly due to the ionization of the neutral gas by the electrons ($-\frac{V_p}{V_v} \frac{dn_e}{dt}$). The evolution of the neutral density is given by

$$\frac{dn_n}{dt} = \Gamma_g - \frac{V_p}{V_v} \frac{dn_e}{dt} \quad (3.16)$$

In eq.(3.16), V_v is the volume of the vacuum vessel in m^3 and Γ_g is the neutral gas influx. This equation is used to impose the condition for particle conservation.

The evolution of the plasma current is given by

$$\frac{dI_p}{dt} = \frac{V_{loop}}{L_p} - \frac{R_p}{L_p} I_p \quad (3.17)$$

In eq.(3.17), V_{loop} is the toroidal loop voltage in V and L_p is the plasma self inductance in H. Here, V_{loop} and L_p are assumed to be constant.

The set of equations described above are solved over the period of the burn-through phase to obtain an estimate of the evolution of the electron and ion temperature, electron and neutral density, plasma current, the Ohmic heating power and the different power loss terms.

3.3 Physics of plasma current ramp-up phase

The plasma current ramp-up starts after the burn-through of the main gas but independent of the charge state of the impurities, and thus may overlap with the burn-through phase. In TCV, usually the plasma current reaches around 50 kA at the end of the plasma burn-through phase, however most discharges require a higher flattop current and thus need to be ramped up further.

To obtain a successful plasma current ramp-up, it is necessary to take into consideration the stability of the plasma position, the stability of non-axisymmetric MHD modes, and the energy and particle confinement of the plasma. The position of the plasma is controlled by external fields generated by PF coils. The radial position control, as an example, requires an increase of the vertical field to balance the hoop force which increases with the plasma current, and feedback control is required. The quickly changing equilibrium and a larger loop voltage and hence eddy current, however, may complicate the correct detection of the radial position.

The MHD stability depends on the shape of the plasma current profile and may lead to early disruption of the plasma [35, 36, 37]. The edge safety factor q_{edge} must be kept above 2.

A disruption can also be triggered when the current profile is too broad, i.e. the plasma internal inductance l_i too low, or when the current density profile is too peaked, i.e. l_i too high [24, 46, 11, 34]. To avoid disruptions during the plasma current ramp up phase, typically the internal inductance is maintained in the range 0.8 – 1.2 in TCV by selecting the plasma current ramp rate [71]. The plasma current is ramped up linearly in TCV, which is accompanied by an expansion of the plasma minor radius as well as an increase in the plasma elongation.

The dynamics of the plasma current ramp-up phase are modeled by solving the set of equations for current diffusion, the electron and ion heat and particle transport. The details for the modeling of the plasma current ramp-up phase are not discussed in this thesis and can be found in [6, 33].

3.4 Conclusion

A general description of the three different phases of the plasma formation in tokamaks was discussed, which forms the basis of the chapters 4 and 5.

Plasma formation in a tokamak can be improved only by developing a better understanding of the physics associated with the different phases of the plasma formation. The breakdown phase of the inductive plasma start-up can be modeled using Townsend model. A successful plasma breakdown is not sufficient to sustain the plasma and may result in a failed plasma formation during the burn-through phase due to insufficient Ohmic heating. In order to sustain the plasma it is necessary to have a plasma current ramp rate which is sufficient to ionize the neutral gas and the main impurities coming from the tokamak first wall. Plasma burn-through phase and the plasma current ramp-up phase may occur simultaneously. During the plasma current ramp-up phase, the plasma current and plasma cross section are further increased in a controlled manner to attain the desired flat-top plasma equilibrium. During this phase care should be taken that the shape of the plasma current density profile is such that it does not trigger a disruption and terminate the plasma.

4 Breakdown scenario

The criterion for the Townsend avalanche must be met for the neutral gas to break down and form a plasma (section 3.1). This chapter focuses on the setup of the breakdown scenario in TCV, the estimation of the different breakdown parameters, the different issues associated with the inductive breakdown in TCV and the experimental results obtained after the implementation of the different strategies to solve the identified issues.

Section 4.1 describes the breakdown strategy in TCV and compares it to the strategies adopted in other tokamak devices. Section 4.2 describes in detail the programming of the magnetic configuration during the inductive breakdown scenario in TCV using MGAMS. Section 4.3 describes the methods that are used to estimate the various breakdown parameters in TCV. These estimates are subsequently used in Section 4.4 in a database for the TCV breakdown scenarios, which reveals systematic differences between the intended and experimentally obtained breakdown positions. Section 4.5 discusses experiments performed to correct the breakdown positions. Section 4.6 then investigates to what degree externally controlled parameters such as the neutral gas pressure, the toroidal electric field and the magnetic configuration can affect the breakdown time and the initial plasma current ramp rate. Lastly section 4.7 concludes on the breakdown studies carried out within this thesis.

4.1 Breakdown strategy in TCV and comparison to other tokamaks

This section describes the breakdown strategy employed and compares it to the strategies adopted in other tokamak devices.

4.1.1 Breakdown strategy in TCV

TCV routinely uses inductive breakdown for the plasma initiation. The breakdown scenario in TCV is prepared using the MGAMS code [27] (section 2.5). Two metal filaments, situated at the top and bottom of the VV, are heated to provide a source of free electrons, which are required to initiate the ionization of the neutral gas. The use of two metal filaments ensures that the

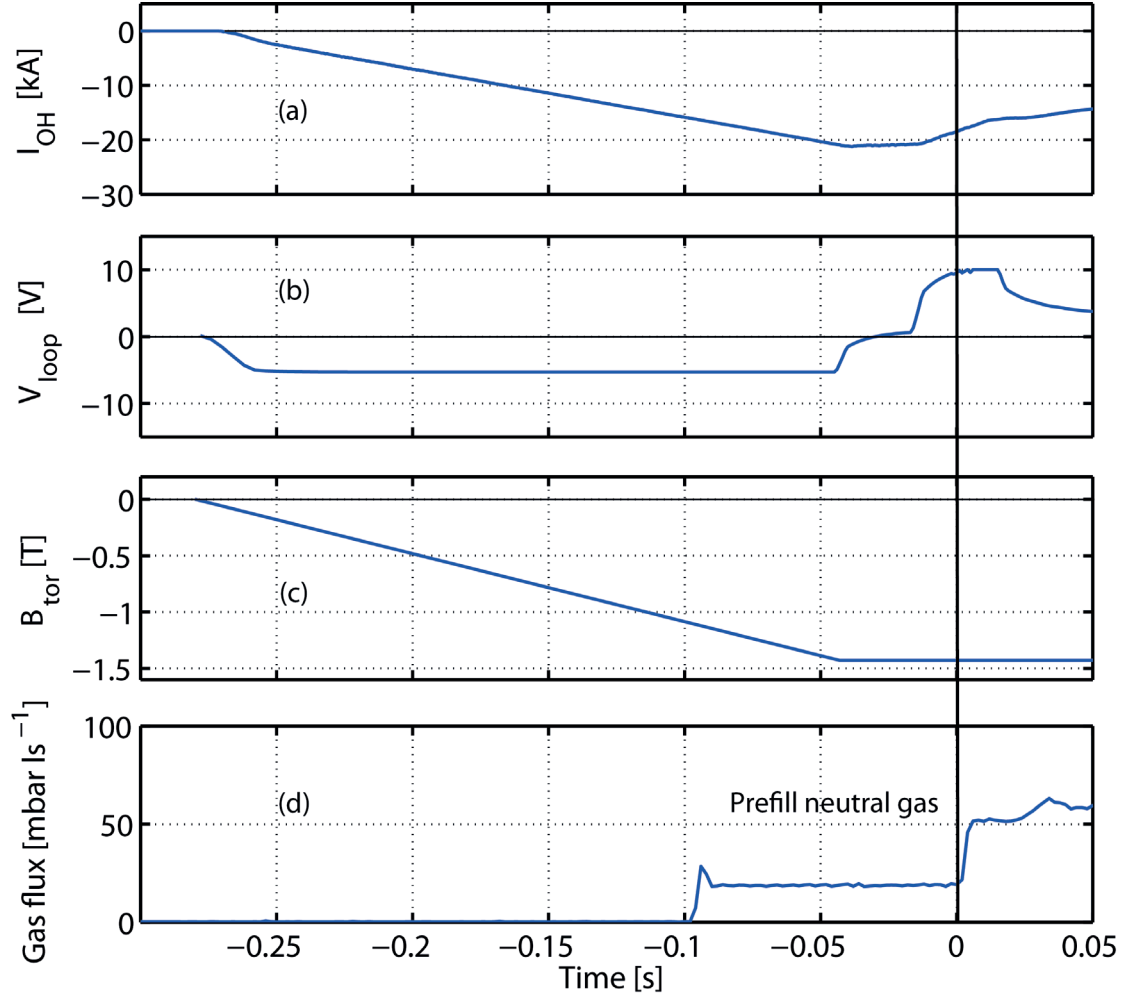


Figure 4.1: Breakdown strategy in TCV. Evolution of (a) the Ohmic coil current (I_{OH}), (b) the resulting loop voltage (V_{loop}), (c) the toroidal field (B_{tor}), and (d) the measured gas flux.

$B \times \nabla B$ drift transports electrons in the direction of the breakdown region for both toroidal field directions. The filaments consist of 1 mm diameter tungsten wires that are 32 mm long and extended in the toroidal direction to minimize the Lorentz force upon them in the toroidal magnetic field. A polarization voltage (U_{pol}) of -900 V is applied between the filament and the VV to push the electrons towards the main plasma breakdown region. The prefill gas injection typically starts at $t = -0.1$ s (Fig. 4.1d). A toroidal electric field is induced by the variation in the magnetic flux of the central solenoid (Ohmic coils). The transformer is pre-magnetized between $t = -0.254$ s and $t = -0.045$ s (Fig. 4.1a), which coincides with the ramp up of the toroidal field (Fig. 4.1c). The OH-coil is discharged starting at $t = -0.014$ s with a controlled, pre-programmed ramp-rate. The increase of the toroidal loop voltage inside the VV is delayed by resistive diffusion of the fields through the vessel wall ($\tau \sim 0.02$ s) and reaches ~ 10 V at $t = 0$ s (Fig. 4.1b). Breakdown before $t = 0$ s is prevented by the application of a vertical field. Once the loop voltage is close to its maximum value, the plasma breakdown is initiated by the

4.1. Breakdown strategy in TCV and comparison to other tokamaks

optimization of the magnetic field configuration using a combination of PF coils to generate a quadrupole null point at the desired breakdown position. A detailed description of the set-up of the magnetic field configuration during the breakdown phase in TCV is discussed in section 4.2.

Even though the breakdown strategy in TCV is largely based on the temporal evolution of the magnetic field configurations, problems to break down are usually addressed by changes in the pref-fill pressure rather than adjustments in the magnetic configuration.

4.1.2 Breakdown strategy in other tokamaks

This section briefly describes the breakdown strategies employed in JET [72, 54, 2, 13] and KSTAR [49, 61, 45, 47, 59].

Breakdown strategies in JET

In JET, the vessel is prefilled with gas several 100 ms before the start of the plasma and the desired loop voltage to ionize the neutral gas is provided by transformer action obtained from a combination of the central solenoid and the vertical field coils [13]. The JET VV has a relatively high resistivity due to resistive bellows between toroidal sectors. Two different methods are used to apply the loop voltage in JET, referred to as mode D and mode B. In mode D, first the primary coil is pre-magnetized with a current (ranging from 10 kA to 30 kA). A hexapolar magnetic field null in the center of the vessel is generated by using an appropriate combination of the coil currents in the primary coil and the vertical field coils. Once the required magnetic configuration is obtained, a loop voltage is generated in the vessel by opening the primary coil circuit to decrease the current in the primary coil with the time constant ($\sim L/R$) of the system. This method can generate loop voltages from 10 V to 30 V depending on the value of the pre-magnetization current. In mode B, the loop voltage is generated by ramping up the applied voltage on the primary coil to high values (~ 15 kV) before the magnetic field configuration is optimized to initiate the plasma start-up. Limits on the voltage ramp rate always leads to a lower loop voltage (ranging from 5 to 10 V) in mode B than in mode D [13].

Breakdown strategy in KSTAR

KSTAR is a superconducting tokamak device with a continuous vacuum vessel. The plasma initiation in KSTAR is obtained with the help of the blip resistor injection system (BRIS) which serves the dual purpose of providing the fast change in the PF coil currents to generate the required loop voltage and also reduce the PF coil driving voltage to satisfy the grid power requirements [49]. In KSTAR, the structural material used for the superconducting coils is Incoloy908, a ferromagnetic material, which distorts the magnetic field configuration during the plasma start-up. Also significant eddy currents are induced in the vacuum vessel during the ramp up of the PF coil currents to generate the required loop voltage to initiate the plasma. The PF coil currents in KSTAR are programmed such that they can produce the magnetic field

null at the desired location by including the contribution from the vessel eddy currents and the Incoloy908 structural components. The plasma initiation in KSTAR is obtained by deliberately delaying the magnetic field null formation until the desired loop voltage is reached [45].

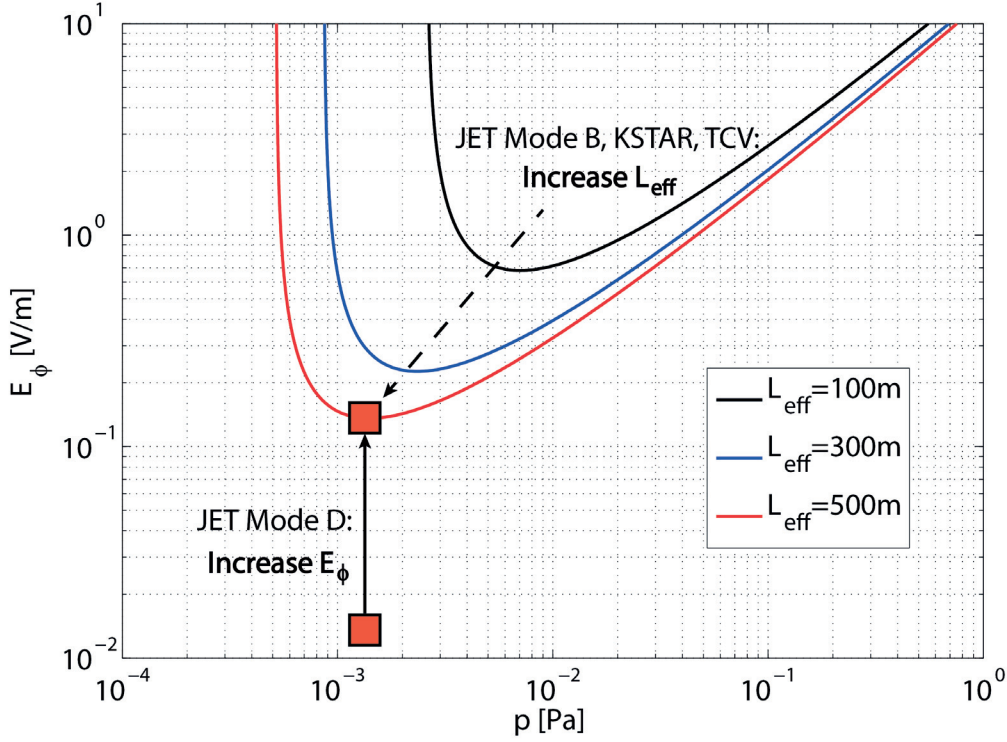


Figure 4.2: Townsend diagram showing the comparison of the breakdown strategies in TCV, JET and KSTAR.

4.1.3 Comparison of the breakdown strategy in TCV with other tokamaks

Plasma initiation in TCV is similar to mode B in JET and to KSTAR. In TCV and KSTAR the vessel has a lower resistivity, which means that the toroidal electric field takes longer to diffuse into the vessel and that eddy currents in the vessel have to be taken into account for the magnetic configuration. The strategy is to first establish the neutral gas pressure and the toroidal electric field with an unfavorable magnetic configuration, allow time for eddy currents in the conducting structure to establish and the electric field to diffuse into the VV, and then optimize the magnetic configuration to generate a poloidal field null that increases the connection length and thus obtain breakdown (Fig. 4.2). This differs from mode D in JET, where the neutral gas pressure and a poloidal magnetic field null with high connection length are established first before the plasma breakdown is initiated by an increase of the toroidal electric field (Fig. 4.2).

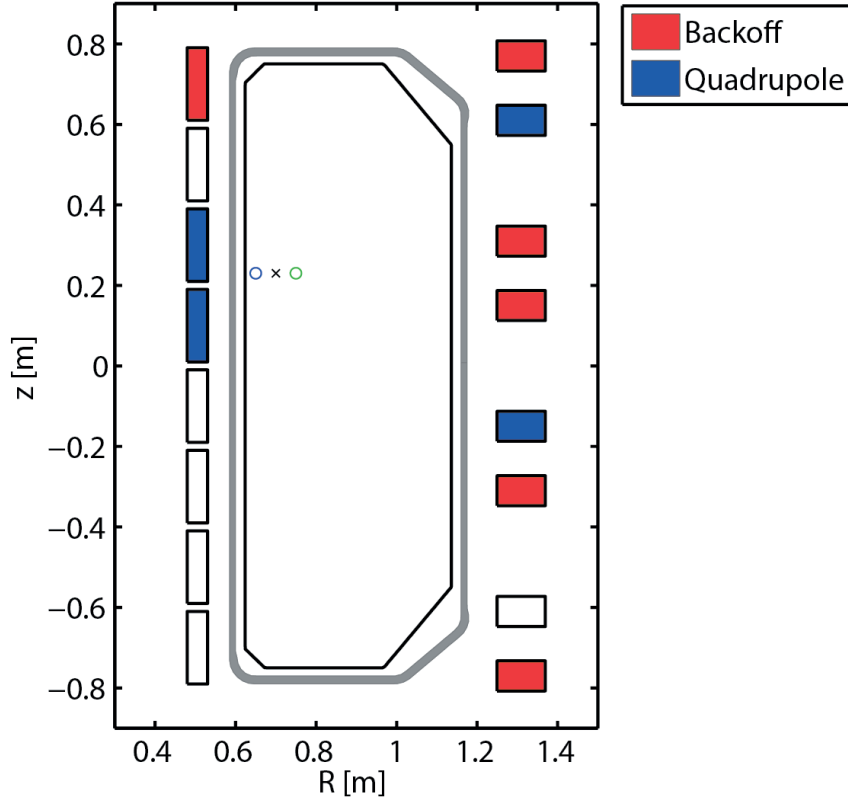


Figure 4.3: Schematic showing the programming of a typical breakdown scenario in TCV at the $Z = +0.23$ m breakdown location. A subset of PF coils is selected as *quadrupole coils* (blue) and another subset as the *back-off coils* (red). The 'o' denotes the two quadrupole control points on the HFS and LFS of the magnetic axis of the first FBTE equilibrium marked with an 'x'.

4.2 Programming of the breakdown magnetic configuration in TCV using MGAMS

The magnetic configuration during the preparation of the breakdown scenario in TCV is set up using MGAMS (section 2.5). Standard TCV breakdown configurations exist at three vertical locations ($Z = +0.23$ m, 0.05 m, -0.23 m) for both toroidal field ($B_\phi > 0$, $B_\phi < 0$) and plasma current directions ($I_p > 0$, $I_p < 0$) amounting to 12 standard breakdown scenarios. During the breakdown phase, the PF coil currents are a superposition of OH back-off currents, which are proportional to I_{OH} , vessel back-off currents, which are proportional to dI_{OH}/dt , currents to generate a vertical field and suppress an early breakdown before $t = 0$ s, quadrupole currents, which remains constant up to $t = 0$ s and are then phased out, and equilibrium currents obtained from the equilibrium code FBTE (section 2.4).

The amplitude of the stray poloidal field generated by the Ohmic coils ($|B_p| \sim 18$ mT at

$|I_{OH}| = 25$ kA) and induced vessel eddy currents ($|B_p| \sim 20$ mT at $V_{loop} = 10$ V) is sufficiently large to significantly affect the magnetic configuration during the plasma initiation and can, thereby, influence the programmed location of the null point and the gradient of the poloidal field at that null point. This stray field is compensated using a subset of PF coils (usually five to six PF coils), referred to as the *back-off* coils (Fig. 4.3). The stray field is minimized within a specified volume ($R \in [0.62 \text{ m } 1.12 \text{ m}]$ and $Z \in [-0.5 \text{ m } 0.5 \text{ m}]$) in the TCV VV and is prescribed by two sets of coefficients, the *OH back-off coefficients* and the *vessel back-off coefficients*, which correspond to the optimal correction currents for a unit OH coil current and to its derivative, respectively. Both the OH and vessel back-off coefficients are pre-calculated and hard-coded in MGAMS.

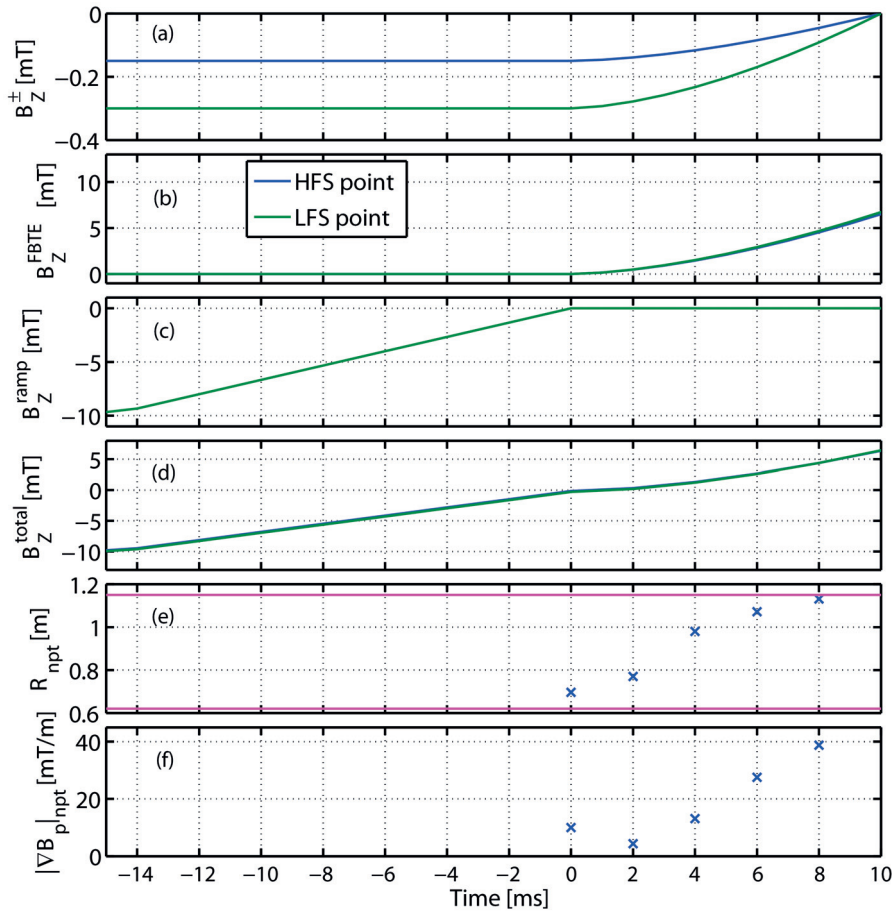


Figure 4.4: Evolution of (a) the imposed quadrupole vertical field (B_z^+), (b) the equilibrium field obtained from FBTE, (c) the vertical field to prevent a early breakdown, (d) the total field at the two quadrupole control points in MGAMS during a standard breakdown scenario, (e) the resulting radial position of the null point and, (f) the gradient of the poloidal field at the intended null point.

Following the back-off of the stray field, a null point is created at the intended breakdown position. The null point is characterized by the gradient of the poloidal magnetic field at the

4.2. Programming of the breakdown magnetic configuration in TCV using MGAMS

null point ($|\nabla B_p|_{\text{npt}}$) and its orientation (α_{npt}). $|\nabla B_p|_{\text{npt}}$ is obtained from the eigenvalue of the matrix of the derivatives of the magnetic field,

$$\vec{\nabla} B_p(R, Z) = \begin{pmatrix} \partial_R B_R & \partial_Z B_R \\ \partial_R B_Z & \partial_Z B_Z \end{pmatrix}. \quad (4.1)$$

The magnetic field is divergence free $\vec{\nabla} \cdot \vec{B}_p = 0$, which implies $\partial_R B_R = -\partial_Z B_Z$. In addition, the absence of plasma current before the breakdown means $\vec{\nabla} \times \vec{B}_p = 0$, implying that $\partial_R B_Z = \partial_Z B_R$. The eigenvalue of the matrix in Eq. (4.1) becomes,

$$\epsilon = \sqrt{(\partial_R B_Z)^2 + (\partial_R B_R)^2}. \quad (4.2)$$

The orientation of the null point α_{npt} corresponds to the direction of the eigenvector of the matrix of the magnetic field derivatives,

$$\tan(\alpha_{\text{npt}}) = \frac{\partial_R B_Z}{\partial_R B_R + \epsilon}. \quad (4.3)$$

The orientation of the null point determines the stability of a current filament in its vicinity, table 4.1. A current filament with a positive current (counter-clockwise when viewed from above) that is displaced to a larger radius than the null point must experience a negative vertical field to be pushed back to the null point. Radial stability, therefore, requires $\partial_R B_Z < 0$. Similarly, a current filament that moves vertically upwards must experience a positive radial field to be pushed back and vertical stability, therefore, requires $\partial_Z B_R > 0$. A quadrupole null point can, therefore, not simultaneously provide radial and vertical stability.

I_p direction	B_Z requirement for R stab.	B_R requirement for Z stab.	α_{npt} for Z stab.
$I_p > 0$	$\partial_R B_Z < 0$	$\partial_Z B_R > 0$	$0^\circ < \alpha_{\text{npt}} < 90^\circ$
$I_p < 0$	$\partial_R B_Z > 0$	$\partial_Z B_R < 0$	$90^\circ < \alpha_{\text{npt}} < 180^\circ$

Table 4.1: Relationship between the orientation of the null point α_{npt} and positional (radial and vertical) stability of the plasma for both directions of the plasma current.

On TCV, vertical stability is chosen over radial stability during breakdown. A favorable orientation for vertical stable plasma of the null point is chosen to be $\alpha_{\text{npt}} = 45^\circ$ for $I_p > 0$ and 135° for $I_p < 0$.

The MGAMS GUI is used to set up the breakdown position by specifying the radial and vertical field values ($B_{R,Z}^\pm$) at two control points (typically located 1 cm to the left and right of the magnetic axis of the first equilibrium), which is sufficient to constrain the position ($R_{\text{npt}}, Z_{\text{npt}}$), $|\nabla B_p|_{\text{npt}}$ and α_{npt} . A linear expansion of the poloidal magnetic field in the vicinity of the two quadrupole control points yields the location of the null point, and using eq.(4.2) and (4.3), its

gradient and orientation.

$$\begin{aligned}\partial_R B_R^x &= \frac{B_R^+ - B_R^-}{0.02} \approx \partial_R B_{R_{\text{npt}}} \\ \partial_R B_Z^x &= \frac{B_Z^+ - B_Z^-}{0.02} \approx \partial_R B_{Z_{\text{npt}}},\end{aligned}$$

where + and – denote the LFS and HFS control points, respectively, and x denotes the nominal position. To ensure a null point at the magnetic axis of the first equilibrium, the imposed fields at the two control points must be equal and opposite, otherwise the intended null point will be shifted. Additionally, B_R^+ and B_R^- must be set to 0 for a favorable null point orientation.

The values of $B_{R,Z}^\pm$ specified in MGAMS GUI were determined empirically from experiments performed on TCV to obtain successful breakdown at different breakdown positions, and for the possible plasma current and toroidal field directions. Therefore, depending on the choice of these empirical values, the intended null point position may differ from the magnetic axis of the first FBTE equilibrium, Fig. 4.4d. The quadrupole field is applied using a separate subset of four PF coils, referred to as *quadrupole* coils, which are located close to the breakdown region. Since the quadrupole field is constant in time (up to $t = 0$ s), it is combined with the compensation of the stray field of the toroidal bus bars. The quadrupole magnetic field configuration, applied at $t = 0$ s, is phased out as $(1 - (t/t_1)^{1.63})$ until the first FBTE equilibrium ($t_1 = 10$ ms) is reached and, simultaneously, the first FBTE equilibrium field ($B_{R,Z}^{\text{FBTE}}$) is phased in as $(t/t_1)^{1.63}$ (Fig. 4.4a and b, respectively).

Additionally, to avoid a premature breakdown, a constant vertical field of magnitude ~ -10 mT is applied from $t = -0.05$ s until $t = -0.015$ s for $I_p < 0$ breakdown scenarios to place the nominal position outside the vessel. After $t = -0.015$ s, this field is linearly phased out by $t = 0$ s (Fig. 4.4c).

4.3 Estimation of the breakdown parameters

The breakdown phase in a tokamak depends on the neutral gas pressure (p_n), the toroidal electric field (E_ϕ) and the magnetic field configuration parametrized by (L_{eff} or $|\nabla B_p|_{\text{npt}}$) (section 3.1). Estimates of these parameters and their temporal evolution are essential to understand the dynamics of the breakdown phase. This section discusses the methods that were developed to estimate p_n , E_ϕ , $|\nabla B_p|_{\text{npt}}$ and L_{eff} .

4.3.1 Estimation of the neutral gas pressure

The neutral gas pressure is one of the control parameters that affects the breakdown. A simple 0D-model of the particle balance ('p-b') is used to estimate the evolution of the neutral gas pressure in TCV leading up to the gas breakdown,

$$\frac{dp_n^{\text{p-b}}(t)}{dt} = \frac{\Gamma_{\text{in,gas}}(t)}{V_{\text{TCV}}} - \frac{p_n^{\text{p-b}}(t)}{\tau_{\text{pump}}} \quad (4.4)$$

4.3. Estimation of the breakdown parameters

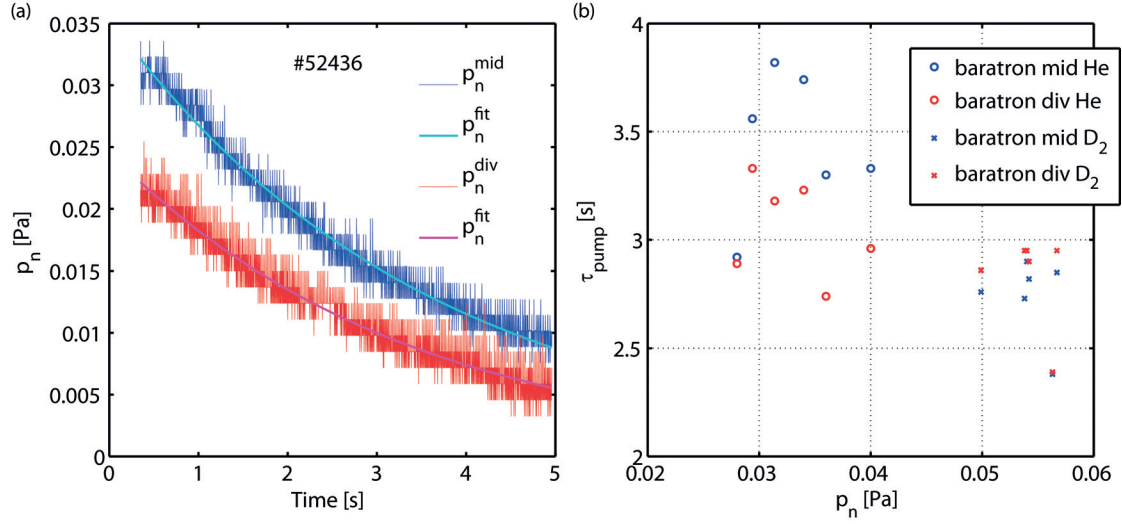


Figure 4.5: (a) Evolution of the neutral pressure measured with baratrons in the outboard mid-plane ('mid') and under the floor ('div') in failed He discharge attempts. (b) Decay time of the neutral gas (τ_{pump}) obtained from exponential fits of the baratron measurements for failed helium and deuterium discharge attempts in TCV.

In this model, the gas flux from the fueling valve ($\Gamma_{\text{in,gas}}$) is assumed to be the sole source of neutral particles inside the TCV VV (volume $V_{\text{TCV}} \approx 4.6 \text{ m}^3$). A decay time (τ_{pump}), is used to model the loss of the neutral gas pressure due to the pumping of the gas by the four turbo pumps installed in TCV and retention of the gas (mainly deuterium) by the graphite tiles of the TCV first wall. The value of τ_{pump} is required in order to obtain an estimate of the neutral gas pressure from particle balance ($p_n^{\text{p-b}}$) by integrating eq.(4.4).

Recently, two baratrons [73] were installed in TCV to measure the neutral gas pressure at the outboard mid-plane (p_n^{mid}) and below the floor (p_n^{div}). An estimate of τ_{pump} was obtained from the neutral gas pressure measured by the two baratrons after the gas input was cut-off in both deuterium and helium discharges, that failed during the burn-through phase. Exponential fits of the pressure decay for various prefill pressures yield $\tau_{\text{pump}} \sim 2.8 \text{ s}$ for deuterium and $\tau_{\text{pump}} \sim 3.3 \text{ s}$ for helium, Fig. 4.6b. The lower value of τ_{pump} for deuterium may be explained by the absorption of deuterium on the graphite tiles of the TCV first wall.

During the breakdown phase, a three parameter fit of $p_n^{\text{mid,div}}(t)$ was used to compare the neutral gas pressure estimate obtained from the particle balance model with the two baratron measurements,

$$\frac{dp_n^{\text{mid,div}}}{dt} = \frac{1}{\tau^{\text{mid,div}}} \left(c^{\text{mid,div}} p_n^{\text{p-b}}(t - \Delta t) - p_n^{\text{mid,div}} \right). \quad (4.5)$$

The three fit parameters are $\tau^{\text{mid,div}}$, which represents the time delay between the two baratron measurements and the pressure in the VV and depends on the conductance between the two baratrons and the VV, $c^{\text{mid,div}}$, which represents the scaling factor to account for the systematic errors in the absolute value of the pressure estimates ($p_n^{\text{p-b}}$ and $p_n^{\text{mid,div}}$), and Δt ,

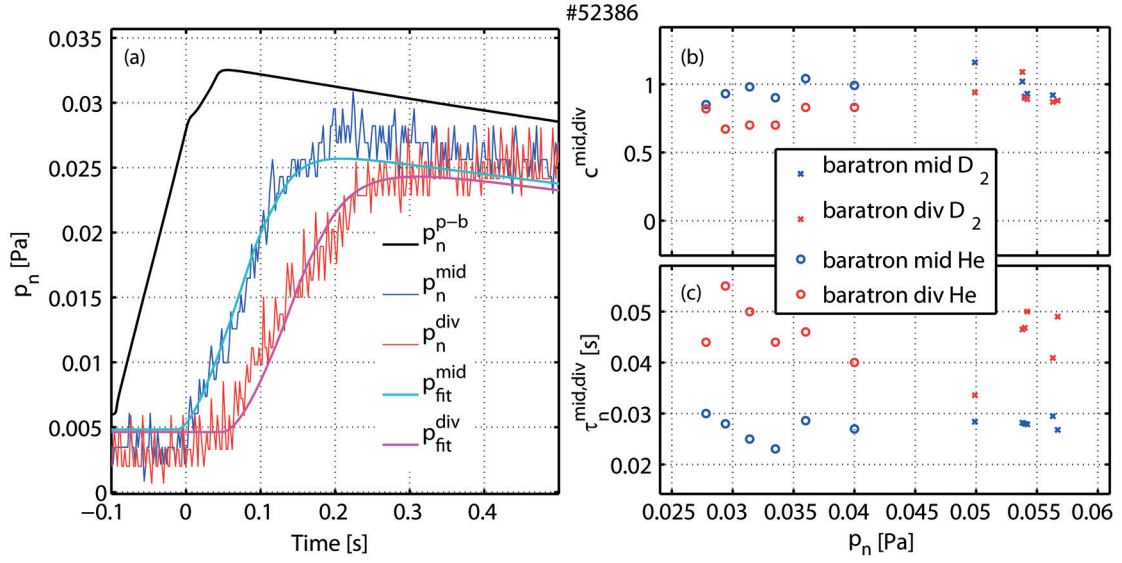


Figure 4.6: Comparison of (a) the two baratron measurements with the fitted neutral gas pressure values obtained from three parameter fit for a helium discharge in TCV, (b) the amplitude modification factor ($c^{mid,div}$) for the two baratrons for helium and deuterium gas, and (c) the time response ($\tau_b^{mid,div}$) for the two baratrons for helium and deuterium discharges.

which accounts for a time lag between the pressure estimates (p_n^{p-b} and $p_n^{mid,div}$). While, the comparisons clearly suggest the existence of a time lag, its origin remains unknown. The comparison between p_n^{p-b} and $p_n^{mid,div}$ was performed for both deuterium and helium plasma discharges that failed during the burn-through phase. The absolute values of the estimates of the neutral gas pressure (p_n^{p-b} and $p_n^{mid,div}$) agree within 95%. The average value of τ^{mid} is 0.027 s and τ^{div} is 0.045 s. The time delay of the two baratrons is independent of the gas type and the time delay of mid-plane baratron is shorter than that below the floor (Fig. 4.6).

Due to the time lag in the baratron measurements, it is not possible to obtain accurate neutral pressure from the baratrons during the breakdown phase, but the comparison increases the confidence in the absolute values obtained from the gas-balance estimate. Hence, the neutral gas pressure estimates obtained from the particle balance model are used for the analysis of the breakdown parameters in this thesis.

4.3.2 Estimation of the toroidal electric field

The loop voltage (V_{loop}) remains approximately constant across the TCV VV, since the Ohmic transformer is designed to minimize the stray magnetic field inside the VV. The toroidal electric field (E_ϕ), therefore, decreases with an increasing major radius (R) and is obtained from V_{loop} measured with flux loops,

$$E_\phi = \frac{V_{loop}}{2\pi R}. \quad (4.6)$$

4.3.3 Estimation of the magnetic configuration up to the time of breakdown

The magnetic field configuration plays an important role in the creation of a stable and reproducible breakdown (section 3.1). Due to the low resistivity of the TCV VV ($\approx 55 \mu\Omega$), the high loop voltage during breakdown induces large eddy currents in the VV. At the maximum loop voltage of ~ 10 V the induced eddy currents are of the order of 200 kA and significantly modify the poloidal magnetic field inside the VV. The poloidal magnetic field distribution up to the time of breakdown can be reconstructed, if the currents in the VV, OH and PF coils are known. The currents in the OH and PF coils are measured with shunts. However, the current distribution in the vessel is neither controlled nor measured directly as it is the result of the electromagnetic interaction between the vessel and the variation of the magnetic field produced by the driven coils. Therefore, the VV current must be estimated from the temporal evolution of the measured coil currents. An estimate of the current distribution in the VV can be obtained from the circuit equation for axisymmetric vessel filaments,

$$0 = R_{VV}I_V + M_{VV}\frac{dI_V}{dt} + M_{Va}\frac{dI_a}{dt}, \quad (4.7)$$

where R_{VV} is the resistivity of the vessel current filaments, which were determined experimentally by fitting of the magnetic measurements [55], M_{VV} are the Green's functions between the vessel current filaments, M_{Va} the Green's functions between the vessel current filaments and the driven coils (OH and PF coils), I_V the vessel current filaments (usually 38 vessel current filaments are used), dI_a/dt the coil current derivatives and dI_V/dt the vessel current derivatives. A procedure to increase the accuracy of the vessel current estimates by also using the magnetic measurements such as the flux loop and magnetic probe measurements was proposed and implemented in the *breakdown* code [68].

The magnetic measurements (poloidal flux, loop voltage, poloidal field and coil currents) are related to the toroidal currents in the system and their derivatives. These relations can be written as a system of linear equations,

$$\mathbf{m}^{\text{model}} = \mathbf{M} [I_a, I_V, \dot{I}_a, \dot{I}_V], \quad (4.8)$$

where $\mathbf{m}^{\text{model}}$ is the vector of the modeled 38 flux loop measurements, 38 loop voltage measurements, 38 magnetic pick up coil measurements, 16 PF coil and 2 OH coil current measurements and \mathbf{M} the coupling matrix between the currents, the current derivatives and the measurements. This model is only valid up to the breakdown time, as it does not consider any plasma current. In the system comprising equations (4.7) and (4.8), the currents and their derivatives are considered as independent variables. The link between these quantities is, therefore explicitly added by imposing,

$$\begin{aligned} \dot{I}_a &= \frac{dI_a}{dt} \\ \dot{I}_V &= \frac{dI_V}{dt}, \end{aligned} \quad (4.9)$$

where \dot{I}_a is the vector of the fitted coil current derivatives, I_a is the vector of the fitted coil currents, \dot{I}_v is the vector of the fitted vessel current derivatives and I_v is the vector of fitted vessel currents.

A least square solution is obtained for equations (4.7) and (4.9) for a sequence of time steps until the breakdown time,

$$\chi_{\min}^2 = \sum_i w_i^2 \left[\mathbf{m}_i^{\text{meas}} - \mathbf{m}_i^{\text{model}} \right]^2 = \sum_i w_i^2 \left[\mathbf{m}_i^{\text{meas}} - (\mathbf{M} \cdot \mathbf{x})_i \right]^2 \quad (4.10)$$

where χ_{\min}^2 is the minimum of the sum of the squared residuals, w_i is the weight of the considered magnetic measurements, $\mathbf{m}_i^{\text{meas}}$ denotes the magnetic measurements, $\mathbf{m}_i^{\text{model}} = (\mathbf{M} \cdot \mathbf{x})_i$ denotes the modeled magnetic measurements, \mathbf{x} is the vector of fitted currents and their derivatives respectively. A unique solution of equation (4.10) for the fitted currents and their derivatives (\mathbf{x}) exists if the matrix \mathbf{M} has linearly independent columns.

To obtain a consistent solution for equations (4.7) and (4.9), weights are assigned to each of the measurements and for chosen as the inverse of the uncertainties of the measurements. To obtain consistency for the fitted current derivatives and the derivatives of the fitted currents, an iterative process is used. Firstly, the magneto static problem is solved (i.e. only eq.(4.8) assuming $\dot{I}_a = 0$ and $\dot{I}_v = 0$) to obtain the coil and vessel currents. These currents are then used to compute the current derivatives from equation (4.9). The solution using a least square fitting method is a vector with the currents in the PF coils and in the vessel at each time step before breakdown. From the computed currents in the PF coils and in the VV, the magnetic field configuration is obtained by,

$$B_{k,x} = b_{k,xa} \cdot I_a + b_{k,xv} \cdot I_v, \quad (4.11)$$

where $B_{k,x}$ is the computed magnetic field with k denoting radial (R) or vertical field (Z) components, x the index of the grid points, $b_{k,xa}$ the matrix containing the relevant Green's functions between the grid points and the coil currents, and $b_{k,xv}$ the matrix containing the relevant Green's functions between the grid points and the vessel current filaments.

Similarly, the poloidal flux can be calculated as,

$$\psi_x = G_{xa} \cdot I_a + G_{xv} \cdot I_v, \quad (4.12)$$

where ψ_x is poloidal flux on the same grid, G_{xa} the matrix containing the relevant Green's functions between the grid points and the coil currents, and G_{xv} the matrix containing the relevant Green's functions between the grid points and the vessel current filaments.

An example of a reconstructed magnetic configuration at the time of the breakdown (section 4.3.4) is shown in Fig. 4.7. The null points are detected using a linear interpolation of the magnetic field on the discrete grid. An estimate of the gradient of the poloidal magnetic field associated with the null points ($|\nabla B_p|_{\text{npt}}$) is also obtained from the poloidal magnetic field distribution, which in turn, yields an estimate of the effective connection length (section 3.1). Since the breakdown should occur close to the null point with the highest effective connection length (section 3.1), the breakdown position ($R_b \approx R_{\text{npt}}$ and $Z_b \approx Z_{\text{npt}}$) can also be estimated

from the poloidal magnetic field distribution.

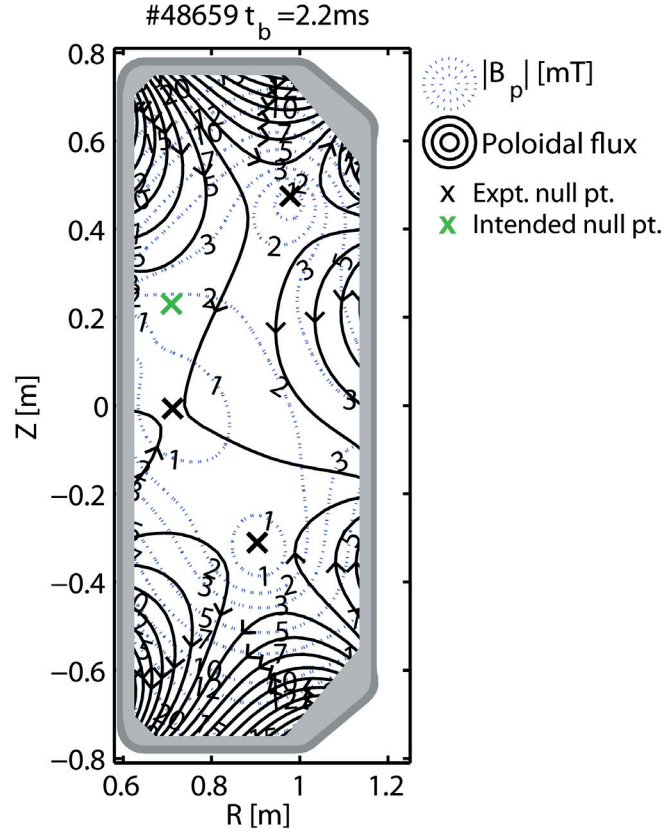


Figure 4.7: Reconstruction of the magnetic field configuration at the time of breakdown obtained using the breakdown code. The green 'x' denotes the programmed breakdown location in MGAMS, and the black 'x' denote the position of the experimental null points. The dotted blue lines denote B_p contours with the numbers indicating its magnitude in mT. The solid black lines are the poloidal flux contours.

Validation of the magnetic field reconstruction

The magnetic reconstruction together with the assumption that the breakdown occurs at the null point with the highest effective connection length, is validated with the FastCam diagnostic (section 2.3.6). The FastCam detects line emission in the visible range of the electromagnetic spectrum, which, during breakdown, dominated by the D_α radiation. Since for electron temperatures between 5 – 20 eV, the D_α emission is proportional to the ionization rate, the location where D_α is detected first corresponds to the breakdown location. The temporal resolution (sub ms) of the FastCam is sufficient to detect the location, where the initial breakdown occurs. The FastCam was operated with a sampling frequency of 5 kHz, and a spatial resolution of 512×1024 pixel. The general tomographic inversion (GTI) package [40] is used to reconstruct the axisymmetric emissivity distribution from the tangential FastCam images. Since this tomographic inversion is under-determined, the GTI package uses a

minimum Fischer regularization to reconstruct the emissivity distribution [5]. The viewing geometry of the FastCam is determined by identifying ports and tile gaps in the FastCam images and comparing them to a pin hole camera model image of the vessel.

The good agreement between the null point location predicted by the *breakdown* code and the location of the initial D_α emission obtained using the inverted FastCam image validates the reconstruction of the magnetic field distribution leading up to the breakdown time. In Fig.4.8, the null point with the longest effective connection length is located at $z_b = 0.153$ m and the location of initial D_α emission obtained from inverted FastCam images is 0.15 m.

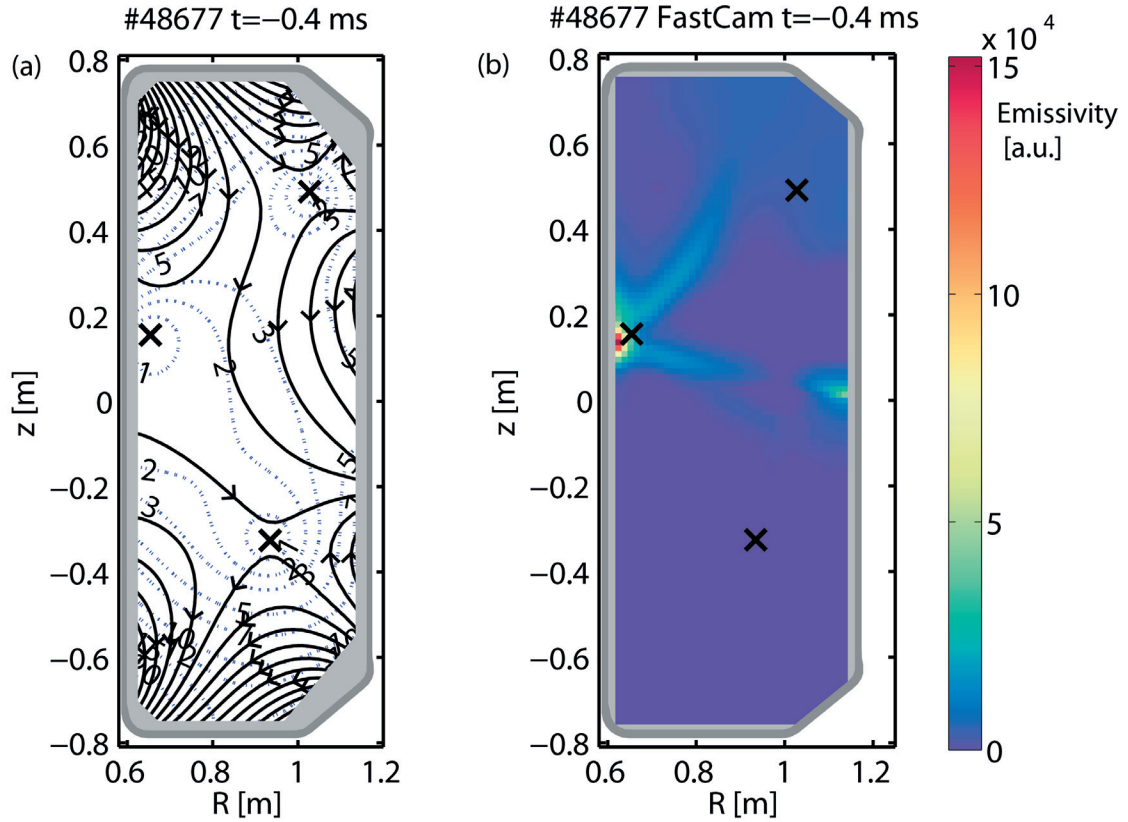


Figure 4.8: Comparison of (a) the reconstructed magnetic field configuration and (b) the inverted fast framing camera image obtained using the GTI package. The 'x' denotes the experimental null point locations obtained from the *breakdown* code.

4.3.4 Estimation of the breakdown time

The breakdown time (t_b) can be estimated as the time when the plasma current obtained from magnetic measurements exceeds the noise level of the measurement. The *breakdown* code uses this method to estimate the breakdown time (Fig. 4.9a) and consequently provide an estimate of the breakdown position, gradient of the poloidal field at the null point and orientation of this null point at this time. The breakdown time can also be defined as the time

at which a D_α signal, indicative of ionizations, is first detected (Fig. 4.9b). Since the noise levels of the two diagnostics are different, the two estimates of the breakdown time differ too, with the D_α breakdown time trailing the plasma current breakdown time by up to 1 – 2 ms. In this thesis, the breakdown time is taken from the increase in the plasma current.

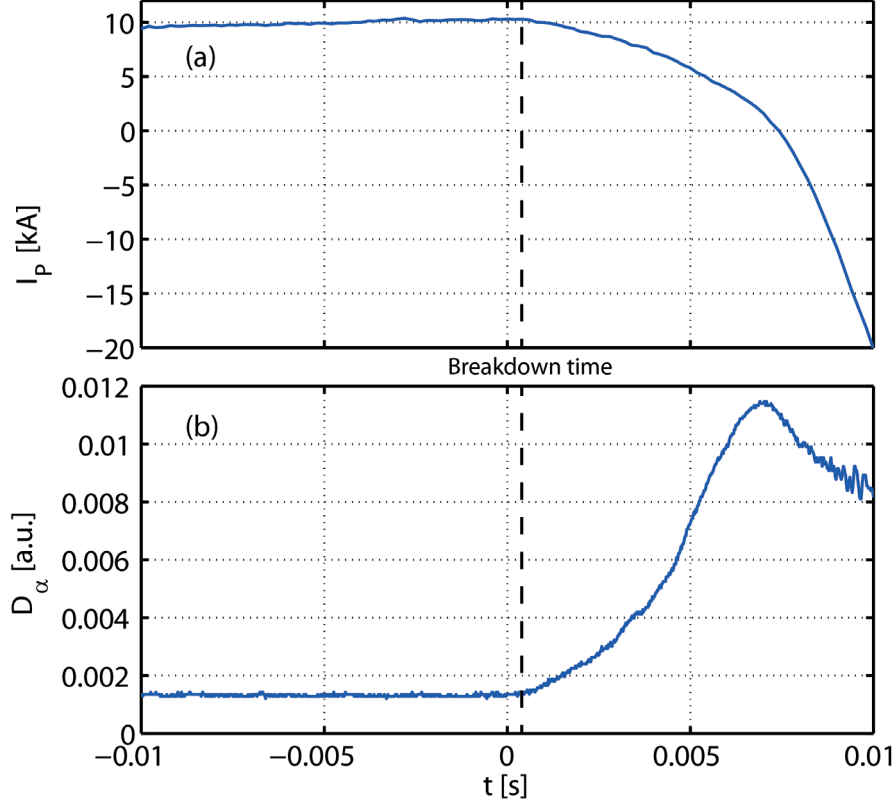


Figure 4.9: The estimation of the breakdown time using the plasma current and the D_α signal. (a) I_p evolution from the magnetic measurements, and (b) D_α signal from the vertical PD. The vertical black dashed line represents the respective breakdown time estimates.

4.4 Analysis of the present TCV breakdown scenario database

A database of breakdown parameters was created for the TCV discharges from shot number #35000 to #54000, corresponding to 9 years of TCV operation (2008-2016), to develop a better understanding of the dynamics of the breakdown phase in TCV. The database includes the estimates of the experimentally obtained breakdown time t_b and the null point position used as the breakdown position (R_b, Z_b).

In total 10760 shots were genuine plasma discharges, only 54 (0.5%) of them have a failed breakdown due to technical issues, such as no injection of neutral gas into the vacuum vessel, absence of the toroidal field or the Ohmic coil current, and issues with the plasma control system. 5936 successful breakdowns were selected for analysis in the database, of which 188 are with $B_\phi > 0$, $I_p > 0$, and 5748 with $B_\phi < 0$, $I_p < 0$ (table 4.2). No discharges with different

Chapter 4. Breakdown scenario

signs of B_φ and I_P were among the selected discharges. The database includes all 3 standard breakdown positions: 2127 breakdowns were programmed at $z = 0.23$ m for plasma equilibrium in the top part of the vessel, 3697 at $z = 0.05$ m for the mid-plane, and 112 at $z = -0.23$ m for plasmas in the lower vessel region.

Discharge type	$z = 0.23$ m	$z = 0.05$ m	$z = -0.23$ m
$B_\varphi > 0, I_P > 0$	54	127	7
$B_\varphi < 0, I_P < 0$	2073	3570	105

Table 4.2: Numbers of 6 standard breakdown scenarios analyzed in the database.

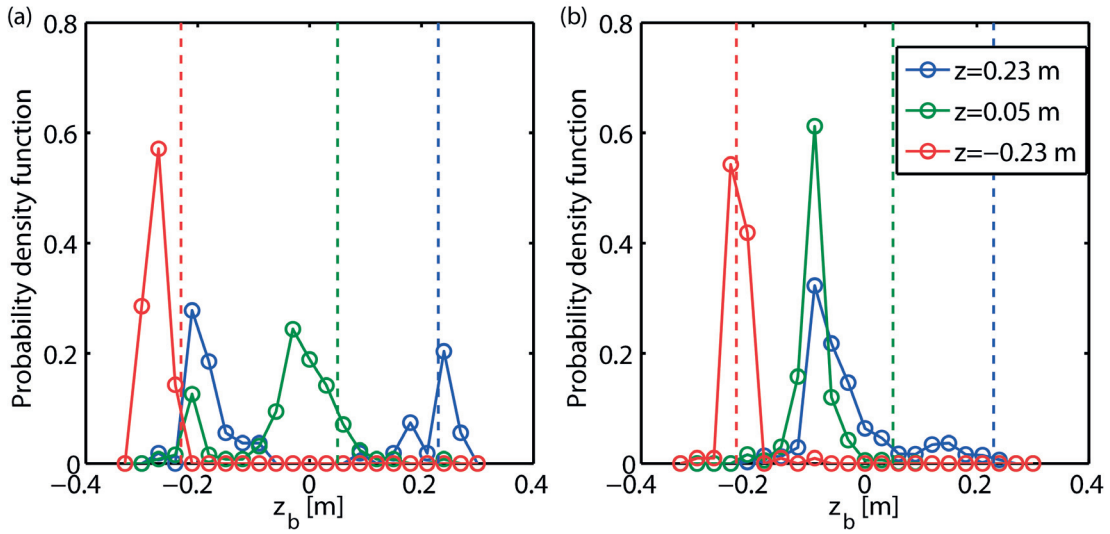


Figure 4.10: Probability density function of experimentally obtained vertical breakdown position Z_b for (a) $B_\varphi > 0, I_P > 0$ and (b) $B_\varphi < 0, I_P < 0$ scenarios. Programmed breakdown at $Z = 0.23$ m (blue), $Z = 0.05$ m (green) and $Z = -0.23$ m (red).

The analysis of the vertical breakdown position shows that the experimentally obtained position Z_b regularly deviates from the intended position, with the extent of the deviation differing among the scenarios (Fig. 4.10). The $Z = 0.23$ m scenario has the largest vertical deviation: with positive B_φ and I_P , only 37% breakdowns are in the vicinity (± 0.05 m) of the intended vertical position, 59% are in the lower vessel region ($Z_b = -0.21$ to -0.09 m); with negative B_φ and I_P , 83% are shifted below the mid-plane ($Z_b = -0.12$ to 0.03 m), only 14% are at in the higher vessel region ($Z_b = 0.06$ to 0.24 m). The deviation is smaller for the $Z = 0.05$ m scenario, with positive B_φ and I_P , 80% are in a ± 0.09 m range centered at the mid-plane, also 13% are at the lower vessel region ($Z_b = -0.21$ m); with negative B_φ and I_P , the breakdowns are almost exclusively (98%) down shifted ($Z_b = -0.15$ to 0.03 m). The $Z = -0.23$ m scenario has the least vertical deviation: with more than 95% breakdowns being in the vicinity of intended vertical position for both B_φ and I_P directions.

The analysis of the database shows that the experimentally obtained breakdown time t_b varies between $t = -5$ to 15 ms. In all scenarios, t_b and V_{loop} have a positive correlation (Fig. 4.11a and

c). The reason is that the maximum value of the loop voltage was asymptotically approached due to the establishment of the stationary eddy currents. Therefore a later breakdown time features a higher loop voltage.

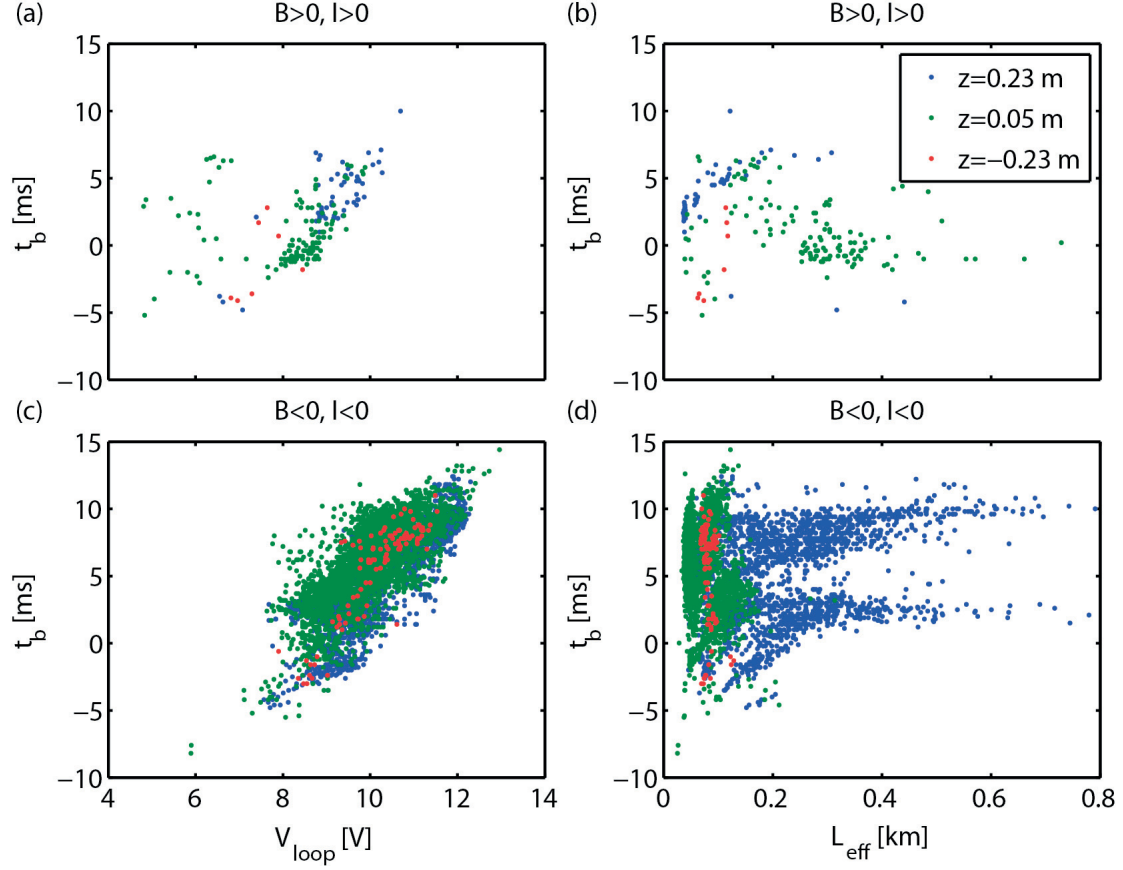


Figure 4.11: Experimentally obtained breakdown time t_b as a function of (left) loop voltage V_{loop} and (right) effective connection length L_{eff} , for (top) $B_\phi > 0, I_P > 0$ and (bottom) $B_\phi < 0, I_P < 0$ scenarios. Magnetic axis of the first FBTE equilibrium at $Z = 0.23$ m (blue), $Z = 0.05$ m (green) and $Z = -0.23$ m (red).

The relation between the breakdown time and the connection length must be treated with caution. The effective connection length is determined by the gradient of the poloidal fields, which was programmed to decrease with time at the intended null point position so that the breakdown time occur between $t = 0$ and 5 ms when the increasing L_{eff} meets the threshold (section 4.2). However, the time evolution of the poloidal field gradient at the experimental obtained null point position would differ from the programmed scenario due to the deviation of breakdown position, which may also result in a discrepancy in the breakdown time. Here only the breakdown scenarios with the negative B_ϕ and I_P are discussed due to better statistics (Fig. 4.11d). A threshold on L_{eff} of approximately 50 – 100 m is observed for the $Z = -0.23$ m and $Z = 0.05$ m scenarios, in which most of breakdowns occur in a particular range of vertical position with smaller deviation from the intended null point position. The $Z = 0.23$ m, on the

other hand, has a larger vertical deviation, and no clear threshold on L_{eff} can be observed. The database shows that the breakdown locations regularly deviate from the intended configuration, and the breakdown can exceed the time range where the strategy is applicable. Despite these large deviations from the original strategy, failures to break down are rare with the legacy scenario.

4.5 Experiments to empirically reduce the discrepancy in breakdown position

The discrepancy in the position of the intended and experimentally obtained null point indicates that the poloidal magnetic field at the nominal null point position, i.e. typically the magnetic axis of the first FBTE equilibrium, is not zero at the breakdown time. The *breakdown* code confirms that a finite radial field value generally exists at the two quadrupole control points in the experimental discharges at the breakdown time. This radial field was found to be predominantly caused by an inaccurate back-off of the stray field generated by the vessel currents. The use of the nominal vessel resistivity to the model vessel current in MGAMS rather than the experimental values was identified as the key reason for this inaccuracy (section 6.1). Another source of additional poloidal field is inaccuracy in the poloidal field coil currents, which arises from the summation of the analogue-electronics based matrix multiplication circuits at the output of the analogue control system. The resulting poloidal field from the coil current errors can be around 4 mT, which has been corrected in the following experiments by using a digital control system.

Experiments were performed to correct the vertical breakdown position by adding offsets to the imposed field B_R^\pm at the two control points in MGAMS. The offsets are chosen to be equal to the negative of the experimentally obtained radial field B_R^{exp} at the two control points,

$$B_R^{\pm, \text{new}} = B_R^{\pm, \text{old}} - B_R^{\text{exp}}. \quad (4.13)$$

The experimentally obtained primary null point position of a typical TCV discharge with $B_\varphi < 0$, $I_p < 0$, and a programmed breakdown at $Z = 0.23$ m is usually shifted to $Z \approx -0.1$ m (Fig. 4.12a), even though MGAMS imposed $B_R^\pm = 0$ mT at $t = 0$ s. The reconstructed magnetic field configuration shows that, at the breakdown time, the radial field at the control points is ~ 1 mT. Repeating the same plasma formation scenario but with $B_R^\pm = -1$ mT results in a displacement of the experimentally obtained primary null point to $Z = 0.18$ m (Fig. 4.12b), reducing the discrepancy to ΔZ_b from 0.33 m to 0.05 m. Hence, this method is effective to reduce the discrepancy in the breakdown position.

It should be noted that this method is only empirical and it does not correct the origin of the additional radial field, i.e. mainly the use of an inaccurate vessel resistivity in MGAMS (chapter 6). An improved discharge preparation procedure including corrections to the vessel resistivity in MGAMS is introduced in chapter 6.

4.6. Experiments to study the effect of breakdown parameters on breakdown time

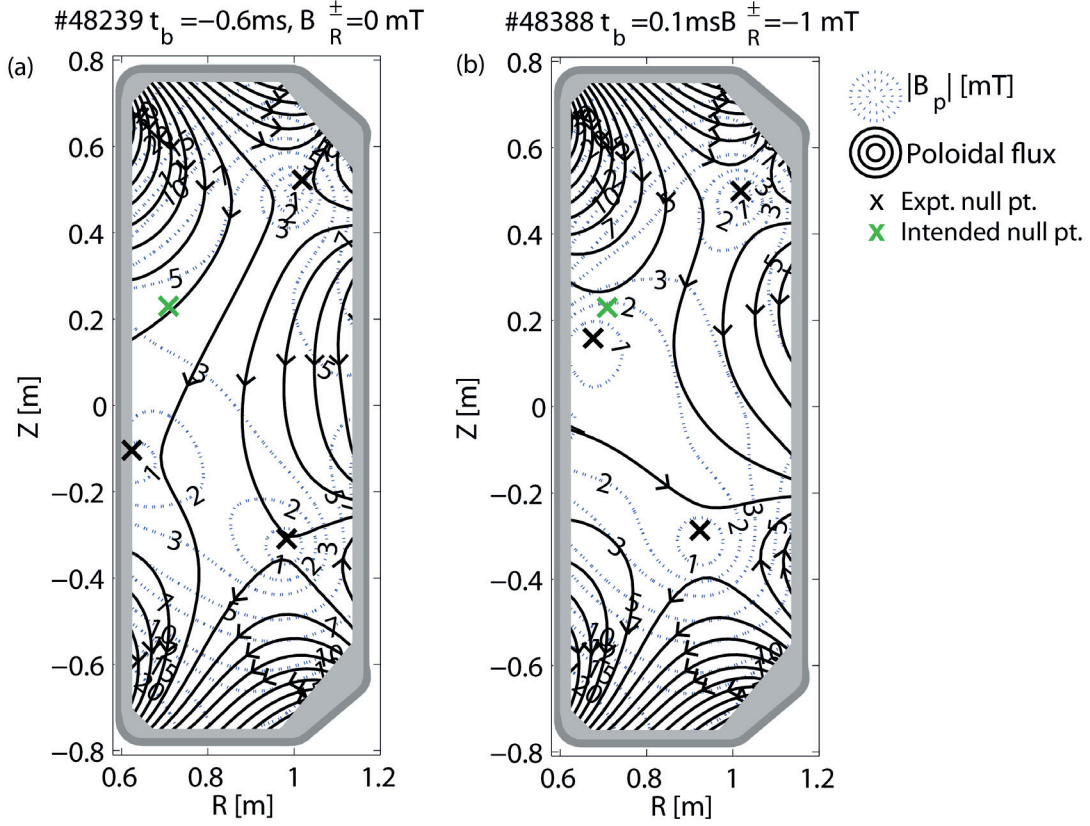


Figure 4.12: Comparison of the reconstructed magnetic field configuration at the time of breakdown for (a) $B_R^\pm = 0$ mT and (b) $B_R^\pm = -1$ mT.

4.6 Experiments to study the effect of breakdown parameters on breakdown time

Experiments were performed to study the effect of the gradient of the poloidal field $|\nabla B_p|_{\text{npt}}$, the prefll neutral gas pressure p_n and the loop voltage V_{loop} , on the breakdown time. The breakdown time is a crucial parameter to achieve a simultaneous double breakdown. The effect of the breakdown parameters on the plasma current ramp rate was also studied to understand their influence on the plasma burn-through and ramp-up phases of the plasma formations (discussed in detail in chapter 5). The motivation of this study is to obtain the operational range for successful plasma formation in TCV and develop tools to control the breakdown time and initial current ramp rate.

4.6.1 Effect of the gradient of the poloidal field

In these experiments, the neutral gas pressure and the loop voltage were kept nearly constant, $p_n = 0.04$ Pa, $V_{\text{loop}} = 10$ V. Only the imposed value of $|B_z^\pm|$ at the two quadrupole control points

in MGAMS was varied. The imposed value in MGAMS defines the gradient $|\nabla B_p|^{\text{MGAMS}} = |B_z^\pm|/0.02$ at $t = 0$, as discussed in section 4.2. The gradient of the poloidal field at the null point is programmed to reduce with time, i.e., the effective connection length L_{eff} increases with time. With a larger initial gradient (shorter initial connection length), and a constant loop voltage and pressure, it should take more time for L_{eff} to reach the threshold value for breakdown.

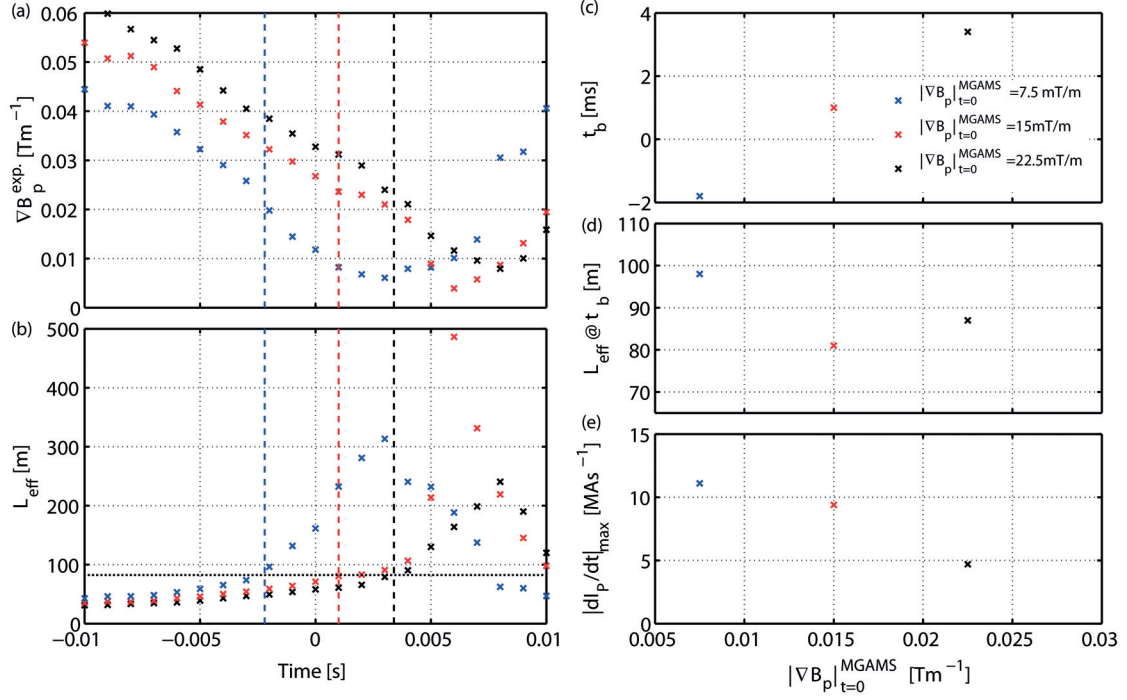


Figure 4.13: Time evolution of (a) poloidal field gradient, (b) effective connection length at the experimentally obtained null point. Effect of programmed value of poloidal field gradient in MGAMS for $t = 0$ on experimentally obtained (c) breakdown time, (d) L_{eff} at null point, (e) initial plasma current ramp rate.

Experimental results showed that the gradients at the experimentally obtained null point at $t = 0$ s were approximately two to three times higher than programmed value (Fig. 4.13a). The value $|\nabla B_p|^{\text{exp}}$ still decreases with time, and L_{eff} at the experimentally obtained null point increases with time (Fig. 4.13b). As expected, the increase in the imposed gradient results in a delayed breakdown (Fig. 4.13c) from $t_b = -1.8$, to 4 ms. The threshold of L_{eff} for breakdown to occur is found to be approximately 90 m (Fig. 4.13d). In addition, the initial plasma current ramp rate is lower with a larger imposed gradient.

4.6.2 Effect of neutral gas pressure

In these experiments, the loop voltage ($V_{\text{loop}} \sim 10$ V) and the imposed gradient in MGAMS at $t = 0$ s ($|\nabla B_p|^{\text{MGAMS}} = 0.0075 \text{ Tm}^{-1}$) were kept constant, and the neutral gas pressure was varied by changing the prefill gas input. The dependence of the breakdown on the neutral gas

4.6. Experiments to study the effect of breakdown parameters on breakdown time

pressure can be explained on the basis of the Townsend model, with a constant loop voltage, the breakdown becomes a function of the prefill gas pressure and the effective connection length.

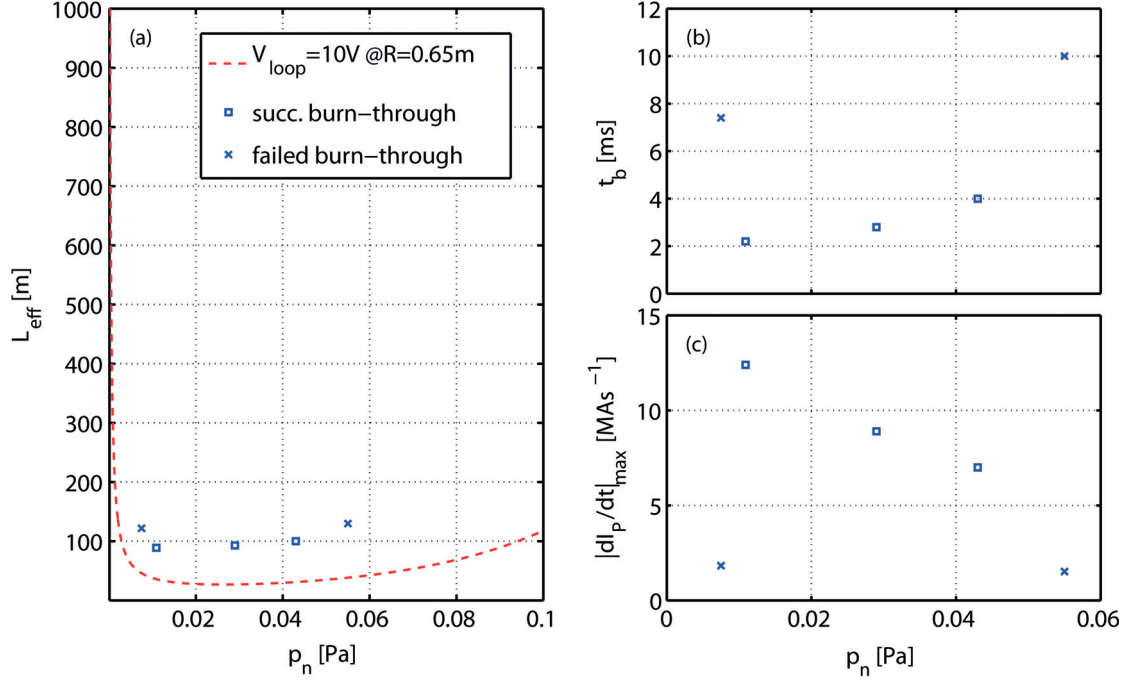


Figure 4.14: (a) Required effective connection length L_{eff} to breakdown as a function of neutral gas pressure p_n at constant loop voltage $V_{\text{loop}} \approx 10$ V, theoretical (red) and experimental (blue). Experimentally obtained (b) breakdown time, (c) initial plasma current ramp rate.

With a constant $V_{\text{loop}} = 10$ V, a longer connection length is required at the lowest ($p_n \sim 0.0075$ Pa) and at the highest pressure ($p_n \sim 0.053$ Pa) for successful breakdown in TCV (Fig. 4.14a). Since the effective connection length increases with time (section 4.6.1), this also leads to a later breakdown time (Fig. 4.14b). The experimentally obtained breakdown time, t_b , lies within the typical time range of 2 – 4 ms for $0.01 < p_n < 0.05$ Pa, and is delayed to 7.4 ms at $p_n = 0.0075$ Pa, and 10 ms at $p_n = 0.055$ Pa. The experimentally obtained L_{eff} at the breakdown time in Fig. 4.14a systematically exceeds the theoretical curve, which may indicate the limits of the 0D model. It can, however, be seen that the dependence on pressure follows the same trend, and the value $L_{\text{eff}} \sim 100$ m is consistent with the experimental results in section 4.6.1. The initial current ramp rate decreases from 12.4 to 7 MA s⁻¹ with pressure in the range of $0.01 < p_n < 0.05$ Pa, and is much lower (< 1.8 MA s⁻¹) for delayed breakdowns, which subsequently fail to burn-through (Fig. 4.14c).

The experiments show that the neutral gas pressure can be used to control the breakdown time and the initial plasma current ramp rate. In fact, it has been used as the primary control parameter in the legacy scenario in an only partially favorable breakdown configuration for the last 25 years.

4.6.3 Effect of toroidal electric field

In these experiments, the loop voltage was varied by changing the reference Ohmic coil current ramp rate in MGAMS between $t = -15$ ms and $t = 10$ ms, while the imposed gradient $|B_z^\pm| = 7.5$ mT and neutral gas pressure $p_n \sim 0.04$ Pa were kept constant. Following the Townsend model, a higher loop voltage should lead to a breakdown at a lower connection length.

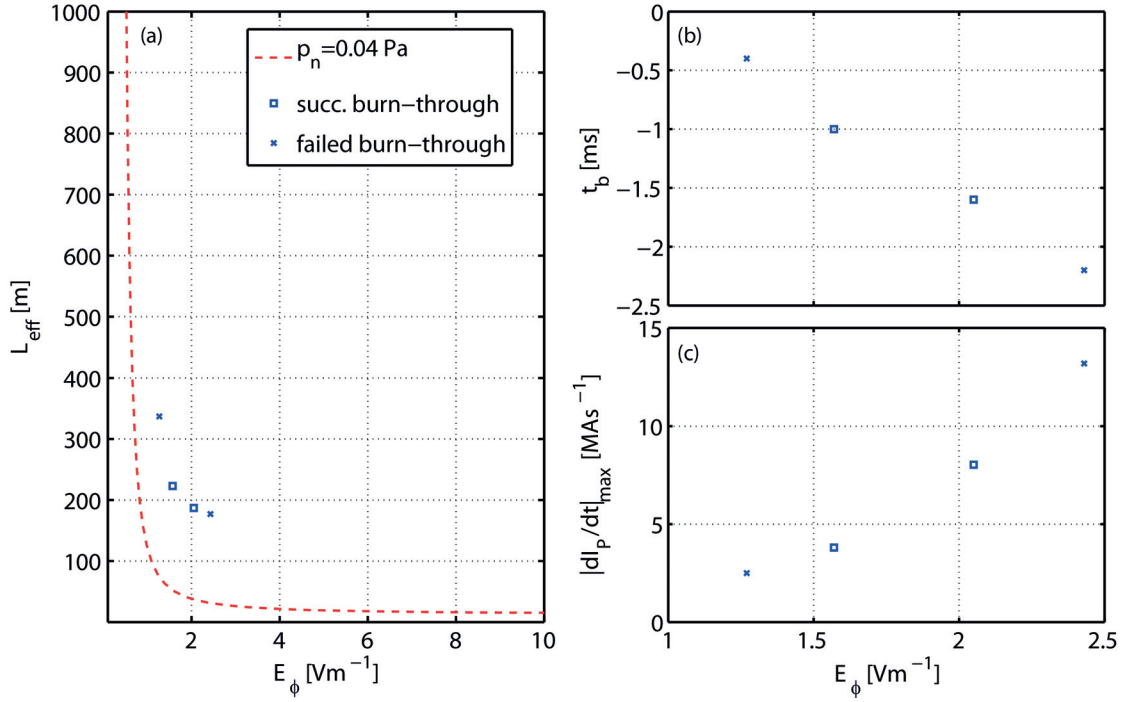


Figure 4.15: (a) Required effective connection length L_{eff} to breakdown as a function of toroidal electric field E_ϕ at constant pressure $p_n = 0.04$ Pa, theoretical (red) and experimental (blue). Experimentally obtained (b) breakdown time, (c) initial plasma current ramp rate.

Increasing the toroidal electric field E_ϕ from 1.27 to 2.43 Vm⁻¹ and V_{loop} from 7 to 10 V decreases the threshold in L_{eff} by more than a factor of two (Fig. 4.15a). Therefore the breakdown time decreases monotonically with the toroidal electric field (Fig. 4.15), from $t = -0.4$ to -2.2 ms. Again the experimentally obtained L_{eff} at the breakdown time in Fig. 4.15a is higher than the theoretical curve. These L_{eff} values are higher, than the value in previous experiments, which is a general observation when the digital control system (SCD) is used to perform the experiments. This is because the offsets in the standard PF coil current are absent in SCD resulting in an improved PF coil current control, which, in turn, can result in a longer L_{eff} as programmed in MGAMS. The initial current ramp rate increases from 2.5 to 13.2 MA s⁻¹ with E_ϕ (Fig. 4.15). The scan also shows that overly high and overly low values of \dot{I}_P , both lead to failed burn-throughs (chapter 5).

4.7 Conclusion

The breakdown strategy in TCV is determined by the low resistivity of the TCV vacuum vessel, which results in large induced vessel currents and a slow diffusion of the electric field into the vessel. The prefill neutral gas pressure and loop voltage are first introduced in the vessel, and then a quadrupole null point is created at $t = 0$ s, the breakdown is then triggered by decreasing the gradient of the null point with time, i.e., increasing the effective connection length until the threshold is met. The magnetic configuration for breakdown is established by first canceling the stray field by *back-off* coils, and then imposing poloidal fields at two quadrupole control points by four *quadrupole* coils to create a quadrupole null point. The value of imposed fields must be chosen to ensure that the position of the null is at the correct location and the orientation of the null favorable for vertical stability.

A database of breakdown for the 6 standard scenarios in TCV, including positive and negative B_ϕ and I_p , at three intended breakdown vertical positions: $Z = 0.23, 0.05$ and -0.23 m, reveals a significant vertical deviation between the intended and experimental breakdown positions. The experimental obtained null point is mostly down shifted to around $Z_b = -0.1$ m for both programmed $Z = 0.23$ and 0.05 m breakdowns with negative B_ϕ and I_p . This deviation of the null point position is caused by an additional poloidal field at the intended position, mainly due to the inaccurate stray field back-off of vessel currents. The model of the vessel current using the nominal vessel resistivity assuming axisymmetry, is different from the experimentally obtained values from the magnetic measurements. Experiments showed that the vertical deviation can be reduced empirically by imposing the negative of the experimentally observed additional field at the two quadrupole control points, to compensate the additional field. However, to systematically correct the deviation, a more generalized solution should use the experimental vessel resistivity to model the vessel current in MGAMS breakdown preparation and taking advantage of the SCD for better PF coil control.

The effect of three different breakdown parameters, i.e., the gradient of the poloidal field $|\nabla B_p|_{\text{npt}}$, the prefill neutral gas pressure p_n and the loop voltage V_{loop} , on the breakdown time and the initial current ramp rate was studied in dedicated experiments, in order to determine the operational range for successful plasma formation in TCV and thereby, obtain means to control them. The results showed that increasing the imposed gradient in MGAMS at $t = 0$ s leads to delayed breakdown because it takes longer for the effective connection length to reach the threshold value necessary for breakdown, and also results in a lower initial current ramp rate due to a smaller null size. Experiments performed to study the influence of the neutral gas pressure on the dynamics of the plasma formation show that at both high and low pressure a longer effective connection length is required which results in a delayed breakdown. Although, successful breakdown was observed at both high and low neutral gas pressures, the discharge attempts failed during the burn-through phase due to the low initial plasma current ramp rate. Experiments showed that the increase of the loop voltage leads to an earlier breakdown time and a higher plasma current ramp rate. From these experiments, it was identified that the plasma formation failed during the burn-through phase at both overly high and overly low plasma current ramp rates.

Chapter 4. Breakdown scenario

The variations of L_{eff} , p_n and V_{loop} are consistent with the Townsend model. The expected behavior allows to control the position and time of the breakdown. It furthermore affects the initial I_p ramp-rate whose control may be important for the burn-through phase. The experiments have also shown that breakdown in TCV is very resilient to deviation from the ideal strategy and not a problem for single-axis plasmas. Accurate control of breakdown location and time is however expected to be crucial for the formation of doublet shaped plasmas.

5 Plasma burn-through and ramp-up scenario

In TCV, most discharges feature inductive breakdown and burn-through. The plasma current plays an important role in the success rate of the burn-through since it determines the Ohmic heating power. Experiments on TCV show that most failures in the plasma formation occur in the time range between $t = 10$ ms and 50 ms, during which the plasma is in the burn-through phase, while the plasma current is being ramped up simultaneously. Therefore, it is difficult to clearly distinguish between the two phases and it is more convenient to discuss the burn-through (section 3.2) and plasma current ramp-up phases (section 3.3) together in this chapter.

Section 5.1 describes the programming of the plasma current ramp-up scenario in TCV using MGAMS and FBTE. In section 5.2, the different methods used to estimate the radial and vertical position of the plasma during the ramp-up phase are discussed. Section 5.3 presents the database for the TCV plasma current ramp-up scenario and discusses possible reasons for failures in the plasma formation. In section 5.4, the experimental results obtained from the implementation of the strategies to improve the plasma current ramp-up scenario in TCV are discussed. Section 5.5 summarizes the conclusions obtained from the plasma burn-through and plasma current ramp-up studies carried out within this thesis.

5.1 Programming of plasma current ramp-up scenario in TCV

The plasma current ramp-up scenario in TCV is programmed using the MGAMS discharge preparation program (section 2.4) and the FBTE free-boundary equilibrium solver (section 2.5). The reference plasma current ramp rate is programmed to provide sufficient Ohmic heating to ionize the impurities in the plasma and sustain the plasma during the ramp-up phase. The plasma cross-section is also programmed to increase along with the plasma current during the plasma current ramp-up phase to keep the value of the safety factor q_{95} above 2 to avoid MHD instabilities (Fig. 5.1). The programmed plasma current ramp rate in TCV is generally set to 2 MA s^{-1} up to $t = 70$ ms to avoid MHD instability due to either too broad or too peaked plasma current density profiles (see section 3.3).

To keep the plasma at the correct radial position, the radially outward hoop force must be

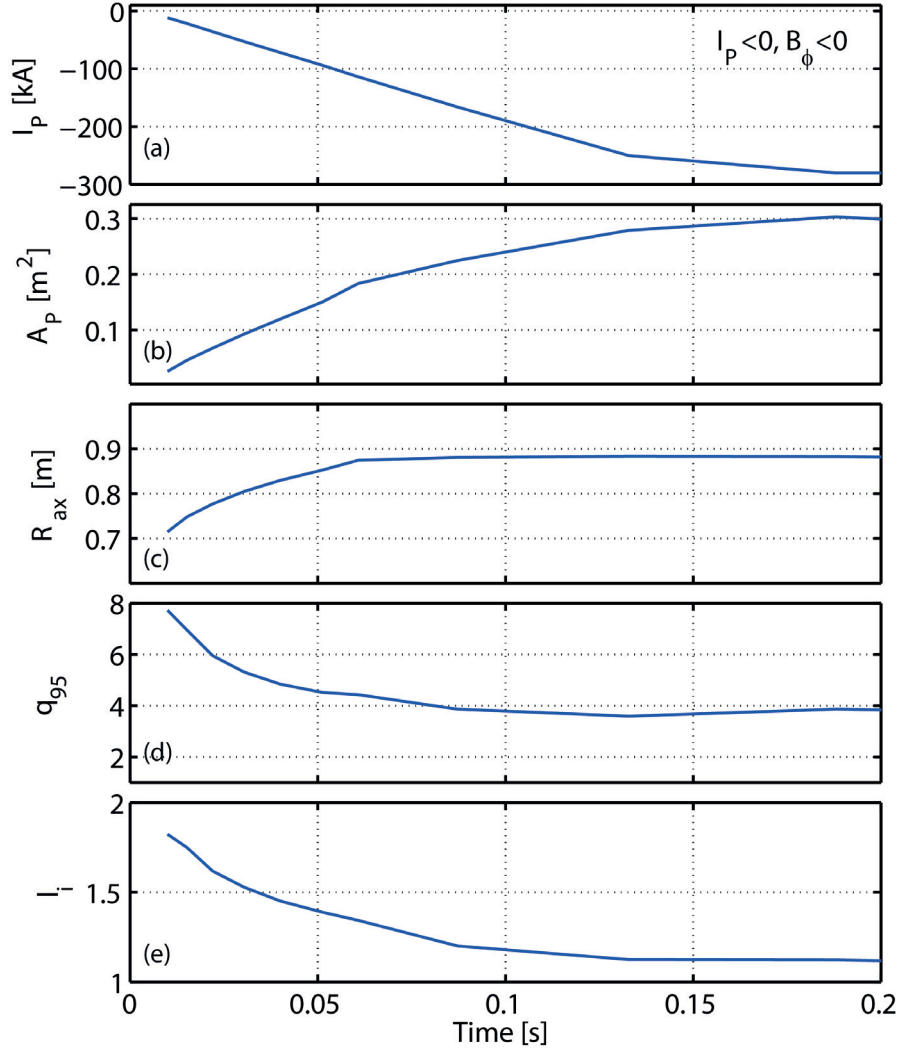


Figure 5.1: Evolution of the programmed (a) plasma current, (b) plasma cross section, (c) radial position of the magnetic axis, (d) safety factor q_{95} and, (e) plasma internal inductance.

balanced by a restoring radial inward force produced by an externally applied vertical field. The radial outward hoop force can be expressed as [21],

$$F_{\text{hoop}} = \frac{\mu_0 I_P^2}{2} \left(\ln\left(\frac{8R}{a\sqrt{\kappa}}\right) + \beta_p + \frac{l_i}{2} - \frac{3}{2} \right), \quad (5.1)$$

where R is the major radius, a the minor radius, κ the elongation, β_p the poloidal beta, and l_i the normalized internal inductance.

A radially inward restoring force must balance this hoop force and can be expressed as,

$$F_{\text{res}} = 2\pi R (I_P \hat{e}_\phi \times B_Z^{\text{ext}} \hat{e}_Z), \quad (5.2)$$

5.1. Programming of plasma current ramp-up scenario in TCV

where I_P is the plasma current, B_Z^{ext} is the external vertical field applied by the external coils (PF coils).

The value of the required vertical field for a specified plasma equilibrium to be at the correct radial position is,

$$B_Z^{\text{ext}} = \frac{|F_{\text{hoop}}|}{2\pi R I_P} = \frac{\mu_0 I_P}{4\pi R} \Gamma, \quad (5.3)$$

where $\Gamma = \ln(8R/(a\sqrt{\kappa})) + \beta_p + l_i/2 - 3/2$.

In TCV, FBTE is used to calculate the PF coil currents required to produce the external vertical field (eq.(5.3)) to keep the plasma equilibria at the correct radial position and with the desired shape until feedback can be applied.

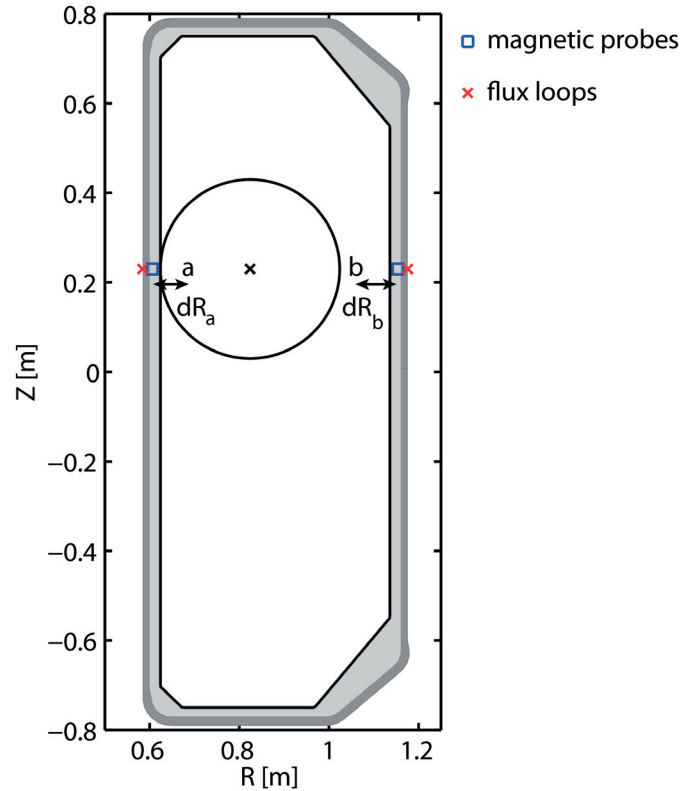


Figure 5.2: Schematic to describe the radial position observer in TCV. Black cross denotes the magnetic axis, a and b are the two fixed control points located on the HFS and LFS respectively where the flux is being extrapolated. The black contour represents the plasma boundary for a single-axis limited plasma configuration

The radial position observer in TCV is based on the extrapolation of the poloidal flux measured using paired flux loops and magnetic probes at two locations on the HFS and LFS of the VV (Fig. 5.2). The flux difference between inner and outer plasma boundary on a near equatorial probe plane is used to estimate the radial position of the plasma [57]. The flux measured on a

control point at the HFS is calculated as,

$$\psi_a = F_{fa} + 2\pi R_{fa} dR_a B_{ma}, \quad (5.4)$$

where F_{fa} denotes the flux loop measurements at the HFS, R_{fa} denotes the radial position of the flux loops at the HFS, B_{ma} the magnetic field probe measurements at the HFS control point and dR_a the distance between the magnetic measurements and the control point at the HFS. The flux measured on a control point at the LFS can be calculated as,

$$\psi_b = F_{fb} + 2\pi R_{fb} dR_b B_{mb}, \quad (5.5)$$

where F_{fb} denotes the flux loop measurements at the LFS, R_{fb} denotes the radial position of the flux loops at the LFS, B_{mb} the magnetic field probe measurements at the LFS control point, and dR_b the distance between the magnetic field probe and the control point at the HFS.

Therefore, the radial position observer defined as the difference between the flux on the HFS and LFS is,

$$\Delta\psi = \psi_a - \psi_b = (F_{fa} + 2\pi R_{fa} dR_a B_{ma}) - (F_{fb} + 2\pi R_{fb} dR_b B_{mb}). \quad (5.6)$$

The PF coils are used as actuators for the radial position feedback control.

In TCV, the control of the plasma current and plasma position during the initial phases of the plasma formation can be divided into, a feed-forward phase in which the Ohmic coil and PF coil currents are calculated based on the programmed plasma equilibrium using MGAMS and FBTE and a feedback phase in which the I_p and position feedback control system based on magnetic measurements seeks to minimize the mismatch between the programmed and the experimental scenarios. The plasma current and position feedback control system is preprogrammed to switch on at $t = 10$ ms. Before $t = 10$ ms, only the Ohmic coil and the PF coil currents are feedback controlled. Therefore, the activation of the I_p and position feedback control system does not take into account the uncertainties in the timing of the breakdown, the experimental plasma current ramp rate and the plasma position. This in turn, can result in a mismatch between the programmed and the experimental plasma current ramp rate and result in oscillations in I_p on activation of the I_p feedback control system (section 5.3).

5.2 Estimation of plasma parameters during the plasma current ramp-up phase

The estimates of the plasma current and the plasma radial and vertical positions are essential to understand the dynamics of the plasma burn-through and ramp-up phase. Magnetic and interferometer measurements are key diagnostics that are able to provide estimates of the plasma current and the plasma position and are discussed in this section.

5.2. Estimation of plasma parameters during the plasma current ramp-up phase

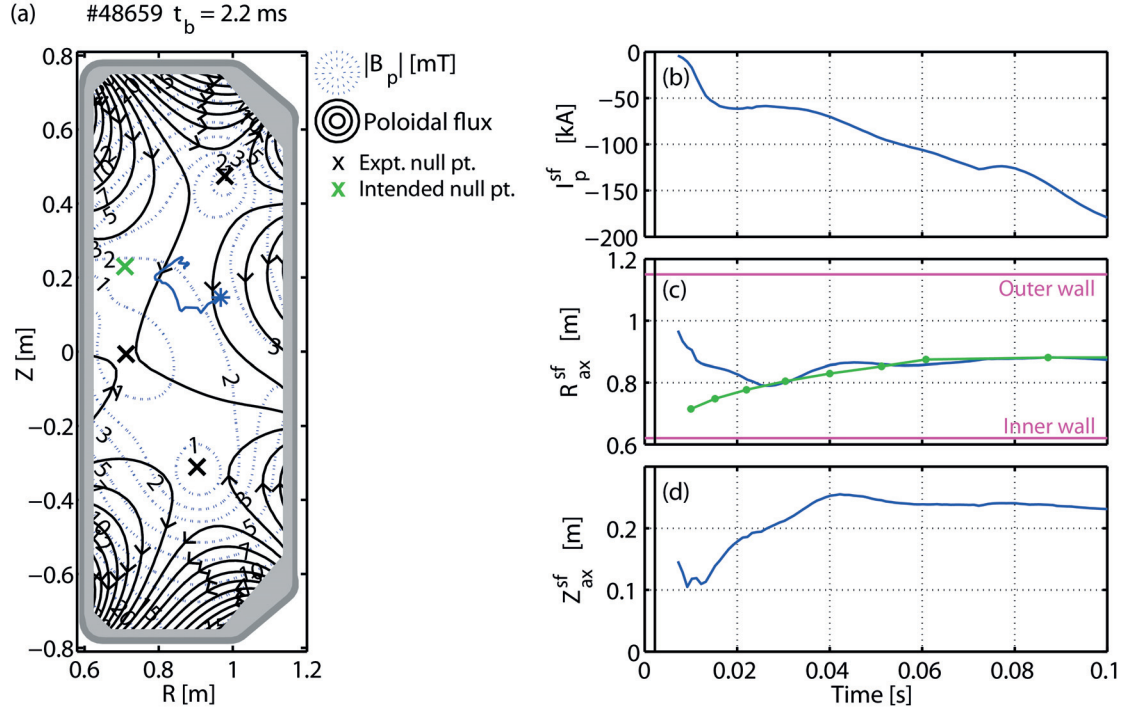


Figure 5.3: (a) Poloidal flux and field distributions at the time of breakdown. Programmed (green cross) and experimental (black cross) null points and evolution of the single filament plasma position (blue line). Evolution of (b) plasma current, (c) plasma radial position, and (d) plasma vertical position obtained using the single filament method. The green line denotes the programmed plasma radial position and the magenta lines correspond to the inner and outer wall of TCV.

5.2.1 Single filament approach

During the ramp up phase both the vessel eddy current and plasma current distributions are not directly measured. In the single filament ('sf') approach the plasma current distribution is modeled by three parameters: the plasma current (I_p), the radial and the vertical position of the plasma filament (R_{ax} and Z_{ax}). Estimates of I_p , R_{ax} and Z_{ax} can be obtained from magnetic measurements. The magnetic measurements include, 38 poloidal flux loop measurements, 38 magnetic field probe measurements, coil current measurements and a plasma current measurement. These magnetic measurements are related to the toroidal currents in the system, which can be expressed as a system of linear equations,

$$\mathbf{m}^{sf} = \mathbf{M}^{sf}(R_{ax}, Z_{ax}) [I_a; I_v; I_p], \quad (5.7)$$

where, \mathbf{m}^{sf} denotes the modeled magnetic measurements during the ramp-up phase, $\mathbf{M}^{sf}(R_{ax}, Z_{ax})$ denotes the Green's functions used to couple the plasma current, vessel eddy currents and coil currents (16 PF and 2 OH) with the magnetic measurements. $\mathbf{M}^{sf}(R_{ax}, Z_{ax})$ is a function of the plasma filament position. Equation(5.7) is reformulated as a non-linear optimization of the

objective scalar multivariate function n_{tot} depending on the variable R_{ax} and Z_{ax} [68]. Here n_{tot} is defined as the ratio between the residue of the least square fit χ_{min}^2 and the variance of the measured quantities σ_y .

$$n_{\text{tot}} = \frac{\chi_{\text{min}}^2}{\sum_i w_i^2 \sigma_{y,i}^2}$$

$$\chi_{\text{min}}^2 = \sum_i w_i^2 [\mathbf{m}_i^{\text{sf}} - (\mathbf{M}^{\text{sf}}(R_{\text{ax}}, Z_{\text{ax}}) \bullet \mathbf{x})_i]^2 \quad (5.8)$$

where, w_i is the weight of the considered magnetic measurements, $\mathbf{m}_i^{\text{meas}}$ denotes the magnetic measurements, $\mathbf{m}_i^{\text{sf}} = (\mathbf{M}^{\text{sf}}(R_{\text{ax}}, Z_{\text{ax}}) \bullet \mathbf{x})_i$ denotes the modeled magnetic measurements and \mathbf{x} is the vector of fitted currents (I_a, I_v and I_p). A solution is obtained by using the Nelder-Mead algorithm [60]. This method to estimate I_p , R_{ax} , Z_{ax} and I_v during the TCV plasma current ramp-up phase was implemented in the *breakdown* code [68].

The results obtained from the single filament model show that the plasma filament position is first detected in the vicinity of the null point with the highest effective connection length and only later moves to the preprogrammed plasma position (Fig. 5.3). The single filament model cannot give accurate solutions when the magnitude of the plasma current is too small (< 10 kA) and systematic errors dominate the magnetic measurements. In addition, it must be noted that the single filament model is only a very simple approximation of a distributed plasma.

5.2.2 Multiple filament approach

An alternative approach based on the least-square fitting of the magnetic measurements can be used to estimate the plasma current distribution by dividing the plasma domain into a number of filaments. In this multiple filaments ('mf') model, an estimate of the plasma current, plasma position and vessel eddy current can be obtained from the magnetic measurements and can be expressed as,

$$\mathbf{m}^{\text{mf}} = \mathbf{M}^{\text{mf}}[I_a; I_v; I_x], \quad (5.9)$$

where \mathbf{m}^{mf} is vector of the modeled magnetic measurements during the ramp-up phase, \mathbf{M}^{mf} are the Green's functions used to couple the plasma current, vessel eddy currents and coil currents (16 PF and 2 OH) with the magnetic measurements. I_x is the current in the plasma filaments.

A least square solution is obtained for equation (5.9),

$$\chi_{\text{min}}^2 = \sum_i w_i^2 [\mathbf{m}_i^{\text{meas}} - \mathbf{m}_i^{\text{mf}}]^2 = \sum_i w_i^2 [\mathbf{m}_i^{\text{meas}} - (\mathbf{M}^{\text{mf}} \bullet \mathbf{x})_i]^2 \quad (5.10)$$

where χ_{min}^2 is the minimum of the sum of the squared residuals, w_i is the weight of the considered magnetic measurements, $\mathbf{m}_i^{\text{meas}}$ denotes the magnetic measurements, $\mathbf{m}_i^{\text{mf}} = (\mathbf{M}^{\text{mf}} \bullet \mathbf{x})_i$ denotes the modeled magnetic measurements and \mathbf{x} is the vector of fitted currents

5.2. Estimation of plasma parameters during the plasma current ramp-up phase

(I_a, I_v and I_x). A unique solution of equation (5.10) for the fitted currents exists if the matrix \mathbf{M}^{mf} has linearly independent columns.

In the multiple filament model, the estimate of the plasma current is obtained by summing over the currents in the plasma filaments,

$$I_p^{\text{mf}} = \sum_x I_x. \quad (5.11)$$

The center of the plasma current distribution yields the plasma position,

$$R_{\text{ax}}^{\text{mf}} = \frac{r_x I_x}{\sum_x I_x},$$

$$Z_{\text{ax}}^{\text{mf}} = \frac{z_x I_x}{\sum_x I_x}, \quad (5.12)$$

where r_x is the radial position of the plasma filaments and z_x is the vertical position of the plasma filaments.

The estimates of the plasma current, plasma radial and vertical positions obtained using the multiple filament method during the plasma ramp-up phase are shown in Fig. 5.4. The systematic errors in the magnetic measurements limits the ability of the multiple filament plasma model to resolve the current distribution for very low plasma current values (< 10 kA). The number of plasma filaments is typically limited to < 12 as a higher number may yield unphysical solutions, such as plasma filaments with currents in the opposite directions.

5.2.3 LIUQE reconstruction

The LIUQE code [31] is the Grad-Shafranov equilibrium solver used in TCV to compute the plasma current density distribution that satisfies the MHD force balance and has the minimum least-square error between the measured and reconstructed magnetic measurements. The LIUQE code solves the Grad-Shafranov equation based on an iterative solution of the Poisson equation coupled with a linear parametrization of the plasma current density [56]. LIUQE also takes into account the influence of the vessel eddy currents on the equilibrium reconstruction. At sufficiently high plasma current equilibrium solvers such as LIUQE yield an accurate estimate of the current and pressure distribution in the plasma.

The equations describing the static ideal MHD equilibrium in an axisymmetric geometry, assuming isotropic pressure are,

$$\begin{aligned} \mathbf{j} \times \mathbf{B} &= \nabla p \\ \nabla \times \mathbf{B} &= \mu_0 \mathbf{j} \\ \nabla \cdot \mathbf{B} &= 0. \end{aligned} \quad (5.13)$$

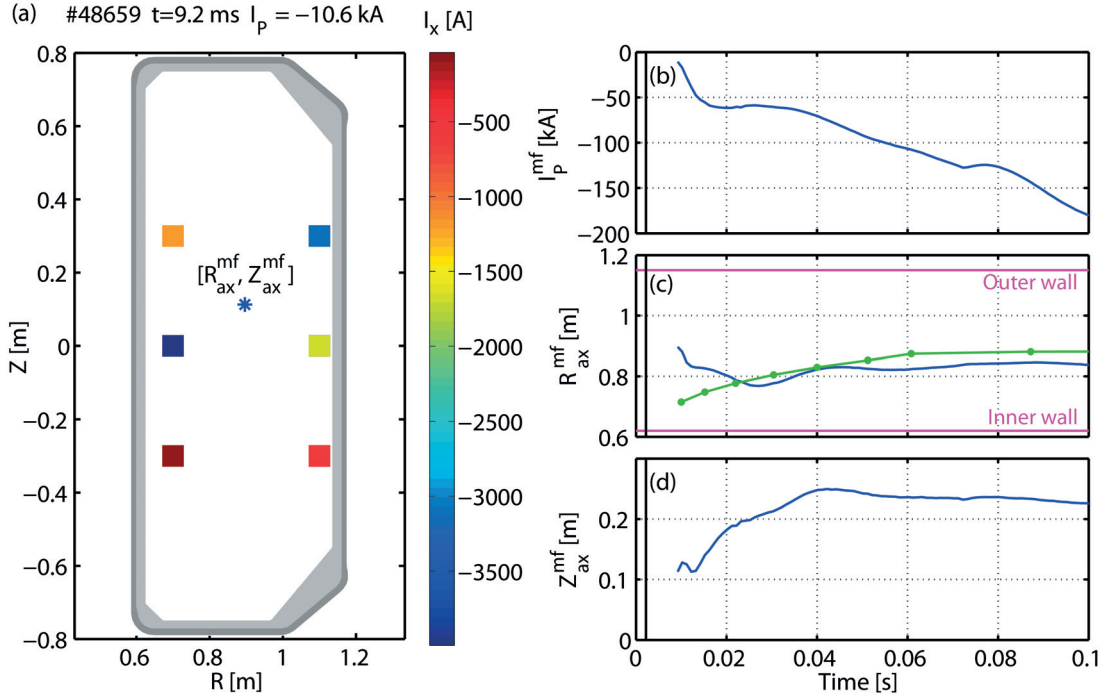


Figure 5.4: (a) Plasma current distribution in the different filaments and plasma position $(R_{ax}^{mf}, Z_{ax}^{mf})$ obtained by the multiple filament method the multiple filament plasma position (blue line). Evolution of (b) the plasma current, (c) plasma radial position, and (d) plasma vertical position obtained using the multiple filament method. The green line denotes the programmed radial position reference.

In cylindrical coordinates R, Z, ϕ , the magnetic field \mathbf{B} can be expressed as,

$$\mathbf{B} = -\frac{1}{2\pi R} \frac{\partial \psi}{\partial Z} \nabla R + \frac{1}{2\pi R} \frac{\partial \psi}{\partial R} \nabla Z + T \nabla \phi \quad (5.14)$$

By substituting eq.(5.14) into Ampere's law to obtain an expression for \mathbf{j} , the MHD force balance equation becomes,

$$\Delta^* \psi = -2\pi \mu_0 r j_\phi, \quad (5.15)$$

where $j_\phi = 2\pi (r dp/d\psi + T/\mu_0 r dT/d\psi)$ and p and T are functions of the poloidal magnetic flux ψ only. The Grad-Shafranov equation is expressed as,

$$\Delta^* \psi = -4\pi^2 \mu_0 r \left(r p' + \frac{T T'}{\mu_0 r} \right), \quad (5.16)$$

where $\Delta^* = r \left(\frac{\partial}{\partial r} \right) \left(r \frac{\partial}{\partial r} \right) + \left(\frac{\partial^2}{\partial z^2} \right)$ is the elliptical operator and $p' = dp/d\psi$ and $T' = dT/d\psi$. Since the toroidal plasma current density contributes to the magnetic measurements, the two arbitrary functions $p'(\psi)$ and $T T'(\psi)$ along with the flux function $\psi(r, z)$ are chosen so as to obtain an optimal agreement between the reconstructed and measured quantities and then

5.2. Estimation of plasma parameters during the plasma current ramp-up phase

they are used to solve eq.(5.16).

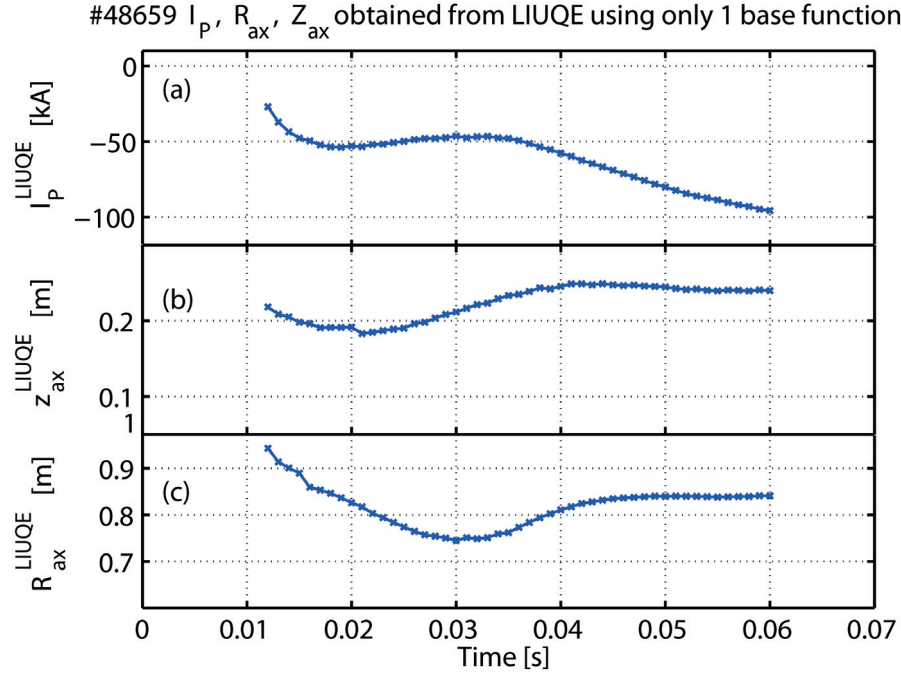


Figure 5.5: Estimation of the (a) plasma current, (b) plasma radial and, (c) plasma vertical positions obtained from the LIUQE code by using only one base function to characterize the plasma current distribution.

During the plasma current ramp up phase, the plasma pressure is low, and can be neglected in the plasma current distribution reconstruction. To improve convergence for low plasma currents and weakly shaped plasmas only one basis function is used for TT' . The evolution of the reconstructed plasma position and plasma current during the current ramp-up phase obtained from LIUQE is shown in Fig. 5.5. The LIUQE reconstruction does usually not converge for plasma current values below 20 kA.

5.2.4 Interferometer measurements

Due to the setup of its chords, the TCV interferometer (section 2.3.3) can be used to estimate the radial plasma position and extent. The estimate is based on the assumption that the electron density is maximum at the magnetic axis of the plasma by fitting measurements in two different ways. One way is to fit the line-integrated density assuming a Gaussian profile,

$$n_e^{\text{int}}(R) = n_{e,0}^{\text{int}} \exp\left[-\left(\frac{R - R_{ax}}{b}\right)^2\right]. \quad (5.17)$$

Here $n_{e,0}^{\text{int}}$ is the central line-integrated density, R_{ax} is the radial position of the magnetic axis, the width of the Gaussian distribution b can be used as an estimate of the horizontal size of the plasma. The other way is to assume a circular plasma and fit the line-integrated density

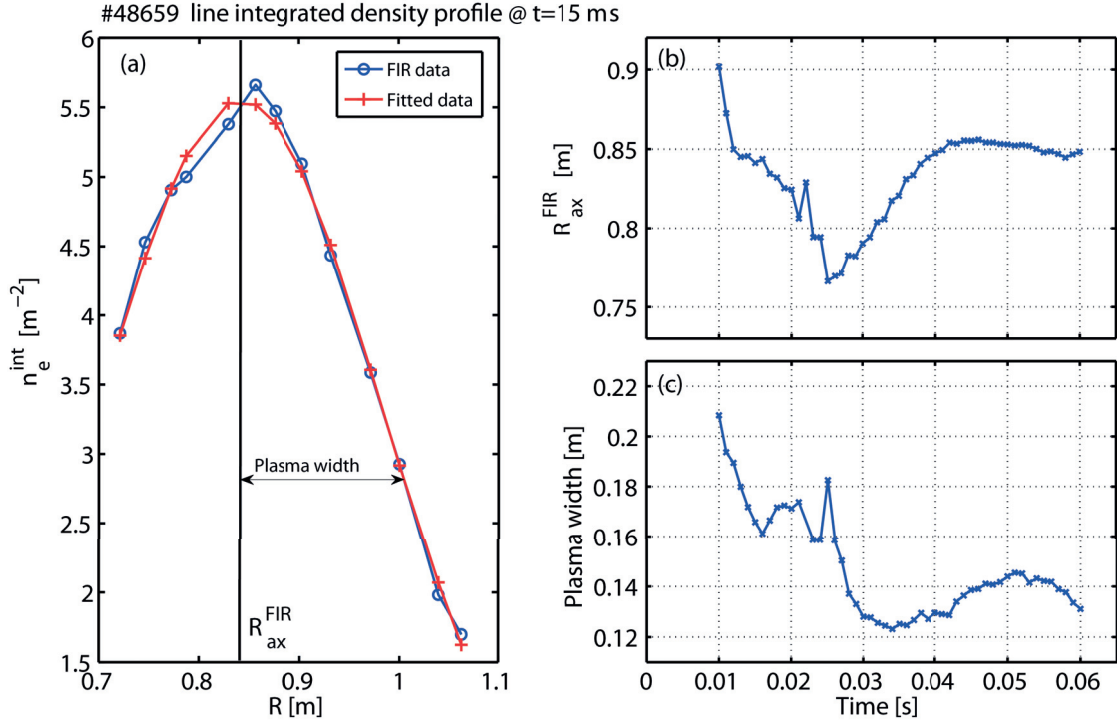


Figure 5.6: (a) Comparison of the FIR measurements with the Gaussian fit yielding the estimates of the radial position of the magnetic axis and the plasma width, (b) evolution of the estimated radial position of the plasma and (c) of the plasma width.

with two-dimensional Gaussian distribution in both radial and vertical direction,

$$n_e^{\text{int}}(R) = \int_{-\infty}^{+\infty} n_{e,0} \exp\left[-\frac{(R - R_{\text{ax}})^2 + Z^2}{b^2}\right] dZ. \quad (5.18)$$

Here $n_{e,0}$ is the electron density at the magnetic axis, the fitted Gaussian width b can be used as an estimate of the plasma radius.

The evolution of fitted radial position of the plasma and its width using the two-dimensional Gaussian fitting for the interferometer measurements during a plasma current ramp-up phase (Fig. 5.6). Due to a poor signal to noise ratio during the breakdown phase, this method can typically be used only after the peak in the D_α signal, which in TCV occurs approximately 10 ms after the experimental breakdown time.

5.3 Analysis of the plasma current ramp-up scenario in TCV

Measurements during the entire plasma formation phase in TCV for a discharge with a plasma current ramp rate, which is close to the reference and for another discharge, where the obtained plasma current ramp rate is much larger than the reference, are shown in Fig. 5.7 and Fig. 5.8, respectively. In the first case (Fig. 5.7), the radial plasma position is initially close to the inner wall and then slowly shifts to the center of the vessel as programmed. The D_α

5.3. Analysis of the plasma current ramp-up scenario in TCV

emission peaks ~ 10 ms after breakdown and is approximately proportional to the increase in density consistent with the idea that it indicates the ionization rate (Fig. 5.7c). After the peak it falls back to a baseline indicating the end of the deuterium ionization phase. The smooth D_α baseline and the low magnetic fluctuation level (Fig. 5.7e), show that no MHD activity is observed in this case. In discharges, where the plasma current ramp rate is even lower, the Ohmic heating may become insufficient to overcome the radiation loss and thus, can cause plasma formation failure.

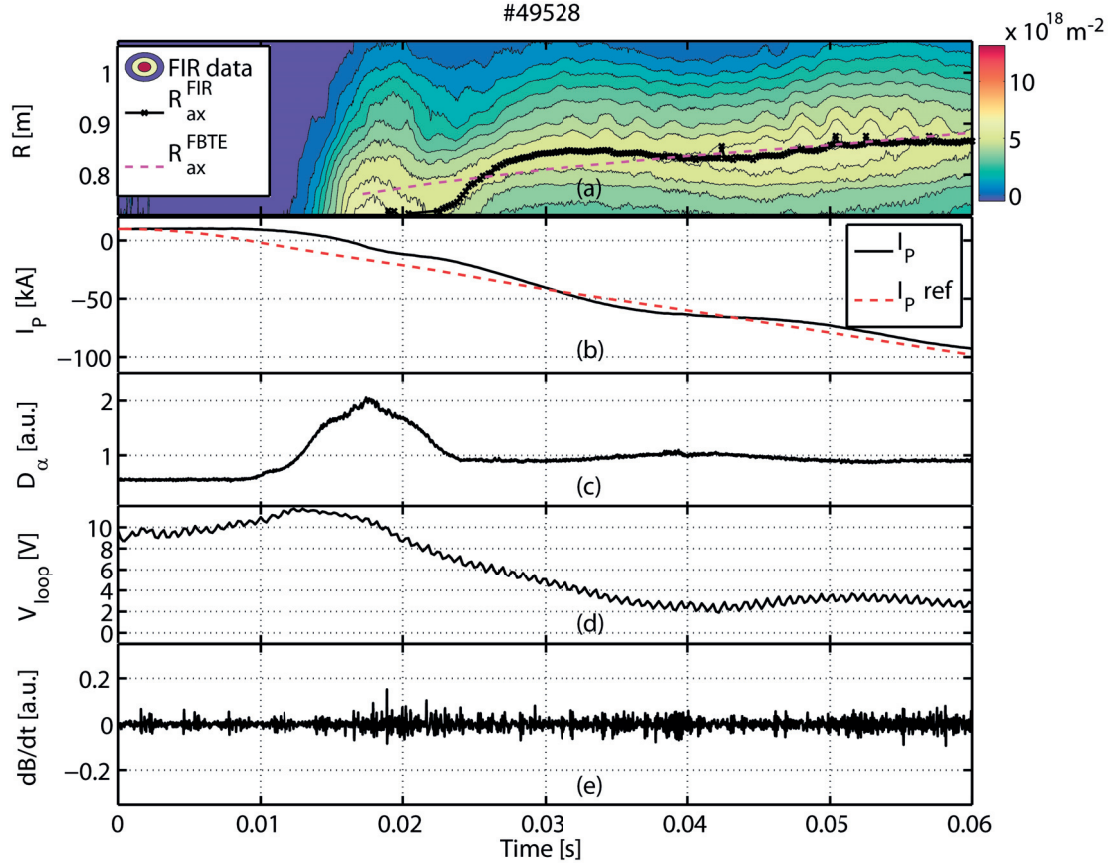


Figure 5.7: Typical TCV plasma current ramp up scenario with current ramp rate close to reference. (a) Evolution of the radial position of the plasma along with the line-integrated plasma density obtained using interferometer (FIR), (b) evolution of I_p , (c) D_α signal from the vertical photo diode, (d) evolution of V_{loop} , and (e) raw magnetic fluctuation signal from the magnetic probe during the plasma formation in TCV.

However, most discharges in TCV have a high initial experimental I_p ramp rate before the I_p feedback control is activated at $t = 10$ ms, which results in a mismatch between the reference and the experimental I_p (Fig. 5.8b). As a consequence the externally applied pre-programmed vertical field is too weak to balance the outward radial hoop force, which leads to a plasma position that is further out than the intended location as long as I_p exceeds its reference and the radial position control is still inactive (Fig. 5.8a). Assuming that both Γ and B_Z^{ext} in eq.(5.3) remains the same during the experimental plasma formation scenario, a relation can

be obtained between ΔI_p and ΔR ,

$$\Delta R = \left(\frac{\mu_0 \Gamma}{4\pi B_Z^{\text{ext}}} \right) \Delta I_p. \quad (5.19)$$

This shows that a difference in the plasma current (ΔI_p) can lead to a radial displacement (ΔR). This model is only valid before the activation of the radial position control system because the control system will modify the reference B_Z^{ext} to reduce the mismatch between the reference and the experimental radial position of the plasma.

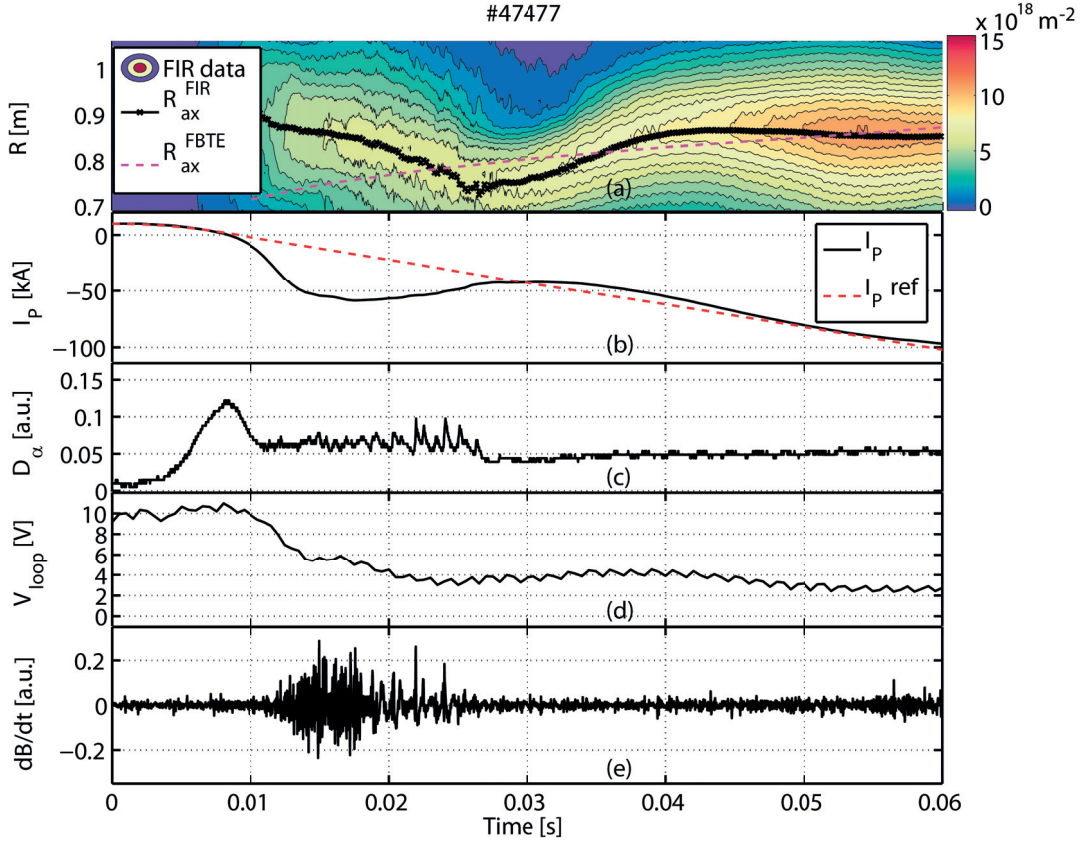


Figure 5.8: Typical TCV plasma current ramp up scenario with a high initial plasma current ramp rate. (a) Evolution of the radial position of the plasma along with the line-integrated plasma density obtained using interferometer (FIR), (b) evolution of I_p , (c) D_α signal from the vertical photo diode, (d) evolution of V_{loop} , and (e) raw magnetic fluctuation signal from the magnetic probe during the plasma formation in TCV.

Once the I_p feedback control is activated, the mismatch in I_p triggers strong oscillations in I_p , which in turn can lead to a decrease in the Ohmic heating power resulting in plasma cooling that can sometimes cause plasma formation failure. An oscillation in the plasma radial position can also be observed at the same time. The feedback performance of the radial position control is also affected by the fact that the reference for the radial observer (section 5.1) is proportional to the current. This problem is aggravated by the fact that the TCV radial

5.3. Analysis of the plasma current ramp-up scenario in TCV

observer does not necessarily cross zero when the radial position is correct, which may lead to an error signal with the wrong sign. Finally, bursts of $n = 1$ MHD activity can be observed from magnetic measurements (Fig. 5.8e) and the D_α signal (Fig. 5.8c). The MHD activity follows the ionization phase indicated by D_α and usually coincides with the reversal of dI_P/dt .

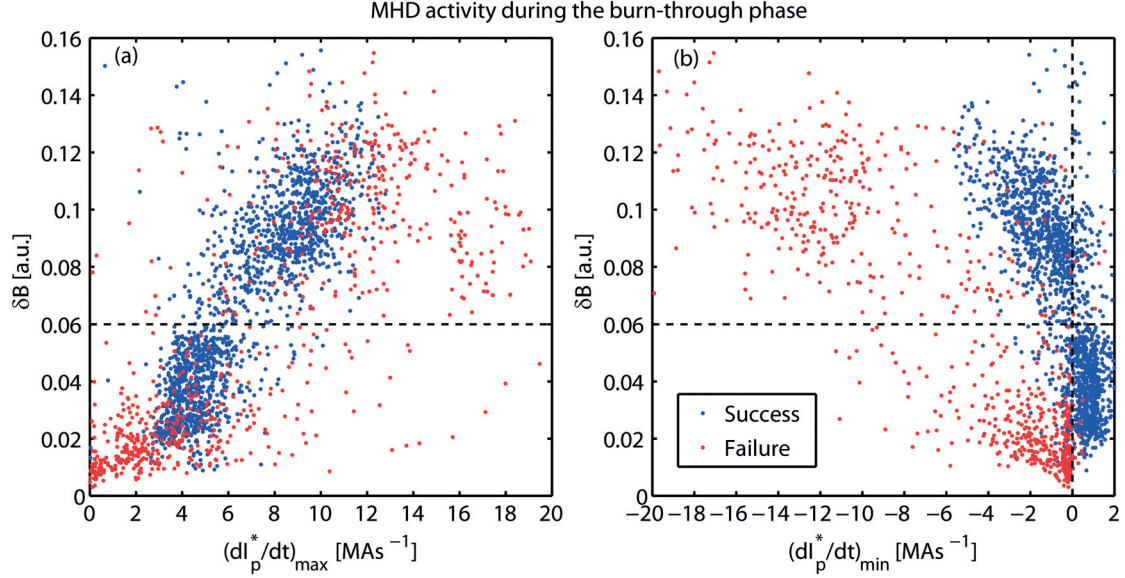


Figure 5.9: Magnetic fluctuation amplitude as a function of (a) maximum experimental plasma current ramp rate and (b) minimum experimental current ramp rate during the successful (blue) and failed (red) TCV ramp-up phases.

A database of 10760 actual TCV plasma current ramp up attempts spanning the discharge range from shot #35000 to #54000 was created to study the influence of the experimental plasma current ramp rate and the MHD activity on the dynamics of the plasma ramp up phase. The database includes 1524 failed burn-throughs corresponding to a failure rate of 15% and 9236 successful ones, including all six breakdown scenarios introduced in Chapter 4. The absolute value of the plasma current was used in the database,

$$I_p^* = I_p / \text{sign}(I_{p,\text{ref}}). \quad (5.20)$$

The maximum of the current ramp rate $\dot{I}_{p,\text{max}}^*$ usually corresponds to the initial ramp rate. While the minimum $\dot{I}_{p,\text{min}}^*$ occurs during the reversal of dI_P/dt caused by the response of the control system to a large ΔI_P . The fast drop of I_P associated with the disruption in failed discharge attempts was not taken into account. The MHD activity is quantified by the average amplitude of the magnetic fluctuations (δB) measured by the magnetic probe with the highest amplitude out of the 38 probes in the poloidal array, i.e., the one closest to the perturbed plasma current, during the time interval when the MHD activity is observed. For failed discharges, the time interval was chosen carefully to avoid any final large perturbation before the disruption.

A subset of 762 failed and 1731 successful burn-throughs is shown in Fig. 5.9. An empirical

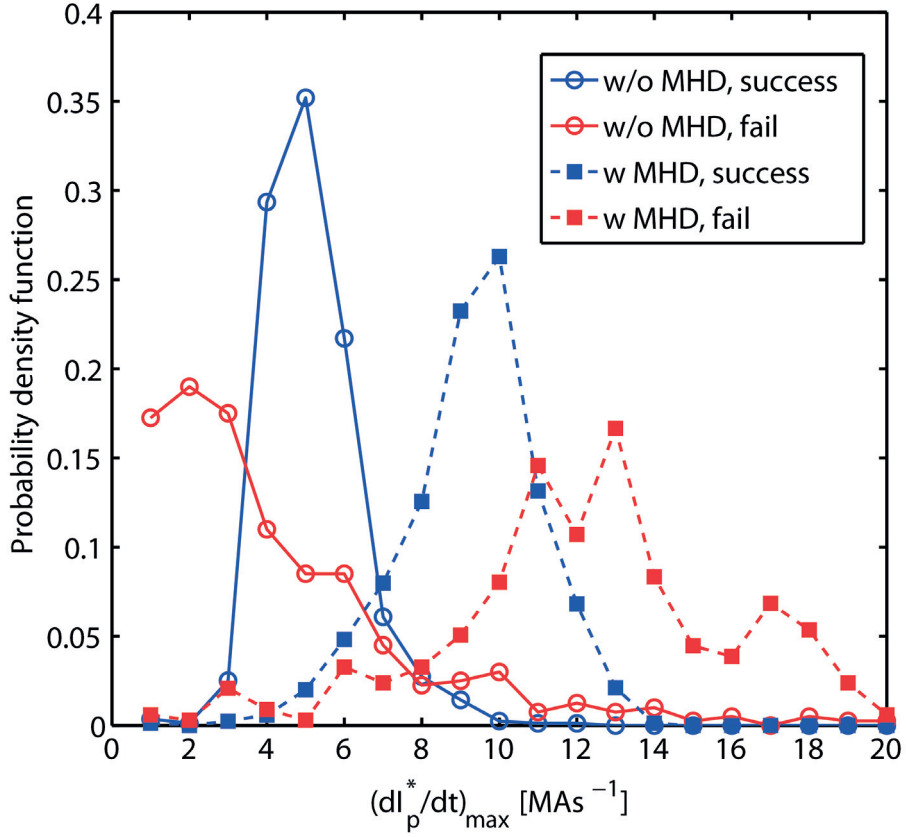


Figure 5.10: Probability density function of maximum experimental plasma current ramp rate for the TCV plasma current ramp-up scenario. The threshold for with or without MHD activity is shown in Fig. 5.9.

threshold of δB amplitude can be observed from the database to separate TCV current ramp up phases into two categories: the discharges with and without MHD activities observed. For each category, the probability density function of $\dot{I}_{p,\max}^*$ for successful and failed discharges is shown in Fig. 5.10. Most discharges with $\dot{I}_{p,\max}^* < 3 \text{ MA s}^{-1}$ result in failed plasma formation but without any MHD activity. High values of $\dot{I}_{p,\max}^*$ generally coincide with MHD activity, with $\dot{I}_{p,\max}^* \approx 7 \text{ MA s}^{-1}$ as the threshold. Very high values of $\dot{I}_{p,\max}^* (> 12 \text{ MA s}^{-1})$ are likely to result in failed plasma formations. Only 2.2% of the successful discharges with MHD activities have $\dot{I}_{p,\max}$ higher than 12 MA s^{-1} , while 48.5% of the failed discharge attempts with MHD activities have $\dot{I}_{p,\max} > 12 \text{ MA s}^{-1}$.

Figure 5.9b shows that the successful discharges without MHD activities have a positive $\dot{I}_{p,\min}^*$, i.e., I_p rising monotonically. It was also observed that the failed plasma discharges with MHD activity had a higher $\dot{I}_{p,\min}^*$ (in absolute value). No clear difference in δB amplitude can be observed for failed and successful discharges with MHD activity. This indicates that the probability of successful plasma formation can be increased by avoiding large oscillations in the plasma current without necessarily avoiding the MHD activity.

5.4 Experiments to improve the TCV plasma current ramp-up scenario

In this section, two different experimental approaches were taken to further investigate and finally attempt to avoid the burn-through failures. One is to modify the breakdown parameters to directly reduce the experimental I_P ramp rate (section 5.4.1), which should result in a lower I_P mismatch and, therefore weaker oscillations from the beginning. The other is to avoid the I_P oscillations through modifications in the control system without changing the error in I_P (section 5.4.2). Comparing the experimental results from these two approaches will then be used to distinguish between the direct effect of a higher I_P ramp rate, such as the outward shift of radial position, and the consequence of the I_P feedback control system response, i.e. the reversal of dI_P/dt and push-back of the radial position, which can lead to insufficient Ohmic heating. It can also verify whether the MHD activity is caused by the initial high I_P ramp rate and outer radial position, i.e., bigger plasma cross section, or the reversal of \dot{I}_P^* , and its importance for a successful plasma formation in TCV.

5.4.1 Experiments to reduce the I_P ramp rate

Variations in the breakdown parameters such as neutral gas pressure, magnetic field configuration and loop voltage can significantly influence the breakdown time as well as the experimental initial I_P ramp rate during plasma formation, as discussed in section 4.6.

5.4.1.1 Reduction of the loop voltage

As the loop voltage is the driving source for the plasma current ramp-up, experiments were performed to study the effect of a reduction of V_{loop} . This was achieved by reducing the programmed Ohmic coil current ramp rate between $t = -15$ and 10 ms using the MGAMS GUI. The prefill gas pressure and the setup of the magnetic configuration were kept constant.

A reduction in V_{loop} results in a decrease of the experimental plasma current ramp rate, and a minor delay in the breakdown time (Fig. 5.11), consistent with the experimental observations in section 4.6.3. A 20% reduction in V_{loop} reduced the experimental $\dot{I}_{P,max}$ by 67%. Such a reduction proved sufficient to avoid the reversal of dI_P/dt as well as the MHD activity. The radial position of the magnetic axis initially remained at the inner wall and only moved slowly to the center as programmed.

The results show that the loop voltage can indeed be used to effectively control the experimental ramp rate and, thereby, avoiding the oscillations in I_P and R_0 , as well as the MHD activity. However, an overly low loop voltage can result in an overly low \dot{I}_P and cause failure in the plasma formation due to insufficient Ohmic heating. Reducing the loop voltage would also decrease the operational window for successful breakdowns.

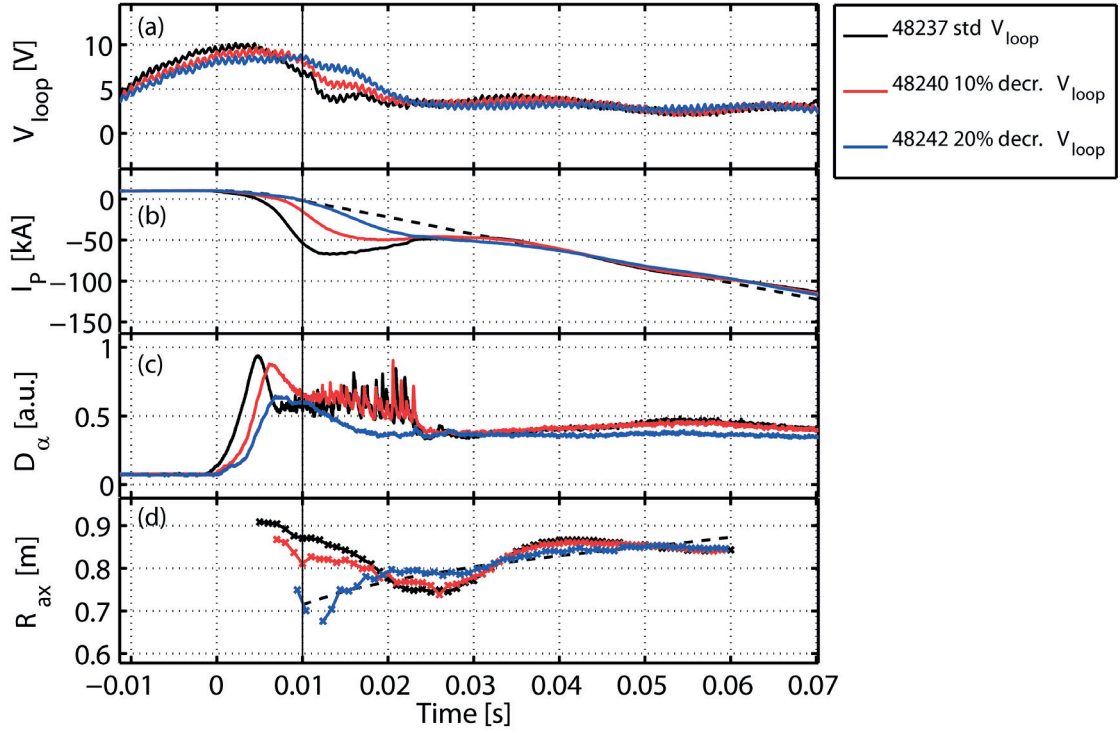


Figure 5.11: Effect of the loop voltage on the burn-through and ramp-up phase. (a) Comparison of different applied V_{loop} . Evolution of (b) I_p , (c) D_α emission along a vertical chord, and (d) the plasma radial position (R_{ax}) obtained from FIR measurements. The black vertical line denotes the activation of the I_p and plasma position feedback control system.

5.4.1.2 Modification of the gradient of the quadrupole field

An alternative way to reduce the ramp rate is to modify the gradient of the poloidal field at the null point. A higher gradient could reduce the physical size of the null and therefore reduce the ramp rate, and also delay the breakdown time (section 4.6.1), which would reduce the error in I_p when the control system is activated.

Experimental results (see Fig. 5.12) show that an increased gradient of the quadrupole field indeed results in a significant delay in breakdown time and also a reduction of the I_p ramp rate. An increase of ∇B_p from 7.5 to 30 mT/m reduced $\dot{I}_{p,max}$ by 47%. The breakdown time was delayed from $t \approx 0$ to > 5 ms. The loop voltage at the breakdown time was only 0.5 V higher due to the delay and thus its effect can be neglected. The delayed breakdown actually resulted in a lower experimental I_p than the reference, and the activation of the feedback control system lead to a faster rise in I_p and an outward movement of the plasma. The initial plasma radial location was still at the inner wall and it was noted that the MHD instability was avoided.

Therefore, the imposed gradient of the quadrupole field in MGAMS can also be used as a tool to reduce the plasma current ramp rate. The extent to which the imposed gradient of the quadrupole field can be increased depends on the neutral gas pressure and toroidal electric

5.4. Experiments to improve the TCV plasma current ramp-up scenario

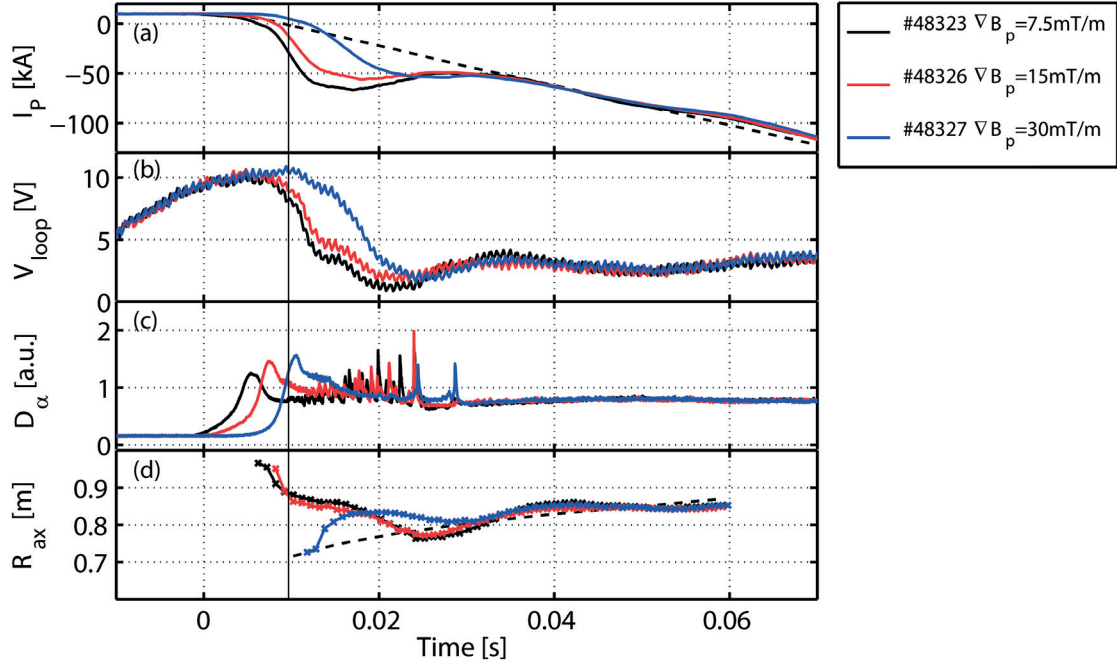


Figure 5.12: Effect of the modification of the gradient of the quadrupole field on the burn-through and ramp-up phase. (a) Comparison of I_p for different gradients of the quadrupole field, (b) evolution of V_{loop} , (c) evolution of D_α emission observed using vertical photodiode, and (d) evolution of the plasma radial position (R_{ax}) obtained from FIR measurements. The black vertical line denotes the activation of the I_p and plasma position feedback control system.

field. This approach also features the problem that it would decrease the operational window for successful breakdowns.

5.4.2 Experiments to control the I_p oscillations

The control system can also be used to avoid the oscillations of I_p and of the radial position, and would also provide further information on the origin and importance of the MHD instability during the ramp-up phase.

5.4.2.1 Early activation of the plasma current feedback control

The first method to improve the plasma current control in the ramp-up phase is to activate I_p feedback control already at $t = 0 \text{ s}$, i.e. before the breakdown has occurred. Between $t = 0$ and 10 ms , a simple proportional feedback term was introduced in the I_p feedback controller. This proportional gain K_p was varied to study its effect on current ramp rate. After $t = 10 \text{ ms}$, the standard I_p feedback control system of TCV was activated.

Experiments were performed with three different value of proportional gain $K_p = 0.01, 0.02$

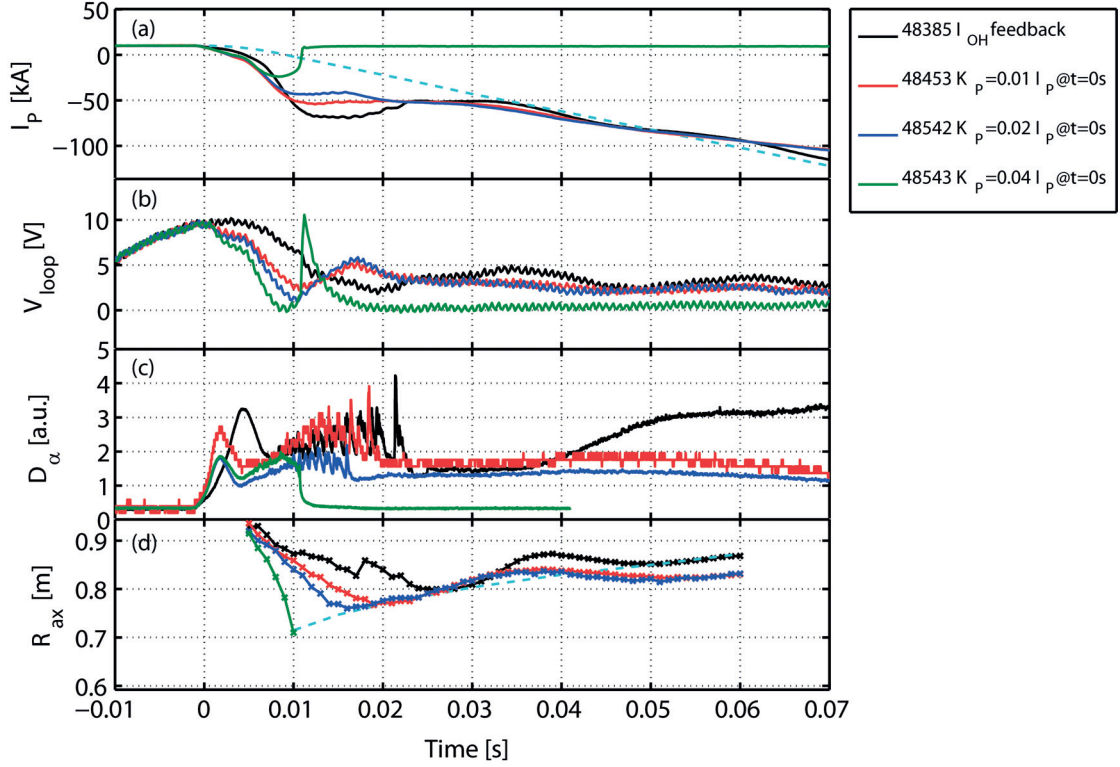


Figure 5.13: Effect of implementation of IP feedback control from $t = 0$ s on the evolution of plasma. (a) Comparison of the I_p evolution for different proportional gains for the I_p feedback control at $t = 0$ s onwards, (b) evolution of V_{loop} , (c) evolution of D_α emission observed using vertical photodiode, and (d) evolution of the plasma radial position obtained from FIR measurements.

and 0.04, respectively. The initial current ramp rate was reduced from 11.3 MA s^{-1} in the reference discharge to approximately $8 - 8.7 \text{ MA s}^{-1}$ (Fig. 5.13a). However, these values were still larger than the empirical threshold for the onset of MHD activity $\dot{I}_{p,max} \approx 7 \text{ MA s}^{-1}$ as discussed in section 5.3 and the MHD activity was always present (Fig. 5.13c). The reduction of $\dot{I}_{p,max}$ was not proportional to K_p . The absolute value of $\dot{I}_{p,min}$ was reduced to ~ 0 , i.e., the oscillation of I_p was reduced. The actuator of I_p control is the Ohmic coil, and thus higher K_p resulted in a stronger reduction of the loop voltage after $t = 0$ s (Fig. 5.13b), which in turn resulted in a lower I_p and an inward shift of the plasma (Fig. 5.13d). Note that the radial position control was not activated in this time range. With the highest chosen proportional gain ($K_p = 0.04$), the plasma current decreases significantly and the plasma formation fails. It is hypothesized that the inward shift of the plasma into the inner wall degrades confinement and the plasma fails to burn through.

The experiments showed that it is the initial I_p ramp rate that results in the onset of MHD activity, not the dI_p/dt reversal. It also suggests that MHD activity alone does not cause the failure. The employing of I_p feedback control between $t = 0$ and 10 ms was able to reduce I_p oscillations. The plasma current value reached after the initial ramp also reduces with higher

5.4. Experiments to improve the TCV plasma current ramp-up scenario

gain. An appropriate gain around $K_p = 0.02$ can be chosen to prevent the failure caused by insufficient Ohmic heating with low I_p . The drawback of this method is that it requires a higher K_p to avoid the oscillations, which results in a lower plasma current. Also the lack of radial position control leads to the plasma being pushed into the inner wall with a low I_p , which further decreases I_p and possibly the confinement. This combination may cause failure in the plasma formation. Therefore, the operational range of K_p is not wide enough to be practical.

5.4.2.2 Bump-less transfer control technique for plasma current and radial position feedback control in TCV

The activation of the I_p feedback control is based on pre-programmed timings defined in MGAMS that do not take into account the uncertainty in the breakdown time, which results in a mismatch between the programmed and experimental I_p ramp rates (section 5.3). An early activation of the I_p feedback control was unable to reduce the oscillations in I_p (section 5.4.2.1) and could result in failed plasma formation. Therefore, to have an effective control over I_p , the activation of the I_p feedback control was made independent of the uncertainty associated with the breakdown time. This was achieved by using a threshold value for I_p after which the I_p feedback control was activated.

To reduce the oscillations in the plasma current due to the mismatch between the programmed and experimental plasma current ramp rate, the *bump-less transfer* control technique [7] for the I_p feedback control was implemented in the SCD. In this technique, the error in the controller is set to zero at the controller activation time before it is phased in with a time constant τ_{bl} resulting in a continuous error signal, and, thereby, avoid control oscillations of I_p . The bump-less transfer control replaces the actual I_p error, $\epsilon_{IP} = I_p^{\text{ref}} - I_p^{\text{meas}}$, where I_p^{ref} is the I_p reference, I_p^{meas} is the I_p measurement, with a bump-less error $\epsilon'_{IP} = \epsilon_{IP} + b$, with,

$$b = \begin{cases} -(I_p^{\text{ref}} - I_p^{\text{meas}}) & \text{if feedback is off} \\ (I_p^{\text{ref}} - I_p^{\text{meas}})(L(s) - 1) & \text{if feedback is on} \end{cases}$$

where, $L(s)$ is a first-order filter ($L(s) \approx 1/\tau_{bl}s + 1$).

The bump-less error can be expressed as,

$$\epsilon'_{IP} = \begin{cases} 0 & \text{if } t \leq t_s \\ \epsilon_{IP} + b & \text{if } t > t_s \end{cases}$$

where, t_s represents the bump-less transfer control technique activation time.

The effectiveness of the bump-less transfer control technique was tested using the linearized plasma model RZIP [12, 51] and a model of the TCV control system in the MATLAB-SIMULINK environment. RZIP is a linear electromagnetic model of a system of the plasma surrounded by the TCV VV, the Ohmic and poloidal field (PF) coils. It is a rigid model, i.e. the plasma can move radially and vertically inside the VV but no deformation of the plasma is allowed. For this application, variations in the coil currents and the plasma current are neglected and

all the quantities that depend on the plasma equilibria are obtained by averaging over the plasma current density distribution. The simulations show that the bump-less transfer control technique can reduce the amplitude of the I_p oscillations (Fig. 5.14). Since the RZIP model in its current form does not allow for time varying equilibria, the numerical simulations are carried out for a plasma in the flat-top phase with a reference for V_{loop} that exceeds the required V_{loop} which is a different situation in comparison to the ramp-up phase. A deviation from a stationary current has been chosen as the test case for the bump-less controller. Therefore, the effectiveness of the implementation of the bump-less transfer technique to control the plasma current during the ramp-up phases might be different from the one observed in the simulation.

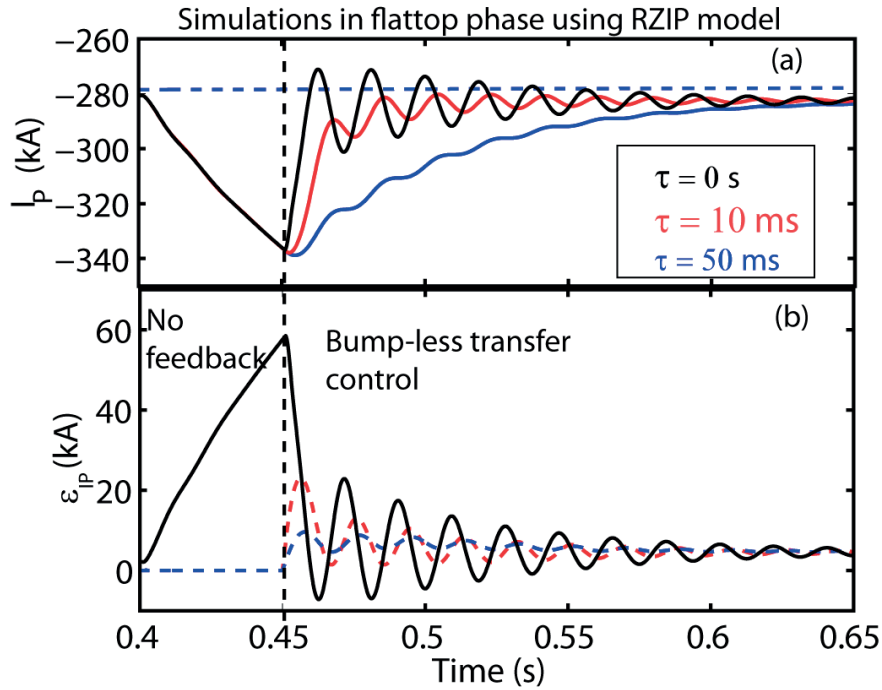


Figure 5.14: SIMULINK simulations to show the effect of the bump-less transfer control technique on the I_p feedback control using the RZIP model. (a) Evolution of I_p for different values of τ_{bl} , the blue dotted horizontal line represents the I_p^{ref} and the black dotted vertical line denotes the time corresponding to the bump-less control technique activation, and (b) evolution of the I_p error (ϵ_{IP}) for different values of τ_{bl} for I_p feedback control.

Since the mismatch in the radial positions arises because of the mismatch in I_p (see section 5.3), the bump-less transfer control technique will result in an even larger mismatch in I_p , which in turn, will result in larger mismatch of the radial position. Therefore, to avoid the oscillations in radial position, the bump-less transfer control technique for the radial position control was also implemented in the SCD.

Experiments were carried out in TCV to test the effectiveness of the bump-less transfer control technique to reduce the oscillations in I_p and the radial position of the plasma for different breakdown locations ($Z = 0.05$ and 0.23 m). The threshold value for I_p to activate the bump-

5.4. Experiments to improve the TCV plasma current ramp-up scenario

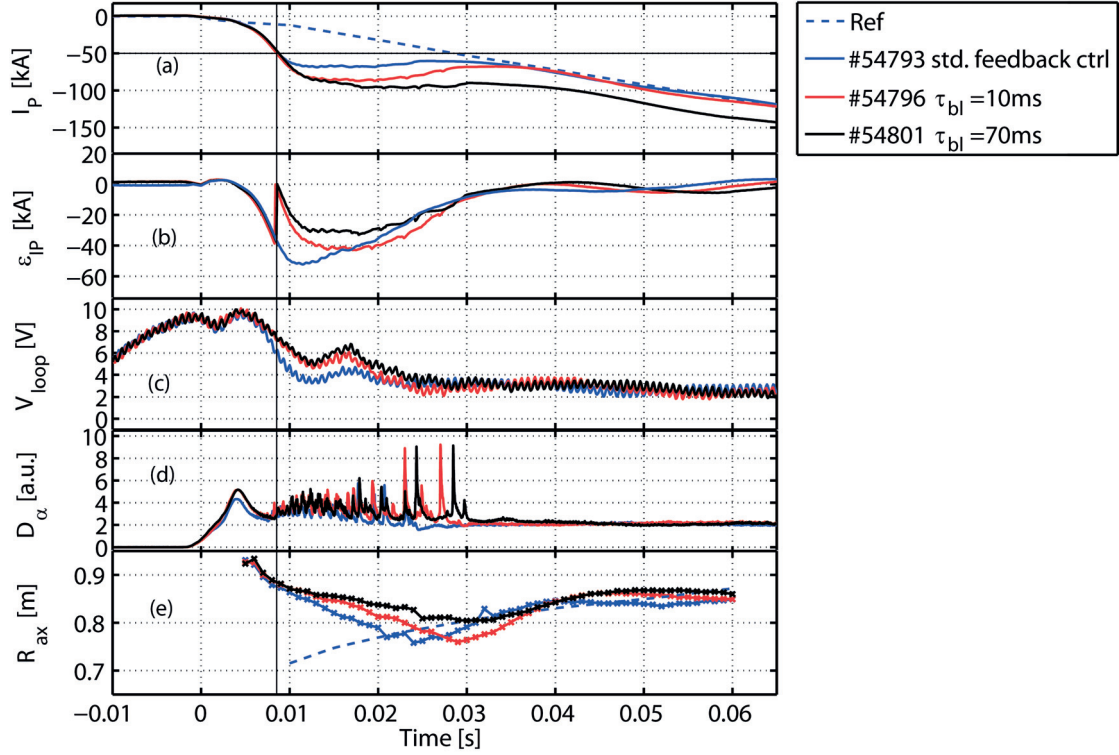


Figure 5.15: Effect of the implementation of bump-less transfer control technique for I_p and radial position feedback control with different τ_{bl} for $z = 0.05$ m breakdown scenario in TCV. (a) Evolution of I_p , black dotted line denotes the I_p reference, (b) evolution of the I_p error, (c) evolution of V_{loop} , (d) D_α signal from the vertical photo diode, and (e) evolution of the plasma radial position (R_{ax}) obtained from FIR measurements. The black vertical line denotes the activation of the bump-less I_p and plasma position feedback control system and the black horizontal line shows the I_p threshold value.

less transfer control for I_p and radial position feedback control was set to 50 kA. The results showed that by increasing the time constant τ_{bl} of the bump-less control loop, the oscillations in I_p were reduced (Fig. 5.15a). As a consequence of the bump-less control, the I_p ramp rate increases, and thus the difference between experimental I_p and the reference becomes larger and persists for a longer time. The radial position of the plasma was also kept in the center of the vessel (Fig. 5.15e). Increasing the time constant τ_{bl} equally reduced the radial oscillations, the oscillations were reduced further with higher τ_{bl} .

The bump-less transfer control did not avoid the onset of the MHD instability (Fig. 5.15d), consistent with the suggested link between its onset and a high I_p ramp rate (section 5.3 and 5.4.2.1). Recall that the success rate of plasma formation with $\dot{I}_{p,max} > 12 \text{ MA s}^{-1}$ was observed to be very small from the database (section 5.3). However, employing the bump-less transfer control technique reduces the I_p oscillations, and results in a higher I_p to prevent failure due to insufficient Ohmic heating. Therefore, the experiments to control the I_p oscillations showed that a high initial current ramp rate and MHD activity do not necessarily cause failure in the plasma formation, as long as the I_p oscillations do not decrease the Ohmic heating

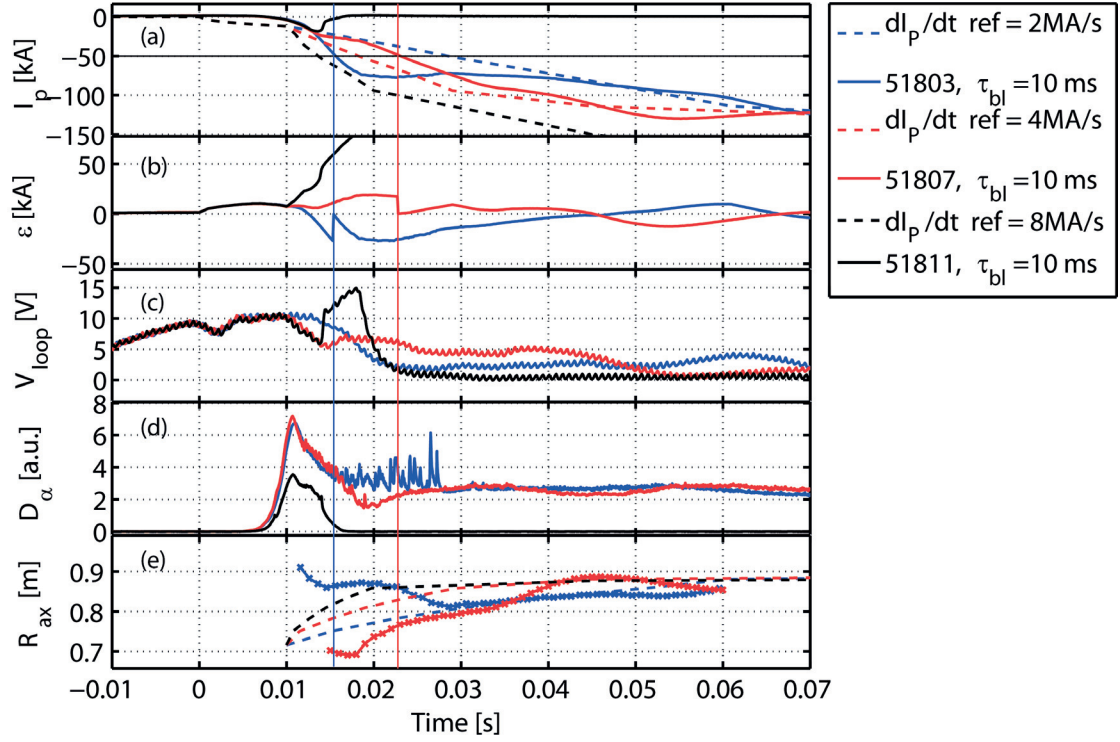


Figure 5.16: Effect of different \dot{I}_p^{ref} on the ramp-up phase. $\dot{I}_p^{\text{ref}} = 2 \text{ MA s}^{-1}$ (blue), 4 MA s^{-1} (red) and 8 MA s^{-1} (black). (a) Evolution of I_p , the dotted lines represent the different I_p references and the solid lines represent the different experimental I_p , (b) evolution of the I_p error, (c) evolution of V_{loop} , (d) D_α signal from the vertical photo diode, and (e) evolution of the plasma radial position (R_{ax}) obtained from FIR measurements. The vertical lines (blue and red) denote the activation of the bump-less I_p and plasma position feedback control system for the different reference I_p ramp rates respectively. The black horizontal line shows the I_p threshold value.

to values that are not sufficient to sustain the burn-through. Compared to the method of early I_p control, the bump-less control technique also reduces the oscillations of the plasma radial position. The overshoot in the plasma current and the subsequent outward shift is self-stabilizing. Therefore, the implementation of the bump-less control technique for the I_p and radial position control can render the plasma formation more reliable.

5.4.2.3 Modification of the reference plasma current ramp rate

The last method used in the experiments was to increase the reference plasma current ramp rate \dot{I}_p^{ref} , to match experimental and reference plasma currents. Additionally, a higher I_p reference engenders a higher programmed external vertical field to balance the outward hoop force. Therefore the radial position of the plasma will remain close to the inner wall with a high experimental current ramp rate. The reference I_p ramp rate was programmed by MGAMS to increase only after the first FBTE equilibrium ($t = 10$ ms) so as to keep the breakdown the

same. The bump-less controller was also used in the experiments with a small time constant ($\tau_{bl} = 10$ ms), activated with a current threshold at $I_p = 50$ kA.

Experiments showed that as the reference I_p and consequently the external applied vertical field increased, the radial position of the plasma remained close to the inner wall (Fig. 5.16e). This, paradoxically, led to a decrease in the experimental I_p ramp rate \dot{I}_p^{exp} (Fig. 5.16a). A hypothesis is that the plasma close to the wall has a smaller cross section and hence a higher resistivity, also the confinement of electrons was worse. This shows that the experimental I_p ramp rate can also depend on the radial location of the plasma, and thus can be controlled by the reference I_p ramp rate. With $\dot{I}_p^{\text{ref}} = 4 \text{ MAs}^{-1}$, \dot{I}_p^{exp} was only $\sim 2 \text{ MAs}^{-1}$ before $t = 1.8$ ms and then increased to $\sim 4 \text{ MAs}^{-1}$ until the bump-less control was activated. A reduced experimental I_p ramp rate also avoided the MHD activity (Fig. 5.16d). When the reference I_p ramp rate was increased to 8 MAs^{-1} from the standard 2 MAs^{-1} , the experimental I_p ramp rate became too small to have sufficient Ohmic heating and the discharge failed to burn through. Therefore, with an appropriate reference current ramp rate ($\dot{I}_p^{\text{ref}} \approx 4 \text{ MAs}^{-1}$), the experimental current ramp rate can be reduced, the plasma can be kept close to the inner wall, and the onset of MHD activity can be avoided. This method can be used with the bump-less control technique simultaneously, and the modification of reference does not further improve the reliability of plasma current formation. It has the advantage that it can be used as an alternative method to control the current ramp rate, plasma position and MHD activity without changing the breakdown parameters compared to the methods discussed in section 5.4.1.

5.5 Conclusion

In this chapter, the burn-through and plasma current ramp-up phase in TCV are both discussed. In the programmed scenario, the plasma cross-section increases linearly, the plasma current ramp rate needs to be sufficiently high to provide sufficient Ohmic heating to sustain the plasma, and sufficiently low so that the safety factor q_{95} stays above 2 and the current density profile is appropriate to avoid MHD instabilities. The poloidal field coil currents are calculated using FBTE to apply an external field to keep the plasma at the correct radial position. In experiments, variations in breakdown parameters influence the plasma current and position and they usually differ from the references, a feedback control system is activated at $t = 10$ ms to control the current and position. A database indicates that $\sim 15\%$ of the TCV discharge attempts fail in the burn-through and current ramp up phase.

An estimate for the plasma current, radial and vertical position during this phase is necessary to study the plasma formation process. This can be provided by fitting the magnetic measurements based on the assumption that the plasma current distribution could be approximated by either a single filament or multiple filaments, valid with plasma currents above 10 kA. The plasma current distribution can also be reconstructed using the LIUQE code. Restricting the current profile to only a single basis function allowed for reconstruction with I_p values as low as 20 kA. A new technique was developed using the multichannel TCV interferometer measurements to determine the radial position and size of the plasma.

TCV experiments showed that the initial plasma current ramp rate plays an important role in the plasma formation. An overly low plasma current ramp rate can cause insufficient Ohmic heating and failure in plasma formation. With a high plasma current ramp rate, a mismatch between the experimental and reference plasma current can be observed. The higher experimental plasma current also causes a higher radial hoop force and cannot be balanced by the programmed external vertical field and leads to the plasma shifting outwards away from the inner wall. At the same time, MHD activity is also observed. This mismatch in the plasma current and radial position then enters the feedback control system as a large error signal when the feedback control is activated. This causes strong oscillations in the plasma current and radial position. When these oscillations are too strong, the plasma current can be transiently too low to provide sufficient Ohmic heating, and the confinement loss increases when the plasma is pushed into the inner wall, which can also cause failure in the plasma formation.

Two different approaches of experiments were taken to improve the scenario. The first one was to control the current ramp rate by breakdown parameters such as imposed gradients and loop voltage. This was verified experimentally to be efficient in controlling the plasma current ramp rate, and thus prevent the problem. The disadvantage is that the operational range, in terms of permissible gas pressure and loop voltage requirements, is decreased for successful breakdowns. The second was to reduce the plasma current and position oscillation so that the Ohmic heating always remains sufficient, while the plasma current ramp rate remains high and MHD activities are seen. Early I_p feedback control can reduce the plasma current oscillation but not the radial position problems. Also the range of proportional gain for the early I_p feedback control to obtain successful plasma formation is small and limiting the extent to which the I_p oscillation can be reduced. A bump-less transfer control technique for the I_p and radial position feedback control was verified experimentally to be efficient in reducing both the plasma current and radial position oscillations, and improve the reliability of the plasma formation in spite of a high experimental plasma current ramp rate. In addition, experiments show that an increased reference plasma current ramp rate can reduce the experimental ramp rate by limiting the radial position of the plasma close to inner wall, for constant breakdown parameters. This method was used with the bump-less control technique simultaneously to improve the plasma current ramp-up scenario in TCV. Though, it should be noted that in this method the reference plasma current ramp rate should not exceed 4 MA s^{-1} to avoid failed plasma formation, in agreement with the legacy breakdown database.

6 New plasma formation scenario in TCV

As discussed in sections 4.4 and 5.3, the standard plasma formation scenarios in TCV, which have evolved through empirical corrections, greatly deviate in several aspects from the original strategy, during the breakdown, burn-through and plasma current ramp-up phases, and can result in failed plasma formations. Knowledge gained through the analysis of the breakdown and of the burn-through and formation phases was combined to improve TCV plasma formation scenarios. These include correction of the mismatch in the breakdown position, avoiding the oscillations in I_p and corrections of radial position during the burn-through and ramp up phase.

Section 6.1 describes the modifications to improve the standard plasma formation scenarios. In section 6.2, the experimental results obtained after the implementation are presented and compared to the standard breakdown scenarios. Section 6.3 describes the two newly developed scenarios at $Z = \pm 0.4$ m in preparation for the creation of a doublet shaped plasma. The results obtained after the implementation of the improved plasma formation scenario are summarized in section 6.4.

6.1 Modifications to improve the plasma formation in TCV

A mismatch between the intended and experimentally obtained breakdown position was identified as one of the problems associated with the $Z = 0.05$ m and $Z = +0.23$ m standard breakdown scenarios in TCV. The mismatch in the breakdown position was due to a difference between the intended and the reconstructed poloidal magnetic field distribution. This difference could be either due to a difference between the programmed and experimental coil currents or a difference between the vessel currents calculated in the MGAMS code and the experimentally obtained vessel currents from the *breakdown* code. A primary difference in the coil currents existed due to the offsets in the outputs of the legacy analogue control system, resulting in a poloidal field of approximately 4 mT at the nominal null point position. These offsets were circumvented by using the digital control system to control the TCV discharges. Even after the correction of the offsets in the coil currents, a difference in the poloidal magnetic field distribution remained. The reconstructed poloidal magnetic field distribution

showed that a finite value of the radial field of approximately 1 mT was present at the intended breakdown position and resulted in a vertical shift of the experimentally obtained null point location. This radial field was found to be predominantly caused by an inaccurate back-off of the stray field generated by the vessel currents. The use of the nominal vessel resistivity assuming axisymmetry to the model vessel current in MGAMS rather than the experimental values obtained from the magnetic measurements was identified as the key reason for this inaccuracy. The experimental resistivity provides a better description of the system than the nominal resistivity. Therefore, a new breakdown scenario was prepared using the experimental vessel resistivity in MGAMS.

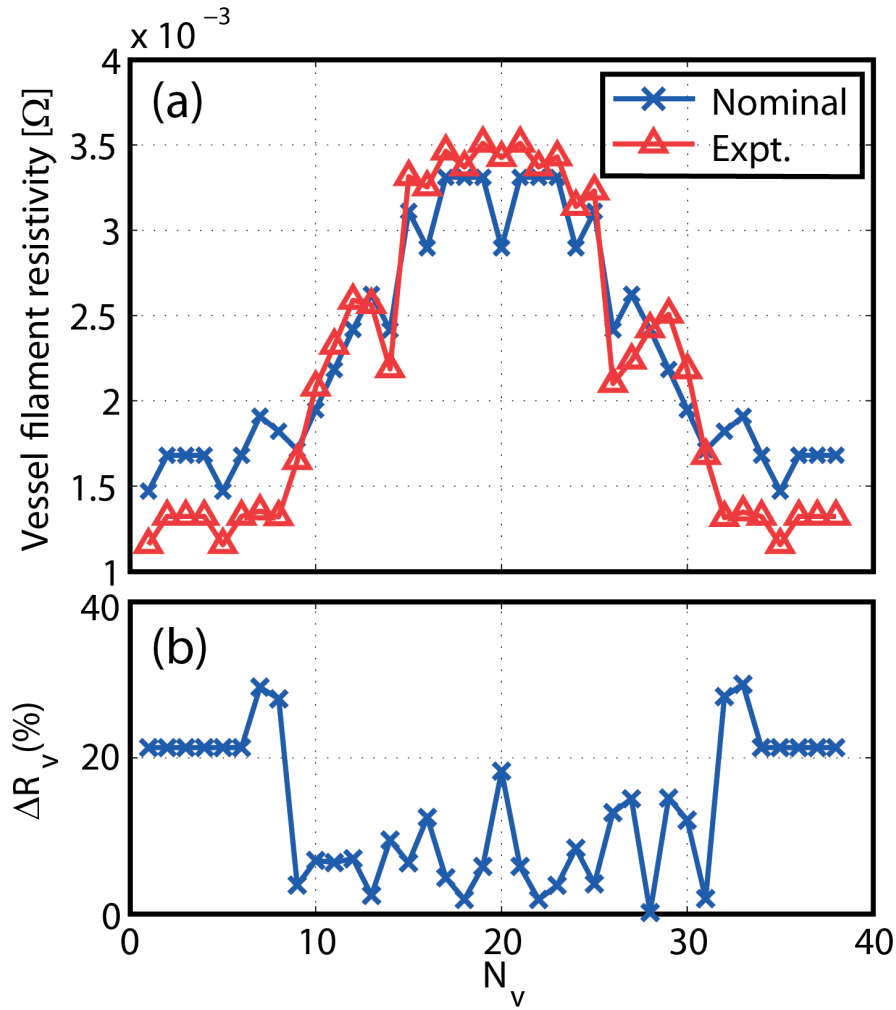


Figure 6.1: (a) The nominal and experimentally obtained vessel filament resistivity and (b) the percentage of difference in resistivity.

Furthermore, the magnetic field configuration at the time of breakdown is determined by two separate sets of PF coils, the *back-off coils*, that compensate for the stray poloidal field generated by the Ohmic coils and the vessel eddy currents and the *quadrupole coils*, used to impose a quadrupole magnetic field. This restricts the choice of the optimal coil combi-

6.1. Modifications to improve the plasma formation in TCV

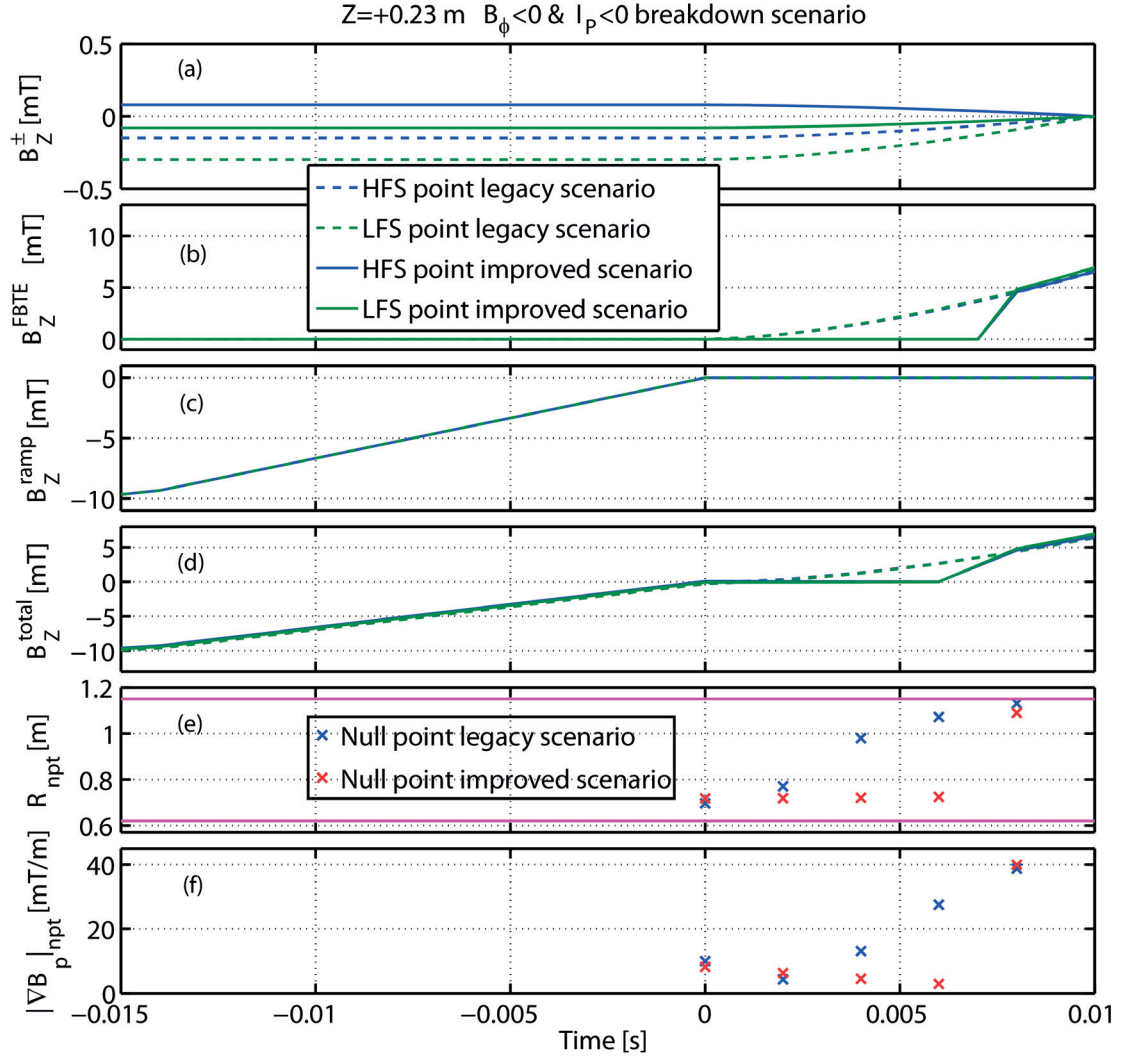


Figure 6.2: Comparison of the evolution of the programmed gradient of the quadrupole magnetic field in MGAMS for the legacy and improved breakdown scenarios in TCV. Evolution of (a) the imposed vertical quadrupole field (B_Z^\pm), (b) the equilibrium vertical field obtained from FBTE (B_Z^{FBTE}), (c) the external vertical field to prevent a early breakdown, (d) the total vertical field at the two quadrupole control points in MGAMS during a standard breakdown scenario, (e) the radial position of the null point (R_{npt}) with the minimum ∇B_p , and (f) ∇B_p at the null point with time.

nations available to obtain breakdown. To provide the flexibility of obtaining breakdown at any desired location in TCV, the new plasma formation scenario uses the same PF coils to compensate for the stray poloidal magnetic field and to generate the intended quadrupole magnetic configuration at the two quadrupole control points specified in MGAMS.

In the standard MGAMS breakdown scenarios, the *quadrupole coils* are used to compensate for the poloidal magnetic field generated by the current in the TF bus bars at the two quadrupole control points. In the new scenario the back-off coils were used for compensation of the field produced by the TF bus bars. This reduces the stray field across a larger spatial extent than just at the two quadrupole points. In addition, the temporal evolution is different from the standard scenario, i.e. the back-off is not phased out with the quadrupole.

The quadrupole magnetic field configuration, specified in MGAMS at $t = 0$ s is phased out as $(1 - (t/t_1)^{1.63})$ until the first FBTE equilibrium ($t_1 = 10$ ms) is reached. Simultaneously, the first FBTE equilibrium field is phased in as $(t/t_1)^{1.63}$ between $t = 0$ s and $t = 10$ ms (section 4.1). As the magnitude of the equilibrium field is much higher than the quadrupole field magnitude, this displaces the intended null point position radially outwards from the position of the magnetic axis of the first FBTE equilibrium (Fig. 6.2e). For the improved breakdown scenario, the contribution of the FBTE field was set to zero between $t = 0$ s and $t = 6$ ms (Fig. 6.2b) to ensure that the null point position remains unchanged during the ramp down of the gradient at the null point position (Fig. 6.2f).

Together with these modifications to improve the breakdown scenario in TCV, the improved plasma formation scenario included a bump-less transfer control technique for the I_p and radial position feedback control, described in section 5.4.2.2, together with a 50% increase in the reference I_p ramp rate over the standard reference I_p ramp rate (see section 5.4.2.3). These modifications aim to improve the match between the experimental and reference plasma current ramp rate and avoid any remaining bump in the I_p control that could cause a failed plasma formation due to insufficient Ohmic heating.

6.2 Experimental results for the improved plasma formation scenario

The changes described in section 6.1 result in an improved back-off and a much smaller residual poloidal field (Fig. 6.3d) compared to the legacy scenario (Fig. 6.3a). The imposed quadrupole vertical field values were chosen to be equal and opposite instead of empirical values, giving a quadrupole null point at the intended location at $Z = +0.23$ m (Fig. 6.3e). As a result, the improved breakdown scenario breakdown gave a much smaller vertical deviation ($\Delta Z = 0.03$ m) between the intended and experimental primary null point position, (Fig. 6.3f), (to be compared to $|\Delta Z| = 0.33$ m with the standard breakdown scenario, Fig. 6.3c). For the improved breakdown scenario at $Z = 0.05$ m the vertical deviation was reduced from 0.13 to 0.01 m between the intended and experimental null point positions. With the implementation of the improved breakdown scenario, a highly improved match between the intended and experimental null point position was also obtained for the $Z = -0.23$ m breakdown position. It

6.2. Experimental results for the improved plasma formation scenario

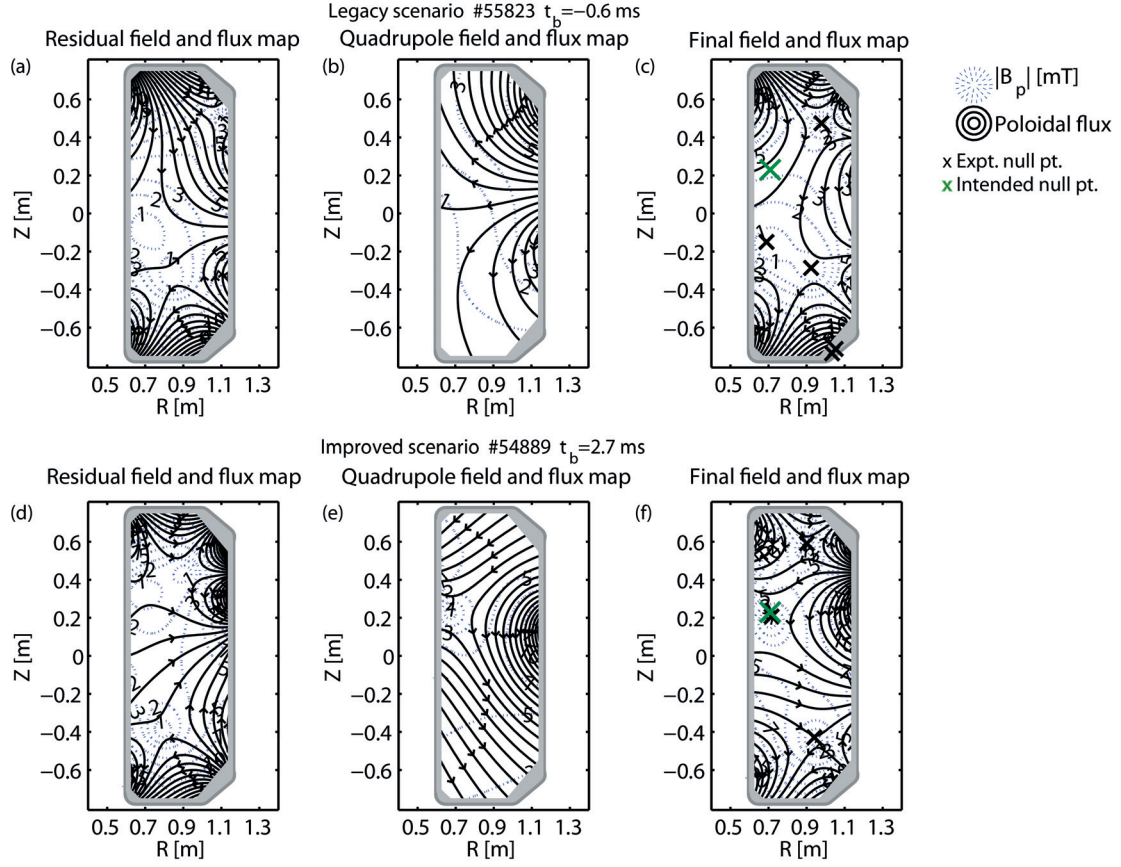


Figure 6.3: Comparison of the reconstructed (a) residual poloidal field and flux after back-off, (b) quadrupole field and flux and (c) final poloidal field at the breakdown time for standard scenario, and (d,e,f) for the improved scenario, respectively, in TCV. The intended null point position (green cross) and the experimental null point position (black cross).

must be noted that the experiments were carried out only for negative B_ϕ and I_p scenarios, thus the effect of the implementation with positive B_ϕ and I_p scenarios is not yet experimentally verified, although a similar improvement is to be expected.

A scan of the imposed gradient of the quadrupole field in MGAMS with the improved scenario was performed. The poloidal field gradient (Fig. 6.4a) decreases and the effective connection length (Fig. 6.4b) increases with time at the experimental obtained null point. The threshold in the effective connection length for breakdown to occur is also found at a similar value $L_{\text{eff}} = 100$ m. Similarly, the increase in $|\nabla B_p|^{\text{MGAMS}}$ leads to a decrease in the initial plasma current ramp rate and delayed breakdown. However, with the improved breakdown scenario, the dependence of the time delay and the initial plasma current ramp rate on the imposed gradient is weaker. Therefore the upper limit of $|\nabla B_p|^{\text{MGAMS}}$ is increased from 0.0225 to 0.064 Tm^{-1} for a successful plasma formation (Fig. 6.4). It also allows for a finer control of breakdown time. At the same imposed gradient, the initial plasma current ramp rate in the improve scenario is, in general, higher than the legacy scenario, so a bump-less transfer technique was useful in preventing the failure of the plasma formation due to strong I_p

oscillations.

A scan of neutral gas pressure was also performed with the improved breakdown scenario. It is to be recalled that in standard TCV operations, the empirically prescribed null configurations were almost never changed and only the neutral pressure varied to achieve a successful breakdown. The measurements show that both the improved and the legacy scenarios follow the Townsend model, that the longer connection length is required at the lowest and highest pressure for successful breakdown. The experiments also suggest a wider operational range for a successful plasma burn-through, that the improved scenario with breakdown at $p_n = 0.0083$ Pa and 0.0528 Pa at $t = 2.4$ ms and 3.9 ms, respectively, still have a sufficiently high plasma current ramp rate ($dI_p/dt = 12.1$ and 5.8 MA/s, respectively) to sustain the Ohmic heating. In comparison, the legacy scenario has a late breakdown ($t_b > 6$ ms) at $p_n = 0.0075$ Pa and 0.055 Pa and too low plasma current ramp rate ($dI_p/dt = 1.8$ and 1.5 MA/s, respectively). The improved scenario only features a similar late breakdown and too low plasma current, which results in a failure during the burn-through phase, at $p_n = 0.0033$ Pa and 0.063 Pa.

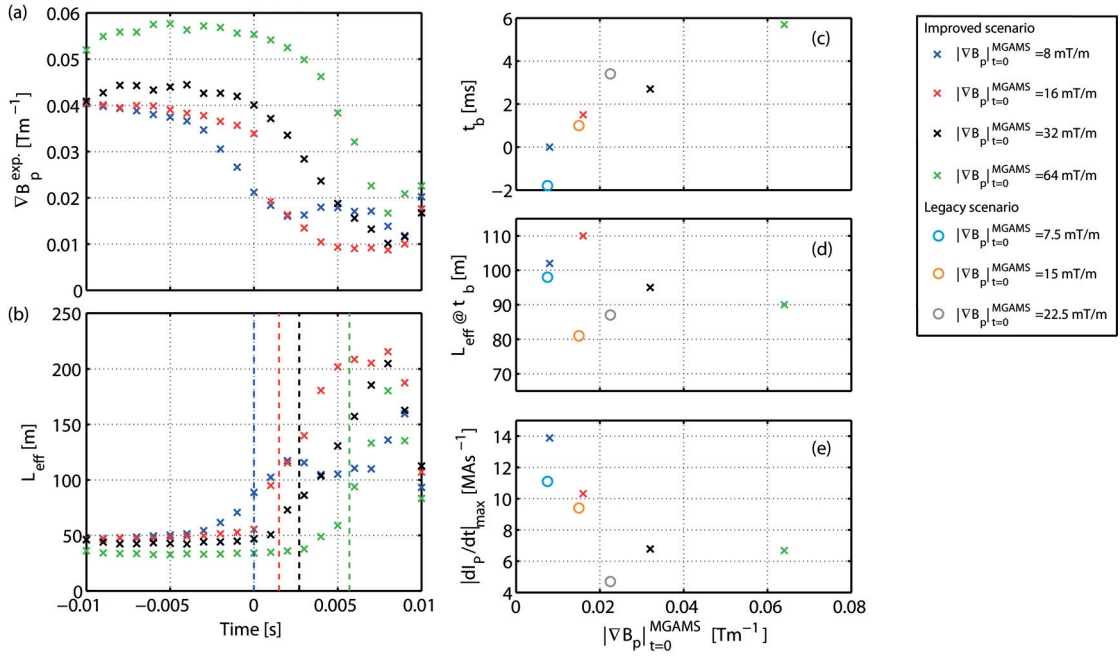


Figure 6.4: Time evolution of (a) poloidal field gradient, (b) effective connection length at the experimentally obtained null point with different imposed gradient of the quadrupole field in the improved scenario. Comparison of the effect of programmed value of poloidal field gradient in MGAMS for $t = 0$ on experimentally obtained (c) breakdown time (t_b), (d) L_{eff} at null point, (e) initial plasma current ramp rate ($(dI_p/dt)_{max}$) for the improved (cross) and legacy (circle) scenarios.

6.3. Development of new plasma formation scenarios (at $Z = \pm 0.4$ m)

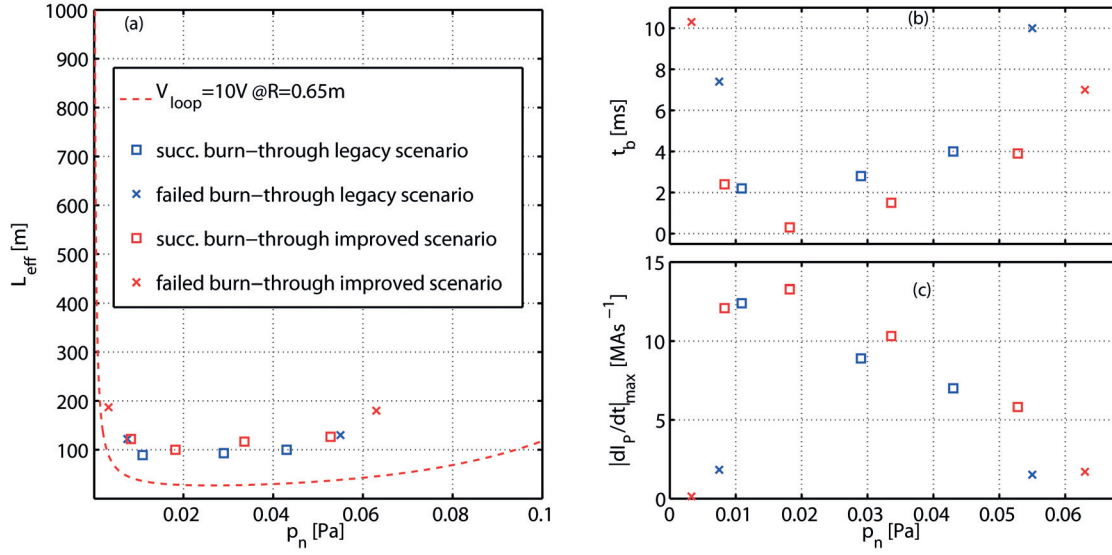


Figure 6.5: Comparison of the effect of the neutral gas pressure for the improved and legacy breakdown scenario on (a) effective connection length (L_{eff}), (b) experimental breakdown time (t_b) and, (c) the maximum of the experimental plasma current ramp rate ($(dI_P/dt)_{\text{max}}$). The standard scenario (blue) and improved scenario (red). In addition, the 'x' denote failed burn-through discharges and the squares denote the successful discharges.

6.3 Development of new plasma formation scenarios (at $Z = \pm 0.4$ m)

With the better understanding of the plasma formation dynamics in TCV, new breakdown scenarios for single-axis breakdown at $Z = +0.4$ m and $Z = -0.4$ m were created. The main difficulty in these scenarios lies in the fact that the efficiency of PF coils in generating radial and vertical fields decreases towards the top and bottom part of the vessel, whereas the gradient of the stray field from the Ohmic and vessel eddy currents increases. The back-off therefore becomes less exact and results in a finite field at the intended null point position again displacing the experimental null point position. These scenarios were developed to determine the values of the prefill neutral gas pressure and the imposed gradient in MGAMS required to obtain successful plasma formation at $Z = +0.4$ m and $Z = -0.4$ m breakdown positions. The understanding gained from these single-axis breakdown scenarios was used to develop the simultaneous double breakdown scenario for the creation of the doublet configuration in TCV (see chapter 7).

Successful and reproducible discharges were achieved in experiments for both $Z = 0.4$ and -0.4 m scenarios. Figure 6.6 and 6.7 shows that a mismatch between experimental and intended null point position is observed in both scenarios, as expected. The experimental null point position is at $R_b = 0.74$ m, $Z_b = 0.27$ m for the $Z = 0.4$ m scenario, with $\Delta R = 0.03$ m and $\Delta Z = 0.13$ m deviation. A radial field of approximately 2 mT was observed at the intended null point position. The gradient at the experimental null point position is 0.016 T/m with an imposed gradient in MGAMS at $t = 0$ s of 0.016 T/m, leading to an initial plasma current ramp rate of 8 MA/s. The bump-less transfer technique is employed with $I_{P,\text{thresh}} = 50$ kA and

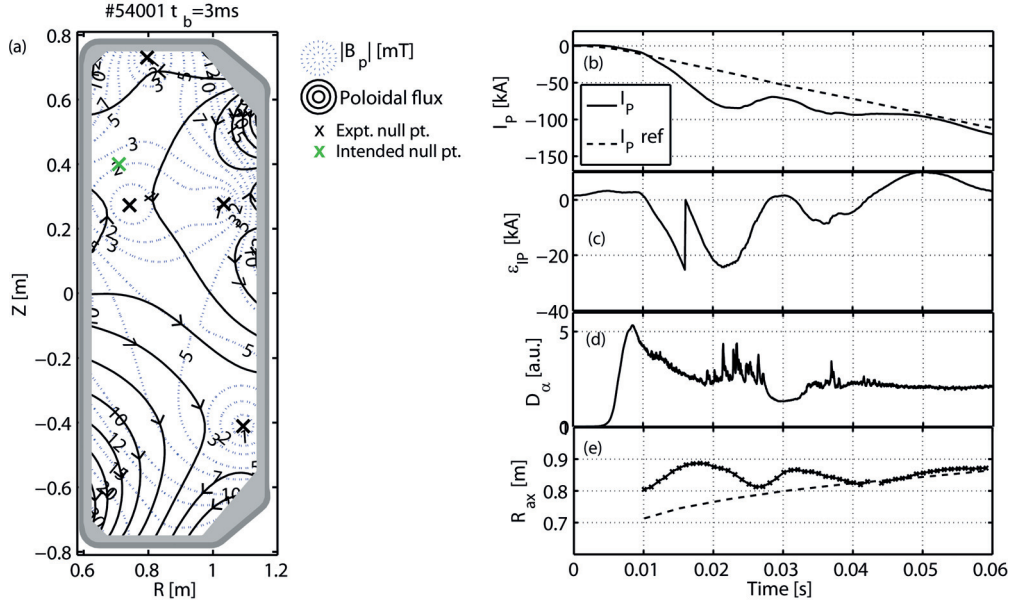


Figure 6.6: (a) Reconstructed poloidal field at the breakdown time. Evolution of (b) plasma current, (c) I_p error, (d) D_α signal and, (e) radial position of the magnetic axis of the plasma.

$\tau_{bl} = 10$ ms and, although I_p and the radial position feature an oscillation, I_p is always higher than the reference, and the plasma isn't pushed to the inner wall, thus the Ohmic heating is still sufficient to sustain the plasma. The oscillations in I_p and radial position were further reduced by increasing the reference I_p ramp rate in conjunction with the bump-less transfer control technique (see section 5.4.2.3).

For the $Z = -0.4$ m scenario, the experimental null point is at $R_b = 0.71$ m, $Z_b = -0.25$ m, with $\Delta R \approx 0.01$ m and $\Delta Z = 0.15$ m deviation. A radial field of approximately 2.3 mT was observed at the intended null point position. The gradient of the poloidal field at the experimentally obtained null point is 0.025 T/m with an imposed gradient in MGAMS at $t = 0$ s of 0.008 Tm^{-1} , leading to an initial plasma current ramp rate of 6 MA/s. The plasma current evolution in the ramp-up phase is very smooth using the bump-less transfer technique ($I_{p,\text{thresh}} = 50$ kA, $\tau_{bl} = 10$ ms), and no oscillations are observed in both I_p and the plasma radial position. A prefill scan showed that although a successful breakdown was obtained, but the plasma failed during the burn-through phase due to an insufficient initial plasma current ramp rate.

6.4 Conclusion

A new plasma formation scenario was proposed and tested in experiments to improve the plasma formation in TCV in the breakdown, the burn-through and ramp-up phases. A mismatch in the breakdown position was reduced to $\Delta Z \leq 0.03$ m for all three breakdown locations ($Z = 0.05$ m and ± 0.23 m). Scans of imposed gradient at the quadrupole points in MGAMS and in the neutral gas pressure show that the new scenario prevents an early breakdown before

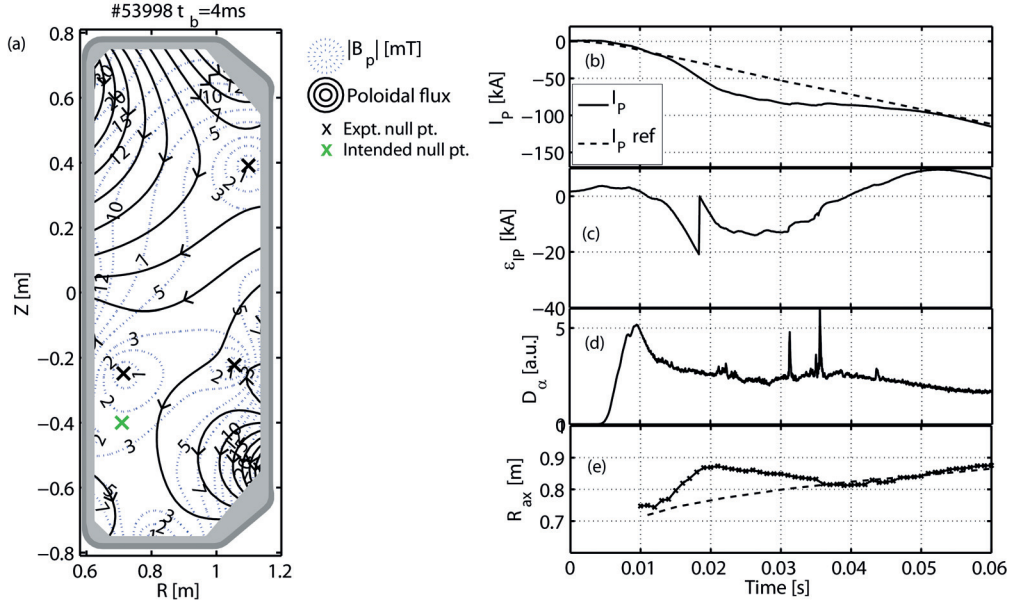


Figure 6.7: (a) Reconstructed poloidal field at the breakdown time. Evolution of (b) plasma current, (c) I_p error, (d) D_α signal and, (e) radial position of the magnetic axis of the plasma.

$t = 0$ s, and extends the operational range to control the breakdown time and initial plasma current ramp rate. The bump-less transfer control technique is used to avoid the oscillations in I_p and plasma radial position, and thus to prevent failure in the plasma formation due to a temporary insufficiency of Ohmic heating. Modification of the reference I_p ramp rate is also employed in some scenarios to control the experimental I_p ramp rate and radial position. With the understanding gained through the analysis of plasma formation, the improvements were applied to create two new breakdown scenarios at the top and bottom part of the vessel ($z = \pm 0.4$ m), where breakdown is more difficult due to inefficiency of radial and vertical field control using PF coil currents. Although a shift of the breakdown position was observed ($\Delta Z = 0.1$ m) for the $Z = +0.4$ m and $Z = -0.4$ m breakdown positions but successful plasma formation was obtained for these scenarios. From these two new scenarios, the neutral gas pressure and the imposed quadrupole field values required for successful breakdown and plasma formation were obtained. These experiments showed that the two new scenarios were highly reproducible, and could be used as a preparation of the simultaneous double breakdown scenario for the creation of doublet shaped plasma.

7 Development of a doublet configuration in TCV

The *doublet* shaped plasma is a plasma configuration which is characterized by two plasma current channels, which flow in the same toroidal direction resulting in the formation of a magnetic X-point between the two channels (figure 7.1). The separatrix is surrounded by closed magnetic surfaces forming a *mantle*. A limiter typically determines the last closed flux surface.

The concept of the doublet shaped plasma configuration was proposed by T. Ohkawa in 1968, and was first studied in the device Doublet-I at General Atomics, San Diego, California [64, 63]. The doublet was motivated by the good confinement properties of similar multipole configurations with internal conductors [64]. The doublet configuration was also predicted to attain higher β values than single-axis plasmas with a circular cross section [63]. The experiments showed that the doublet configuration appeared to be in stable MHD equilibrium, but strong radiative cooling by impurity ions, prevented estimates of the confinement time [64]. Doublet-II and Doublet-IIA devices were built to determine whether the doublet configuration can obtain higher β values than plasmas with a circular cross section with the same safety factor and poloidal beta (β_p) [62, 38]. It was concluded that the plasma confinement in doublets and circular cross section plasmas of comparable dimensions with similar current densities and safety factors was similar [62]. The last device to study the doublet configuration was Doublet III, and no further research was carried out after DIII was converted to DIII-D [75]. Research was abandoned in the early 1980s in favor of tokamaks as the control of the doublet configuration proved to be challenging.

Theoretical calculations show that the main advantage of the doublet configuration is that the doublets have the same beta limit as the single axis plasmas with the same elongation, but a much lower vertical growth rate [14, 15]. It is, furthermore suspected that doublet plasmas may develop an internal transport barrier at the internal separatrix, similar to the H-mode edge transport barrier. The presence of the mantle between the internal separatrix and the Scape-Off Layer (SOL) may also have advantageous power exhaust properties. The mantle can be a cold plasma region characterized by a high fraction of volumetric losses. This should reduce the power reaching the solid surfaces of the reactor in the plasma channel, and thereby, increase the lifetime of the plasma-facing components of the device. Lastly,

doublet shaped plasma configuration experiments may advance the understanding of the magnetic reconnection physics that takes place in the vicinity of the X-point when the two current channels merge. The development of a stable and controlled doublet configuration is a prerequisite and, thereby, a first step for any of these studies.

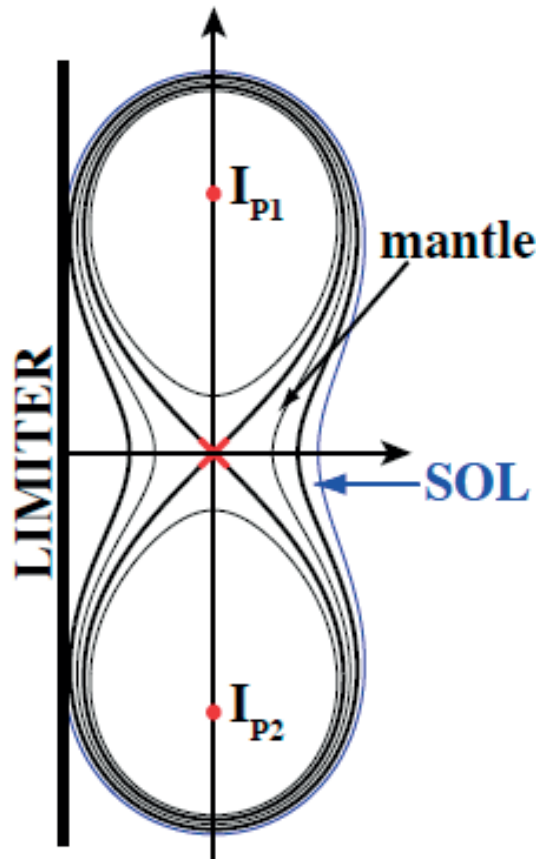


Figure 7.1: Schematic showing the doublet shaped plasma configuration. The red circles denote the two plasma magnetic axes and the red cross denotes the X-point. Image source: [68]

Presently, TCV is the only tokamak, which may have the capability to create the doublet shaped plasma configuration due to the high flexibility of the 16 independently powered shaping coils and the high elongation of its vacuum vessel. The merging of the two droplet shaped plasmas, which was the strategy used in DIII [75], is also considered to be the most promising strategy to create the doublet shaped plasma configuration in TCV [26]. The creation of two droplet shaped plasmas requires simultaneous breakdown at two locations with the two magnetic null points having similar magnetic properties so that the plasma current in both the plasmas is approximately equal. In an earlier attempt, a transient Ohmic doublet configuration with a plasma current of 100 kA has been obtained in TCV for a very short time [26]. Further attempts to obtain doublets in TCV were made in 2009, but successful simultaneous double breakdown with inductive start-up could not be achieved [68]. Successful ECRH-assisted

double breakdowns were obtained but, the plasma current in the two droplets could not be sustained [68].

A fresh attempt is made to create and control the doublet configuration in TCV based on the improved understanding of the plasma formation dynamics gained during the work performed in this thesis. This chapter describes the implementation of the new strategy to obtain a reproducible doublet breakdown in TCV with inductive only plasma-start up (section 7.1) and the implementation of the different feedback control schemes to control the position and plasma current of the doublet shaped plasma scenario (section 7.2). The experimental results obtained during this thesis are discussed in section 7.3 and section 7.4 summarizes the conclusion of the development of the doublet shaped plasma configuration in TCV.

7.1 Programming of simultaneous double breakdown

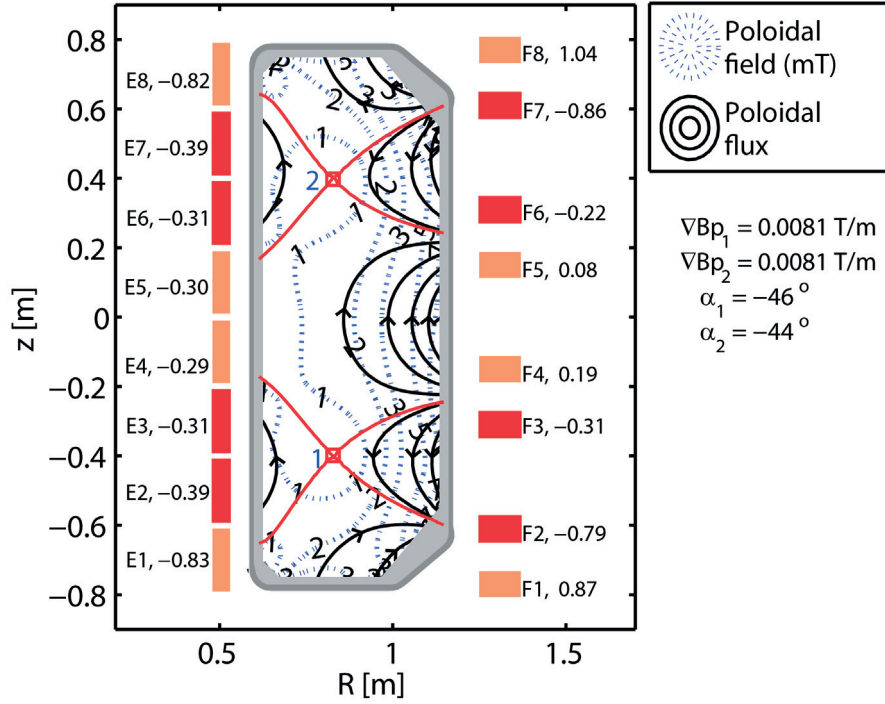


Figure 7.2: Poloidal field magnetic reconstruction obtained using MGAMS code for doublet scenario, with coil currents in [kA] and the quadrupole PF coils (red).

In TCV, the most promising strategy to create the doublet shaped plasma scenario is the merging of two droplets [26]. This requires to have a simultaneous double breakdown and therefore two magnetic nulls with similar magnetic properties. If one null has a higher gradient than the other, as discussed in Chapter 4, it would have a delayed breakdown and lower plasma current ramp rate. The resulting asymmetry in plasma currents would lead to a thermal instability and the disappearance of one of the droplets, which will be discussed in section 7.2.1. If the two droplet currents are equal, they can both grow and form a doublet.

The vertical separation of the two null points should be as large as possible to minimize the

interaction between the two droplets. However, the ability to apply vertical and radial fields with the poloidal field coils decreases towards the top and bottom part of the TCV VV, and the stray field has a higher gradient and is more difficult to back-off. As a follow up to the two newly developed single-axis scenarios, described in Chapter 6, the simultaneous double breakdown is developed.

The stray field configuration is not exactly up-down symmetric since the TF bus bars and the effective vessel resistance, influenced by ports, break the symmetry. Therefore it is necessary to use the new method (section 6.1) to calculate the back-off coefficients, in which the back-off for the field generated by TF bus bars as well as experimental vessel resistivity are considered. All 16 PF coils are used to back-off the field at $Z = \pm 0.4$ m simultaneously. Although the considered optimization volume extends only ± 0.05 m around $Z = \pm 0.4$ m, the stray field at $Z = 0$ m is also close to zero due to the symmetry of the coils. Additional bias currents are applied to the poloidal field coils near the mid-plane in order to remove a third null point, which otherwise naturally forms in the mid-plane.

The imposed radial and vertical field ($B_{R,Z}^{\pm}$) values at $t = 0$ s are prescribed separately in MGAMS for the $Z = 0.4$ m and $Z = -0.4$ m locations to provide flexibility in controlling the two null points. The PF coil combinations used to apply the quadrupole field is [E6,E7,F6,F7] for the top null, and [E1,E2,F1,F2] for the bottom null. After the implementation of the methods to optimize the magnetic configuration for the simultaneous breakdown at two locations, two magnetic null points with similar magnetic properties ($|\nabla B_p| = 0.0081$ T/m, $\alpha_{npt} = -45^\circ$) are obtained (Fig. 7.2).

7.2 Feedback phase of doublet shaped plasma configuration

As for single axis plasmas the vertical position is unstable and must be controlled. In addition to a vertical displacement of the entire plasma (Q mode), doublets also exhibit a mirror symmetric mode (S mode), where both current channels move in opposite directions. In addition, the system of two plasma droplets with Ohmic heating alone is thermally unstable. This section discusses the strategies which were implemented in the digital control system to independently control the current and position of the two droplet plasmas. Section 7.2.1 discusses the strategy to independently control the plasma current in the two droplets. Section 7.2.2 discusses the rigid plasma model developed for the doublet shaped plasma configuration. Section 7.2.3 discusses the strategies proposed to independently control the radial and vertical position of the two droplets and in section 7.2.4 the results of the stability analysis for the closed-loop vertical position control system of the droplet shaped plasma configuration are discussed.

7.2.1 Plasma current control for the two droplet shaped plasmas

Since the Ohmic coil produces a uniform loop voltage inside the VV, it is not possible to use it as an actuator to independently control the plasma current in the two droplets. The decrease

7.2. Feedback phase of doublet shaped plasma configuration

of the plasma resistance with an increasing electron temperature (with $R_p \propto T_e^{-1.5}$), leads to an instability in the sharing of inductively driven current in Ohmically heated droplets. The droplet with the higher current also receives more Ohmic heating. The resulting lower resistance increases the current imbalance further. To avoid the inherent thermal instability of an Ohmically heated doublet, ECRH can be used as an actuator to independently heat the two droplets and thereby, control their temperature and, hence, resistivity. Simulations performed in [68] showed that the time response and power of the TCV ECRH system is adequate to control the Ohmically driven current in both droplets.

Plasma current observer

Two separate plasma current observers are required to independently control the plasma current in the two droplets. The two plasma current observers can be constructed from the magnetic measurements which include the 38 flux loop measurements, 38 magnetic field probe measurements, I_p measurement and the coil current measurements. The poloidal flux measured by the flux loops can be modeled as,

$$\psi_f = M_{fy}I_y + M_{fa}I_a, \quad (7.1)$$

where ψ_f is the poloidal flux measurement, M_{fa} is the Green's functions between the poloidal flux loops and the active coils, I_a denotes the active coil currents, M_{fy} denotes the Green's functions between the poloidal flux loops and the plasma filaments, and I_y denotes the current in the plasma filaments (usually 8 or 12).

The poloidal field measured by the magnetic field probes can be modeled as,

$$B_m = b_{my}I_y + b_{ma}I_a, \quad (7.2)$$

where B_m denotes poloidal magnetic field measurements, b_{ma} the Green's functions between the poloidal magnetic field probes and the active coils, and b_{my} the Green's functions between the poloidal magnetic field probes and the plasma filaments.

The plasma current can be modeled as the sum of the current in the plasma filaments,

$$I_p = \sum_y I_y. \quad (7.3)$$

The plasma current in each filament can be obtained by combining eq.(7.1)-(7.3),

$$m = M^{\text{obs}}[I_a; I_x], \quad (7.4)$$

where M^{obs} denotes the Green's functions used to couple the plasma current and the active coil currents with the magnetic measurements and m denotes the magnetic measurements. For an up-down symmetric plasma configuration, the observers can be defined such that a subgroup of the plasma filaments are used to model the upper plasma column and another

subgroup to model the lower plasma column,

$$I_y = \begin{bmatrix} I_y^{top} \\ I_y^{bot} \end{bmatrix}, \quad (7.5)$$

where I_y^{top} denotes the current in the upper plasma filaments and I_y^{bot} denotes the current in the lower plasma filaments.

Plasma current actuator

Two ECRH launchers belonging to two separate ECRH clusters (A and B) with independent power supplies are used to independently control the plasma current in the two droplets. One of the ECRH launchers should heat the top plasma droplet, and the other ECRH launcher should heat the bottom plasma droplet. In this feedback scheme, both launchers initially apply a constant ECRH power to both droplets. When the currents in the droplets deviate, the ECRH power to both droplets is adjusted in opposite direction by an amount that is proportional to the difference in the plasma current between the two droplets ($\Delta I_p^C = \sum I_y^{top} - \sum I_y^{bot}$). The value of the initial ECRH power must be carefully chosen to avoid the limits of the ECRH clusters. For the cluster A, the lower limit is set to be 75 kW and for cluster B it is 180 kW. The control algorithm to independently control the plasma current in the two droplet shaped plasmas with ECRH as actuator was implemented in the TCV digital control system.

7.2.2 Plasma model for the doublet shaped plasma

The RZIP model, which is a plasma model that was developed to study the vertical stability of conventional plasma configuration, was extended to doublet configurations [68]. The RZIP model [12, 51] is a linearized rigid plasma model, which is based on the assumption that the plasma can move in the radial and vertical direction, but the shape of the plasma cannot deform. The model for the single-axis plasma is extended to two droplets that can move in different directions. The extended RZIP model [68] is referred to as the RZIP2 model and the complete equations are presented in the Appendix. In this model the plasma inertia is neglected as it does not play a significant role for vertical instabilities with low growth rates ($\gamma_v < 1000 \text{ s}^{-1}$), which are controllable by the slow feedback control system of TCV [28]. The plasma current distribution in each is assumed to be constant. It is assumed that small variations in the PF coil voltages result in small changes in the plasma currents, PF coil currents, vessel currents and the radial and vertical positions from the unperturbed equilibrium state calculated with the FBTE code. The vessel current can be obtained by taking into account the electromagnetic interaction that occurs among the vessel filaments and with the two plasma droplets (denoted plasma 1 and 2) and the active coils,

$$M_{vv}\dot{I}_v + R_v I_v + M_{va}\dot{I}_a + \frac{d}{dt}(M_{vp1}I_{p1}) + \frac{d}{dt}(M_{vp2}I_{p2}) = 0, \quad (7.6)$$

7.2. Feedback phase of doublet shaped plasma configuration

where R_v denotes the vessel resistance, M_{va} denotes the Green's functions between the vessel filaments and the active coils. The matrix M_{vp1} denotes the Green's functions between the vessel filaments and the top plasma current, M_{vp2} the Green's functions between the vessel filaments and the bottom plasma, I_{p1} and I_{p2} denote the plasma currents in the top and the bottom plasma, respectively. Both M_{vp1} and M_{vp2} can change with time due to the movement of the droplets.

Similarly, the circuit equation for the active coils is,

$$M_{aa}\dot{I}_a + R_a I_a + M_{av}\dot{I}_v + \frac{d}{dt}(M_{ap1}I_{p1}) + \frac{d}{dt}(M_{ap2}I_{p2}) = V_a, \quad (7.7)$$

where R_a denotes the active coil resistances, V_a denotes the active coil voltages, M_{aa} denotes the Green's functions between the active coils, M_{ap1} denotes the Green's functions between the active coils and plasma 1, M_{ap2} denotes the Green's functions between the active coils and plasma 2.

The circuit equation for the plasma 1 is,

$$\frac{d}{dt}(L_{p1}I_{p1}) + \frac{d}{dt}(M_{p1a}I_a) + \frac{d}{dt}(M_{p1v}I_v) + \frac{d}{dt}(M_{p1p2}I_{p2}) + R_{p1}I_{p1} = 0, \quad (7.8)$$

where R_{p1} denotes the plasma resistance of plasma 1, L_{p1} is the self-inductance of plasma 1, M_{p1p2} denotes the Green's functions between the two plasma droplets, M_{p1a} denotes the Green's functions between the plasma 1 and the active coils, M_{p1v} denotes the Green's functions between the plasma 1 and the vessel filaments.

The vertical force balance for the two droplet plasmas is considered separately in the model. The vertical force balance for the plasma 1 is,

$$m_{p1} \frac{d^2 Z_1}{dt^2} = \sum F_{z1} = -2\pi R_1 I_{p1} B_{r1}(R_1, Z_1, I_a, I_v, I_{p2}), \quad (7.9)$$

where m_{p1} denotes the inertia of the plasma 1, R_1 denotes the magnetic axis of plasma 1, B_{r1} denotes the radial field produced by the active coils, vessel current and I_{p2} . Due to the low inertia of the plasma, the term in the L.H.S of eq.(7.9) is neglected. The time derivative of eq.(7.9) can be written as,

$$0 = \frac{d}{dt} [-2\pi R_1 I_{p1} B_{r1}(R_1, z_1, I_a, I_v, I_{p2})]. \quad (7.10)$$

The radial force balance for the plasma 1 can be written as,

$$m_{p1} \frac{d^2 R_1}{dt^2} = \sum F_{R1} = \frac{\mu_0}{2} I_{p1}^2 \Gamma_1(R_1, t) + 2\pi R_1 I_{p1} B_{z1}(R_1, Z_1, I_a, I_v, I_{p2}), \quad (7.11)$$

where $\Gamma_1 = \ln(8R_{01}/a_1\sqrt{\kappa_1}) + \beta_{p1} + l_{i1}/2 - 1.5$, B_{z1} denotes the vertical field produced by the active coils, vessel current and I_{p2} .

Chapter 7. Development of a doublet configuration in TCV

Again assuming that the inertia term is zero, the time derivative of eq.(7.11), can be written as,

$$0 = \frac{d}{dt} \left[\frac{\mu_0}{2} I_{p1}^2 \Gamma_1 \right] + \frac{d}{dt} [2\pi R_1 I_{p1} B_{z1}(R_1, Z_1, I_a, I_v, I_{p2})]. \quad (7.12)$$

The above set of equations are linearized around an equilibrium point and expressed in the matrix representation as,

$$M\dot{\vec{x}} + R\vec{x} = \vec{u}, \quad (7.13)$$

where M and R are matrices containing the Green's functions and the resistances of the coils, vessel and two plasma droplets respectively. The vector \vec{u} denotes the inputs to the system and \vec{x} is the vector containing the states of the system. The states of the two droplet systems are,

$$\vec{x} = \begin{bmatrix} \delta I_a \\ \delta I_v \\ \delta I_{p1} \\ \delta I_{p2} \\ I_{p01} \delta R_1 \\ I_{p02} \delta R_2 \\ I_{p01} \delta Z_1 \\ I_{p02} \delta Z_2 \end{bmatrix}. \quad (7.14)$$

Equation(7.13), can be expressed in the state space form as,

$$\dot{\vec{x}} = A\vec{x} + B\vec{u}, \quad (7.15)$$

where $A = -M^{-1}R$, $B = M^{-1}$. This equation is called the state equation of the system and the eigenvalues of matrix A defines the stability of the system. Positive eigenvalues indicate that the system is unstable.

For the doublet configuration, two vertically unstable modes were identified from the eigenvalue analysis of the RZIP2 model. In one of the vertically unstable modes, the two plasmas move in the same vertical direction (Q mode), whereas in the other mode, a mirror symmetric displacement of the two plasmas in the vertical direction (S mode) is observed. The S mode has generally a much higher growth rate than the Q mode. The RZIP2 model can provide an estimate of the vertical growth rates of the doublet configuration in TCV and was also used to study the feasibility of vertical position control in TCV and optimize the gain settings (section 7.2.4).

7.2.3 Strategies to control the position of the two droplet shaped plasmas

In TCV, two different system of actuators can be used to control the vertical position of the conventional single-axis plasma. The slow vertical position control system uses a combination of the external PF coils to produce the desired radial magnetic field to control the vertical position of the plasma. The slow vertical position control system can control vertical instabilities with growth rates up to 1000 s^{-1} because the radial field of the PF coils takes approximately 8 ms to penetrate the vessel walls. Therefore, a fast vertical position control system also exists in TCV, which uses the internal G coils as actuators to control vertical instability growth rates up to 10^4 s^{-1} .

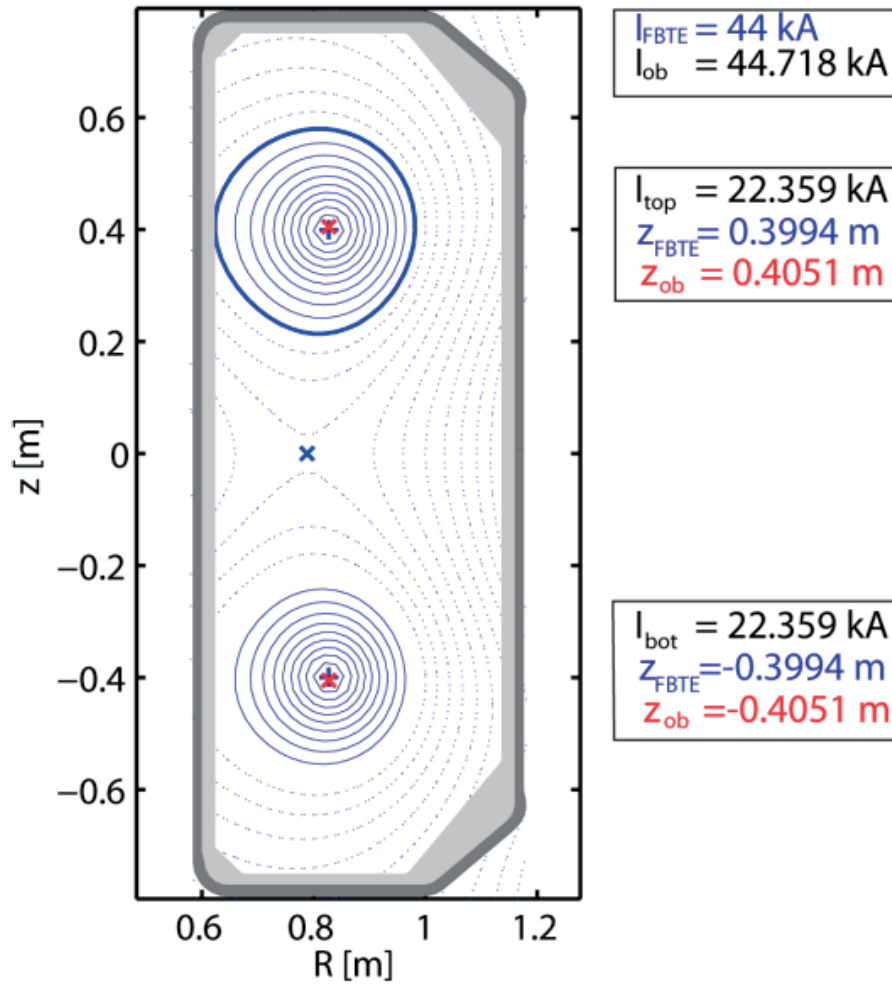


Figure 7.3: Comparison of the programmed plasma current and vertical position with the estimation from the droplet observer. Red crosses denote the vertical position of the two droplet plasmas obtained using vertical position observer, and blue pluses denote the programmed vertical position in FBTE.

The upper and lower G-coils are connected in series and can only control the Q mode. The

S-mode must be controlled with the slow PF coils. Since the S mode has a higher vertical growth rate than the Q mode, the slow PF coils can be used as actuator for the entire vertical position control of this plasma configuration. Similar to the single-axis plasma configuration, the use of proportional-derivative controller to independently control the position of the two droplets was proposed.

Vertical position observer

Two distinct observers are required to independently control the vertical position of the two droplets. The estimates of the vertical position observers are obtained from the magnetic measurements, in the same way as for the plasma current observers (section 7.2.1). For an up-down symmetric plasma configuration, the vertical observers for the two droplets can be defined using eq.(7.5),

$$Z I_P = \begin{bmatrix} Z I_P^{top} \\ Z I_P^{bot} \end{bmatrix} = \begin{bmatrix} (Z^{top} - Z_{ax}^{top}) \cdot I_y^{top} \\ (Z^{bot} - Z_{ax}^{bot}) \cdot I_y^{bot} \end{bmatrix}, \quad (7.16)$$

where Z^{top} denotes the vertical position of the upper plasma filaments, Z_{ax}^{top} denotes the programmed vertical position of the magnetic axis of the upper plasma column, Z^{bot} denotes the vertical position of the lower plasma filaments, and Z_{ax}^{bot} denotes the programmed vertical position of the magnetic axis of the lower plasma column.

The accuracy of the vertical position observers for the two droplet shaped plasmas was estimated using the simulated magnetic measurements for the doublet equilibrium calculated with FBTE. The estimates of the two vertical position observers agree with the vertical position of the magnetic axis in FBTE within $\Delta Z = Z_{FBTE} - Z_{obs} \sim 6$ mm (figure 7.3). These vertical observers were implemented in the Matlab version of the MGAMS code.

Droplet configuration radial position observer

The radial position observer for the two droplets was constructed in the same way as for the single-axis plasma configuration (section 5.1) by choosing the paired flux loops and magnetic probes corresponding to the radial position of the two plasma columns,

$$\begin{aligned} \Delta \psi^{[top,bot]} &= \psi_a^{[top,bot]} - \psi_b^{[top,bot]} \\ &= \left(F_{fa}^{[top,bot]} + 2\pi R_{fa}^{[top,bot]} dR_a B_{ma}^{[top,bot]} \right) - \left(F_{fb}^{[top,bot]} + 2\pi R_{fb}^{[top,bot]} dR_b B_{mb}^{[top,bot]} \right), \end{aligned} \quad (7.17)$$

where $F_{fa}^{[top,bot]}$ and $F_{fb}^{[top,bot]}$ are the flux loop measurements at the HFS and LFS for the two droplets respectively, $R_{fa}^{[top,bot]}$ and $R_{fb}^{[top,bot]}$ denote the radius of the flux loops at the HFS and LFS for the two droplets respectively, $B_{ma}^{[top,bot]}$ and $B_{mb}^{[top,bot]}$ denote the magnetic field probe measurements at the two control points on the HFS and LFS for the two droplets respectively, and dR_a and dR_b are the distances between the magnetic measurements and the control

points on the HFS and LFS of the droplets.

7.2.3.1 Position control system actuators

Combinations of the PF coil currents are used as actuator to independently control the radial and vertical position of the two droplets. The combinations are chosen such that the coupling of the PF coils with the one droplet is maximized and the effect on the other droplet is minimized.

The radial field at the magnetic axis of the two plasma columns needs to be maximized to independently control the vertical position of the two droplet shaped plasmas. Similarly, the vertical field at the magnetic axis of the two plasma columns needs to be maximized to independently control the radial position of the two droplet shaped plasmas.

The radial field for the top plasma is calculated as,

$$B_{R1} = b_{R1a} \bullet I_a, \quad (7.18)$$

where B_{R1} denotes the radial field at the magnetic axis of the top plasma, b_{R1a}^R denotes the Green's functions between the magnetic axis of the top plasma and the PF coils, and I_a denotes the PF coil currents.

The radial field for the bottom plasma is,

$$B_{R2} = b_{R2a} \bullet I_a, \quad (7.19)$$

where B_{R2} denotes the radial field at the magnetic axis of the bottom plasma, b_{R2a} denotes the Green's functions between the magnetic axis of the bottom plasma and the PF coils.

The vertical field for the top plasma is,

$$B_{Z1} = b_{Z1a} \bullet I_a, \quad (7.20)$$

where B_{Z1} denotes the vertical field at the magnetic axis of the top plasma, b_{Z1a} denotes the Green's functions between the magnetic axis of the top plasma and the PF coils.

The vertical field for the bottom plasma is,

$$B_{Z2} = b_{Z2a} \bullet I_a, \quad (7.21)$$

where B_{Z2} denotes the vertical field at the magnetic axis of the bottom plasma, b_{Z2a} denotes the Green's functions between the magnetic axis of the bottom plasma and the PF coils.

Combining equations (7.18)-(7.21) yields,

$$\begin{bmatrix} B_{R1} & 0 & 0 & 0 \\ 0 & B_{R2} & 0 & 0 \\ 0 & 0 & B_{Z1} & 0 \\ 0 & 0 & 0 & B_{Z2} \end{bmatrix} = \begin{bmatrix} b_{R1c} \\ b_{R2c} \\ b_{Z1c} \\ b_{Z2c} \end{bmatrix} \bullet I_a. \quad (7.22)$$

The optimized PF coil current combinations to independently control the radial and vertical position of the two droplet shaped plasma is obtained by solving eq.(7.22). The PF coil combination of F1, F4, F5 and F8, which was previously used by F.Hofmann, was chosen as actuators for the radial and vertical position control of the two droplets.

7.2.4 Stability analysis of the vertical position control for doublet shaped plasma

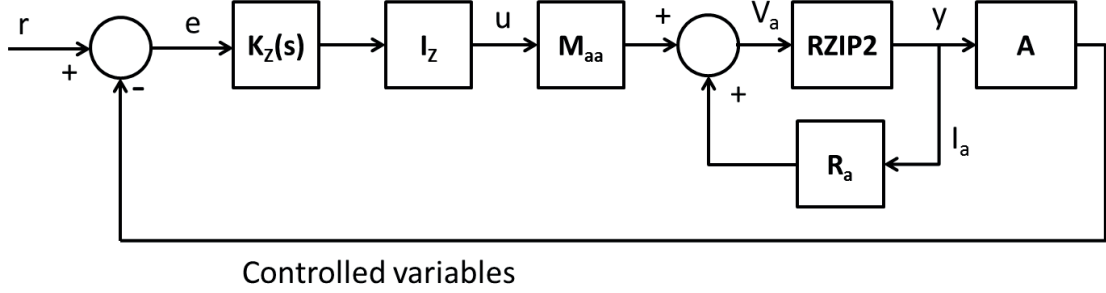


Figure 7.4: Schematic block diagram for the vertical position control system of the two droplet shaped plasma configuration in TCV.

The schematic of the block diagram used to determine the closed loop stability of the vertical position control system for the two droplets in TCV is shown in figure 7.4. In the block diagram, the plant is represented by the RZIP2 model whose inputs are the PF coil voltages (V_a) and the outputs(y) are the magnetic measurements, i.e., poloidal flux loop measurements, magnetic field probe measurements, coil currents and vessel currents. The blocks R_a and M_{aa} take into account the resistive coil voltage compensation and the mutual decoupling of PF coils respectively. The block A denotes the linear combinations of magnetic measurements that can be used to construct the controlled variables, which in this case are the two independent vertical position observers (ZI_P^{top} and ZI_P^{bot}). I_Z is used to select the F coil combinations used for the vertical position control of the two droplets and $K_Z(s)$ denotes the diagonal proportional-derivative controller used to independently control the vertical position of the two droplets. The variable r denotes the references for the vertical position of the two droplets (ZI_{Pref}^{top} and ZI_{Pref}^{bot}). The control law for the system in figure 7.4 can be written as,

$$V_a = M_{aa} I_Z K_Z(s) (r - Ay) + R_a I_a y \quad (7.23)$$

The performance of the vertical position control system for the two droplets was studied to obtain estimates of the proportional and derivative gains required to control the vertical position. The stability of the closed loop system was computed as a function of the proportional gain (G_P) and the derivative gain (G_D) for different plasma equilibria. From the closed loop stability analysis a set of stable gains for G_P and G_D was identified (figure 7.5). Since the stability analysis discussed here, neglects the delay in the power supplies of the PF coils (~ 1 ms), the predictions for the stability domain of the vertical position control system is expected to be smaller and it may not be possible to control high vertical growth rates.

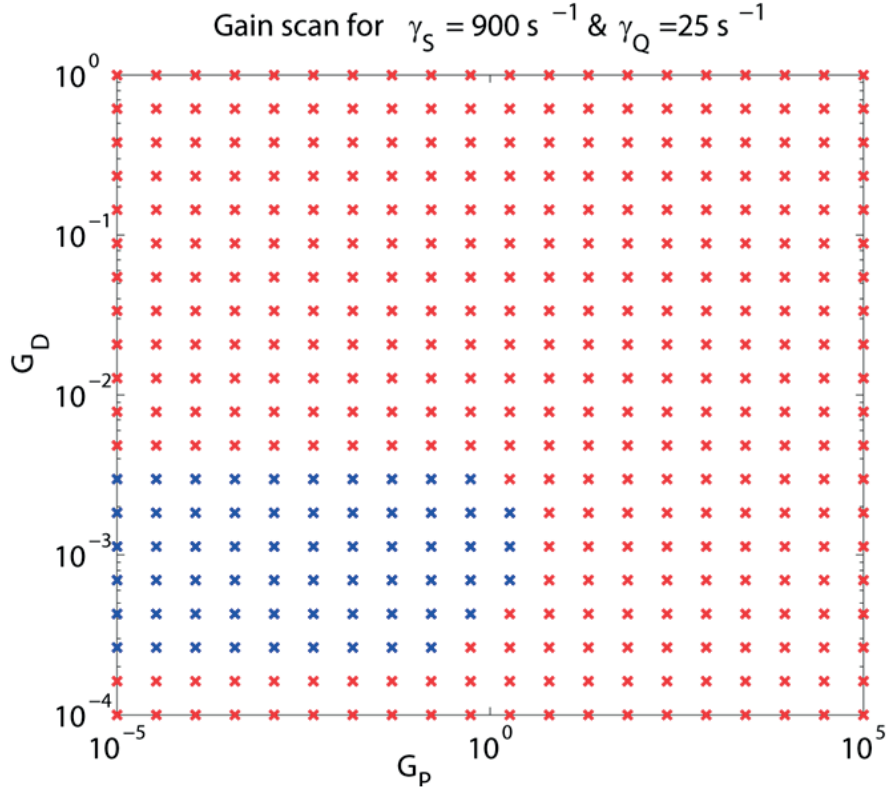


Figure 7.5: Stability of the vertical position control system of the two droplet shaped plasma configuration as a function of the proportional gain (G_P) and derivative gain (G_D). The open loop growth rate of S mode ($\gamma_S = 900 \text{ s}^{-1}$) and that of Q mode ($\gamma_Q = 25 \text{ s}^{-1}$). Vertically unstable (red 'x') and stable (blue 'x').

7.3 Experimental results to create doublet shaped plasma scenario

This section discusses the experimental results obtained for the development of the doublet shaped plasma configuration in TCV. Section 7.3.1 discusses the experimental results in the breakdown phase. Section 7.3.2 discusses the experimental results in the ramp-up phase obtained in Ohmic heated only plasmas. The plasma current is in feed forward phase, while the results of feedback vertical position control are also discussed. Section 7.3.3 discusses the experimental results obtained in the feedback phase after the implementation of ECH plasma current control.

7.3.1 Experimental results in simultaneous double breakdown

With the implemented breakdown scenario (section 7.1), simultaneous double breakdown was achieved using inductive plasma initiation alone. The reconstruction of the poloidal magnetic field distribution shows that the two primary null points at the breakdown time are at $R_{\text{top}}^{\text{exp}} = 0.91 \text{ m}$, $Z_{\text{top}}^{\text{exp}} = 0.31 \text{ m}$ and $R_{\text{bot}}^{\text{exp}} = 0.75 \text{ m}$, $Z_{\text{bot}}^{\text{exp}} = -0.33 \text{ m}$ (figure 7.6 (a)). Compared

to the programmed breakdown scenario at $R_{\text{top,bot}}^{\text{MGAMS}} = 0.83$ m, $Z_{\text{top,bot}}^{\text{MGAMS}} = \pm 0.4$ m, both null points are shifted around 8 cm vertically towards the mid-plane, and 8 cm horizontally with the top null point shifted radially outwards, and the bottom null point shifted radially inwards. The poloidal field value at the intended breakdown positions is approximately 1 mT. This mismatch in experimental and intended null point position is similar to the two new developed single-axis breakdown scenarios at $Z = \pm 0.4$ m discussed in section 6.3, with the same possible reason being the high stray field gradient and low efficiency of coil current back-off. The double breakdown scenario is highly reproducible, and the mismatch in the breakdown positions does not change from shot to shot. The FastCam measurements confirmed that light is emitted from both, the top and bottom parts of the vessel.

Both the experimental and imposed gradients at the top and bottom null points are equal, with $|\nabla B_p|^{\text{exp}} = 0.013$ T/m at the two magnetic null points, and the imposed $|\nabla B_p|^{\text{MGAMS}} = 0.008$ T/m. As discussed in Chapter 4, the equal gradients at both null points are expected to result in a simultaneous breakdown and the same plasma current ramp rate. The simultaneous breakdown time is also indicated by the D_α measurements obtained from the lateral photodiodes (Fig. 7.6). The signals from the photodiodes located at top #3 and bottom #8 ports of the TCV VV are both normalized to the first ionization peak value. The D_α signals both start to increase at the breakdown time $t_b = 1.2$ ms and reach the peak at ~ 3.85 ms, and then drop with the bottom D_α signal decreasing faster than the top one. After the first D_α peak, the two signals start to differ at $t \approx 7$ ms. While the bottom D_α signal increases again and has large fluctuations, the top D_α signal remains nearly constant until $t = 18$ ms, when it slowly starts to drop to zero until the disruption. This indicates that the two plasmas have different features in the burn-through phase.

7.3.2 Experimental results in the ramp-up phase with Ohmic heating

Similar to the discussions for the single-axis plasma formation in Chapter 5, the burn-through and plasma current ramp-up phase are treated together. As a first step, the experimental results with only Ohmic heating are presented. In these experiments neither standard I_p feedback control nor ECH feedback control for I_p was used, however the plasma position feedback control was activated at $t = 10$ ms.

The plasma current and position in the two droplets were estimated with a double filament approach extended from the single filament model discussed in section 5.2.1. The model was only valid from $t \sim 6$ ms when the plasma current in each droplet exceeds approximately 10 kA. The results show that the two droplets exist until $t = 20$ ms with Ohmic heating only. The two droplets have the same I_p ramp rate, as expected from the equal gradients of the two null points, and I_p in each droplet reaches up to 50 kA (Fig. 7.7 (a)). The top plasma current starts to decrease at $t = 18$ ms, which coincides with the decrease in the top D_α signal. Figure 7.7 (b) shows that the vertical position of the two droplets are already shifted towards the mid-plane compared to their breakdown position. The top plasma is initially located at $Z \approx 0.23$ m, and then moves vertically downwards from ~ 8 ms until it merges with the bottom plasma after $t = 20$ ms. The bottom plasma initially moves down to $Z \approx -0.25$ m at $t = 7$ ms, and then the

7.3. Experimental results to create doublet shaped plasma scenario

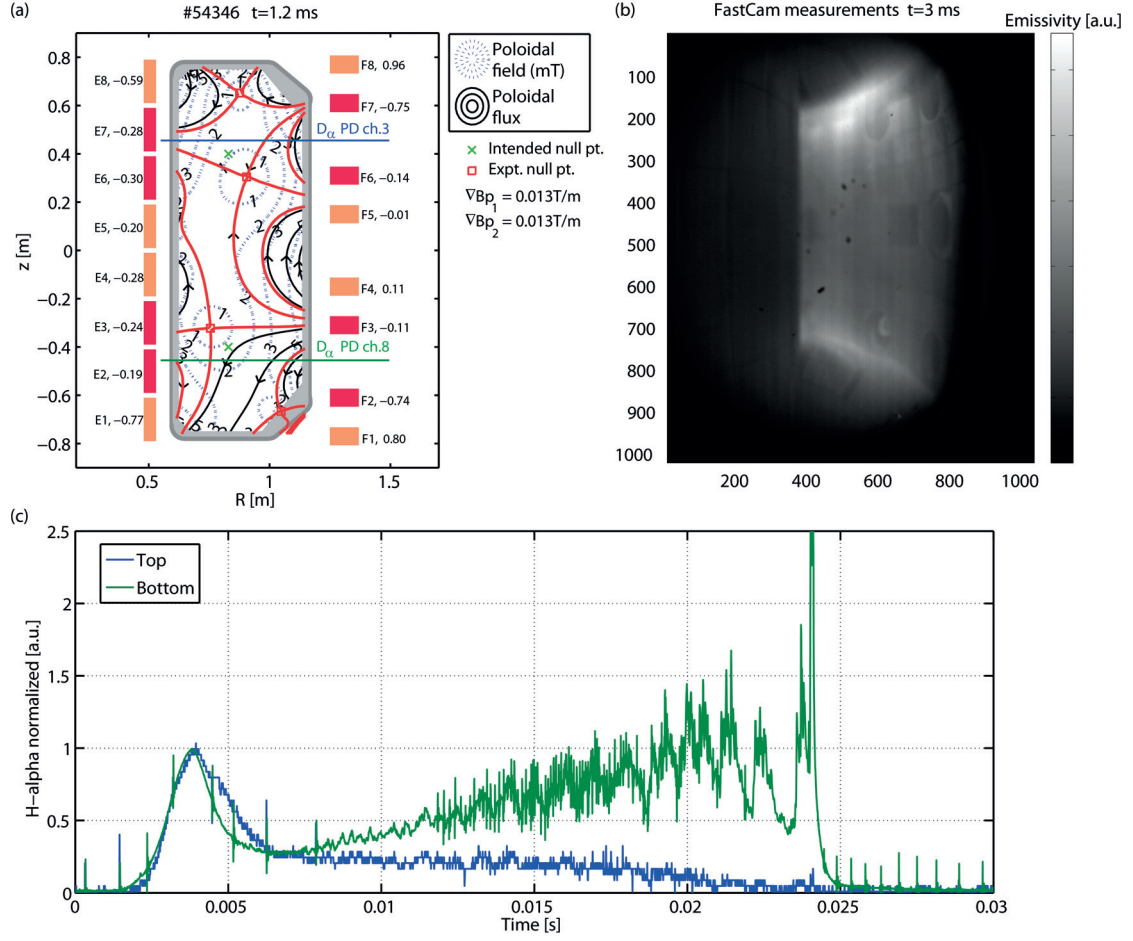


Figure 7.6: (a) Poloidal field magnetic reconstruction obtained using the *breakdown* code, with coil currents in [kA], the quadrupole PF coils (red), and the schematic view of two lateral D_α line-of-sights. (b) FastCam measurements for the double breakdown. (c) D_α measurements obtained from top (blue) and bottom (green) PDs, normalized w.r.t. the ionization peak.

position remains almost unchanged. Figure 7.7 (c) shows that the initial radial position of the top plasma is the same as its breakdown radial position $R = 0.91$ m, while the bottom plasma is at $R = 0.83$ m.

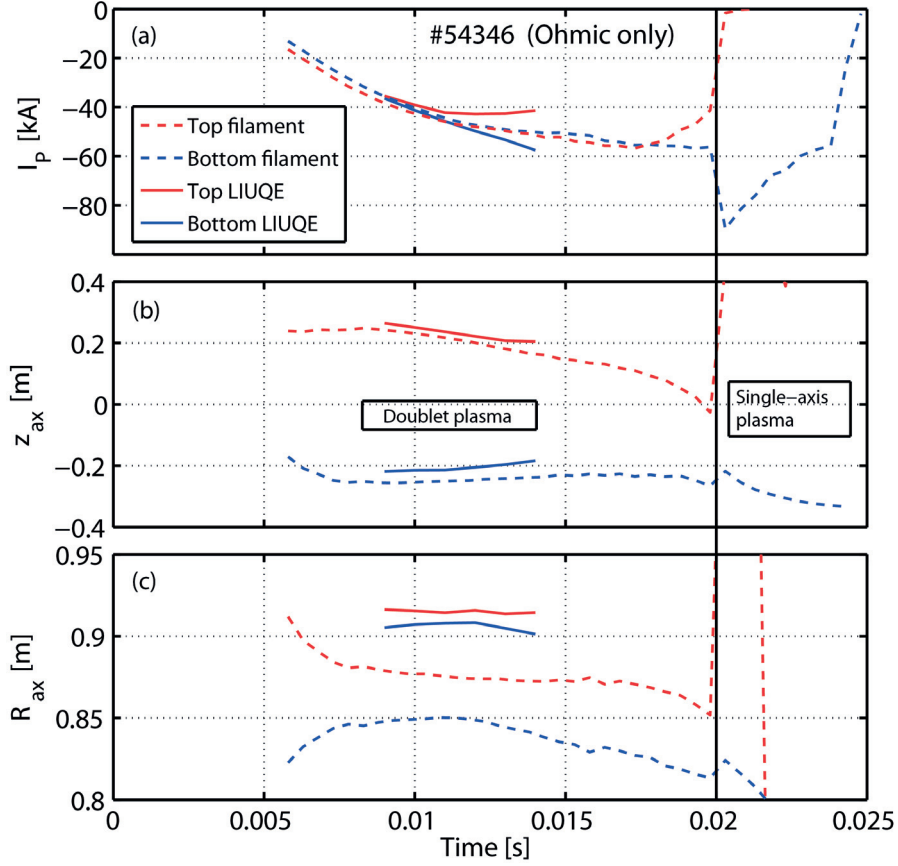


Figure 7.7: (a) Plasma current, (b) vertical position and (c) radial position of the top (red) and bottom (blue) droplet, obtained from a double filament model (dashed) and LIUQE equilibrium reconstruction (solid) in a doublet shaped plasma with Ohmic heating alone. The two droplets converge into one single-axis plasma after $t = 0.02$ s (black line).

The equilibrium reconstruction code LIUQE, which is routinely used to reconstruct TCV configurations, was extended to doublet configurations [58]. In the LIUQE reconstruction for the doublet equilibrium, the pressure was set to zero, which should lead to a systematic radial shift of the plasma, which may be negligible in Ohmic plasmas, and the mantle is assumed to be current-less. The results obtained from LIUQE are available from $t = 9$ to 14 ms, and show the existence of two plasma droplets (Fig. 7.7). The I_p ramp rate obtained from LIUQE for the two droplets are similar at the beginning. While the bottom I_p ramp rate remains nearly constant, the top I_p ramp rate decreases with time and becomes negative at $t = 14$ ms. This results in a large difference of I_p at $t = 14$ ms, with $I_p^{\text{top}} = -41$ kA and $I_p^{\text{bot}} = -58$ kA, which indicates a thermal instability. LIUQE results also show that the magnetic axis of both plasmas are shifting vertically towards each other between $t = 9 - 14$ ms, with the top one shifted 6 cm from $Z = 0.27$ to 0.21 m, and the bottom one shifted from $Z = -0.22$ to -0.18 m. A mismatch in

7.3. Experimental results to create doublet shaped plasma scenario

plasma radial position also exists between LIUQE and the filament model results, that LIUQE results show the magnetic axis of the two plasmas are around $R = 0.91$ m, which is 5 – 7 cm more outside than the results from the filament model.

The temperature and density measurements obtained from the Thomson scattering diagnostic confirm the presence of two plasma droplets (figure 7.8). Because of the relatively low density in the initial phase of plasma formation, the three lasers of the Thomson scattering diagnostic are triggered simultaneously to increase the signal to noise ratio (see section 2.3.4), albeit reducing the time resolution and only allowing measurements at one time point during the 20 ms discharge duration. Because the discharges are highly reproducible, comparison of multiple temperature and density profiles can be achieved by shifting the triggering time in repeat discharges. Figure 7.8 shows that two plasma columns can be observed with high temperature (100 – 200 eV) in each core and low temperature (20 – 50 eV) in the mantle. The Thomson scattering measurements also show the vertical down-shift of the top plasma, with its peak temperature moving from $Z = 0.40$ m at $t = 0.006$ s to $Z = 0.17$ m 11 ms later. At the same time the bottom peak remains approximately at the same vertical position close to $Z = -0.30$ m. The temperature peak of the top plasmas agrees well with LIUQE, whereas the peak of the bottom plasma is somewhat lower. The top plasma is always somewhat cooler than the bottom plasma. Interestingly the density profile is not double peaked like the temperature profile, instead it has a broad peak near the center of the entire plasma. The density peak is tilted towards the bottom at $t = 17$ ms. The peak value of the density profile increases from $4.7 \times 10^{18} \text{ m}^{-3}$ at $t = 6$ ms to $9.7 \times 10^{18} \text{ m}^{-3}$ at $t = 17$ ms.

It can be observed from the filament model, LIUQE and Thomson scattering measurements that the top plasma moves down towards the bottom during the ramp-up and finally merges with the bottom plasma at $t = 20$ ms, even though the plasma position feedback control was activated at $t = 10$ ms. In order to improve the vertical position control, the proportional gain K_p was increased in three discharges from 0.17 to 1.7 beyond which problems in the shot preparation procedure were encountered. No visible effect on the vertical position was observed with any value of K_p . The effectiveness of the coil combination for vertical control was also taken into consideration. The original coil combination [F1,F4,F5,F8] were designed for vertical control with two droplets at $Z = \pm 0.4$ m. However, in experiments the initial vertical position of the two droplets at $t = 10$ ms was at ± 0.23 m, where the original coil combination is less effective. Therefore a new coil combination with [F2,F4,F5,F7] was tested with a same proportional gain scan, but the experiments did not result in an improved position control. Another attempt was made to obtain the double breakdown at $Z = \pm 0.5$ m, so that the vertical separation between the two droplets would be larger when the feedback control system was activated. The $Z = \pm 0.5$ m breakdown could not be controlled well enough to have a simultaneous breakdown, since the stray field gradient is even higher at $Z = \pm 0.5$ m. None of the attempts succeeded in the control the vertical position of the top droplet with Ohmic heating alone.

There are several observations which still remain an open issue and require further investigations. The first one is the reason behind the downward shift of the top droplet. While the S-mode is predicted to be the most unstable mode, section 7.2, the bottom plasma should

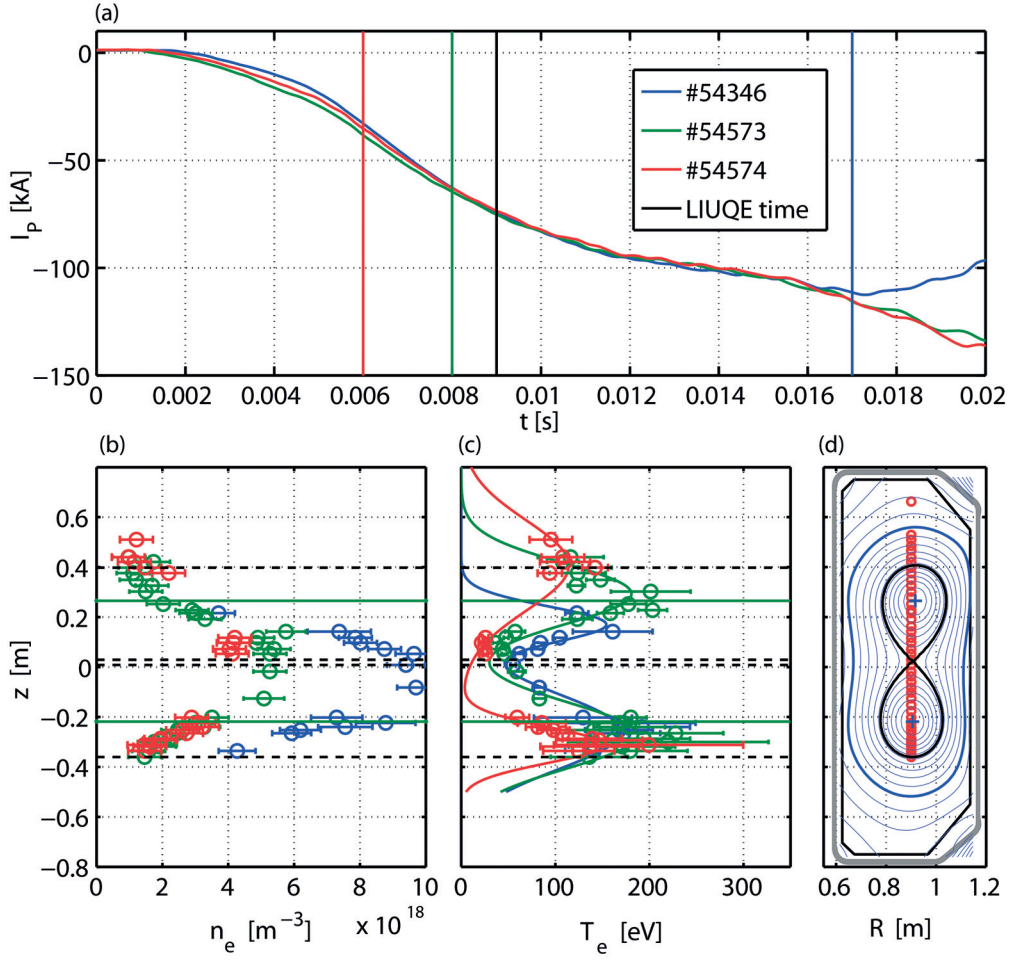


Figure 7.8: (a) Plasma current evolution with time for TCV discharge #54346 (blue), #54573 (green) and #54574 (red) with Thomson measurement at $t = 0.006$, 0.008 and 0.017 s, respectively, and the available LIUQE reconstruction time $t = 0.009$ s. (b) Vertical distribution of electron density and (c) temperature measured by Thomson scattering in the three discharges, with the vertical position of separatrix (black dashed) and two magnetic axis (green solid) at LIUQE time. A double peak Gaussian fitting was made for the temperature measurement for each time. (d) LIUQE reconstruction at $t = 0.009$ s with separatrix (black) and LCFS (blue), as well as Thomson measurement position (red).

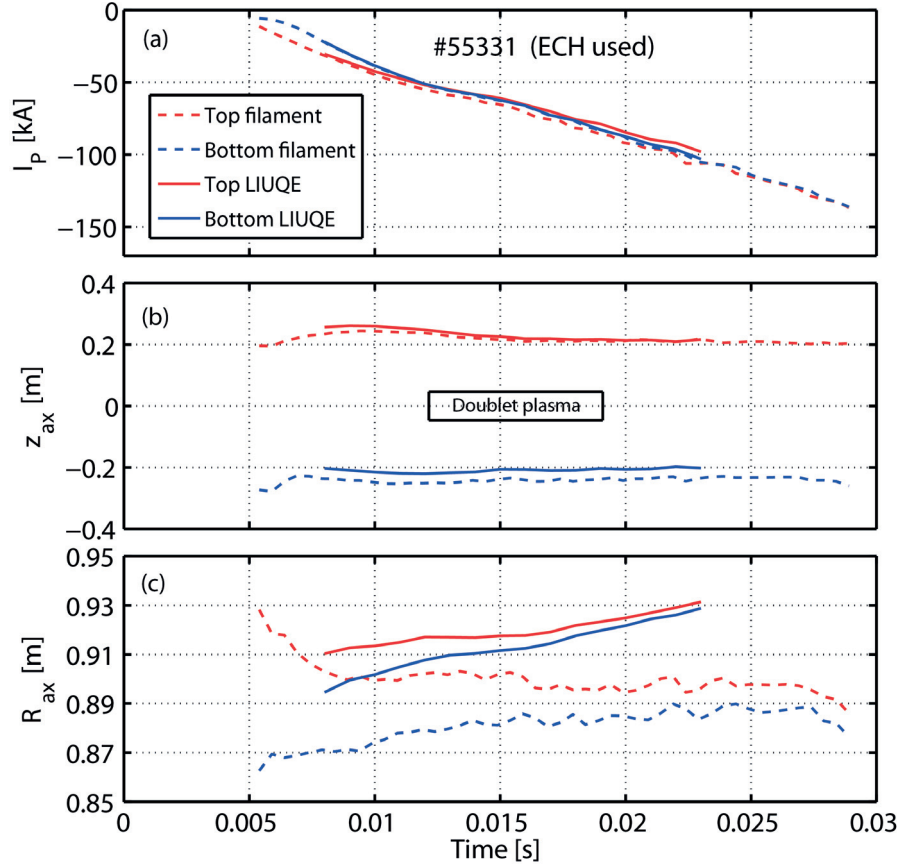


Figure 7.9: (a) plasma current, (b) vertical position and (c) radial position of the top (red) and bottom (blue) droplet, obtained from a double filament model (dashed) and LIUQE equilibrium reconstruction (solid) in a doublet shaped plasma with 900 kW heating the top and 750 kW heating the bottom.

also move towards the top. Secondly, the temperature peaks measured with Thomson scattering are initially further apart than the magnetic axes according to magnetic reconstructions. Finally, the broad density profile with a single maximum indicates that the density is not constant on flux surfaces. The plasma have a high density and low temperature at the middle region of the mantle.

7.3.3 Experimental results in the ramp-up phase with ECH feedback control

The plasma current in each droplet can be ramped up to 50 kA, which has provided the possibility for ECH actuated plasma current control. Experiments were performed to further ramp the plasma current to higher values and ultimately reach the flattop, with the ECH to control the plasma current in each droplet individually. The bump-less transfer control technique was also employed in some discharges. At first, a constant ECH power was used for heating, and multiple discharges with different ECH powers were carried out to study the effect and

establish a basis for feedback control. The experiments showed that it is necessary to apply more ECH power to the top droplet in order to sustain the plasma longer, which is consistent with the LIUQE results from the Ohmic discharge that suggest a lower I_P in the top plasma. With $P_{ECH}^{top} = 900$ kW and $P_{ECH}^{bot} = 750$ kW, both plasmas could be sustained until $t = 30$ ms with I_P in each droplet reaching up to 130 kA according to the double filament model (Fig. 7.9). The plasma current evolution in the two plasmas is almost identical. The vertical position of the top plasma was kept nearly constant at $Z = 0.21$ m and the bottom plasma is at $Z = -0.24$ m. The radial position of both plasmas is approximately $R = 0.89$ m. However, the plasma disrupts before reaching the flattop, even with a 260 kA total current. There are no indications that the two droplets merge prior to the disruption.

The LIUQE reconstructions also show that there is hardly any difference between the plasma currents in the top and bottom plasma. The two plasmas are vertically stable. The magnetic axis of the top plasma shifts from $Z = 0.26$ down to 0.21 m from $t = 10$ to 20 ms, and then stays unchanged. For the bottom plasma it is always around $Z = -0.21$ m. The discrepancy between the radial positions of LIUQE and the filament mode still exists.

The electron temperature and density profiles obtained from the Thomson scattering diagnostic (Fig. 7.10) show that the EC heating increase the core temperature to 1300 eV compared to 200 eV in the Ohmic discharges. At the same time the core density increases from 0.9 to $1.3 \times 10^{19} \text{ m}^{-3}$. Another difference is that the temperature drop at the mid-plane becomes less pronounced. A large temperature gradient can, however, be observed in the vicinity of the separatrix by comparing the Thomson measured temperature profile and the LIUQE reconstruction. The vertical position with a large temperature gradient near the mid-plane does not exactly correspond to the separatrix, this mismatch might be caused by the uncertainties in the equilibrium reconstruction, which could be due to the assumption that no plasma current is present in the mantle region.

The tomographic inversion of the XTOMO measurements also indicate the presence of two distinct regions with higher soft X-ray emissivity. Comparison of the XTOMO inversion with the LIUQE reconstruction shows that the location of highest soft X-ray emissivity agrees well with the magnetic axis of the top plasma droplet (Fig. 7.11). However, there remains a mismatch between the region of the highest soft X-ray emissivity and the reconstructed magnetic axis of the bottom plasma droplet (Fig. 7.11).

One of the most surprising observation in the ECH doublet plasmas is that heating the core of one droplet can also lead to the temperature increase in the other droplet. Figure 7.12 shows the temperature and density profiles as well as the LIUQE equilibrium at $t = 10$ ms for four ECH doublet discharges. The first three discharges are with a total 1200 kW heating power (450 kW in L4 and 750 kW in L1) and the last one is with 900 kW heating power (both 450 kW in L4 and L6). No significant change can be observed in density profiles. The electron temperature profiles of #55645 and #55648 are almost identical, despite that one is heating the top and the other is heating the bottom plasma. The peak temperature is approximately 800 eV and the mantle temperature in the center is $\sim 400 - 450$ eV. In #55658, the ECH is heating the center of the entire plasma. The temperature profile still has the double peaked feature, which confirms that the double peaked temperature profile is indeed due to the doublet mag-

7.3. Experimental results to create doublet shaped plasma scenario

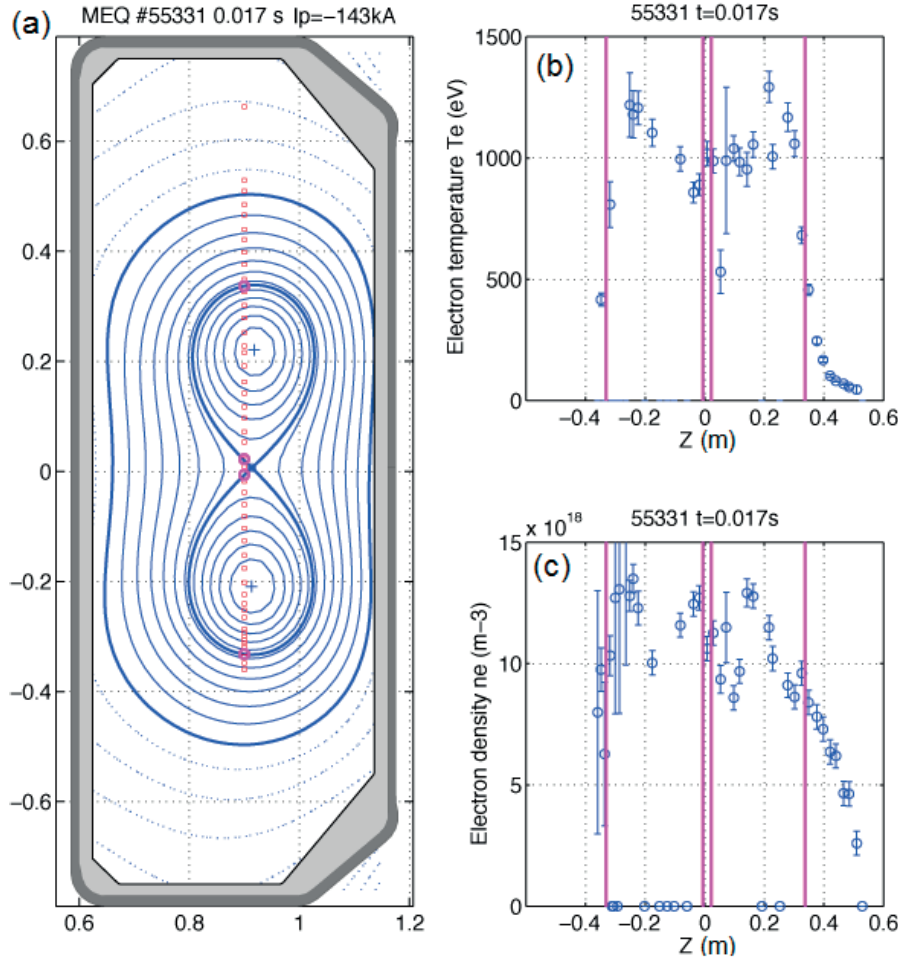


Figure 7.10: Thomson measurements for the doublet shaped plasma configuration with ECRH heating for both plasma. (a) LIUQE equilibrium reconstruction of the doublet shaped plasma showing the Thomson measurement points, (b) temperature profile, and (c) density profile.

netic configuration instead of off-axis heating in a highly-elongated plasma. Interestingly, the temperature profile of the top plasma is almost identical to the previous two discharges with core heating, while the bottom plasma temperature profile extends towards the mid-plane, although the heating is actually applied with a small angle ($\theta = 10^\circ$) towards the top. If the ECH is applied to the edge of the separatrix on the top (#55582), the heating is inefficient and results in a much lower temperature profile. The peak temperature is only ~ 400 eV while the center mantle temperature is ~ 200 eV, i.e., the peak temperature only doubled from the Ohmic plasma with 900 kW heating applied, and is only half compared to the case of core heating.

The observation that heating one droplet would lead to equal temperature increase in the other one, suggests that the transport barrier is located outside the separatrix, while rapid transport along the separatrix leads to a good power sharing among the droplets. As a consequence, ECH is not an effective tool to control the plasma current in the two droplets independently. This

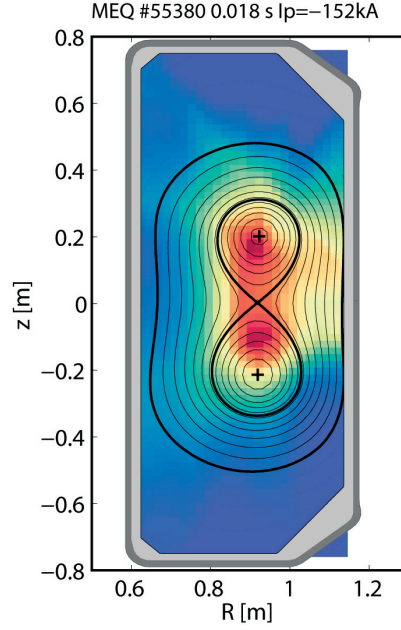


Figure 7.11: Tomographic inversion of XTOMO measurements for a doublet shaped plasma discharge in TCV.

observation, as well as the different shape of the density and temperature profiles, indicate that a fundamental difference might exist between a doublet and a single-axis plasma on the heat and particle confinement and transport. Further experimental investigations and modeling are required to understand these observations.

7.4 Conclusion

To obtain a simultaneous breakdown at two locations inside the TCV VV by using only inductive plasma start-up, modifications were proposed in the MGAMS breakdown preparation. The reconstruction of the poloidal magnetic field obtained from the *breakdown* code shows that simultaneous breakdown occurs at two locations inside the TCV VV, with around 8 cm position mismatch in both radial and vertical directions. Clear indications of a simultaneous double breakdown are also seen in FastCam and D_α measurements. The breakdown is highly reproducible, and the two null points have the same gradient.

An RZIP2 model was used to model the plasma response of the doublet shaped plasma configuration. Strategies were proposed to independently control the plasma current and plasma radial and vertical position of the two droplets. A stability analysis of the vertical position control system was performed using the RZIP2 model to estimate the proportional and derivative gains.

The experimental results obtained for the development of the doublet shaped plasma scenario shows the existence of two vertically separated plasma droplets in TCV. With Ohmic heating

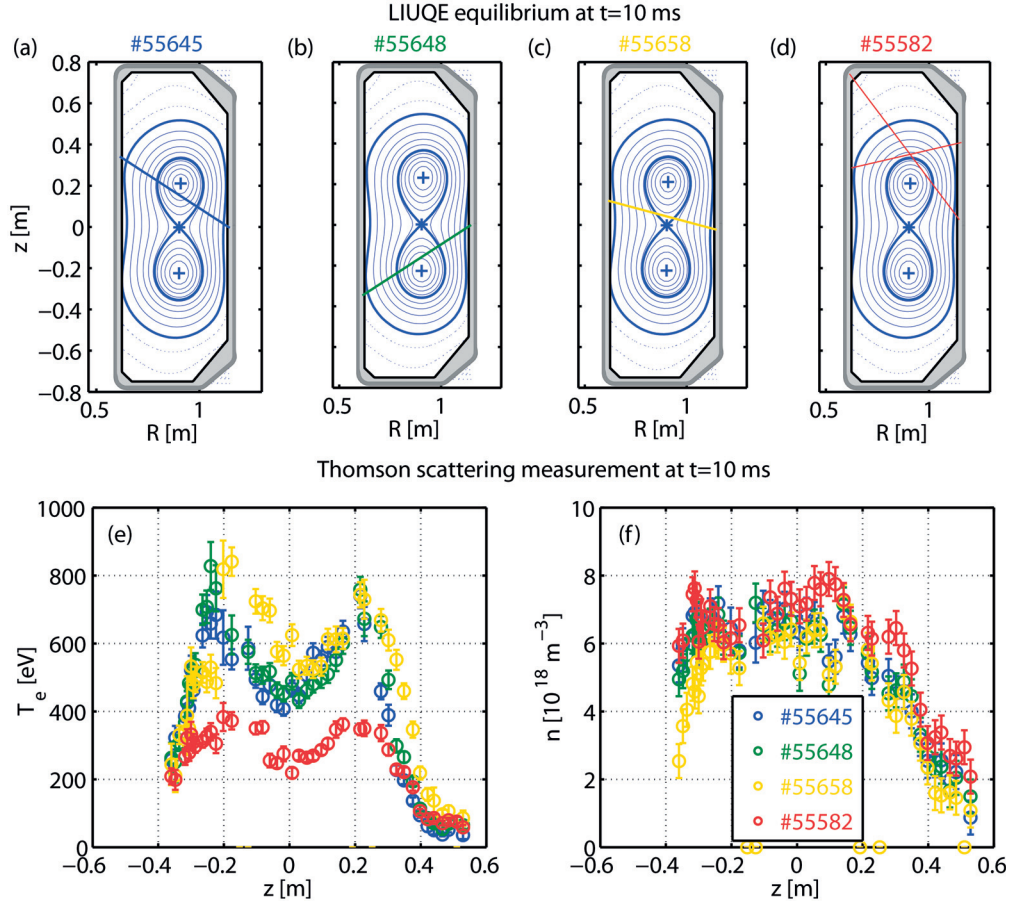


Figure 7.12: LIUQE reconstructed equilibrium of doublet discharge (a) #55645 with ECH heating top plasma core, (b) #55648 with ECH heating bottom plasma core, (c) #55658 with ECH heating center mantle, (a) #55582 with ECH heating top mantle. The first three discharge are heated from two ECH launchers from the mid-plane, the fourth one uses one launcher from mid-plane and the other from $Z = 0.4$ m. Vertical profile of (d) electron temperature and (e) density measured by Thomson scattering system in these discharges.

only, a current of 50 kA could be obtained in each of the two plasma droplets for 20 ms. However, the filament models for the doublet shaped plasma scenario, shows that the top plasma starts to move vertically downwards and merges with the bottom plasma after $t = 20$ ms. The downward shift of the top plasma is also observed from temperature profiles obtained from the Thomson scattering measurements. The vertical temperature profile is double peaked with peak temperature up to 200 eV. A discrepancy exists between the double filament model and LIUQE reconstruction, that I_p in the two plasmas is estimated to be the same by the former and different by the latter, which may induce the thermal instability. Several attempts including increasing the proportional gain, modification of control coil combination and plasma breakdown location to control the vertical shift of the top plasma proved to be unsuccessful.

Experiments showed that the use of ECRH power to heat the two plasma droplets, allowed to extend the current ramp with the current in each droplet reaching up to 130 kA. Also the temperature profiles obtained from Thomson measurements, showed a higher temperature (up to 1.3 keV) in plasma discharges with ECRH heating than in discharges with Ohmic heating alone. ECRH heating leads to strong temperature gradients in the vicinity of the separatrix. The tomographic inversion of the XTOMO measurements also confirms the presence of two distinct regions with higher soft X-ray emissivity. Both the double filament model and LIUQE reconstruction show that the two plasmas have the same current and their vertical position keep nearly unchanged with the ECH. However, the discharges disrupted before reaching the flattop, the reason remain an open issue.

One of the most surprising observation is that the ECRH heating of one plasma resulted in an equal increase of the temperature in both plasma droplets. This suggests that a transport barrier may be located outside the separatrix. As a consequence ECRH is not an effective tool to control the current sharing between the droplets. One possible solution is to use ECCD as the actuator for plasma current control, which has been attempted in the final stage of the experiment but needs to be further investigated.

8 Conclusion

In this thesis, the TCV single-axis plasma formation scenarios were studied to develop a better understanding of their dynamics and identify potential issues associated with the breakdown, burn-through and plasma current ramp-up phases. Understandings gained through the analysis were used to program a reliable and smooth plasma formation at several positions within the TCV vessel, and then to revisit the formation of the doublet plasma formation. A successful simultaneous double breakdown, burn-through and ramp-up of the plasma current in the two droplets was achieved in TCV.

As a first step, a database of key parameters that characterize the plasma formation scenarios for almost 20000 TCV discharge attempts was created. The database shows that 15% of the plasma formation attempts in TCV failed during the burn-through phase, whereas only 0.5% discharges failed to breakdown. Most of the failed breakdowns were caused by technical issues, such as the absence of injection of neutral gas, the absence of a toroidal electric field, the absence of toroidal magnetic field, or problems with the hardware and/or software of TCV plasma control system. The implementation of plasma formation is, therefore, separated into two parts, with one effort aiming at correcting the location where the gas breaks down, and another effort at an improved reliability of plasma formation in the burn-through and plasma current ramp-up phase.

In the breakdown phase, a large mismatch between the intended and experimental breakdown position was observed for the $Z = 0.05$ and the $Z = 0.23$ m standard vertical breakdown positions, and for both I_P and B_ϕ directions. This mismatch was caused by an additional poloidal field mainly due to errors in the back-off of the stray field generated by vessel currents. The use of a nominal vessel resistivity assuming axisymmetry in MGAMS to model the vessel currents was identified as the main reason for the mismatch in the breakdown positions. Correction of the breakdown position was important to obtain a better agreement between the entire programmed and experimental magnetic field configuration, and thereby, provide a better control of the breakdown time and plasma current ramp rate. Experiments showed that the vertical deviation can be reduced empirically by imposing the negative of the experimentally observed additional field at the two quadrupole control points, to compensate the additional field. The use of breakdown parameters to control the breakdown time and initial plasma

current ramp rate was verified in experiments. The results show that increasing the imposed gradient in MGAMS leads to delayed breakdown and a lower current ramp rate; a neutral gas pressure operational window was observed, that too high and too low pressure both result in delayed breakdown and a too low plasma current ramp rate to successfully burn-through; increase of the loop voltage leads to a earlier breakdown time and a higher plasma current ramp rate. These observations are consistent with the Townsend model and the time evolution of the experimental gradient of the null point.

Analysis of TCV experiments shows that the initial plasma current ramp rate plays an important role in the plasma formation. A too low plasma current ramp rate can cause insufficient Ohmic heating and failure in plasma formation. With a high plasma current ramp rate, a mismatch between the experimental and reference current can be observed, the higher experimental plasma current also causes a higher radial hoop force than the balance force from the programmed external vertical field and leads to the plasma shifting outwards from the inner wall, and also MHD activity is observed. This mismatch then enters the feedback control system as a large error signal when the feedback control is activated, causes strong oscillations of the plasma current and the radial position. When this oscillation is too strong, the plasma current becomes too low to provide sufficient Ohmic heating. The insufficient Ohmic heating and/or the decreased cross section and hence a higher resistivity as well as increased confinement loss when the plasma is pushed into the inner wall, can also cause failure in plasma formation. Experiments showed that it is efficient to control the plasma current ramp rate and thus prevent the problem by breakdown parameters, such as imposed gradients and loop voltage, however the method risks to decrease the operational range for successful breakdowns. Other experiments took the approach to reduce the plasma current and position oscillation by modifications in the control system, such as early I_P control and the bump-less transfer control technique. The experiments verified that the origin of the MHD activities is the initial high plasma current ramp rate instead of the dI_P/dt reversal. The results showed that strong oscillations for the I_P and radial position control can be avoided with the bump-less transfer control technique to provide reliable and sufficient Ohmic heating, which results in successful plasma formation despite a high plasma current ramp rate and MHD activities. In addition, experiments show that increased reference plasma current ramp rate can reduce the experimental ramp rate by limiting the radial position of the plasma close to inner wall, without changing breakdown parameters. With an appropriate reference I_P ramp rate, this method can be used with the bump-less control technique simultaneously to improve the plasma current ramp-up scenario in TCV.

Understanding gained through the analysis of the breakdown phase and of the burn-through and formation phase was combined to implement the standard plasma formation scenarios in TCV. The implementation include corrections of the mismatch in breakdown position by using experimental vessel resistivity to model the vessel currents in MGAMS and using back-off coils to cancel the stray field generated by currents in TF bus bars, also modification in the time evolution of applied quadrupole and equilibrium fields to prevent an early breakdown before $t < 0$ s and to extend the operational range for breakdown to occur. The bump-less transfer control technique and modifications of reference I_P ramp rate are employed to have a smooth

and reliable burn-through and ramp-up phase. Experiments proved that for all three standard breakdown positions the mismatch between the intended and experimental obtained vertical position was reduced to ≤ 0.03 m, and a wider operational range of breakdown parameters for breakdown time and ramp rate control was obtained. The improvements were also applied to create two new scenarios at the top ($Z = 0.4$ m) and bottom part ($Z = -0.4$ m) of the vessel in preparation of the creation of doublet shaped plasma.

The second part of this thesis focuses on developing a doublet shaped plasma configuration. The doublet is a highly unconventional plasma configuration, which was researched in the 1970s but that research was abandoned due to difficulties to control the configuration. TCV's modern and unique shaping capabilities warrant an effort to revisit the configuration. A successful and highly reproducible simultaneous double breakdown at two locations in TCV was achieved and verified by FastCam and D_α measurements. The similar magnetic properties of the two magnetic null points ensured that the plasma current ramp rate in the two droplets were close and the plasma currents in both droplets was ramped up to 50 kA each with Ohmic heating alone. The vertical temperature profile measured by Thomson scattering diagnostic is double peaked with high peak temperature up to 200 eV and low mantle temperature at 20 – 50 eV at both the center and the edge. Surprisingly the density profile is single-peaked in the center. The top plasma was observed to always move vertically downwards and merges with the bottom plasma after $t = 20$ ms. Several attempts were made to control the vertical shift of the top plasma, however were not successful in Ohmic discharges. The use of ECRH power to heat the two plasma droplets, resulted in an increase in the I_p (up to 130 kA each), electron temperature (up to 1.3 keV in the two cores), and stabilized the vertical shift of the top plasma. The ECRH heating also leads to strong temperature gradients in the vicinity of the separatrix. However, the discharges disrupted before reaching the flattop, and the reason remained an open issue. In order to prolong the plasma duration, attempts were made to use of ECH as an actuator to control the two currents independently. One of the most surprising observation is that the ECRH heating of one plasma resulted in an equal increase of the temperature in both plasma droplets. This suggest that the transport barrier is located outside the separatrix. As a consequence ECRH is not an effective tool to control the current sharing between the droplets. One possible solution is to use ECCD as the actuator for plasma current control, which has been attempted in the final stage of the experiment but needs to be further investigated. These experimental results indicate that a fundamental difference might exist between a doublet and a single-axis plasma on the heat and particle confinement and transport. Although a stationary doublet regime was not yet achieved, the basis for further experimental investigations to understand the physics of doublets was established.

A Appendix

The RZIP2 model was developed by EPiras [68] and was re-derived in this thesis with minor modifications which will be discussed here. This model includes the circuit equations for the PF coils, the vessel current, the two plasma currents, and also the radial and vertical force balance equations for the two plasma columns. Spatially dependent quantities are obtained by averaging over the plasma current distribution derived from a doublet equilibrium calculated with the FBTE code,

$$\langle A \rangle = \frac{\sum_i A(R_i, Z_i) j_\varphi(R_i, Z_i)}{\sum_i j_\varphi(R_i, Z_i)}, \quad (\text{A.1})$$

where A is the considered parameter of interest, j_φ is the plasma current density distribution, R_i and Z_i are the radial and vertical co-ordinates.

The top droplet is denoted as plasma 1 and the bottom droplet as plasma 2.

The vessel current can be obtained by taking into account the electromagnetic interaction that occurs among the vessel filaments, the two plasma droplets and the active coils and modeled as,

$$M_{vv} \dot{I}_v + R_v I_v + M_{va} \dot{I}_a + \frac{d}{dt} (M_{vp1} I_{p1}) + \frac{d}{dt} (M_{vp2} I_{p2}) = 0, \quad (\text{A.2})$$

where R_v denotes the vessel resistance, M_{va} denotes the Green's functions between the vessel filaments and the active coils. The values of R_v and M_{va} are assumed to be time independent since the position of the vessel filaments and the coil currents remains static. The matrix M_{vp1} denotes the Green's functions between the vessel filaments and the top plasma current, M_{vp2} the Green's functions between the vessel filaments and the bottom plasma, I_{p1} denotes the plasma current at the top and I_{p2} denotes the plasma current at the bottom. Both M_{vp1} and M_{vp2} can change with time due to the rigid movement of the droplets in both radial as well as vertical direction.

Similarly, the circuit equation for the active coils is,

$$M_{aa} \dot{I}_a + R_a I_a + M_{av} \dot{I}_v + \frac{d}{dt} (M_{ap1} I_{p1}) + \frac{d}{dt} (M_{ap2} I_{p2}) = V_a, \quad (\text{A.3})$$

Appendix A. Appendix

where R_a denotes the active coil resistances, V_a denotes the active coil voltages, M_{aa} denotes the Green's functions between the active coils, M_{ap1} denotes the Green's functions between the active coils and plasma 1, M_{ap2} denotes the Green's functions between the active coils and plasma 2.

The circuit equation of plasma 1 can be expressed as,

$$\frac{d}{dt}(L_{p1}I_{p1}) + \frac{d}{dt}(M_{p1a}I_a) + \frac{d}{dt}(M_{p1v}I_v) + \frac{d}{dt}(M_{p1p2}I_{p2}) + R_{p1}I_{p1} = 0, \quad (\text{A.4})$$

where R_{p1} denotes the plasma resistance of plasma 1, L_{p1} is the self-inductance of plasma 1, M_{p1p2} denotes the Green's functions between the two plasma droplets, M_{p1a} denotes the Green's functions between the plasma 1 and the active coils, M_{p1v} denotes the Green's functions between the plasma 1 and the vessel filaments.

Similarly, the circuit equation of the plasma 2 can be modeled as,

$$\frac{d}{dt}(L_{p2}I_{p2}) + \frac{d}{dt}(M_{p2a}I_a) + \frac{d}{dt}(M_{p2v}I_v) + \frac{d}{dt}(M_{p2p1}I_{p1}) + R_{p2}I_{p2} = 0 \quad (\text{A.5})$$

where, R_{p2} denotes the plasma resistance of plasma 2, L_{p2} is the self-inductance of plasma 2, M_{p2a} denotes the Green's functions between the plasma 2 and the active coils, M_{p2v} denotes the Green's functions between the plasma 2 and the vessel filaments.

In this model, the vertical force balance for the two droplet plasmas is considered separately. The vertical force balance for the plasma 1 can be expressed as,

$$m_{p1} \frac{d^2 Z_1}{dt^2} = \sum F_{z1} = -2\pi R_1 I_{p1} B_{r1}(R_1, Z_1, I_a, I_v, I_{p2}) \quad (\text{A.6})$$

where, m_{p1} denotes the inertia of the plasma 1, R_1 denotes the magnetic axis of plasma 1, B_{r1} denotes the radial field produced by the active coils, vessel current and I_{p2} . Due to the low inertia of the plasma, the term in the L.H.S of eq. A.6 is neglected. The time derivative of eq.(A.6) can be written as,

$$0 = \frac{d}{dt} [-2\pi R_1 I_{p1} B_{r1}(R_1, z_1, I_a, I_v, I_{p2})] \quad (\text{A.7})$$

Similarly, the time derivative of the vertical force balance for the plasma 2 can be expressed as,

$$0 = \frac{d}{dt} [-2\pi R_2 I_{p2} B_{r2}(R_2, Z_2, I_a, I_v, I_{p1})] \quad (\text{A.8})$$

where, R_2 denotes the major radius of plasma B_{r2} denotes the radial field produced by the active coils, vessel current and the I_{p1} .

The radial force balance consists of two components:(i) the Lorentz force acting on the plasma due to the vertical magnetic field and (ii) the hoop force generated by the plasma geometry and plasma pressure. The radial force balance for the plasma 1 can be written as,

$$M_{p1} \frac{d^2 R_1}{dt^2} = \sum F_{R1} = \frac{\mu_0}{2} I_{p1}^2 \Gamma_1(R_1, t) + 2\pi R_1 I_{p1} B_{z1}(R_1, Z_1, I_a, I_v, I_{p2}) \quad (\text{A.9})$$

where, $\Gamma_1 = \ln(8R_{01}/a_1\sqrt{\kappa_1}) + \beta_{p1} + l_{i1}/2 - 1.5$, B_{z1} denotes the vertical field produced by the active coils, vessel current and I_{p2} .

Again assuming that the inertia term is zero, the time derivative of eq.(A.9), can be written as,

$$0 = \frac{d}{dt} \left[\frac{\mu_0}{2} I_{p1}^2 \Gamma_1 \right] + \frac{d}{dt} [2\pi R_1 I_{p1} B_{z1}(R_1, Z_1, I_a, I_v, I_{p2})] \quad (\text{A.10})$$

The time derivative of the radial force balance for the plasma 2 can be written as,

$$0 = \frac{d}{dt} \left[\frac{\mu_0}{2} I_{p2}^2 \Gamma_2 \right] + \frac{d}{dt} [2\pi R_2 I_{p2} B_{z2}(R_2, Z_2, I_a, I_v, I_{p1})] \quad (\text{A.11})$$

where, $\Gamma_2 = \ln(8R_{02}/a_2\sqrt{\kappa_2}) + \beta_{p2} + l_{i2}/2 - 1.5$, B_{z2} denotes the vertical field produced by the active coils, vessel current and I_{p1} .

The above set of equations are linearized around an equilibrium point, i.e. $I_a = I_{a0} + \delta I_a$, $I_v = I_{v0} + \delta I_v$, $I_{p1} = I_{p01} + \delta I_{p1}$, $I_{p2} = I_{p02} + \delta I_{p2}$, $R_1 = R_{01} + \delta R_1$, $R_2 = R_{02} + \delta R_2$, $Z_1 = Z_{01} + \delta Z_1$, $Z_2 = Z_{02} + \delta Z_2$, and the linearized system of equations are described below.

The linearized vessel circuit equation after neglecting the zero order terms,

$$\begin{aligned} & M_{vv}\delta\dot{I}_v + R_v\delta I_v + \frac{\partial M_{vp1}}{\partial R_1}\delta\dot{R}_1 I_{p01} + \frac{\partial M_{vp2}}{\partial R_2}\delta\dot{R}_2 I_{p02} \\ & + \frac{\partial M_{vp1}}{\partial Z_1}\delta\dot{Z}_1 I_{p01} + \frac{\partial M_{vp2}}{\partial Z_2}\delta\dot{Z}_2 I_{p02} + M_{va}\delta\dot{I}_a + M_{vp10}\delta\dot{I}_{p1} + M_{vp20}\delta\dot{I}_{p2} = 0 \end{aligned} \quad (\text{A.12})$$

Similarly, the linearized circuit equation for the active coils becomes,

$$\begin{aligned} & M_{aa}\delta\dot{I}_a + R_a\delta I_a + \frac{\partial M_{ap1}}{\partial R_1}\delta\dot{R}_1 I_{p01} + \frac{\partial M_{ap2}}{\partial R_2}\delta\dot{R}_2 I_{p02} \\ & + \frac{\partial M_{ap1}}{\partial Z_1}\delta\dot{Z}_1 I_{p01} + \frac{\partial M_{ap2}}{\partial Z_2}\delta\dot{Z}_2 I_{p02} + M_{av}\delta\dot{I}_v + M_{ap10}\delta\dot{I}_{p1} + M_{ap20}\delta\dot{I}_{p2} = \delta V_a \end{aligned} \quad (\text{A.13})$$

The linearized circuit equation for plasma 1 becomes,

$$\begin{aligned} & L_{p01}\delta\dot{I}_{p1} + \frac{dL_{p1}}{dR_1}\delta\dot{R}_1 I_{p01} + 2\pi R_{01} B_{z01}\delta\dot{R}_1 + M_{p1a}\delta\dot{I}_a + M_{p1v}\delta\dot{I}_v + M_{p1p2}\delta\dot{I}_{p2} \\ & + \frac{\partial M_{p1p2}}{\partial R_2}\delta\dot{R}_2 I_{p02} + \frac{\partial M_{p1p2}}{\partial Z_2}\delta\dot{Z}_2 I_{p02} + R_{p1}\delta I_{p1} = 0 \end{aligned} \quad (\text{A.14})$$

The linearized circuit equation for plasma 2 becomes,

$$\begin{aligned} & L_{p02}\delta\dot{I}_{p2} + \frac{dL_{p2}}{dR_2}\delta\dot{R}_2 I_{p02} + 2\pi R_{02} B_{z02}\delta\dot{R}_2 + M_{p2a}\delta\dot{I}_a + M_{p2v}\delta\dot{I}_v + M_{p2p1}\delta\dot{I}_{p1} \\ & + \frac{\partial M_{p2p1}}{\partial R_1}\delta\dot{R}_1 I_{p01} + \frac{\partial M_{p2p1}}{\partial Z_1}\delta\dot{Z}_1 I_{p01} + R_{p2}\delta I_{p2} = 0 \end{aligned} \quad (\text{A.15})$$

Appendix A. Appendix

The linearized time derivative of the vertical force balance for plasma 1,

$$\begin{aligned} & -2\pi R_{01} I_{p01} \left(\frac{\partial B_{R1}}{\partial Z_1} \delta \dot{Z}_1 + \frac{\partial B_{R1}}{\partial R_1} \delta \dot{R}_1 - \frac{1}{2\pi R_{01}} \frac{\partial M_{p1a}}{\partial Z_1} \delta \dot{I}_a - \frac{1}{2\pi R_{01}} \frac{\partial M_{p1v}}{\partial Z_1} \delta \dot{I}_v \right. \\ & \left. - \frac{1}{2\pi R_{01}} \frac{\partial M_{p1p2}}{\partial Z_1} \delta \dot{I}_{p2} \right) = 0 \end{aligned} \quad (\text{A.16})$$

The linearized time derivative of the vertical force balance for plasma 2,

$$\begin{aligned} & -2\pi R_{02} I_{p02} \left(\frac{\partial B_{R2}}{\partial Z_2} \delta \dot{Z}_2 + \frac{\partial B_{R2}}{\partial R_2} \delta \dot{R}_2 - \frac{1}{2\pi R_{02}} \frac{\partial M_{p2a}}{\partial Z_2} \delta \dot{I}_a - \frac{1}{2\pi R_{02}} \frac{\partial M_{p2v}}{\partial Z_2} \delta \dot{I}_v \right. \\ & \left. - \frac{1}{2\pi R_{02}} \frac{\partial M_{p2p1}}{\partial Z_2} \delta \dot{I}_{p1} \right) = 0 \end{aligned} \quad (\text{A.17})$$

The linearized time derivative of the radial force balance for plasma 1,

$$\begin{aligned} & 2\pi \left[\delta \dot{R}_1 I_{p01} B_{z01} + R_{01} \delta \dot{I}_{p1} B_{z01} + R_{01} I_{p01} \left(\frac{1}{2\pi R_{01}} \frac{\partial M_{p1s}}{\partial R_1} \delta \dot{I}_a + \frac{1}{2\pi R_{01}} \frac{\partial M_{p1v}}{\partial R_1} \delta \dot{I}_v \right. \right. \\ & \left. \left. + \frac{1}{2\pi R_{01}} \frac{\partial M_{p1p2}}{\partial R_1} \delta \dot{I}_{p2} + \frac{\partial B_{z1}}{\partial R_1} \delta \dot{R}_1 + \frac{\partial B_{z1}}{\partial Z_1} \delta \dot{Z}_1 \right) \right] + \mu_0 I_{p01} \Gamma_{01} \delta \dot{I}_{p1} + \frac{\mu_0}{2R_{01}} I_{p01}^2 \delta \dot{R}_1 \\ & = -\frac{\mu_0}{2} I_{p01}^2 \delta \dot{\Gamma}_1 \end{aligned} \quad (\text{A.18})$$

The linearized time derivative of the radial force balance for plasma 2,

$$\begin{aligned} & 2\pi \left[\delta \dot{R}_2 I_{p02} B_{z02} + R_{02} \delta \dot{I}_{p2} B_{z02} + R_{02} I_{p02} \left(\frac{1}{2\pi R_{02}} \frac{\partial M_{p2a}}{\partial R_2} \delta \dot{I}_a + \frac{1}{2\pi R_{02}} \frac{\partial M_{p2v}}{\partial R_2} \delta \dot{I}_v \right. \right. \\ & \left. \left. + \frac{1}{2\pi R_{02}} \frac{\partial M_{p2p1}}{\partial R_2} \delta \dot{I}_{p1} + \frac{\partial B_{z2}}{\partial R_2} \delta \dot{R}_2 + \frac{\partial B_{z2}}{\partial Z_2} \delta \dot{Z}_2 \right) \right] + \mu_0 I_{p02} \Gamma_{02} \delta \dot{I}_{p2} + \frac{\mu_0}{2R_{02}} I_{p02}^2 \delta \dot{R}_2 \\ & = -\frac{\mu_0}{2} I_{p02}^2 \delta \dot{\Gamma}_2 \end{aligned} \quad (\text{A.19})$$

These set of linearized equations describe the plasma response model for the two droplet shaped plasma. The equations A.12, A.13, A.14, A.15, A.16, A.17, A.18, A.19, can be combine to be expressed in the matrix representation as,

$$M\vec{\dot{x}} + R\vec{\dot{x}} = \vec{\dot{u}} \quad (\text{A.20})$$

where, M , R , \vec{x} and \vec{u} are defined as,

$$M = \begin{pmatrix} M_{aa} & M_{av} & M_{ap1} & M_{ap2} & \frac{\partial M_{ap1}}{\partial R1} & \frac{\partial M_{ap2}}{\partial R2} & \frac{\partial M_{ap1}}{\partial Z1} & \frac{\partial M_{ap2}}{\partial Z2} \\ M_{va} & M_{vv} & M_{vp1} & M_{vp2} & \frac{\partial M_{vp1}}{\partial R1} & \frac{\partial M_{vp2}}{\partial R2} & \frac{\partial M_{vp1}}{\partial Z1} & \frac{\partial M_{vp2}}{\partial Z2} \\ M_{p1a} & M_{p1v} & L_{p01} & M_{p1p2} & M_{p1R1} & \frac{\partial M_{p1p2}}{\partial R2} & M_{p1Z1} & \frac{\partial M_{p1p2}}{\partial Z2} \\ M_{p2a} & M_{p2v} & M_{p2p1} & L_{p02} & \frac{\partial M_{p2p1}}{\partial R1} & M_{p2R2} & \frac{\partial M_{p2p1}}{\partial Z1} & M_{p2Z2} \\ \frac{\partial M_{p1a}}{\partial R1} & \frac{\partial M_{p1v}}{\partial R1} & M_{R1p1} & \frac{\partial M_{p1p2}}{\partial R1} & M_{R1R1} & M_{R1R2} & M_{R1Z1} & M_{R1Z2} \\ \frac{\partial M_{p2a}}{\partial R2} & \frac{\partial M_{p2v}}{\partial R2} & \frac{\partial M_{p2p1}}{\partial R2} & M_{R2p2} & M_{R2R1} & M_{R2R2} & M_{R2Z1} & M_{R2Z2} \\ \frac{\partial M_{p1a}}{\partial Z1} & \frac{\partial M_{p1v}}{\partial Z1} & M_{Z1p1} & \frac{\partial M_{p1p2}}{\partial Z1} & M_{Z1R1} & M_{Z1R2} & M_{Z1Z1} & M_{Z1Z2} \\ \frac{\partial M_{p2a}}{\partial Z2} & \frac{\partial M_{p2v}}{\partial Z2} & \frac{\partial M_{p2p1}}{\partial Z2} & M_{Z2p2} & M_{Z2R1} & M_{Z2R2} & M_{Z2Z1} & M_{Z2Z2} \end{pmatrix} \quad (\text{A.21})$$

$$R = \begin{bmatrix} R_a & 0 & 0 & 0 & 0 & 0 & 0 & 0 \\ 0 & R_v & 0 & 0 & 0 & 0 & 0 & 0 \\ 0 & 0 & R_{p1} & 0 & 0 & 0 & 0 & 0 \\ 0 & 0 & 0 & R_{p2} & 0 & 0 & 0 & 0 \\ 0 & 0 & 0 & 0 & 0 & 0 & 0 & 0 \\ 0 & 0 & 0 & 0 & 0 & 0 & 0 & 0 \\ 0 & 0 & 0 & 0 & 0 & 0 & 0 & 0 \\ 0 & 0 & 0 & 0 & 0 & 0 & 0 & 0 \end{bmatrix} \quad (\text{A.22})$$

$$\vec{x} = \begin{bmatrix} \delta I_a 0.3em \delta I_v \\ \delta I_{p1} \\ \delta I_{p2} \\ I_{p01} \delta R_1 \\ I_{p02} \delta R_2 \\ I_{p01} \delta Z_1 \\ I_{p02} \delta Z_2 \end{bmatrix} \quad (\text{A.23})$$

$$\vec{u} = \begin{bmatrix} \delta V_a 0.3em 0 \\ 0 \\ 0 \\ S_{R1} \\ S_{R2} \\ 0 \\ 0 \end{bmatrix} \quad (A.24)$$

The eq.(A.20), can be expressed in the state space form as,

$$\dot{\vec{x}} = A\vec{x} + B\vec{u} \quad (A.25)$$

where, $A = -M^{-1}R$, $B = M^{-1}$, \vec{x} denotes the states of the system, \vec{u} denotes the inputs of the system. This equation is called the state equation of the system and the eigenvalues of matrix A defines the stability of the system. The positive eigenvalues of matrix A , shows that the system is unstable.

Bibliography

- [1] BP Statistical Review of World Energy, 2016.
- [2] R. Albanese, F. Maviglia, P. J. Lomas, A. Manzanares, M. Mattei, A. Neto, F.G. Rimini, P.C. de Vries, and JET EFDA Contributors. Experimental results with an optimized magnetic field configuration for JET. *Nuclear Fusion*, 52:123010, 2012.
- [3] H. Anand, C. Galperti, S. Coda, B. P. Duval, F. Felici, T. Blanken, E. Maljaars, J.-M. Moret, O. Sauter, T. P. Goodman, and D. Kim. Distributed digital real-time control system for the TCV tokamak and its applications. *Nuclear Fusion*, 57:056005, 2017.
- [4] M. Anton, M. J. Dutch, and H. Weisen. Relative calibration of photodiodes in the soft-x-ray spectral range. *Review of scientific instruments*, 66(7):3762, 1995.
- [5] M. Anton, H. Weisen, M. J. Dutch, and et. al. X-ray tomography on the TCV tokamak. *Plasma Phys. Control. Fusion*, 38:1849, 1996.
- [6] J. F. Artaud, V. Basiuk, F. Imbeaux, M. Schneider, J. Garcia, G. Giruzzi, and et. al. The CRONOS suite of codes for integrated tokamak modelling. *Nuclear Fusion*, 50:043001, 2010.
- [7] K. J. Astrom and T. Hagglund. *Advanced PID Control*. ISA-The Instrumentation, Systems and Automation Society, 2006.
- [8] S. Barry, C. Nieswand, and S. L. Prunty. Far-infrared Polarimetry on the TCV tokamak. In *8th International Symposium on Laser-aided plasma diagnostics*, number September, 1997.
- [9] R. Behn, J. H. Rommers, R. A. Pitts, Z. A. Pietrzyk, R. Chavan, and B. Marletaz. A Thomson scattering diagnostic for measurements in the divertor region of TCV. *Review of scientific instruments*, 70(1):768, 1999.
- [10] V. A Belyakov, K. M. Lobanov, L. P. Makarova, and et. al. Plasma initiation stage analysis in tokamaks with TRANSMAX code. *Plasma Devices and Operations*, 11(3):193, 2003.
- [11] D. J. Campbell, E. Lazzaro, M. F. F. Nave, and et. al. Plasma resistivity and field penetration in JET. *Nuclear Fusion*, 28(6):981, 1988.

Bibliography

- [12] A. Coutlis, I. Bandyopadhyay, J. B. Lister, P. Vyas, R. Albanese, D. J. N. Limebeer, F. Villone, and J. P. Wainwright. Measurement of the open loop plasma equilibrium response in TCV. *Nuclear Fusion*, 39(5):663, 1999.
- [13] P.C. de Vries, A.C.C. Sips, H.T. Kim, P.J. Lomas, F. Maviglia, R. Albanese, I. Coffey, E. Joffrin, M. Lehnen, A. Manzanares, M. O'Mulane, I. Nunes, G. van Rooij, F.G. Rimini, M.F. Stamp, and JET EFDA Contributors. Characterisation of plasma breakdown at JET with a carbon and ITER-like wall. *Nuclear Fusion*, 53(5):053003, 2013.
- [14] L. Degtyarev, A. Martynov, S. Medvedev, F. Troyon, and L. Villard. External Kink Mode stability of tokamaks with finite edge current density in plasma outside separatrix. In *23rd EPS Conference on Controlled Fusion and Plasma Physics, Kiev*, page 1191, 1996.
- [15] L. Degtyarev, A. Martynov, S. Medvedev, and L. Villard. Beta limits against External Kink Modes in Tokamaks taking into account plasma outside separatrix. In *24th EPS conference, Berchtesgaden*, number vol. II, page 845, 1997.
- [16] B. P. Duval, J.-M. Moret, A. P. Rodrigues, and et. al. Digital Control System for the TCV Tokamak. In *14th IEEE-NPSS Real Time Conference, 2005.*, page 33, 2005.
- [17] W. C. Elmore and M. A. Heald. *Physics of Waves*. Dover Publications, 1985.
- [18] D. Fasel, A. Favre, J.-D. Pahud, A. Perez, and F. Puchar. 19 rectifiers to supply the coils of the TCV tokamak. In *Proc. 16th Symposium on Fusion Technology*, volume 2, 1991.
- [19] A. Favre, J.-M. Moret, R. Chavan, A. Elkjaer, D. Fasel, F. Hofmann, J. B. Lister, J.-M. Mayor, and A. Perez. Control of highly vertically unstable plasmas in TCV with internal coils and fast power supply. In *Proc. 19th Symposium on Fusion Technology*, 1997.
- [20] F. Felici. *Real-Time Control of Tokamak Plasmas : from Control of Physics to Physics-Based Control*. PhD thesis, Ecole Polytechnique Federale de Lausanne, 2011.
- [21] Jeffrey Freidberg. *Ideal Magnetohydrodynamics*. Cambridge University Press, 2014.
- [22] I. Furno. *Fast transient transport phenomena measured by soft X-ray emission in TCV tokamak plasmas*. PhD thesis, Ecole Polytechnique Federale de Lausanne, 2001.
- [23] T. P. Goodman and the TCV team. Experience in integrated control of the multi-megawatt electron cyclotron heating system on the TCV tokamak : the first decade. *Nuclear Fusion*, 48(5):054011, 2008.
- [24] R. S. Granetz, I. H. Hutchinson, and D. O. Overskei. Disruptive MHD activity during plasma current rise in Alcator A tokamak. *Nuclear Fusion*, 19(12):1587, 1979.
- [25] F. Hofmann. FBT - a free-boundary tokamak equilibrium code for highly elongated and shaped plasmas. *Computer Physics Communications*, 48(2):207, 1988.

-
- [26] F. Hofmann, M. J. Dutch, J. B. Lister, Y. Martin, and J.-M. Moret. On the possibility of creating doublet-shaped plasmas in TCV. In *23rd EPS Conference on Controlled Fusion and Plasma Physics, Kiev*, number 1, page 127, 1996.
 - [27] F. Hofmann, M. J. Dutch, and J.-M. Moret. Plasma shape control in TCV using MGAMS. In *22nd EPS Conference on Controlled Fusion and Plasma Physics , Bornemouth, UK*, number August, 1995.
 - [28] F. Hofmann, M. J. Dutch, D. J. Ward, M. Anton, I. Furno, J. B. Lister, and J.-M. Moret. Vertical instability in TCV: comparison of experimental and theoretical growth rates. *Nuclear Fusion*, 37(5):681, 1997.
 - [29] F. Hofmann and S. C. Jardin. Plasma shape and position control in highly elongated tokamaks. *Nuclear Fusion*, 30(10):2013, 1990.
 - [30] F. Hofmann, J. B. Lister, M. Anton, S. Barry, and et. al. Creation and control of variably shaped plasmas in TCV. *Plasma Phys. Control. Fusion*, 36:B277, 1994.
 - [31] F. Hofmann and G. Tonetti. Tokamak equilibrium reconstruction using Faraday rotation measurements. *Nuclear Fusion*, 28(10):1871, 1988.
 - [32] I. H. Hutchinson. *Principles of Plasma Diagnostics*. Cambridge University Press, 1987.
 - [33] F. Imbeaux, J. Citrin, J. Hobirk, G. M. D. Hogeweyj, F. Köchl, V. M. Leonov, S. Miyamoto, Y. Nakamura, V. Parail, G. Pereverzev, A. Polevoi, I. Voitsekhovitch, V. Basiuk, R. Budny, T. Casper, J. Ferreira, A. Fukuyama, J. Garcia, Y. V. Gribov, N. Hayashi, M. Honda, I. H. Hutchinson, G. Jackson, A. A. Kavin, C. E. Kessel, R. R. Khayrutdinov, C. Labate, X. Litaudon, P.J. Lomas, J. Lönnroth, T. Luce, V. E. Lukash, M. Mattei, D. Mikkelsen, I. Nunes, Y. Peysson, P. Politzer, M. Schneider, G. Sips, G. Tardini, S. M. Wolfe, and V. E. Zhogolev. Current ramps in tokamaks: from present experiments to ITER scenarios. *Nuclear Fusion*, 51(8):083026, 2011.
 - [34] ITER Physics Expert group. Chapter 8 : Plasma operation and control. *Nuclear Fusion*, 39(12):2577, 1999.
 - [35] G. L. Jackson, T. A. Casper, T. C. Luce, D. A. Humphreys, J. R. Ferron, A. W. Hyatt, E. A. Lazarus, R. A. Moyer, T. W. Petrie, D. L. Rudakov, and W. P. West. ITER startup studies in the DIII-D tokamak. *Nuclear Fusion*, 48(12):125002, 2008.
 - [36] G. L. Jackson, T. A. Casper, T. C. Luce, D. A. Humphreys, J. R. Ferron, A. W. Hyatt, J. A. Leuer, T.W. Petrie, F. Turco, and W. P. West. Simulating ITER plasma startup and rampdown scenarios in the DIII-D tokamak. *Nuclear Fusion*, 49(11):115027, 2009.
 - [37] G. L. Jackson, P. A. Politzer, D. A. Humphreys, and et. al. Understanding and predicting the dynamics of tokamak discharges during startup and rampdowna). *Physics of Plasmas*, 17(056116), 2010.

Bibliography

- [38] T. H. Jensen, R. K. Fisher, C. L. Hsieh, M. A. Mahdavi, V. Vanek, and T. Ohkawa. Confinement of plasma in the Doublet-II device. *Physical Review Letters*, 34(5):257, 1975.
- [39] L C Johnson and E Hinnov. Ionization, recombination, and population of excited levels in hydrogen plasmas. *Journal of Quantitative Spectroscopy and Radiative Transfer*, 13(4):333, 1973.
- [40] J. Kamleitner. *Suprathermal electron studies in Tokamak plasmas by means of diagnostic measurements and modeling*. PhD thesis, Ecole Polytechnique Federale de Lausanne, 2015.
- [41] H. T. Kim, A. C. C. Sips, P.C. de Vries, and JET EFDA Contributors. Plasma burn-through simulations using the DYON code and predictions for ITER. *Plasma Physics and Controlled Fusion*, 55:124032, 2013.
- [42] H.T. Kim, W. Fundamenski, A. C. C. Sips, and EFDA-JET. Enhancement of plasma burn-through simulation and validation in JET. *Nuclear Fusion*, 52(10):103016, 2012.
- [43] H.T. Kim, A. C. C. Sips, W. Fundamenski, and EFDA-JET. PSI effects on plasma burn-through in JET. *Journal of Nuclear Materials*, 438:S1271–S1274, 2013.
- [44] H.T. Kim and A.C.C. Sips. Physics of plasma burn-through and DYON simulations for the JET ITER-like wall. *Nuclear Fusion*, 53(8):083024, 2013.
- [45] Jayhyun Kim, S.W. Yoon, Y.M. Jeon, J.a. Leuer, N.W. Eidietis, D. Mueller, S. Park, Y.U. Nam, J. Chung, K.D. Lee, S.H. Hahn, Y.S. Bae, W.C. Kim, Y.K. Oh, H.L. Yang, K.R. Park, H.K. Na, and KSTAR team. Stable plasma start-up in the KSTAR device under various discharge conditions. *Nuclear Fusion*, 51(8):083034, 2011.
- [46] H. Kuwahara, A. D. Cheetham, and A. H. Morton. Observation of $m = 7 / n = 3$, $m = 5 / n = 2$ and $m = 3 / n = 1$ MHD modes during plasma current ramping in the LT-4 tokamak. *Nucle*, 26(8):1092, 1986.
- [47] M. Kwon, Y. K. Oh, H. L. Yang, and et. al. Overview of KSTAR initial operation. *Nuclear Fusion*, 51:094006, 2011.
- [48] H. B. Le, F. Felici, J. I. Paley, B. P. Duval, J.-M. Moret, S. Coda, O. Sauter, D. Fasel, and P. Marmillod. Distributed digital real-time control system for TCV tokamak. *Fusion Engineering and Design*, 89:155, 2014.
- [49] G. S. Lee, S. M. Hwang, C. S. Chang, H. Y. Chang, M. H. Cho, B. H. Choi, and et. al. The KSTAR project : An advanced steady state superconducting tokamak experiment. *Nuclear Fusion*, 40(3Y):575, 2000.
- [50] J. B. Lister, F. Hofmann, J.-M. Moret, and et. al. The control of tokamak configuration variable plasmas. *Fusion technology*, 32:321, 1997.

-
- [51] J. B. Lister, A. Sharma, D. J. N. Limebeer, Y. Nakamura, J. P. Wainwright, and R. Yoshino. Plasma equilibrium response modelling and validation on JT-60U. *Nuclear Fusion*, 42:708, 2002.
- [52] B. Lloyd, P. G. Carolan, and C. D. Warrick. ECRH-assisted start-up in ITER. *Plasma Phys. Control. Fusion*, 38:1627, 1996.
- [53] B. Lloyd, G. L. Jackson, T. S. Taylor, E. A. Lazarus, T. C. Luce, and R. Prater. Low voltage Ohmic and electron cyclotron heating assisted startup in DIII-D. *Nuclear Fusion*, 31(11):2031, 1991.
- [54] F. Maviglia, R. Albanese, A. Alonso, P. J. Lomas, and JET EFDA Contributors. Electromagnetic analysis of breakdown conditions in JET. *Fusion Engineering and Design journal*, 86:675, 2011.
- [55] J.-M. Moret, F. Buhlmann, D. Fasel, F. Hofmann, and G. Tonetti. Magnetic measurements on the TCV Tokamak. *Review of scientific instruments*, 69(6):2333, 1998.
- [56] J.-M. Moret, B. P. Duval, H. B. Le, S. Coda, F. Felici, and H. Reimerdes. Tokamak equilibrium reconstruction code LIUQE and its real time implementation. *Fusion Engineering and Design*, 91:1, 2015.
- [57] J.-M. Moret, F. Hofmann, S. Coda, and F. Piras. MGAMS revisited and revealed, 2011.
- [58] J.-M. Moret, J. Sinha, and H. Reimerdes. LIUQE for doublets, 2016.
- [59] D. Mueller. The physics of tokamak start-up. *Physics of Plasmas*, 20(2013):058101, 2013.
- [60] J. A. Nelder and R. Mead. A simplex method for function minimization. *The Computer Journal*, 7(4):308, 1965.
- [61] Yeong-kook Oh, W. C. Kim, K. R. Park, and et. al. Commissioning and initial operation of KSTAR superconducting tokamak. *Fusion Engineering and Design*, 84:344, 2009.
- [62] T. Ohkawa, C. C. Baker, N. H. Brooks, and et. al. Studies of non-circular cross-section toroids in the Doublet II and IIA device. In *Fifth IAEA conference, Tokyo, 11-15 November*, page 281, 1974.
- [63] T. Ohkawa and T. H. Jensen. Parameter studies for Tokamaks and Doublets. *Plasma Physics*, 12:789, 1970.
- [64] T. Ohkawa and H. G. Voorhies. Plasma current multipole experiments. *Physics Review Letters*, 22(24):1275, 1969.
- [65] J. Ongena, R. Koch, R. Wolf, and H. Zohm. Magnetic-confinement fusion. *Nature Physics*, 12:398, 2016.

Bibliography

- [66] J. I. Paley, S. Coda, B. P. Duval, F. Felici, J.-M. Moret, and TCV team. Architecture and Commissioning of the TCV Distributed Feedback Control System. In *2010 17th IEEE-NPSS Real Time Conference*, page 1, 2010.
- [67] R. Papoular. The genesis of toroidal discharges. *Nuclear Fusion*, 16:37, 1976.
- [68] F. Piras. *Extremely Shaped Plasmas to Improve the Tokamak Concept*. PhD thesis, Ecole Polytechnique Federale de Lausanne, 2011.
- [69] R. A. Pitts, R. Chavan, and J.-M. Moret. The design of central column protection tiles for the TCV tokamak. *Nuclear Fusion*, 39(10):1433, 1999.
- [70] H. Reimerdes. *MHD stability limits in the TCV tokamak*. PhD thesis, Ecole Polytechnique Federale de Lausanne, 2001.
- [71] A. Scarabosio, A. Pochelon, and Y. Martin. MHD Instabilities during Current Ramp Up as a Function of Plasma Shape in the TCV Tokamak. *Plasma Phys. Contr. Fusion*, 26B:3, 2002.
- [72] A. Tanga, P. R. Thomas, J. G. Cordey, and et. al. Start-up of the Ohmic phase in JET. In *Tokamak Start-up*, pages 159–180. 1986.
- [73] C. Theiler, B. Lipschultz, J. Harrison, B. Labit, H. Reimerdes, C. Tsui, W. A. J. Vijvers, B. P. Duva, S. Elmore, P. Innocente, U. Kruezi, T. Lunt, R. Maurizio, F. Nespoli, U. Sheikh, A. J. Thornton, S. H. M. van Limpt, K. Verhaegh, and N. Vianello. Results from recent detachment experiments in alternative divertor configurations on TCV. *Nuclear Fusion*, 57:72008, 2017.
- [74] J. S. Townsend. XVII. The Conductivity produced in gases by the motion of negatively charged ions. *Philosophical Magazine Series 6*, 1(2):198, 1901.
- [75] J. C. Wesley, T. Angel, C. J. Armentrout, D. R. Baker, F. P. Blau, G. Bramson, N. H. Brooks, R. W. Callis, R. P. Chase, J. C. Deboo, J. S. Degraessie, S. E. Ejima, R. K. Fisher, E. S. Fairbanks, R. J. Groebner, A. J. Lieber, J. M. Lohr, M. A. Mahdavi, F. B. Marcus, C. H. Meyer, P. I. Petersen, W. W. Pfeiffer, W. Petrie, P. J. Rock, M. T. Saito, R. P. Seraydarian, A. M. Sleeper, J. N. Smith, J. R. Smith, R. T. Snider, R. D. Stambaugh, R. Stav, T. Tamano, T. Taylor, D. F. Vaslow, T. S. Wang, and S. S. Wojtowicz. Shaping and characteristics of Ohmically heated non-circular plasmas in Doublet-III. In *8th IEAE Conference, Brussels*, number 1, page 35, 1980.
- [76] John Wesson. *Tokamaks*. CLARENDON PRESS-OXFORD, third edit edition, 2004.

Acknowledgements

First of all, I would like to take this opportunity to express my sincere gratitude to my supervisors Dr. Basil Duval and Dr. Holger Reimerdes for their guidance and encouragement. I have always appreciated that they have taken time out of their hectic schedules to clear my doubts and explain me the operation of the TCV tokamak. Their in-depth knowledge and experience in this field has also enhanced my understanding of tokamak and plasma physics. Thank you for your support and helping me improve.

A special thanks to Dr. Stefano Coda and Dr. Jean-Marc Moret to take time out of their busy schedules and help me understand the TCV control system and also with the implementation of the doublet scenario preparation in TCV.

I am very grateful to Dr. Federico Felici for teaching me the basics of control engineering and give his expert opinion on the control algorithms implemented during my thesis.

A big thanks to Dr. Cristian Galperti for his help and support to implement the different control algorithms in the digital control system. All the discussions with him have been very useful to improve my understanding of the control system and Simulink.

Thanks to Dr. Tim Goodman for helping me understand the ECRH system in TCV. I would also like to thank Dr. Benoit Labit, Dr. Patrick Blanchard and Dr. Christian Theiler for their help to understand the different diagnostics in TCV.

A special thanks to the whole TCV team, physics operators (PdJ's) and gyrotron operators (GdJ's) for their help and support for the TCV experimental campaign during my thesis work.

Thanks to Edith and Roxane for the help with administrative work during my thesis. Thanks a lot to Thushi for the friendly reminders to fill in the time sheets at the end of the month.

A big thanks to all my old and new office mates Fabio, Federico, Fabian, Mengdi, Alex, Francesco, Pedro for all the interesting discussions during these 5 years of my thesis. I am very grateful to Oulfa for her help in translating my abstract into French. A special thanks to Himank and Isha for being great friends and the wonderful time I had with them. I would also like to thank Zhouji for the valuable discussions on programming and plasma physics. I would also like to thank all the other SPC Ph.D. students for the memorable experience I had in SPC.

Acknowledgements

Also thanks a lot to my other friends in Lausanne Sowmya, Ketki, Anupam, Mayur, Manisha, Harpreet, Govinda and Naomi for the nice time I had here.

A special thanks to Ankur for being there always and bringing positivity in my life. I am very grateful to you for being so supportive and motivating me. I am very grateful to Kittu for being my cute little angel and always making me smile.

Last but not the least I would like to thank my parents who have always encouraged me to pursue my goals. I am very grateful to them for understanding me and standing my by side during the hard times in my life. Both of you have been my biggest strength and I could achieve this only because of you. I am very lucky to have you both as my parents and I dedicate my Ph.D. to both of you.

Lausanne, 11 July 2017

J. S.

Curriculum Vitae

Joyeeta Sinha

EPFL SB SPC SPC-TCV
PPH 273 (Bâtiment PPH)
Station 13
CH-1015 Lausanne

Email: joyeeta.sinha@epfl.ch
Tel.: +41 21 69 36588
Mob. No: +41786055628

Education:

Ph.D. in Plasma Physics , 2012-2017	École polytechnique fédérale de Lausanne , Route Cantonale, 1015, Lausanne, Switzerland. Dissertation Topic: <i>Plasma breakdown and current formation in single core and doublet configurations on TCV</i>
M.Tech in Nuclear Science & Technology , 2008-2011.	University of Delhi , New Delhi, India. Overall percentage: 81.3%.
Master Thesis , April 2010-August 2010	CERN (European Organization for Nuclear Research) , Switzerland. Dissertation: <i>Preparation of the measurement set-up for the evaluation of the Silicon sensors for the CMS Tracker upgrade.</i>
Masters in Nuclear Plant Design , 2009-2010.	Université de Paris Sud XI, ENSTA Paristech , France. Credits: 14.21/20, 60 ECTS.
B.Sc (Hons.) Physics , 2005-2008.	Hindu College, University of Delhi , New Delhi, India. Overall percentage: 86.2%.
Indian School Certificate Examination (ISCE) , 2004-05	Sacred Heart Convent School , Jamshedpur, India. Overall percentage: 93%
Indian Certificate of Secondary Education Examination (ICSEE) , 2003	D.B.M.S.English School , Jamshedpur, India. Overall percentage: 89%

Training experience:

Fusion reactor design , 2011	Institute of plasma research (IPR) , India.
Fission reactor simulator , 2010	Tricastin nuclear power plant , France.
Constructional aspect , 2010	EPR , Flamanville, France.

Fellowship & Awards:

French Scholarship, 2009-2010	Masters in Nuclear Energy , Paris, France
First position, 2004-2005	Indian School Certificate Examination , Jamshedpur, India

Publications and Conference:

41st European Physical Society Conference on Plasma Physics , Berlin, Germany, June 23-27 2014	Poster presentation: "Understanding the dynamics of the inductive plasma initiation in the TCV tokamak", P5.070.
4th FuseNet PhD Event in Lisbon, Portugal, November 18-20, 2014	Poster presentation: "Understanding the dynamics of the inductive plasma initiation in the TCV tokamak"
58th Annual Meeting of the APS Division of Plasma Physics , San Jose, United States, October 31-November 4, 2016	Poster presentation: "Understanding the dynamics of the inductive plasma formation and its application to create doublet shaped plasma in the TCV tokamak"

